

# Fusion Materials Research at Oak Ridge National Laboratory in Fiscal Year 2021



M. G. Burke  
Y. Katoh  
S. Melton  
F. W. Wiffen

Approved for public release.  
Distribution is unlimited.

**December 2021**

## DOCUMENT AVAILABILITY

Reports produced after January 1, 1996, are generally available free via US Department of Energy (DOE) SciTech Connect.

**Website** [www.osti.gov](http://www.osti.gov)

Reports produced before January 1, 1996, may be purchased by members of the public from the following source:

National Technical Information Service  
5285 Port Royal Road  
Springfield, VA 22161  
**Telephone** 703-605-6000 (1-800-553-6847)  
**TDD** 703-487-4639  
**Fax** 703-605-6900  
**E-mail** [info@ntis.gov](mailto:info@ntis.gov)  
**Website** <http://classic.ntis.gov/>

Reports are available to DOE employees, DOE contractors, Energy Technology Data Exchange representatives, and International Nuclear Information System representatives from the following source:

Office of Scientific and Technical Information  
PO Box 62  
Oak Ridge, TN 37831  
**Telephone** 865-576-8401  
**Fax** 865-576-5728  
**E-mail** [reports@osti.gov](mailto:reports@osti.gov)  
**Website** <http://www.osti.gov/contact.html>

This report was prepared as an account of work sponsored by an agency of the United States Government. Neither the United States Government nor any agency thereof, nor any of their employees, makes any warranty, express or implied, or assumes any legal liability or responsibility for the accuracy, completeness, or usefulness of any information, apparatus, product, or process disclosed, or represents that its use would not infringe privately owned rights. Reference herein to any specific commercial product, process, or service by trade name, trademark, manufacturer, or otherwise, does not necessarily constitute or imply its endorsement, recommendation, or favoring by the United States Government or any agency thereof. The views and opinions of authors expressed herein do not necessarily state or reflect those of the United States Government or any agency thereof.

**ORNL/TM-2021/2352**

Materials Science and Technology Division

**FUSION MATERIALS RESEARCH AT OAK RIDGE NATIONAL LABORATORY IN  
FISCAL YEAR 2021**

Compiled by:

M.G. Burke  
Y. Katoh  
S. Melton  
F.W. Wiffen

Date Published: December 2021

Prepared by  
OAK RIDGE NATIONAL LABORATORY  
Oak Ridge, TN 37831-6283  
managed by  
UT-BATTELLE, LLC  
for the  
US DEPARTMENT OF ENERGY  
under contract DE-AC05-00OR22725



We dedicate this report to the memory of our  
respected colleague

**LIZHEN TAN**



December 29, 1973 – January 22, 2022

*“Gone But Not Forgotten”*



## CONTENTS

<b>CONTENTS .....</b>	<b>v</b>
<b>1. INTRODUCTION .....</b>	<b>1</b>
<b>2. ADVANCED STEELS .....</b>	<b>3</b>
2.1 ADVANCE CASTABLE NANOSTRUCTURED ALLOYS FOR FIRST- WALL/BLANKET APPLICATIONS – AN ARPA-E GAMOW PROJECT .....	3
2.2 EFFECTS OF CARBON IN CASTABLE NANOSTRUCTURED ALLOYS – ALLOY DESIGN AND MECHANICAL PROPERTIES .....	5
2.3 EFFECTS OF CARBON IN A TAILORED CASTABLE NANOSTRUCTURED ALLOYS – ION IRRADIATION AND HELIUM IMPLANTATION .....	8
2.4 FRACTURE TOUGHNESS OF HFIR IRRADIATED F82H-MOD 3 .....	10
2.5 IRRADIATION HARDENING-EMBRITTEMENT OF RAFM AND ODS STEELS.....	12
2.6 THE EFFECT OF HELIUM ON RADIATION HARDENING OF F82H-IEA STEEL .....	15
2.7 TRANSMISSION ELECTRON MICROSCOPY OF IRRADIATED F82H STEELS.....	18
2.8 ATOM PROBE TOMOGRAPHY OF NANOCUSTERING IN IRRADIATED F82H.....	22
2.9 IRRADIATION CREEP OF F82H PRESSURIZED TUBES .....	24
2.10 STEM AND APT CHARACTERIZATION OF IRRADIATED EUROFER97.....	27
2.11 DEFECTS IN IRRADIATED ISOTOPICALLY-TAILORED RAFM STEELS .....	29
2.12 DEVELOPMENT OF TRANSFORMATION ENHANCED ODS Fe-Cr ALLOYS.....	32
2.13 ATOM PROBE TOMOGRAPHY OF HARDENING IN IRRADIATED ODS STEELS .....	34
2.14 Fe-Cr-Al ODS ALLOYS FOR FUSION REACTOR APPLICATIONS.....	39
2.15 EVALUATION OF ADVANCED 3Cr-3WVTa BAINITIC STEELS.....	44
2.16 MECHANICAL ALLOYING OF A NOVEL AUSTENITIC DUAL-PRECIPITATION STRENGTHENED STEELS .....	46
<b>3. CERAMIC AND COMPOSITE MATERIALS.....</b>	<b>49</b>
3.1 CHARACTERIZATION OF SiC: HIGH-ENERGY XRD AND MICRO- MECHANICAL TESTING .....	49
<b>4. HIGH HEAT FLUX AND PLASMA FACING MATERIALS.....</b>	<b>52</b>
4.1 ELECTRICAL RESISTIVITY OF IRRADIATED TUNGSTEN: PHENIX COLLABORATION.....	52
4.2 THERMAL DIFFUSIVITY OF IRRADIATED TUNGSTEN – PHENIX/TITAN COLLABORATION.....	57
4.3 TUNGSTEN BASE COMPOSITES .....	60
4.4 MATERIALS FOR FRONTIER IRRADIATIONS IN HFIR.....	63
<b>5. PLASMA MATERIALS INTERACTIONS.....</b>	<b>65</b>
5.1 DAMAGE-MECHANISM INTERACTIONS AT THE PLASMA-MATERIALS INTERFACE.....	65
<b>6. LIQUID METAL COMPATIBILITY .....</b>	<b>69</b>
6.1 LIQUID METAL COMPATIBILITY IN FUSION SYSTEMS.....	69
<b>7. EXPLORATORY, UNIQUE AND INNOVATIVE MATERIALS.....</b>	<b>71</b>
7.1 IMPROVED CREEP BEHAVIOR OF A COPPER ALLOY FOR FUSION APPLICATIONS .....	71
7.2 SOLID-STATE BREEDER MATERIALS – THEORY AND MODELING .....	74
<b>8. GASES IN MATERIALS.....</b>	<b>77</b>
8.1 THERMALLY-DRIVEN EVOLUTION OF HELIUM-IMPLANTED SURFACE GRAINS IN WARM-ROLLED TUNGSTEN.....	77

<b>9.</b>	<b>ADVANCED MANUFACTURING.....</b>	<b>80</b>
9.1	ADVANCED MANUFACTURING OF TUNGSTEN FOR DIVERTOR COMPONENTS – AN ARPA-E GAMOW PROJECT.....	80
9.2	TRANSITION STRUCTURE BETWEEN A RAFM STEEL AND TUNGSTEN – AN ARPA-E GAMOW PROJECT .....	84
9.3	BENCHMARKING ADDITIVE MANUFACTURING OF A 9Cr-2WVTa STEEL .....	87
9.4	ADDITIVE MANUFACTURING OF SILICON CARBIDE FOR FUSION APPLICATIONS .....	89
9.5	SOLID-STATE BREEDER MATERIALS BY ADDITIVE MANUFACTURING.....	91
<b>10.</b>	<b>COMPUTATIONAL MATERIALS SCIENCE .....</b>	<b>94</b>
10.1	MECHANICAL PROPERTIES AND RADIATION EFFECTS IN FUSION MATERIALS.....	94
10.2	STUDY OF DEFECT DIFFUSION PROPERTIES IN TUNGSTEN-BASED ALLOYS .....	97
<b>11.</b>	<b>INTERNATIONAL COLLABORATIONS .....</b>	<b>100</b>
11.1	US-JAPAN (QST) COLLABORATION ON STRUCTURAL MATERIALS .....	100
11.2	US-JAPAN FRONTIER PROGRAM .....	101
11.3	US-EUROFUSION PROJECT .....	102
<b>12.</b>	<b>EXPERIMENTAL TECHNIQUES AND LABORATORY SYSTEMS .....</b>	<b>103</b>
12.1	ADVANCED CHARACTERIZATION.....	103
12.2	SMALL SPECIMEN TEST TECHNIQUE (SSTT) DEVELOPMENT: MASTER CURVE FRACTURE TOUGHNESS ROUND ROBIN STUDY.....	107
12.3	MINIATURE MECHANICAL TESTS FOR TUNGSTEN-BASED MATERIALS.....	110
<b>13.</b>	<b>HFIR IRRADIATION PROGRAM.....</b>	<b>114</b>
13.1	CAPSULE DESIGN FOR FRONTIER TASK 1 HFIR IRRADIATIONS .....	114
13.2	CAPSULE DESIGN FOR FRONTIER TASK 2 HFIR IRRADIATIONS .....	116
13.3	FRONTIER TASK 3 – HFIR LIQUID METAL COMPATIBILITY CAPSULE .....	118
13.4	CAPSULE DESIGN FOR THE QST IRRADIATION OF F82H STEEL IN HFIR.....	120
13.5	HFIR IRRADIATION EXPERIMENTS.....	122
<b>14.</b>	<b>AWARDS, HONORS AND RECOGNITION .....</b>	<b>124</b>
14.1	AWARDS DURING FY2021.....	124
14.2	PUBLICATION HONORS IN FY2021 .....	125
14.3	PROFESSIONAL RECOGNITION IN FY2021 AND CONTINUING .....	126
<b>15.</b>	<b>PUBLICATIONS AND PRESENTATIONS IN FISCAL YEAR 2021 .....</b>	<b>128</b>
15.1	PAPERS PUBLISHED IN FY21.....	128
15.2	REPORTS ISSUED IN FY21.....	132
15.3	PAPERS SUBMITTED IN FY21.....	133
15.4	PRESENTATIONS DELIVERED IN FY21 .....	134

## LIST OF FIGURES

Figure 1.	Calculated temperature-dependent phase fraction in the VIM (left), ESR-top (middle), and ESR-bottom (right) ingots, indicating the potential formation of FeTiP in the VIM ingot due to its high-P content, large fractions of $M_2O_3$ and a small fraction of Z-phase in the ESR ingot due to the significantly increased oxygen and nitrogen content, and significantly reduced MC fraction in the ESR ingot due to the significantly reduced Ti and Ta content.....	4
Figure 2.	Calculated temperature-dependent phase mole fraction in CNA8 (solid lines) and CNA9 (dashed lines).....	6
Figure 3.	EBSD IPF of CNA8 and CNA9 indicating the grain structures and orientations.....	6
Figure 4.	EDS maps of Cr and Ti from CNA8 and CNA9, indicating the distribution of Cr-rich and Ti-rich precipitates.....	7
Figure 5.	Temperature-dependent (a) yield and ultimate strength and uniform and total plastic elongation, and (b) Charpy impact absorbed energies of CNA8 and CNA9.....	7
Figure 6.	(a) Specimen holder for single beam ion irradiation, showing the four thermocouples welded to the guide bars. Ion irradiation was perpendicular to the sample surface. (b) The calculated $Fe^{3+}$ damage dose (the 100 dpa case) and $He^{2+}$ doses are shown in red and blue, respectively, for a dual ion-irradiation experiment. A depth between 800 and 1400 nm achieves the targeted $\sim 10$ appm/dpa ratio. ....	9
Figure 7.	Comparison of depth-dependent cavity sizes for CNA8 and CNA9 that shows larger cavities in CNA9 at all depths for 50 dpa dual-ion irradiation. The bubble number density follows the trend of the $He^{2+}$ dose for both steels. ....	9
Figure 8.	Master Curve test results for F82H-Mod 3 steel irradiated in HFIR in the F13A5 rabbit capsule [1].....	11
Figure 9.	Effect of irradiation temperature on Master Curve reference temperature shift $\Delta T_0$ for F82H-Mod 3 steel irradiated to 18-28 dpa. ....	11
Figure 10.	Dose-dependence of Vickers microhardness for F82H-IEA heat, Eurofer97 variants, MA957, 12YWT and PM2000 after neutron irradiation at 300°C in HFIR.....	13
Figure 11.	Temperature-dependent Vickers microhardness for MA957, 12YWT and PM2000 alloys after neutron irradiation in HFIR. The neutron dose values are noted, and high dose F82H-IEA and Eurofer97 data are shown for comparison.....	13
Figure 12.	Vickers indentation hardness of F82H irradiated in HFIR to conditions shown in the figure. ....	16
Figure 13.	Engineering stress-strain curves of $^{54}Fe$ -F82H, F82H-IEA and unirradiated F82H-IEA, showing irradiation-induced hardening and loss of ductility. ....	16
Figure 14.	Annular dark-field (ADF) STEM image and STEM-EDX elemental maps obtained from the irradiated F82H-IEA heat, 4.5 dpa, 300°C. Discrete Cr-rich $M_{23}C_6$ carbides are visible. ....	19
Figure 15.	High Angle ADF (HAADF) STEM image and corresponding STEM-EDX elemental maps of a GB triple point in the irradiated F82H-IEA steel, 4.5 dpa, 300°C, showing elemental segregation of Cr/Si, some slight Ni segregation, and W/V depletion. ....	19

Figure 16.	Bright-field (BF) and low angle annular dark field (LAADF) STEM images of dislocation loops in HFIR irradiated F82H-IEA heat, 4.5 dpa, 300°C. Imaging performed with $\langle 110 \rangle$ type g vector indicated by the white arrows, close to $[001]$ zone axis, deviation parameter $s > 0$ . .....	20
Figure 17.	Bright-field STEM images showing $a\langle 100 \rangle$ loops (blue arrows) and $a/2\langle 111 \rangle$ type loops (red arrows), in HFIR irradiated F82H-IEA heat, 4.5 dpa, 300°C. The same area was tilted and analyzed using different g vectors. In this example, zone axis = $[001]$ , deviation parameter $s > 0$ . The direction of the g vectors is shown. ....	21
Figure 18.	APT analysis of HFIR irradiated F82H-IEA steel, $\sim 4.5$ dpa, 300°C. (a) Atom maps. (b) Iso concentration surface contour plots showing Mn and Si segregation/clustering in the material, including RIS to dislocation loops. More data analysis is ongoing with source APT software, OSCAR (S. Levine, A. Bhattacharya, C. Pareige, S.J. Zinkle et al. ORNL Fusion Semi Annual 2021). .....	23
Figure 19.	APT study of RIS on dislocation loops in HFIR-irradiated F82H-IEA steel, $\sim 4.5$ dpa, 300°C. The figure shows 2D contour plots of elemental segregation on a dislocation loop. ....	23
Figure 20.	STEM analysis of dislocation loops in HFIR irradiated Eurofer97 (2.94 - 3.24 dpa, $300 \pm 30^\circ\text{C}$ ) showing fraction of sessile $a\langle 100 \rangle$ loops and glissile $a/2\langle 111 \rangle$ loops. Blue arrows point to $a\langle 100 \rangle$ type loops while red arrows show $a/2\langle 111 \rangle$ type loops. Same area was imaged under different diffraction vectors (g vectors) noted in the figure, along $Z = [001]$ zone axis. APT characterization (lower section) shows RIS driven Mn-N co-segregation along dislocation lines and dislocation loops (using a X% Mn and Y% N iso-concentration surface). Quantitative APT analysis with OSCAR data analysis algorithm is ongoing. ....	28
Figure 21.	STEM analysis of $^{54}\text{Fe}$ -F82H alloy irradiated to $\sim 66$ dpa, 2.3 appm He/dpa at 300°C. Medium angle annular dark field image down $[001]$ zone axis showing large ( $> 50\text{-}70$ nm diameter) $a\langle 100 \rangle$ type dislocation loops (indicated by arrows). STEM-EDX elemental maps showed dislocation loops that appeared to include Cr segregation driven by RIS. Under and over-focus bright-field TEM images show nanoscale cavities in the irradiated steel because He generation. No grain boundary cavity formation was detected in this steel. ....	30
Figure 22.	Combined Cr and Si STEM-EDX elemental map indicating RIS of Si and depletion of Cr on boundaries. ....	31
Figure 23.	HR-TEM image of an $\text{M}_{23}\text{C}_6$ carbide in $^{54}\text{Fe}$ -F82H steel remained crystalline after irradiation to $\sim 66$ dpa, 2.3 appm He/dpa at 300°C. ....	31
Figure 24.	Microstructure of the M4 alloy. (a) Bright-field TEM micrograph showing the ultra-fine grain containing a high dislocation density and (b) EFTEM Fe-M jump ratio map showing the nano-size oxide particles dispersed within grains and on the grain boundary. ....	33
Figure 25.	Cross-section of the extruded M4 bar showing the ODS section enclosed in the steel can. ....	33
Figure 26.	Atom maps from PM2000 irradiated at 500°C to 8.7 dpa. (a) Cr map with 30 at.% iso-surfaces (b) Al map with 15 at.% iso-surfaces (c) Ti map with 3 at.% iso-surfaces. ....	35
Figure 27.	Atom maps from MA957 irradiated at 500°C to 8.7 dpa. (a) Cr map with 25 at.% iso-surfaces (b) Ni map with 3 at.% iso-surfaces (c) Ti map with 3 at.% iso-surfaces (d) TiO map with 2 at.% iso-surfaces. ....	36

**Figure 28.** Optical cross-section micrographs of FeCrAlZr powders, a) and b) as-received gas atomized powder, c) and d) powder after 2 h of ball milling, e) and f) powder after 40 h of ball milling. .... 41

**Figure 29.** Measurements from optical images shown in Figure 28, a) particle size, b) particle roundness. .... 41

**Figure 30.** BSE-SEM micrographs and corresponding Zr, Y and Fe EDS maps of FeCrAlZr(Y<sub>2</sub>O<sub>3</sub>) powders, a)-d) AR, e)-h) 2hBM, i-l) 40hBM. .... 42

**Figure 31.** (a) Charpy absorbed energy of the original and modified steel weldments measured at room temperature, and (b) the DBTT of the modified steel as a function of tempering condition. .... 45

**Figure 32.** Larson-Miller Parameter plot of the base and the cross-weld materials for the original and the modified 3Cr-3WVTa steels. .... 45

**Figure 33.** Log plot of the powder particles size plotted against the milling time. Individual particle sizes (diamond symbol) are shown as data points on the left side, while the mean, median, and the 5, 25, 75, and 95% quartiles are presented on the right side of each milling time. The 25 to 75 % area is shown as the blank area inside the 5 to 95% whiskers. Pure nickel powder particles assumed to be below 12 micron were not counted for the powder particle sizes. .... 47

**Figure 34.** STEM-MAADF images taken from a fine-grained austenite area (a) and a bimodal grain size area (b). The interaction of dislocations with ODS particles can be observed in (c) and the size and form of single ODS particles can be extracted from (d). High-resolution phase contrast image of a single ODS particle is exhibited in image (e). (f) Fast Fourier Transformation of (e) with a diffraction pattern simulation of austenite (red) and Y4Al2O9 (ICSD No. 252973, cyan pattern) being overlaid by SingleCrystal™. The austenite matrix is oriented along the [110] zone-axis, whereas the ODS particle is oriented in [010] zone-axis. .... 48

**Figure 35.** State-of-the-art X-ray diffraction analysis disclosed hidden damaged structure in SiC neutron irradiated with applied tensile stress. .... 50

**Figure 36.** (a) Representative secondary electron micrograph of a SiC/SiC composite micropillar with interface angle of 30° and (b) resolved shear stress at failure as a function of PyC interphase thickness for four types of SiC/SiC composites. In the graph (b), SCF and JCR indicate batch IDs of the matrix densification. HNS and SA3 stand for reinforcement fibers of Hi-Nicalon Type-S and Tyranno SA3 SiC fibers, respectively. .... 51

**Figure 37.** (Left) Diagram of 3 mm electrical resistivity measurement device. Positions of Cu electrodes are shown in orange. (Right) Effect of sample orientation and GB “length” in the direction of the current. .... 53

**Figure 38.** EBSD inverse pole figure grain orientation maps of unirradiated W samples revealed differences in crystallographic texture, grain size and shape for samples cut in the two different directions. Equivalent grain diameter histograms (bin size = 0.25µm) are presented for the equiaxed (A-T series) and histograms of the major/minor grain dimensions (B-T series). .... 54

**Figure 39.** Resistivity of B-oriented samples as a function of arbitrary measurement angle. Average values are shown in large, solid marks with individual measurements given with smaller, lighter marks. A sine wave fit is shown in the first row, approximating expected resistivity for any angle. Samples in the bottom row exhibit no such orientation dependence. The 0° angle is arbitrary for each sample. .... 54

**Figure 40.** BT-series resistivity averages plotted with respect to apparent GB density in the direction of the current, with a linear fit extrapolated to approximate the zero-grain boundary case..... 55

**Figure 41.** Electrical resistivity plotted as a function of calculated Re content for SCW and PCW materials. Data obtained for unirradiated W-Re alloys by Hasegawa [1] and Tanno [2] are included for comparison..... 55

**Figure 42.** Schematic showing the temperature-fast fluence irradiation matrix of SCW tensile samples from the PHENIX and TITAN projects. Initial work is divided into phases (represented by the colored ovals) to maximize early insight into thermal, dose, and shielding effects on thermal transport properties. .... 58

**Figure 43.** Selected thermal diffusivity curves for SCW irradiated at high (>690°C) temperature. (a) The unshielded data obtained as a function of fluence, and temperature exhibit a clear effect of dose on diffusivity. (b) Comparison of diffusivity as a function of irradiation temperature and fluence for the shielded and unshielded samples. The calculated transmutation levels are included in the legend..... 58

**Figure 44.** Relationship between thermal diffusivity data and Re + Os content measured at four different temperatures. Published literature thermal diffusivity values for irradiated and non-irradiated W/Re alloys and irradiated SCW are also included for comparison. .... 59

**Figure 45.** EBSD orientation maps of pure W and W-3%Re as-fabricated, heat-treated at 850°C, irradiated at 850°C and at 1100°C..... 60

**Figure 46.** A 4-point bend test of SiCf/W composite specimen. The material does not show overall brittle behavior..... 61

**Figure 47.** SiCf/W composite specimen after a 4-point bend test. It is noted that the interlayer where it is present allows debonding of the fiber..... 62

**Figure 48.** (a) Electron backscatter diffraction inverse pole figure map of electron beam additively-manufactured W. (b) W-Grade 92 steel laminate. (d) W-Cu particle-reinforced composite..... 63

**Figure 49.** (a) Fibers loaded in fiber holder tube before they are fully inserted into the tube. (b) Three loaded tubes with the 16 μm fibers extending beyond the ends of the tube. .... 64

**Figure 50.** An example of a bubble EELS spectrum with the extracted plasmon peaks (blue) and helium peak (pink). .... 66

**Figure 51.** A montage of EELS analyses of helium bubbles in tungsten nano-tendrils. Red markers are measured data, vertical dashed lines are the measured helium centroid, and the black lines are the model..... 66

**Figure 52.** Pressures at 300 K, estimated from  $n_{He}$  via the MLB equation of state, as related to bubble radius and estimated helium peak centroid energy..... 67

**Figure 53.** Several hypothetical configurations of bubbles within the experimental situation. .... 68

**Figure 54.** (a) Specimen mass change of TCL specimens in flowing Sn after 1000 h as a function of estimated temperature in the hot leg (HL) and cold leg (CL). Specimens of three FeCrAl alloys were exposed with large mass losses observed in the hot leg. Examples from two specimens are shown in (b)..... 70

**Figure 55.** Specimen mass change of TCL specimens in flowing PbLi after 1000 h as a function of estimated temperature in the hot and cold legs. The CVD SiC specimens are shown with closed diamonds and the aluminized F82H specimens are open circles. .... 70

Figure 56.	Calculated volume fraction of precipitates as a function of temperature for (a) CCNZ G2 and (b) CCNZ G1. ....	72
Figure 57.	Microstructure of as-aged CCNZ G2 alloy. (Left): micron scale Cr <sub>2</sub> Nb and Cr precipitates and (right): nanoscale Cr and Cu <sub>5</sub> Zr precipitates. ....	73
Figure 58.	The creep test results of CCNZ G2 alloy compared with those of CCZ and CCNZ G1 alloys, together with optical micrographs of the fractured creep specimens. ....	73
Figure 59.	Thermal conductivity as a function of temperature for Li <sub>2</sub> TiO <sub>3</sub> (a leading breeder candidate) and a Li <sub>2</sub> BeSiO <sub>4</sub> hybrid ceramic. Significantly greater thermal conductivity is achieved in the hybrid material. ....	75
Figure 60.	Phonon dispersion curves for unit cells of Li <sub>2</sub> TiO <sub>3</sub> with single Li-vacancies (denoted by the + in the cell figures at top.) In all configurations presented, the unit cells are stable. ....	76
Figure 61.	Phonon dispersion curves for 2 configurations of Li-di-vacancies within the unit cells. In the configuration on the left-hand-side, the structure is stable; the structure on the right is unstable. ....	76
Figure 62.	Orientation maps after TDS annealing for (a)-(c) as-polished and (d)-(i) He-implanted W. Inset at bottom-right in (f) shows corresponding IPF. ....	78
Figure 63.	Distribution histograms of (a) grain size and (b) misorientation angle $\theta$ for as-polished and He-implanted W before (black and green) and after (red and blue) annealing. ....	78
Figure 64.	Cross-section sample prepared from the He-implanted W specimen after TDS annealing. (a) IPF orientation map showing the He implanted region near the top surface. (b) FIB ion channeling contrast image showing the small surface grains and large bulk grains. (c) (d) TEM micrographs of the small surface grains and subsurface He bubbles. The superimposed plot in (c) and (d) is the calculated He concentration profile $C_{He}$ versus ion penetration depth, $L$ . ....	79
Figure 65.	a) Representative tungsten EBM build of density cubes for exploring process window b) Variation in density of tungsten density cubes as function of process parameters. ....	81
Figure 66.	Impact of cooling on the quality of the EBM tungsten material a) Representative near-IR layer image of a build containing nine tungsten density blocks being processed with identical process parameters. b) Thomas process map showing the imparted normalized energy for the tungsten processing space. c) Modified Thomas processing map accounting for cooling effects on the process space. ....	81
Figure 67.	Obtained fiber textures observed within the process window for high-quality crack free and dense EBM tungsten a) {001} fibers aligned with the build direction b) Mix {001}/{111} fiber texture c) {111} fiber texture aligned with the build direction. ....	82
Figure 68.	Repetitive vertical and transverse bulk tungsten sample builds fabricated through EBM for mechanical sample extraction for high temperature quasi-static tensile testing. ....	82
Figure 69.	Calculated isothermal sections of Fe-Cr-Al, V-Cr-Al and V-Cr-W phase diagrams at 1100 and 600°C, respectively, showing an extensive bcc single solid solution phase (green areas) with individual composition as red stars. ....	85
Figure 70.	Calculated interdiffusion composition profiles at RAFMS/FeCrAl, FeCrAl/VCrAl, VCrAl/VCrTi and VCrTi/W interfaces for given temperature and time. ....	85

Figure 71.	Microstructural characterization of interfaces in an as-sintered multilayer structure. ....	86
Figure 72.	STEM-EDX map and corresponding HR-TEM image and FFTs of V-rich MX and Cr-rich $M_{23}C_6$ . ....	88
Figure 73.	(a) Delta ferrite area fraction, martensite lath size and $M_{23}C_6$ sizes plotted for the different heat treatments; (b) Particle number density and particle sizes of MX and $M_{23}C_6$ precipitates are plotted for all conditions. ....	88
Figure 74.	Irradiation-induced volume changes in various SiC ceramics. ....	90
Figure 75.	Strength of irradiated SiC ceramics relative to strengths of unirradiated materials. ....	90
Figure 76.	a) SEM SE micrograph showing powder particles distributed on a carbon sticky pad. b) powder particle size distribution as determined from the micrograph. ....	92
Figure 77.	Higher magnification SEM SE micrograph showing surface topography of a typical powder particle. ....	92
Figure 78.	XRD results a) from both materials showing same structure and phase; b) pair distribution function showing evidence of loss of short-range ordering in the powder compared to the bulk. ....	93
Figure 79.	Photograph showing the results from the first attempt of binder jet print at ORNL. The resultant material was not adequately consolidated. ....	93
Figure 80.	Stress-strain dependence of an $\frac{1}{2}\langle 111 \rangle \{110\}$ edge dislocation passing through the center of spherical 100 at.% Re coherent bcc precipitates of different sizes at 300K. The maximum stress on each curve is the corresponding critical resolved shear stress (CRSS) and is shown in the plot insert. ....	95
Figure 81.	Calculated CRSS of all precipitates modeled in this work and voids in W from [3] for the ambient temperature of 300K treated within the BSK model [1, 2]. ....	95
Figure 82.	Analysis of data generated from the model. a) The temporal evolution of the distance between the interstitial defect (dumbbell or crowdion) center and Re atom (blue line): $\Delta = d_{\text{int}} - d_{\text{Re}}$ . The green line indicates the instant interstitial atom configuration: “0” means it is a $\frac{1}{2}\langle 110 \rangle$ dumbbell whereas “1” means that is a $\frac{1}{2}\langle 111 \rangle$ crowdion.; b) The temporal evolution of the distance between the initial, $d_0$ , and instant, $d_t$ , positions of interstitial defect (dumbbell or crowdion) center (red line) and Re atom (blue line) $\Delta = d_t - d_0$ . ....	98
Figure 83.	Temporal evolution of mean square displacements (MSD) of W (blue line) and Re (red line). Displacements of Re-atom are multiplied by 10 for visualization. ....	98
Figure 84.	Mass spectra in the 4-12 m/c (Da) region of a $TiB_2$ specimen displaying the single and double charged $^{10/11}B$ isotopic peaks as a function of laser power during APT data acquisition. A change in the peak ratios is observed. ....	104
Figure 85.	Mass-to-Charge-State for the range in which the double charge state Fe isotopes lie. The green line shows the data obtained from APT experiments; the red circles shows the relative natural abundances scaled to the $^{56}Fe^{2+}$ peak. An excess of $^{54}Fe$ , $^{57}Fe$ , and $^{58}Fe$ is evident. ....	105
Figure 86.	APT atom maps of the primary elements from the refractory high entropy alloy. A uniform distribution of elements is observed in all cases. Artifacts observed in the Ta and W maps arise from specimen fractures during data acquisition. The length of the reconstruction is 250 nm. ....	106
Figure 87.	Master Curve test results for Eurofer97 batch-3 in the top row and F82H-BA12 in the bottom row. ....	108

**Figure 88.** Comparison of measured Master Curve reference temperature  $T_{0Q}$  for Eurofer97 batch-3 and F82H-BA12 tested with three different specimen types. Error bars correspond to  $\pm$  one standard deviation. .... 108

**Figure 89.** Effect of fatigue pre-crack front straightness on the measured Master Curve reference temperatures. .... 109

**Figure 90.** Bend test results for the 3 mm discs. Specimens were 0.5 mm thick except for polycrystalline tungsten (PCW) that was machined to a thickness of 0.25 mm. Specimens were bent until fracture and the elastic strain is not shown. Only the 0.25 mm thick PC-W and W-Cu showed room temperature plasticity. Tungsten-silicon carbide (W-SiC) fractured in the elastic region for discs of the thicknesses tested. .... 111

**Figure 91.** Shear punch test results for W-Cu shown with the elastic region removed and other specimens with the elastic region shown to best illustrate room temperature brittleness. Five shear punch tests were performed on tabs from W-Cu tensile specimens. The other tests were performed on 0.5 mm thick W-SiC and PCW discs and on a 0.25 mm thick PCW disc. .... 111

**Figure 92.** Span-thickness analysis to select the appropriate thickness for room temperature testing W within the specimen size constraints for neutron-irradiated materials. At a 16 to 1 ratio (blue), the load measurement was near the limits of the load cell sensitivity. Additionally, the preloading due to the weight of load train parts caused the bend stress calculation to be artificially low by 220 MPa. The sample with the 8 to 1 ratio (black) showed the most plasticity consistent with the ductile fracture surface. At a 6 to 1 ratio (red), curve was closer in strength value to the brittle fracture stress for the 4 to 1 ratio sample and exhibited little plasticity. All W specimens at a ratio of 4 to 1 showed brittle fracture, with Weibull statistic deviations in flexural strength. .... 112

**Figure 93.** Fracture surfaces are oriented so the side that was in tension during the 3-point bend test is shown on the lower edge of each image. The a) PCW and b) W-Cu composite have indications of ductile-like fracture. The c) W-SiC composite image displays the secondary electron (SE) contrast between the darker SiC and brighter W. This material exhibited brittle failure. .... 112

**Figure 94.** SEM SE images of the die side of the discs (opposite of the side the punch acted on) after shear punch testing. a) The punch cleanly removed a cylindrical section from the W-Cu sample. On the inside walls of the hole, vertical striations are seen because of the ductility of the Cu. b) The PCW micrograph shows the fractured partially-punched out center of the specimen with no view of the shear fracture surface. .... 113

**Figure 95.** Results of the 3-point bend test of irradiated specimens at a 4:1 span:thickness ratio. PCW with 1.5  $\mu$ m grain size shown by circles. SCW with (110) face at the tension surface shown by triangles. Color corresponds to dose: black = 0 dpa, orange = 0.30 dpa, red = 0.70 dpa. .... 113

**Figure 96.** Representative thermal analysis of Frontier Task 1 tungsten irradiation capsules with 3 mm diameter disc design (left) and fracture toughness design (right) for irradiation in HFIR. .... 114

**Figure 97.** Frontier Task 1 W fracture toughness capsule build, with fiber option. .... 115

**Figure 98.** W fiber container with fiber specimens prior to fiber ends trimmed. .... 115

**Figure 99.** FR32 – 3mm diameter disc capsule parts at beginning of assembly. .... 115

**Figure 100.** Representative thermal analysis of Frontier Task 2 tungsten irradiation capsules with 6 mm diameter disc design for irradiation in HFIR. .... 116

**Figure 101.** Layout of Frontier 6 mm diameter disc capsule prior to assembly. .... 117

**Figure 102.** W and W/Cu 6 mm diameter disc specimens. .... 117

**Figure 103. CAD representation (left) with Sn hidden for ease of viewing and representative thermal analysis (right) of Frontier Task 3 molten Sn corrosion irradiation capsules. .... 118**

**Figure 104. Frontier Task 3 molten Sn rabbit capsule internal parts. .... 119**

**Figure 105. Frontier Task 3 molten Sn rabbit capsule specimen region assembly..... 119**

**Figure 106. Components for the FH51 low dose tensile capsule during assembly..... 120**

**Figure 107. FH62 low dose bend bar capsule components during assembly..... 121**

## LIST OF TABLES

<b>Table 1. Summary of the non-irradiated and irradiated tensile properties. <math>\sigma_{YS}</math> = yield stress, <math>\sigma_{UTS}</math> = ultimate tensile stress, UEp = uniform plastic elongation, TEp = total plastic elongation.....</b>	<b>17</b>
<b>Table 2. Summary of continuous dilatometer analysis [1] of PCT TMs.....</b>	<b>25</b>
<b>Table 3. Summary of thermal design results and achieved PCT temperature from inner TMs .....</b>	<b>25</b>
<b>Table 4. Summary of thermal design results and achieved PCT temperature from holder TMs .....</b>	<b>25</b>
<b>Table 5. OSCAR APT Cluster Analysis Parameters .....</b>	<b>34</b>
<b>Table 6. Quantitative results for Cr-rich clusters in neutron irradiated PM2000.....</b>	<b>35</b>
<b>Table 7. Quantitative results for Al/Ti rich clusters in neutron irradiated PM2000.....</b>	<b>36</b>
<b>Table 8. Quantitative results for Cr-rich clusters in neutron-irradiated MA957.....</b>	<b>37</b>
<b>Table 9. Quantitative results from Ni/Ti-enriched solute clusters in neutron-irradiated MA957.....</b>	<b>37</b>
<b>Table 10. Hall flow test results.....</b>	<b>41</b>
<b>Table 11. Nominal compositions of the steels in weight percent (balance Fe).....</b>	<b>44</b>
<b>Table 12. Expressions for estimating the obstacle strength parameter <math>\alpha</math> for Re precipitates and voids, and particular values of <math>\alpha</math> for obstacles of different diameters. The core radius of the <math>\frac{1}{2}\langle 111 \rangle</math> dislocation is taken as its Burgers vector length in W at T=300K: <math>r_0= b =0.273\text{nm}</math>.....</b>	<b>96</b>
<b>Table 13. HFIR operating record for FY2021.....</b>	<b>122</b>
<b>Table 14. The rabbit capsules to continue irradiation in HFIR .....</b>	<b>122</b>
<b>Table 15. The rabbit capsules that completed irradiation in FY2021.....</b>	<b>123</b>

## 1. INTRODUCTION

*M.G. Burke, F.W. Wiffen and Yutai Katoh ([Katohy@ornl.gov](mailto:Katohy@ornl.gov))*

The materials science challenge of providing a suite of suitable materials to satisfy the technology to achieve fusion energy is addressed in this ORNL program. The inability of currently available materials and components to withstand the harsh fusion nuclear environment requires development of new materials, and an understanding of their response to the fusion environment. The overarching goal of the ORNL fusion materials program is to provide the applied materials science support and materials understanding to underpin the ongoing DOE Office of Science - Fusion Energy Sciences program, in parallel with developing the materials for fusion power systems. In this effort the program continues to be integrated both with the larger U.S. and international fusion materials communities and with the U.S. and international fusion design and technology communities.

The excitement of this program comes from the priorities given to this subject in the two recent fusion reviews, by the FESAC and NAS committees. An important element of those recommendations is the support for the long-advocated Fusion Prototypic Neutron Source, and for the Fusion Pilot Plant study that will help focus program direction and efforts.

This tenth annual report of the ORNL Fusion Reactor Materials Program summarizes the accomplishments in Fiscal Year 2021 (FY). The year was again productive but reflected somewhat the restrictions due to COVID19. The prevalence of COVID19 in the U.S. disrupted all program work since mid-March 2020. No program travel, workshops, nor in-person technical meetings occurred during FY2021. Our program responded with somewhat limited experimental work, actively working from home, and videoconferencing replacing the more “normal” workflow. This has increased the flow of technical papers into the publication pipeline. In this new work regime ORNL access has been allowed for use of the experimental equipment but has not allowed the normal flow of assignees from our international collaboration partners. It has also limited access for students doing thesis research using the ORNL experimental equipment. However, productivity has steadily returned to near-normal levels over the latter half of FY2020 and throughout FY2021 as team members adapted to work-from-home challenges and the limitations of COVID19 avoidance.

Following the pattern of planning used in this program, work for the two years FY2020 and FY2021 was focused on having the data and productivity to support a strong presence at the ICFRM20, organized by Spain scheduled for October 2021. The result was more than 40 authored and coauthored papers that will be presented to the virtual gathering of the world fusion materials community.

Two ARPA-E GAMOW proposals selected in FY2020 were initiated in FY2021. A collaboration with LLNL and TAMU is exploring Additive Manufacturing options for fabrication of Plasma Facing Components, and an ORNL effort is scaling up Castable Nanostructured Alloy production. Both projects will be active over the next three years.

The major elements of this long-running ORNL program continue to pursue development of low activation structural materials, with the greatest effort directed at the Reduced Activation Ferritic/Martensitic Steels, higher strength/higher creep resistant/coolant compatible/radiation tolerant advanced steels, and Silicon Carbide Composites. Tasks within the steels portfolio are pursuing several options for advanced steels: These include development of Castable Nanostructured Alloys, exploratory work on Bainitic steels and Oxide Dispersion Strengthened (ODS) steels, and aluminum-containing iron-based alloys that promise improved liquid metal compatibility. Parallel to this is the increased emphasis on radiation effects, high heat flux testing and the development of refractory metals, especially tungsten

materials. This includes the development and evaluation of new tungsten materials, and the study and understanding of the irradiation performance of tungsten. Newer efforts also support the Blanket and Fuel Cycle Programs. In each case the materials are being developed in a design-informed fashion where properties improvements are led by fusion-relevant design studies and directed at advancing the Technology Readiness Level of the material systems.

Effort continues on tasks initiated in FY2019, the investigation of application of Additive Manufacturing (AM) technologies to the production of materials and components for fusion systems. The production of simulated tungsten divertor components using electron beam powder bed fusion and binder jet technologies are underway, with exploratory trials of AM to produce silicon carbide composites also undertaken this year.

Limited integrated fundamental modeling is included in the program, directed especially at understanding experimentally observed behavior. Recent focus has been on the irradiation effects in the W-Re-Os system and on exploring new options for solid ceramic tritium breeder candidate materials.

This fusion materials program makes heavy reliance on neutron irradiation in the High Flux Isotope Reactor (HFIR) at ORNL, complemented by limited use of ion irradiation facilities when these are better suited to explore fundamental aspects of materials behavior under irradiation. Associated with the HFIR irradiations is the infrastructure needed to evaluate the effects of the irradiation on the material properties and microstructures. This infrastructure includes: 1) hot cells, which are needed for capsule/experiment disassembly and for testing highly radioactive specimens; and 2) the Low Activation Materials Development and Analysis (LAMDA) Laboratory, which contains shielded test equipment for lower level radioactive materials. Maintaining, upgrading, and replacing these state-of-the-art suite of instruments and test stands is an ongoing effort, shared with other programs focused on similar needs.

Limited support of the FES System Studies team, “Materials Engineering in Support of the FNSF Program” provides materials expertise to that team and is a valuable link to the design community.

The fusion materials effort consists of a wide array of tasks and collaborations with both US and international partners. The major continuing international collaborating partners are the Japan Agency for Quantum and Radiological Science and Technology (QST, focused on structural materials), the Japanese National Institute for Fusion Sciences (the FRONTIER collaboration) and the Karlsruhe Institute of Technology in Germany, acting for EUROfusion (examining steel materials).

Productivity and recognition of the ORNL Fusion Materials Program is demonstrated in Chapter 14 Awards, Honors and Recognition and Chapter 15 Publications and Presentations.

This research is funded by the Department of Energy, Office of Science, Office of Fusion Energy Sciences. We would like to acknowledge the active guidance that Daniel Clark of FES provides in setting the direction and priorities of this work, and his help in the effective conduct of the program.

## 2. ADVANCED STEELS

### 2.1 ADVANCE CASTABLE NANOSTRUCTURED ALLOYS FOR FIRST-WALL/BLANKET APPLICATIONS – AN ARPA-E GAMOW PROJECT

L. Tan, W. Tang, T. Graening, Y. Yang ([yangying@ornl.gov](mailto:yangying@ornl.gov)), Y. Katoh (ORNL), K. Field (U. of Michigan)

#### OBJECTIVE

This project is to establish a US RAFM (Reduced-Activation Ferritic-Martensitic) steel based on the carbide CNAs (Castable Nanostructured Alloys) for use in the integrated first-wall and blanket systems of advanced fusion reactors by demonstrating the viability and advantages of CNAs through the production and performance evaluation of ton-scale heats.

#### SUMMARY

The comparison of laboratory-scale carbide-CNAs with laboratory-scale carbonitride-CNAs and literature data for Eurofer97, F82H, and oxide-dispersion-strengthened (ODS) alloy such as 14YWT indicated the advantages of carbide-CNAs. This provides the foundation for the scale-up study of carbide-CNA under the ARPA-E GAMOW project. The project was started on March 15, 2021. A summary report itemizing the benchmark conditions for the scale-up carbide-CNAs was produced after a comprehensive review of literature data relevant to this project. The other major task in this fiscal year is procuring ton-scale heat of carbide-CNA and weld wires. The chemistry of the first melted ingot of the ton-scale carbide-CNA had significant deviations from the target composition with some impurity element content noticeably higher than the specified upper limits. Because of the unacceptable steel chemistry and no constructive resolutions to solve this issue, and subsequent discussions with the sponsors (ARPA-E and FES) of this project, the decision was made to procure the ton-scale heat of carbide-CNA from a foreign company. A Germany company (producer of Eurofer97) and a Japanese company (producer of F82H) are being contacted to select a producer of the ton-scale carbide-CNA. The other procurement, a 1/4-ton heat of carbide-CNA as the source for 1 inch-diameter rods and 0.045-inch-diameter weld wires, resulted in a 1/4-ton carbide-CNA ingot with satisfactory chemistry.

#### PROGRESS AND STATUS

Since the start of the ARPA-E GAMOW project, this work has been focused on three tasks.

- The first task is a comprehensive literature review to determine benchmark conditions for the scale-up of carbide-CNAs. This task was successfully completed in the third quarter of FY2021.
- The second task is procuring ton-scale heats of carbide-CNA and weld wires. Because of the high priority of “U.S. Manufacturing Plan” for this project, the procurement was conducted domestically. The ton-scale heat of carbide-CNA order was placed in June 2021. The first ingot had been melted by vacuum induction melting (VIM) followed by electro-slag remelting (ESR), which yielded an ingot chemistry significantly off the target composition with some impurity element content noticeably above the specified upper limits for the carbide-CNA. The ingot chemistry is not acceptable for this project’s studies as suggested in *Figure 1* and the vendor cannot provide constructive resolutions to solve the composition issue. After discussions with the sponsors (ARPA-E and FES) of this project, the decision was made to open the procurement of the ton-scale heat of carbide-CNA to foreign companies. A Germany company (producer of Eurofer97) and a Japanese company (producer of F82H) are being contacted to select a company to produce the ton-scale heat of carbide-CNA. The order for starting stock for weld wires (0.045-

inch-diameter) was placed in August 2021. The wire will be converted from 1-inch-diameter rods processed from a 1/4-ton heat of carbide-CNA. The chemistry of this 1/4-ton ingot meets the target chemistry requirement.

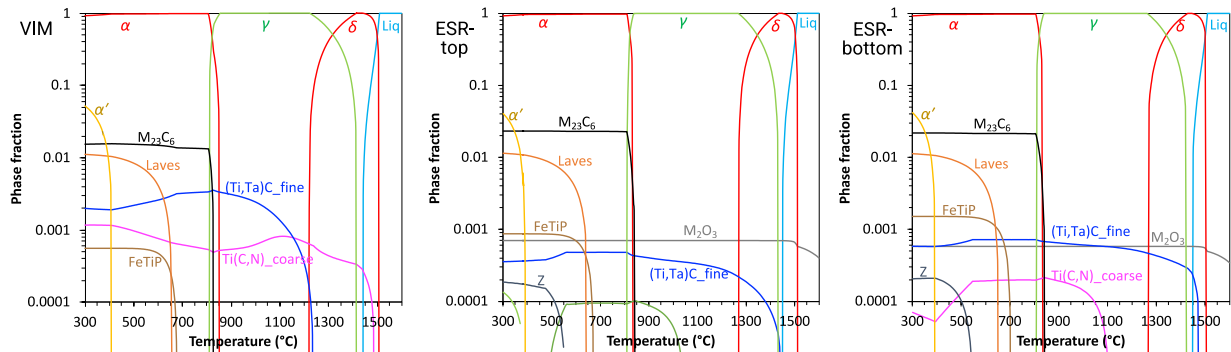


**Figure 1. Calculated temperature-dependent phase fraction in the VIM (left), ESR-top (middle), and ESR-bottom (right) ingots, indicating the potential formation of FeTiP in the VIM ingot due to its high-P content, large fractions of  $M_2O_3$  and a small fraction of Z-phase in the ESR ingot due to the significantly increased oxygen and nitrogen content, and significantly reduced MC fraction in the ESR ingot due to the significantly reduced Ti and Ta content.**

- The third task, Technology-to-Market (T2M), is in progress. The project had a poster at the ARPA-E Summit 2021, which had a successful exposure and established connections with a few privately funded Fusion startup companies.

### Future Work

Procure ton-scale carbide-CNA from a foreign company; Evaluate microstructure and basic mechanical properties of the 1-inch-diameter rods from the 1/4-ton ingot; Continue the T2M activities.

## 2.2 EFFECTS OF CARBON IN CASTABLE NANOSTRUCTURED ALLOYS – ALLOY DESIGN AND MECHANICAL PROPERTIES

L. Tan, W. Zhong, and Y. Yang ([yangying@ornl.gov](mailto:yangying@ornl.gov))

### OBJECTIVE

Preliminary performance comparisons showed advantages of carbide CNAs (Castable Nanostructured Alloys) over carbonitride-CNAs. To further improve carbide-CNAs, one direction is to refine the alloying composition. Carbon in the alloy is critical to stabilizing the austenite phase over a larger temperature range and to determining the formation and amount of carbides. The goal of this work is to understand the effects of carbon content on the microstructures and mechanical properties of carbide-CNAs.

### SUMMARY

Two heats of CNAs, CNA8 and CNA9, were designed and fabricated, with CNA9 having about one order of magnitude less  $M_{23}C_6$  than CNA8, but with a similar amount of MC to that of CNA8. Results of microstructural characterization indicated comparable grain structures for the two steels with MC in two size levels in the two steels, and with noticeable  $M_{23}C_6$  in CNA8 but no detectable  $M_{23}C_6$  in CNA9. Tensile tests indicated comparable strength and elongation at temperatures from room temperature to 700°C. Charpy impact tests showed higher upper-self energy (USE) with higher ductile-brittle transition temperature (DBTT) for the low-C CNA9 compared with the high-C CNA8. Both heats have significantly higher USE and lower DBTT than Grade 91.

### PROGRESS AND STATUS

Because of the high coarsening rate of Cr-rich  $M_{23}C_6$ , minimizing the  $M_{32}C_6$  amount while maintaining a high density of MC (M=Ti/Ta/W/etc.) is hypothesized to provide better mechanical properties for ferritic-martensitic steels, including CNAs. Therefore, two steels were designed with different carbon contents using computational thermodynamics to promote maximized comparable amounts of MC but significantly different amounts of  $M_{23}C_6$ . Because two previous heats showed noticeably different grain structures, two new laboratory-scale heats of high-C CNA8 and low-C CNA9 were fabricated by vacuum arc melting into large buttons and then vacuum drop casting into  $25.4 \times 25.4 \times 152$  mm. The ingots were hot rolled to 6.3-mm thick plates and finally normalized for 15 minutes at 1100°C and 1050°C, respectively, then tempered for 30 minutes at 750°C and air cooled.

**Figure 2** shows the calculated temperature-dependent phase mole fractions based on the measured chemistry of the plates, with the solid and dashed lines denoting the phases in CNA8 and CNA9, respectively. Other than the comparable MC amount, the  $M_{23}C_6$  amount is about one order of magnitude lower in the low-C CNA9. The reduced carbon also decreased the austenite temperature range in CNA9 and thus altered its normalization temperature as described above.

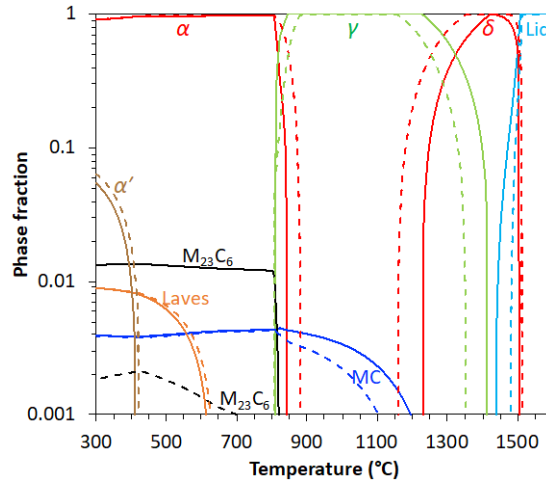


**Figure 2.** Calculated temperature-dependent phase mole fraction in CNA8 (solid lines) and CNA9 (dashed lines).

**Figure 3** shows electron backscattered diffraction (EBSD) inverse-pole figures (IPF) taken from CNA8 and CNA9, showing fine microstructures containing laths. It indicates comparable grain sizes without preferred grain orientations for the two steels.

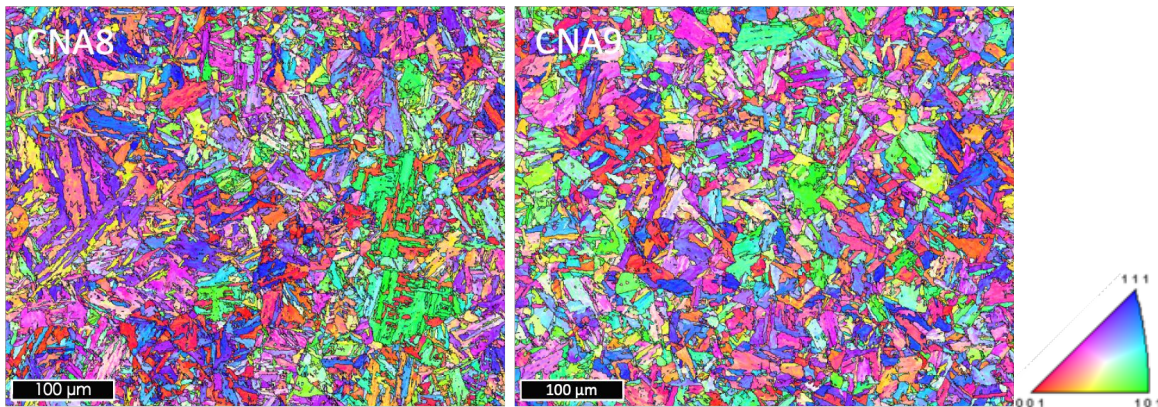


**Figure 3.** EBSD IPF of CNA8 and CNA9 indicating the grain structures and orientations.

**Figure 4** shows energy dispersive x-ray spectroscopy (EDS) maps of Cr and Ti, acquired in scanning transmission electron microscopy (STEM) mode. The EDS maps indicate that CNA8 contains both MC and  $M_{23}C_6$  whereas CNA9 only shows MC because the small  $M_{23}C_6$  amount in CNA9 is difficult to detect by TEM; this is consistent with the alloy design (**Figure 2**). MC precipitates have both coarse and fine sizes, with the fine MC at significantly higher number density. The fine MC in CNA8 is not as uniformly distributed in the matrix as that in CNA9. The fine MC in CNA8 is comparable to that in CNA9 Ti-map **Figure 4** (right) in some regions but is coarser MC in other regions.

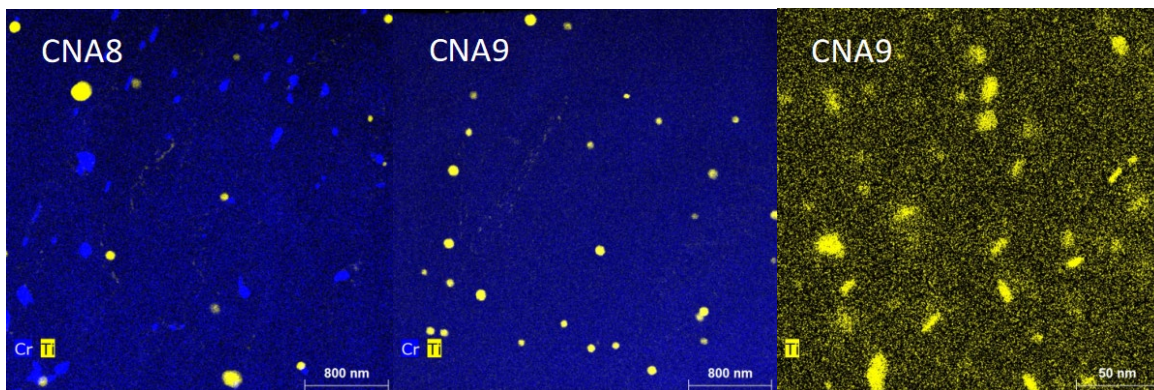


**Figure 4.** EDS maps of Cr and Ti from CNA8 and CNA9, indicating the distribution of Cr-rich and Ti-rich precipitates.

Tensile tests were conducted for the two steels using type SS-3 miniature specimens oriented along the rolling direction; the temperature-dependent yield strength, ultimate tensile strength, uniform plastic elongation (UPE), and total plastic elongation (TPE) results are shown in **Figure 5a**. The low-C CNA9 had strength and elongation comparable to the high-C CNA8. Half-size Charpy V-notch impact specimens in the T–L (transverse–longitudinal) orientation were tested to determine upper-shelf energy (USE) and ductile-brittle transition temperature (DBTT). The test results and the fitted curves for the two heats are shown in **Figure 5b** and are compared to literature results of Grade 91 tested using the same type specimens. The two heats had significantly higher USE and lower DBTT than Grade 91. The low-C CNA9 had higher USE but higher mathematical DBTT ( $T_0 = USE/2$ ) than the high-C CNA8.

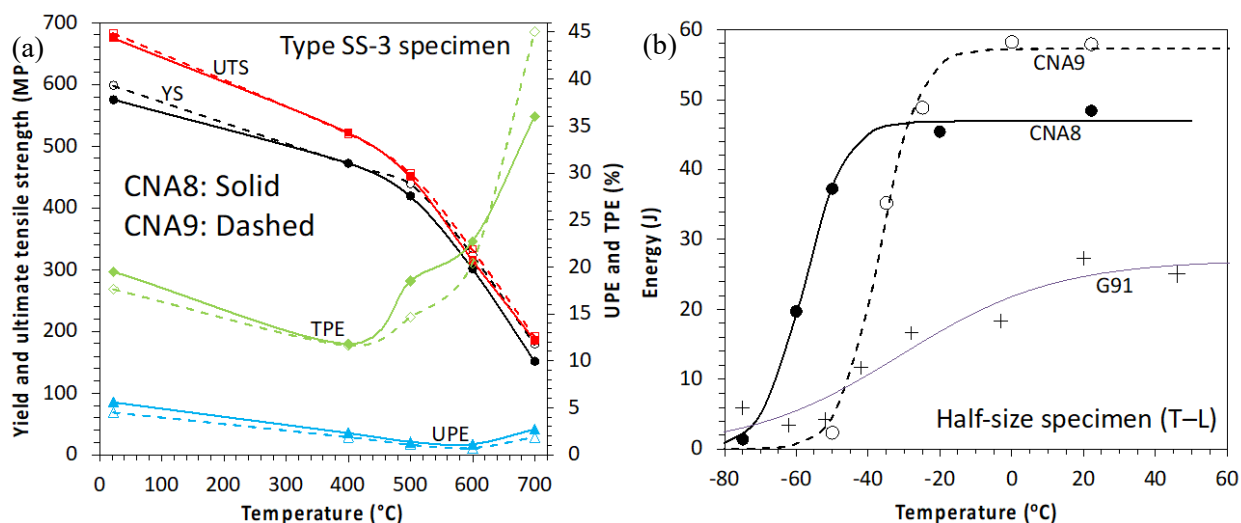


**Figure 5.** Temperature-dependent (a) yield and ultimate strength and uniform and total plastic elongation, and (b) Charpy impact absorbed energies of CNA8 and CNA9.

**Future Work**

Selected creep tests for CNA8 and CNA9 specimens will be conducted.

## 2.3 EFFECTS OF CARBON IN A TAILORED CASTABLE NANOSTRUCTURED ALLOYS – ION IRRADIATION AND HELIUM IMPLANTATION

T. Graening, W. Zhong, Y. Yang ([yangying@ornl.gov](mailto:yangying@ornl.gov)), L. Tan (ORNL), and P. Patki, K. Field, (Univ. of Michigan)

### OBJECTIVE

Carbide CNAs (Castable Nanostructured Alloys) have  $M_{23}C_6$  and MC as the two principal precipitate types. Appropriate carbon content control can produce steels having either  $M_{23}C_6$  and MC precipitates or only MC precipitates, as detailed in section 2.02 on carbon effects in carbide-CNAs. The different precipitate configurations provide a good opportunity to study the effect of precipitate type on radiation resistance. This work is directed at understanding the effects of the  $M_{23}C_6$  and MC precipitates on the ion irradiation and helium implantation responses of carbide-CNAs.

### SUMMARY

High-C CNA8 (0.1 wt.%) and low-C CNA9 (0.05 wt.%) were fabricated with CNA9 having  $M_{23}C_6$  amount about one order of magnitude lower than in CNA8 but MC amounts comparable. Both single beam ( $Fe^{3+}$ ) and dual beam ( $Fe^{3+} + He^{2+}$ ) ion irradiations were conducted at 500 °C on polished samples of the two steels. The ion irradiation achieved doses of 50 and 100 displacements per atom (dpa) at the mid-range of the irradiation depth. The implanted helium was maintained at ~10 atom part per million (appm) per dpa within the 50 and 100 dpa irradiation dose region. Preliminary microstructural characterization of the ion-irradiated low-C CNA9 indicated an increased cavity diameter at 50 and 100 dpa doses under dual ion irradiation. Cavity number densities were approximately 10 times higher when 100 dpa doses were reached.

### PROGRESS AND STATUS

Ion irradiation experiments were conducted at the University of Michigan Ion Beam Laboratory. Samples of CNA8 and CNA9 were mechanically polished to 1200 grit and electropolished using 10% perchloric acid with 90% methanol. Single beam irradiations using defocused 9 MeV  $Fe^{3+}$  ions and dual beam irradiations using defocused 9 MeV  $Fe^{3+}$  ions plus 3.42 MeV  $He^{2+}$  ions with a dose rate of  $7 \times 10^{-4}$  dpa/s were performed at a target temperature of 500 °C. The temperature was maintained via a Variac transformer and monitored using thermocouples spotwelded to guide bars which sandwiched the samples as shown in **Figure 6a**. **Figure 6b** shows the calculated dose-depth profiles, achieving a 10  $He^{2+}$  appm/dpa at a target ion irradiation depth of 1200 nm, where the  $Fe^{3+}$  irradiation dose was ~50 (not shown in **Figure 6b**) and ~100 dpa. A special foil degrader mechanism was used to get a flat ~10  $He^{2+}$  appm/dpa between 800 and 1400 nm.

Microstructural characterization of the samples irradiated to doses of 50 dpa and 100 dpa from single- and dual-beam ion irradiations was performed on FIB specimens using STEM-EDS, STEM, and TEM techniques. The focus of the dual-ion-irradiations was to investigate the potential sink strength of precipitates. However, at 100 dpa, few fine precipitates were observed, possibly due to dissolution. Nevertheless, cavity sizes and densities as a function of ion irradiation depth were investigated and results are shown in **Figure 7**. The difference of the carbon content between CNA8 and CNA9 clearly has an impact on the cavity sizes and densities. The lower carbon led to larger cavities as shown on the left side of **Figure 7** and roughly the same number density at 50 dpa, but to a reduced number density at 100 dpa (not shown here).

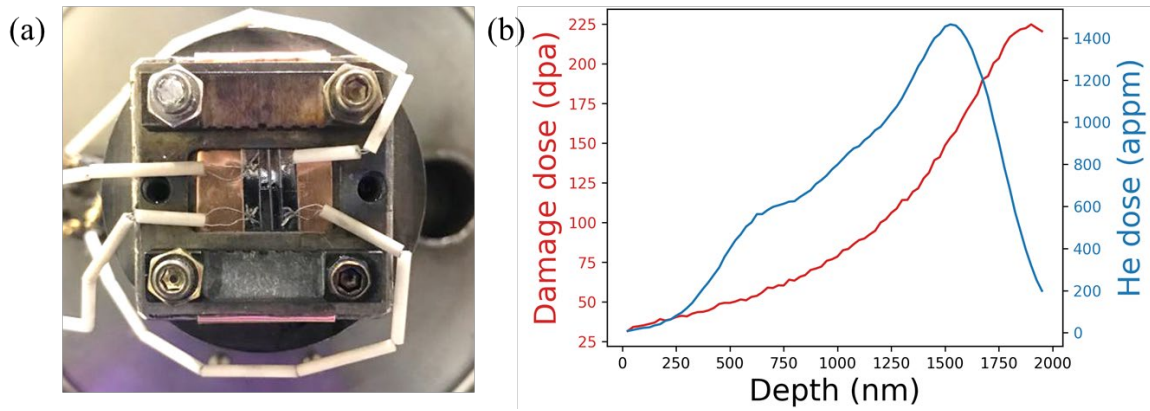


**Figure 6. (a)** Specimen holder for single beam ion irradiation, showing the four thermocouples welded to the guide bars. Ion irradiation was perpendicular to the sample surface. **(b)** The calculated  $\text{Fe}^{3+}$  damage dose (the 100 dpa case) and  $\text{He}^{2+}$  doses are shown in red and blue, respectively, for a dual ion-irradiation experiment. A depth between 800 and 1400 nm achieves the targeted  $\sim 10$  appm/dpa ratio.

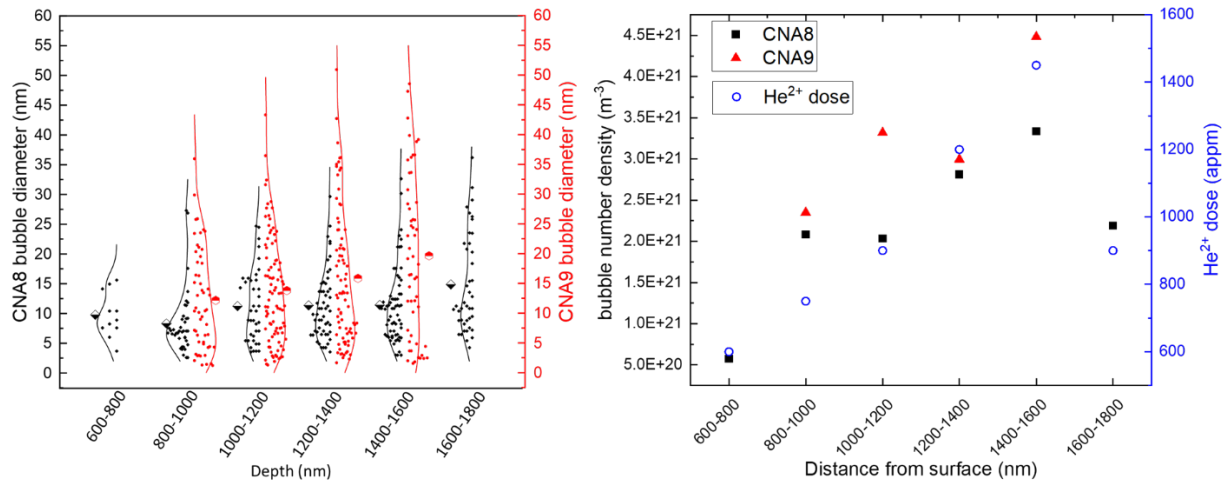


**Figure 7. Comparison of depth-dependent cavity sizes for CNA8 and CNA9 that shows larger cavities in CNA9 at all depths for 50 dpa dual-ion irradiation. The bubble number density follows the trend of the  $\text{He}^{2+}$  dose for both steels.**

**Future Work**

Microstructural characterization and analyses of the ion-irradiated samples from the two heats will continue.

## 2.4 FRACTURE TOUGHNESS OF HFIR IRRADIATED F82H-MOD 3

X. Chen ([chenx2@ornl.gov](mailto:chenx2@ornl.gov)), R. Swain, J. Reed, A. Campbell, J.W. Geringer, M.A. Sokolov, and Y. Katoh

### OBJECTIVE

The aim of this task was to study the effects of irradiation temperature, dose, materials composition, Ni doping, and He production on fracture toughness of F82H irradiated in High Flux Isotope Reactor (HFIR).

### SUMMARY

The F82H-Mod3 M4CVN bend bar specimens were irradiated in HFIR in the rabbit capsule. The irradiation lasted for 16 reactor cycles with an accumulated irradiation dose of ~28 displacements per atom (dpa). The irradiation temperature for the specimens was 369°C based on the SiC thermometry specimen measurements. The measured Master Curve reference temperature ( $T_{0q}$ ) was -57°C. Compared to the unirradiated state (T-S orientation), the irradiation resulted in a 59C-deg increase in  $T_{0q}$  for F82H-Mod 3.

### PROGRESS AND STATUS

Alloy F82H-Mod 3 M4CVN miniature four-notch bend bar specimens were irradiated in the rabbit capsule F13A5. The initial irradiation was planned for 9 cycles in the HFIR at Oak Ridge National Laboratory (ORNL) but was extended to 16 total cycles with an accumulated irradiation dose of ~28 displacements per atom (dpa). Based on post-irradiation evaluation of SiC temperature monitors [1], the irradiation temperature for the M4CVN specimens was calculated to be 369°C, which was higher than the target irradiation temperature of 300°C.

Vickers microhardness measurements were performed near the fatigue pre-crack end of each notch to measure the extent of irradiation hardening. Four measurements were made for each notch with a Mitutoyo HV-120B hardness tester with 1 kg force and 15 sec dwell time. Compared with the unirradiated hardness of 210-220 HV, F82H-Mod 3 exhibited a very small amount of irradiation hardening (~227 HV) after 28 dpa irradiation at 369°C [1].

Transition fracture toughness testing based on the Master Curve method in the ASTM E1921 standard was performed on two M4CVN specimens of F82H-Mod 3 [1]. In total, eight notches were tested to calculate the Master Curve reference temperature,  $T_{0q}$ . **Figure 8** shows the Master Curve test results with  $T_{0q}=-57^\circ\text{C}$ . Compared with the unirradiated state (T-S orientation), the irradiation resulted in a 59C-deg increase in  $T_{0q}$  for F82H-Mod 3. Further comparison with F82H-Mod 3 irradiated to similar dose levels (18-28 dpa) but at different irradiation temperatures is shown in **Figure 9**. A significant irradiation temperature effect on embrittlement can be observed: at the lowest irradiation temperature of 300°C, where the most severe irradiation embrittlement with 137C-deg increase in  $T_0$  was observed. At 400°C irradiation temperature, mild irradiation embrittlement with 13C-deg increase in  $T_0$  was observed. The result from this study is in the middle of this irradiation temperature range, consistent with the actual irradiation temperature determined for specimens in capsule F13A5.

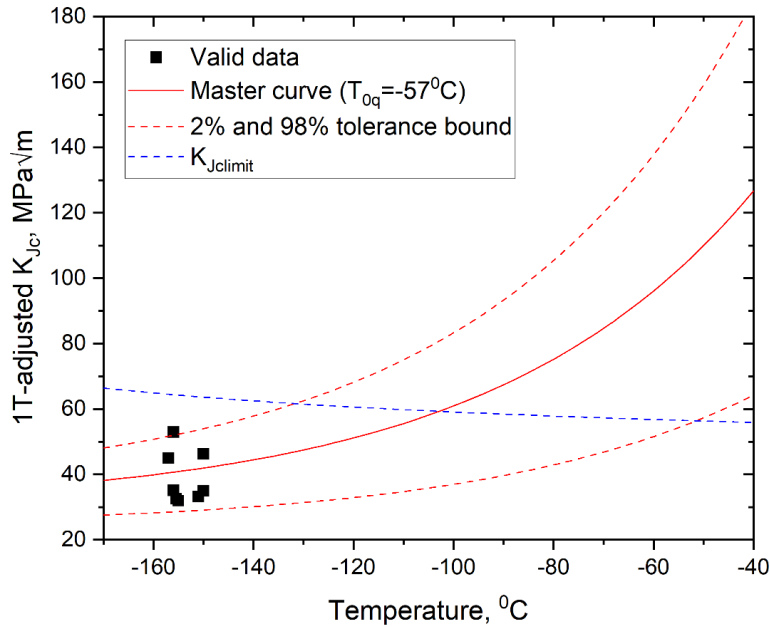


**Figure 8. Master Curve test results for F82H-Mod 3 steel irradiated in HFIR in the F13A5 rabbit capsule [1].**

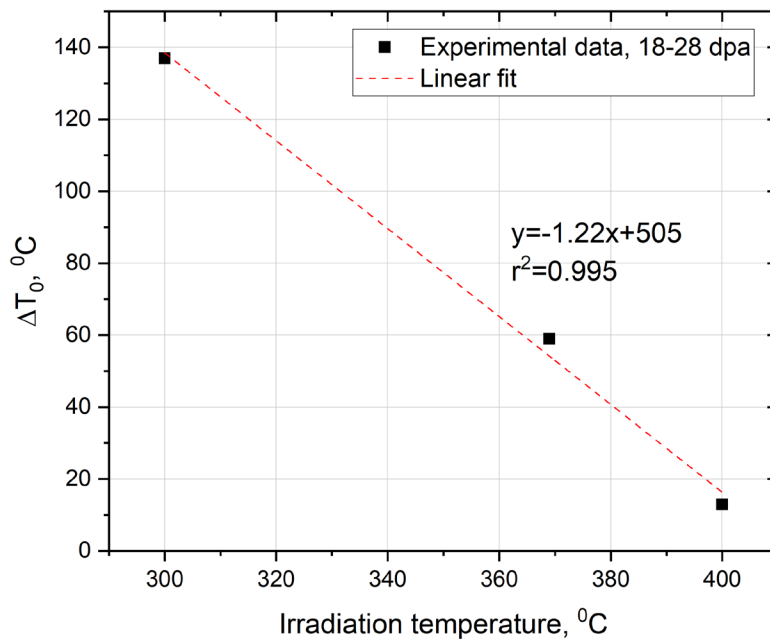


**Figure 9. Effect of irradiation temperature on Master Curve reference temperature shift  $\Delta T_0$  for F82H-Mod 3 steel irradiated to 18-28 dpa.**

**Reference**

[1] X. Chen et al., “Post-irradiation evaluation of fracture toughness properties of F82H-Mod3 irradiated in HFIR rabbit capsule F13A5”, FUSION MATERIALS SEMI-ANNUAL PROGRESS REPORT FOR THE PERIOD ENDING December 31, 2020, DOE-ER-0313/69, pp. 180, 2021.

## 2.5 IRRADIATION HARDENING-EMBRITTEMENT OF RAFM AND ODS STEELS

A. Bhattacharya ([bhattacharya@ornl.gov](mailto:bhattacharya@ornl.gov)), S.M. Levine, J. Reed, D.T. Hoelzer, J.W. Geringer, Y. Katoh, S.J Zinkle (ORNL), and T. Nozawa (QST-Japan)

### OBJECTIVE

This task is directed at understanding the dose- and temperature-dependent irradiation behavior of reduced activation ferritic-martensitic (RAFM) and oxide dispersion strengthened (ODS) steels. Samples of steels irradiated in HFIR over the range  $\sim 3.5$  to  $> 60$  dpa at temperatures of 300, 400 and 500 °C were available for the task. A specific aim was to quantify the low temperature hardening-embrittlement (LTHE).

### SUMMARY

The LTHE behavior of 4 steels (9% Cr base F82H-IEA steel, 14% Cr base MA957, 12% Cr base 12YWT and 18% Cr-5.5%Al base PM2000) irradiated in HFIR was assessed using Vickers microhardness tests. These hardness data were compared with results from Eurofer97 irradiated under similar conditions in HFIR. Hardening in F82H increased with neutron dose. After an initial sharp increase in the hardening at low doses, microhardness appeared to increase up to  $\sim 50$  dpa. For steel irradiated to  $\sim 80$  dpa, a reduction in the average hardness was observed; this may be related to fluctuations in the irradiation temperature. All ODS steels tested showed significant hardening for irradiation temperatures as high as 500 °C for relatively low dose irradiations ( $\sim 4.5 - 13$  dpa). This hardening response differs from the behavior of RAFM steels which do not typically show a significant increase in hardness for  $T_{irr} > 350$  °C [1]. The unexpected hardening response of the ODS alloys suggests that there may be a different underlying irradiation damage mechanism in these alloys compared to RAFM steels, which requires fundamental analysis. Tensile tests of ODS steels were recently completed and data analysis will include comparisons to the yield strength assessed from the hardness data.

Microstructural analysis of these ODS steels irradiated at elevated temperatures has been performed using atom probe tomography (APT) analysis and is detailed in a separate section of this report.

### PROGRESS AND STATUS

#### Introduction

##### Comparing dose and temperature dependent hardening in F82H-IEA and ODS alloys

Vickers microhardness data generated from F82H-IEA steel irradiated at 300 °C is plotted as a function of the neutron dose in **Figure 10**. The non-irradiated and as-irradiated hardness of the three ODS alloys are also presented for comparison. The irradiation-induced hardness increased for F82H irradiated to 50 dpa. The data indicate a slight decrease in hardness for the highest neutron dose; however, further analysis of the irradiation temperature and net accumulated dose are required. MA957 and 12YWT, which were significantly harder in the non-irradiated condition, also experienced irradiation-induced hardening. PM2000, which was the softest steel among the studied materials, showed the highest hardness increase when irradiated at 300 °C. Data from 10 different Eurofer97 variants irradiated in HFIR to similar low doses as F82H are also included in **Figure 10**; note that both Eurofer97 variants and F82H experienced similar irradiation-induced hardening.

**Figure 11** shows the irradiation temperature dependence of hardness for the HFIR-irradiated ODS alloys. All ODS alloys exhibited significant irradiation-induced hardening at all irradiation temperatures.

However, the average hardness did not decrease significantly for irradiations at 400 and 500 °C. These results were not expected because RAFM steels typically do not show significant LTHE for  $T_{irr} > \sim 330-350$  °C [1]. The hardening trends for the three ODS alloys were qualitatively similar despite their different chemistries and microstructure. Currently, the lower temperature limit imposed due to LTHE considerations for RAFM steels in fusion environments is set at  $\sim 350$  °C [1]. If ODS steels exhibit significant hardening, as indicated by the present results, it is likely the lower temperature limit for ODS steels for fusion in-vessel structures may have to be raised significantly. The 12YWT alloy, with the lowest Cr content, showed the lowest hardness increase among these ODS alloys. This is expected because lower Cr level implies lower fraction of embrittling Cr rich  $\alpha'$  phase formation in this alloy.

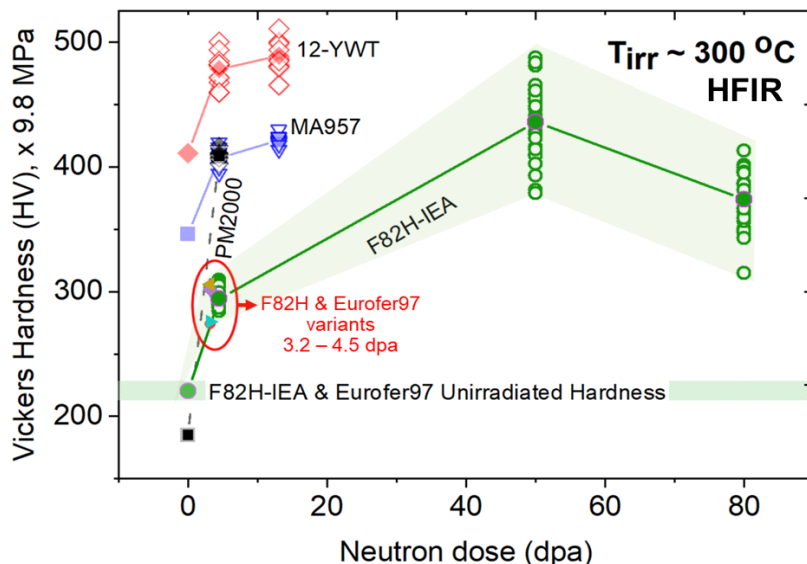


Figure 10. Dose-dependence of Vickers microhardness for F82H-IEA heat, Eurofer97 variants, MA957, 12YWT and PM2000 after neutron irradiation at 300°C in HFIR.

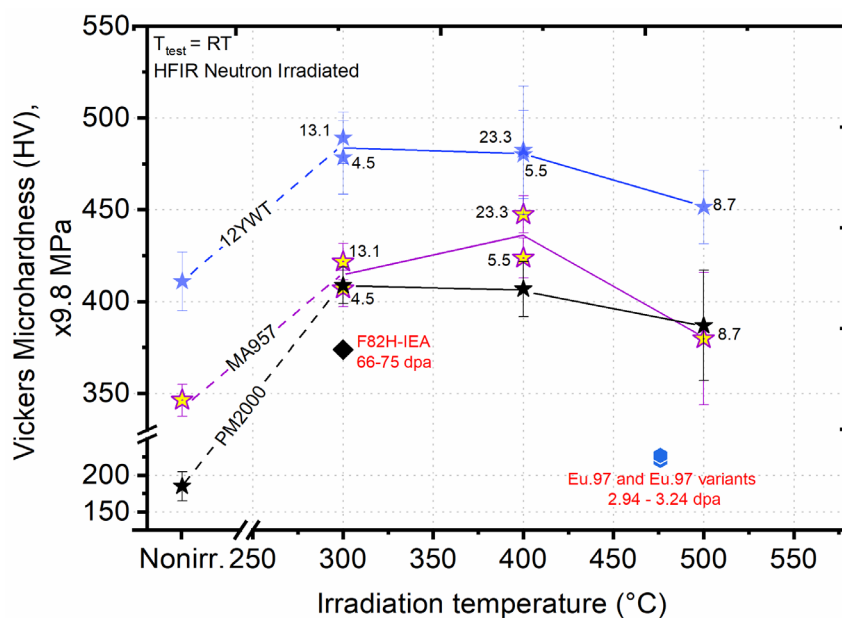


Figure 11. Temperature-dependent Vickers microhardness for MA957, 12YWT and PM2000 alloys after neutron irradiation in HFIR. The neutron dose values are noted, and high dose F82H-IEA and Eurofer97 data are shown for comparison.

### **Future Work**

Tensile data will be analyzed to validate Vickers hardness results, and the fracture surfaces of the tensile specimens will be evaluated.

### **References**

- [1] E. Gaganidze and J. Aktaa. Assessment of neutron irradiation effects on RAFM steels. *Fus. Eng. Des* 88 (2013) 118-128.

## 2.6 THE EFFECT OF HELIUM ON RADIATION HARDENING OF F82H-IEA STEEL

A. Bhattacharya ([bhattacharya@ornl.gov](mailto:bhattacharya@ornl.gov)), J. Reed, X. Chen, J.W. Geringer, Y. Katoh (ORNL), and T. Nozawa (QST-Japan)

### OBJECTIVE

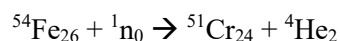
This task is directed at understanding the effect of helium (He) on irradiation hardening-embrittlement in RAFM steels. Reference F82H-IEA steel and  $^{54}\text{Fe}$  based F82H were irradiated in HFIR in the JP29 irradiation experiment and examined in this task. The neutron dose was  $\sim 66$  dpa at  $T_{\text{irr}} = 292\text{-}302$  °C, with He production of 0.3 and 2.3 appm He/dpa (without and with  $^{54}\text{Fe}$  respectively). The mechanical properties measured were indentation microhardness and uniaxial tensile.

### SUMMARY

Vickers indentation microhardness was measured on  $^{54}\text{Fe}$ -F82H, and F82H-IEA irradiated in the same capsules in the HFIR JP29 experiment to quantify the effect of He. In the absence of an  $^{54}\text{Fe}$  F82H archival sample to verify the starting isotopic distribution, we conservatively assumed the sample to be constituted of  $>99\%$   $^{54}\text{Fe}$ , thereby generating  $\sim 152$  appm He. Indentation test data showed no major effect on irradiation hardening for the two tested materials. Uniaxial tensile tests revealed unexpected results. The yield and ultimate tensile stresses of the  $^{54}\text{Fe}$ -based sample were lower than those for the steel without He. However, the uniform and total elongation of sample with  $^{54}\text{Fe}$  was reduced by nearly 50%. Non-irradiated archival material is needed to better understand the irradiated properties.

### PROGRESS AND STATUS

Understanding the effect of He on mechanical property degradation, particularly low temperature hardening embrittlement (LTHE), of RAFM steels is a critical challenge to predict the in-service performance of fusion first-wall/blanket and plasma-facing structures [1], but LTHE is not well-understood [2]. Until a fusion prototypic neutron source (FPNS) where fusion relevant He along with high neutron doses may be achieved for testing RAFM/ODS steels is available, isotopic tailoring of RAFMS steels with elements that have high  $(n, \alpha)$  reaction cross-section in HFIR irradiation provides a unique approach for He generation. In this context, F82H steels produced using  $^{54}\text{Fe}$  isotope were irradiated in HFIR. Nuclear transmutation of  $^{54}\text{Fe}$  to produce He in steels in the HFIR spectra follows the reaction:



The F82H-IEA and  $^{54}\text{Fe}$ -F82H samples were evaluated to quantify the effect of He generation due to the presence of  $^{54}\text{Fe}$ . Vickers hardness tests were performed in the hot cells on the head/grip sections of undeformed SS-J3 flat tensile samples with 1 kg load and a 15 s dwell time in accordance with ASTM E384 Standard Test Method for Micro indentation Hardness of Materials. The hardness data are shown in the scatter plot in **Figure 12**. No notable effect of  $^{54}\text{Fe}$  addition, i.e., no effect of He, was observed in the irradiated hardness values. However, compared to non-irradiated F82H-IEA, both irradiated materials showed significant irradiation hardening.

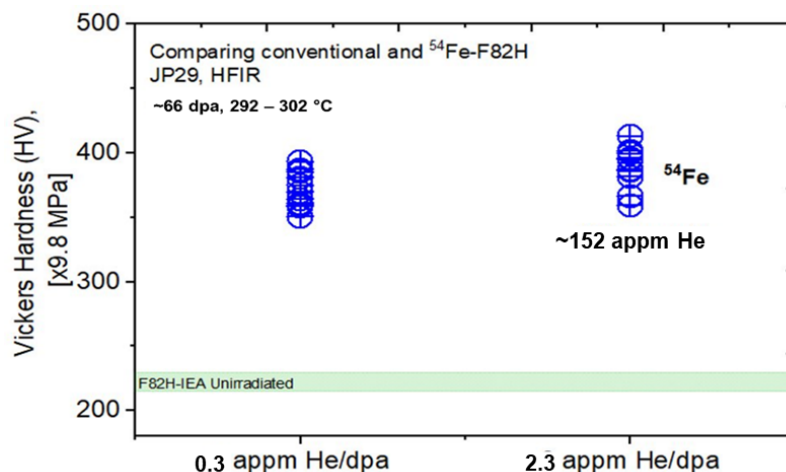


**Figure 12.** Vickers indentation hardness of F82H irradiated in HFIR to conditions shown in the figure.

Uniaxial tensile test results for  $^{54}\text{Fe}$ -F82H are compared with high dose F82H-IEA and non-irradiated F82H-IEA results in **Figure 13**. The tensile tests were performed on SSJx specimens following ASTM E8 Standard Test Methods for Tension Testing of Metallic Materials, using a strain rate of  $10^{-3} \text{ s}^{-1}$  ( $5 \times 10^{-3} \text{ mm/s}$  extension rate). The specimens were shoulder loaded for testing in an Instron 3367 tensile machine equipped with a 5 kN load cell and connected with Instron Bluehill3 analysis software. Note that the elastic portion of the stress-strain curves includes machine compliance with elongation estimated from machine stroke in the absence of an extensometer. As a result, the slope of this region varied for different samples. Data summarized in **Table 1** were tabulated using the tangent modulus method, unaffected by machine compliance in the elastic regime. Similar to results from the hardness tests, the irradiated materials exhibited an increase in yield stress, consistent with the increase in hardness. However, the yield stress increase in F82H-IEA was slightly higher than the  $^{54}\text{Fe}$  specimen, which was not expected and requires a further careful interpretation of the thermometry data from the irradiation capsule. The ductility of the  $^{54}\text{Fe}$  sample was severely reduced as compared to F82H-IEA, which suggests potential embrittlement due to the presence of He. A summary of the tensile properties is provided in **Table 1**.

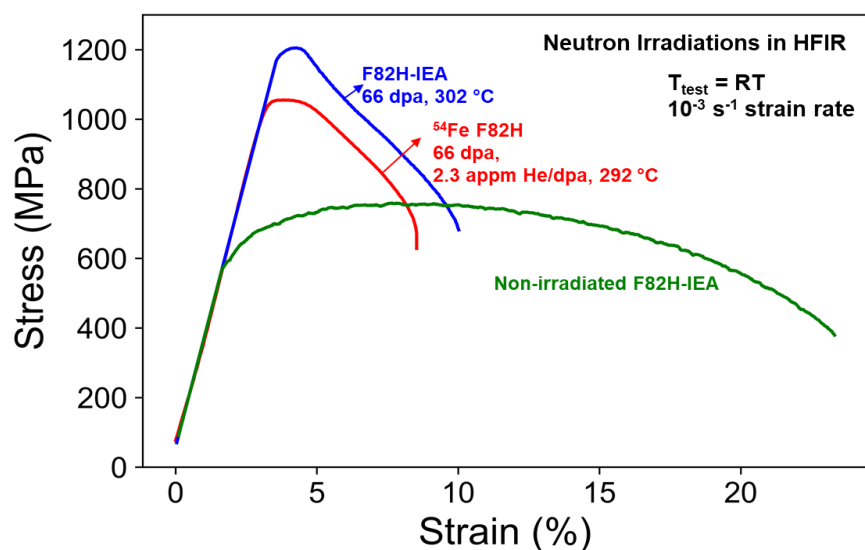


**Figure 13.** Engineering stress-strain curves of  $^{54}\text{Fe}$ -F82H, F82H-IEA and unirradiated F82H-IEA, showing irradiation-induced hardening and loss of ductility.

**Table 1. Summary of the non-irradiated and irradiated tensile properties.  $\sigma_{YS}$  = yield stress,  $\sigma_{UTS}$  = ultimate tensile stress,  $UE_p$  = uniform plastic elongation,  $TE_p$  = total plastic elongation**

Steels	$\sigma_{YS}$ MPa	$\sigma_{UTS}$ MPa	Elongation plastic	
			$UE_p$ %	$TE_p$ %
Non-irradiated F82H-IEA	612	771	5.8	16.7
Irradiated F82H-IEA	1198	1203	0.61	10.1
Irradiated 54Fe-F82H	1052	1057	0.34	6.2

### Future Work

Atom probe tomography analysis will be performed to characterize the microstructure of the  $^{54}\text{Fe}$  specimen to help understand the mechanical test data. Analysis of STEM data is ongoing.

### References

- [1] E. Gaganidze and J. Aktaa. Assessment of neutron irradiation effects on RAFM steels. *Fus. Eng. Des* (88) 2013 (118-128).
- [2] Y. Dai, G. Odette, Y. Yamamoto, The effects of helium in irradiated structural alloys, *Comprehensive Nuclear Materials* (2012), vol. 1, pp. 141-193.
- [3] S.J. Zinkle et al. Development of next generation tempered and ODS reduced activation ferritic/martensitic steels for fusion energy applications. *Nucl. Fusion* (57) 2017 092005.

## 2.7 TRANSMISSION ELECTRON MICROSCOPY OF IRRADIATED F82H STEELS

A. Bhattacharya ([bhattacharya@ornl.gov](mailto:bhattacharya@ornl.gov)), J.W. Geringer, Y. Katoh (ORNL), and T. Nozawa (QST-Japan)

### OBJECTIVE

This task is aimed at understanding the microstructural evolution in neutron-irradiated F82H steels. F82H-IEA steels irradiated in HFIR to ~4.5 dpa at 300 °C were evaluated. The specific objective was to quantify the irradiation-induced microstructural development and assess any microchemical changes that could degrade the steels' performance.

### SUMMARY

Microstructural analysis showed dislocation loops in the HFIR-irradiated F82H-IEA steel. The g·b analysis was performed in the matrix within the thin laths, revealing a high concentration of a<100> type dislocation loops. The results contradict the current state-of-knowledge regarding these steels based on surrogate ion irradiations where the highly glissile a/2<111> type defects are predominant for irradiation temperatures below 350 °C. Transmission electron microscopy (TEM) showed no major effect of irradiation on M<sub>23</sub>C<sub>6</sub> carbides in this steel. Further, analytical scanning TEM (STEM) characterization showed radiation-induced segregation (RIS) of Ni on grain boundaries –not expected since there is supposedly no Ni in this clean F82H-IEA steels. Atom probe tomography experiments on the same material are reported separately.

### PROGRESS AND STATUS

- Irradiation Experiment: HFIR RB15J
- Material: F82H-IEA steel
- Conditions: ~4.5 dpa, 300 °C
- Sample ID: OX1 and OX2
- Two FIB samples characterized

Diffraction contrast and analytical STEM-EDX characterization of F82H-IEA irradiated to ~4.5 dpa at 300°C was performed using FEI F200X Talos STEM in the LAMDA lab. **Figure 14** presents an energy dispersive X ray spectroscopy (EDX) map of the irradiated foils. Cr/W/V rich carbides were seen, expected to be the M<sub>23</sub>C<sub>6</sub> carbides. No evidence of pure Ta/V rich MX phase was detectable – which is expected in the IEA heat. Chemical distributions across prior austenite grain boundaries (PAGB) and lath boundaries was also studied. **Figure 15** shows EDX mapping of a grain boundary (GB) triple point where Cr/Si segregated, while W and V were depleted. The STEM-EDX in **Figure 15** also indicates unexpected presence of Ni on the grain boundaries. Because RAFM steels do not typically contain Ni, this result is surprising. More advanced analysis, using statistical data analysis tools is ongoing to better understand the Ni segregation issue. Ni segregation is also recently reported in other RAFM steels irradiated in HFIR, including Eurofer97 [1].

In addition to elemental characterization, STEM characterization was used to quantify the irradiation-induced extended defects. After irradiation, dislocation loops formed in the material. **Figure 16** presents different areas of the foil where the dislocation loop microstructure overview is visible inside the nanometric laths. Most dislocation loops were between ~8-20 nm in diameter and are believed to be the primary source of radiation hardening.

Using g.b analysis, Burgers vector of the dislocation loops was identified. An example of this is shown in **Figure 17**, where the same nanograin was tilted along different g vectors to identify the visibility-invisibility patterns of the loops. The study revealed both  $a\langle 100 \rangle$  and  $a/2\langle 111 \rangle$  type dislocation loops in the sample. In **Figure 17** blue arrows point to  $a\langle 100 \rangle$  type loops while the red arrows point to  $a/2\langle 111 \rangle$  type loops. The concentration of both the loop families was nearly equal in proportions. This result is opposite to what is known after ion irradiations in Fe-Cr based alloys such as RAFM steels where mostly  $a/2\langle 111 \rangle$  type loops are reported below  $\sim 350$  °C [2]. This result also supports data on Eurofer97 irradiated in HFIR to similar doses, results of which are separately reported in this annual report.

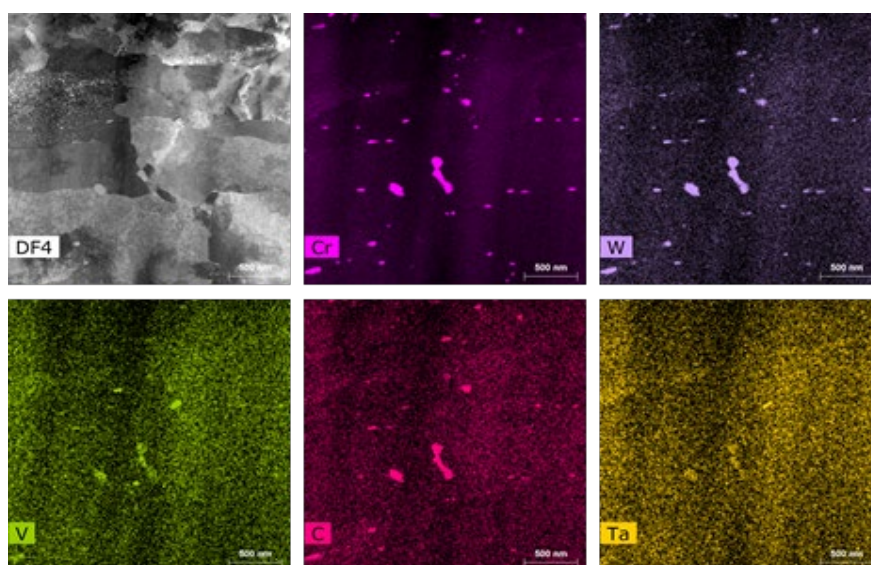


**Figure 14. Annular dark-field (ADF) STEM image and STEM-EDX elemental maps obtained from the irradiated F82H-IEA heat, 4.5 dpa, 300°C. Discrete Cr-rich  $M_{23}C_6$  carbides are visible.**

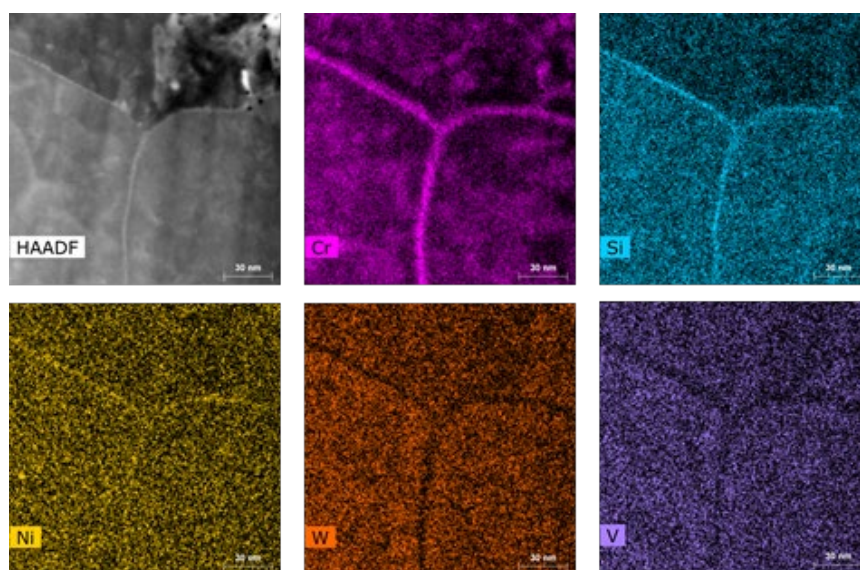


**Figure 15. High Angle ADF (HAADF) STEM image and corresponding STEM-EDX elemental maps of a GB triple point in the irradiated F82H-IEA steel, 4.5 dpa, 300°C, showing elemental segregation of Cr/Si, some slight Ni segregation, and W/V depletion.**

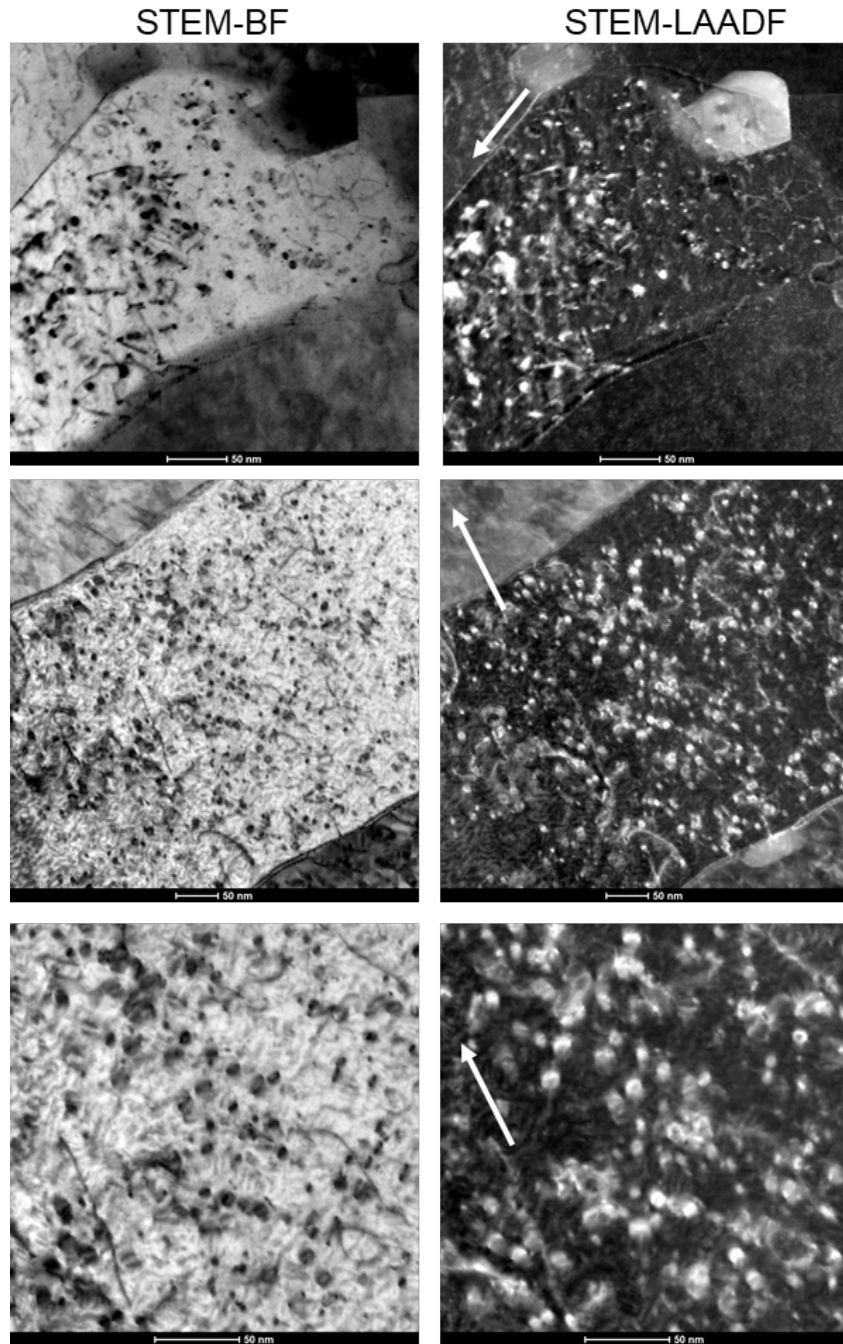


**Figure 16. Bright-field (BF) and low angle annular dark field (LAADF) STEM images of dislocation loops in HFIR irradiated F82H-IEA heat, 4.5 dpa, 300°C. Imaging performed with  $\langle 110 \rangle$  type g vector indicated by the white arrows, close to [001] zone axis, deviation parameter  $s > 0$ .**

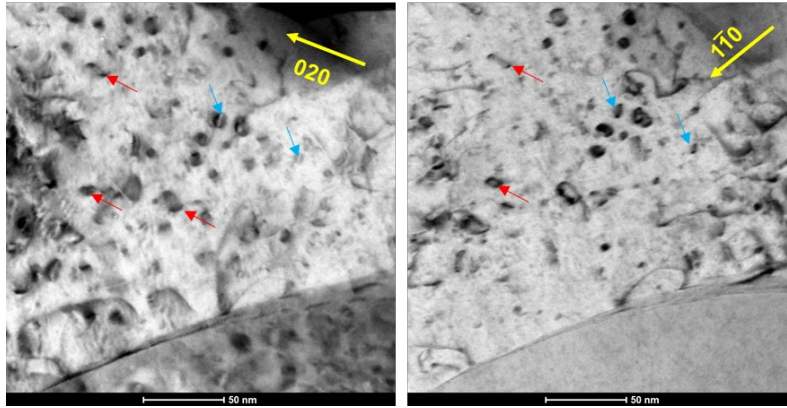


**Figure 17. Bright-field STEM images showing  $a\langle 100 \rangle$  loops (blue arrows) and  $a/2\langle 111 \rangle$  type loops (red arrows), in HFIR irradiated F82H-IEA heat, 4.5 dpa, 300°C. The same area was tilted and analyzed using different  $g$  vectors. In this example, zone axis =  $[001]$ , deviation parameter  $s > 0$ . The direction of the  $g$  vectors is shown.**

### Future Work

The combined STEM and APT data will be used to quantify hardening using dispersed barrier hardening models.

### References

- [1] K. Wang, C.M Parish, K.G. Field, L. Tan, Y. Katoh, Segregation behavior and phase instability of Eurofer97 after neutron irradiation to 72 dpa. *J. Nucl. Mater.* 547 (2021) 152834.
- [2] Z. Yao, M.L. Jenkins, M. Hernández-Mayoral & M.A. Kirk, The temperature dependence of heavy-ion damage in iron: A microstructural transition at elevated temperatures, *Phil. Mag* 90:35-36, (2010) 4623-4634.

## 2.8 ATOM PROBE TOMOGRAPHY OF NANOCLUSTERING IN IRRADIATED F82H

A. Bhattacharya ([bhattacharya@ornl.gov](mailto:bhattacharya@ornl.gov)), S.M. Levine, J. Poplawsky, T. Nozawa, J.W. Geringer, and Y. Katoh

### OBJECTIVE

This task is aimed at understanding neutron irradiation-induced solute nanoclustering in RAFM steels. F82H-IEA steel irradiated in HFIR to ~4.5 dpa at 300 °C was studied. The APT analysis was performed to complement the mechanical property tests and STEM analysis performed and reported elsewhere in this report.

### SUMMARY

APT analysis identified irradiation-induced solute clustering throughout the matrix of the irradiated steel. Radiation-induced segregation (RIS)-driven formation of Mn-enriched solute clusters was detected; these solute-enriched clusters were also nucleated heterogeneously on dislocation lines and dislocation loops. These Mn-enrich solute clusters also contained Si and some P was detected specifically in clusters that formed on dislocation loops. No Cr-enriched co-clustering was detected which suggests that at low doses < 5 dpa, clustering of Cr is not a factor contributing to hardening-embrittlement of RAFM steels. Results highlight commonalities between Fe-Cr based bcc RAFM steels and the solute-enriched clustering (still not fully understood) in low alloy RPV steels and welds where irradiation-induced Mn-Ni-Cu-Si solute-enriched clusters cause hardening.

### PROGRESS AND STATUS

- Irradiation Experiment: HFIR-RB15J
- Material: F82H-IEA steel
- Conditions: ~4.5 dpa, 300 °C
- Sample ID: OX1 and OX2

Atom probe tomography (APT) studies were used to characterize the irradiation-induced microstructure of F82H-IEA steel. For this purpose, needle-shaped samples were prepared in the focused ion beam (FIB) facility at LAMDA lab, and subsequently analyzed at 40 K in the CAMECA LEAP 4000X HR APT at the ORNL CNMS facility. **Figure 18a** shows the reconstructed APT “atom maps” from the needle. The distribution of Fe and Cr atoms appears homogeneous, but the Mn and Si atoms were distributed inhomogeneously. To better understand the Mn, Si distribution, cluster analysis based on iso-concentration algorithm produced the results in **Figure 18b**, showing the presence of solute-enriched clusters containing Mn and Si. These appear to be preferentially associated with dislocation loops and line dislocations. Solute clustering on dislocation loops is further evidenced in **Figure 19** with local atom maps and 2D contour plots of an identified loop. It is evident that Mn, Si, and P are enriched at the dislocation cores. In non-irradiated conditions, there is no thermodynamic force driving Mn, Si, and P-enriched-clustering in the bcc Fe-Cr system. The presence of Mn, Si, P-enriched solute clusters in F82H will contribute to the low temperature hardening-embrittlement (LTHE) in this class of steels. In RPV steels, irradiation-induced solute clustering of Mn, Ni, Cu, Si is well-known and contributes to radiation hardening and increases in yield strength. The presence of irradiation-induced solute-enriched clusters in bcc Fe-Cr based RAFM steels suggest commonalities with the low alloy RPV steels and welds.

**Future Work**

Modeling using dispersed barrier hardening is ongoing to incorporate Mn, Si, P-enriched solute cluster data, and quantify the contribution to hardening. Parallel analysis of the collected data sets with *open-source APT software, OSCAR* (S. Levine, A. Bhattacharya, C. Pareige, S.J. Zinkle et al. ORNL Fusion Semi Annual 2021), is also ongoing.

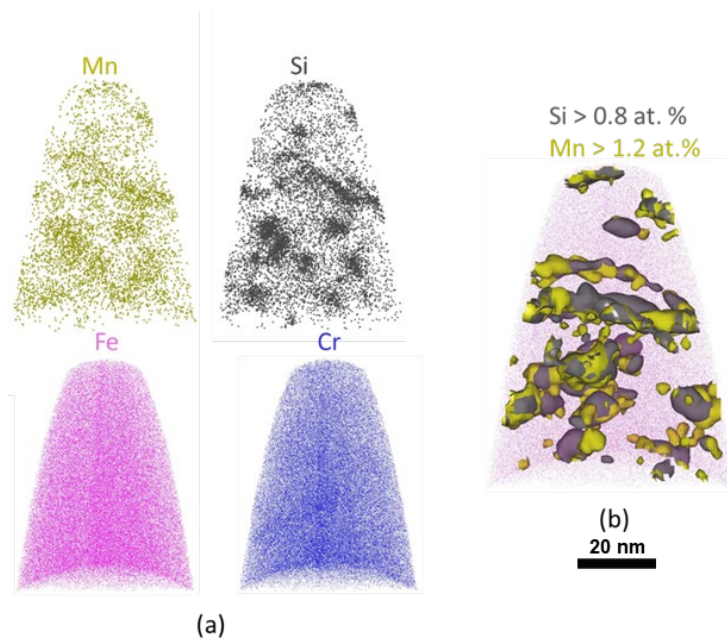


**Figure 18.** APT analysis of HFIR irradiated F82H-IEA steel, ~4.5 dpa, 300°C. (a) Atom maps. (b) Iso concentration surface contour plots showing Mn and Si segregation/clustering in the material, including RIS to dislocation loops. More data analysis is ongoing with source APT software, OSCAR (S. Levine, A. Bhattacharya, C. Pareige, S.J. Zinkle et al. ORNL Fusion Semi Annual 2021).

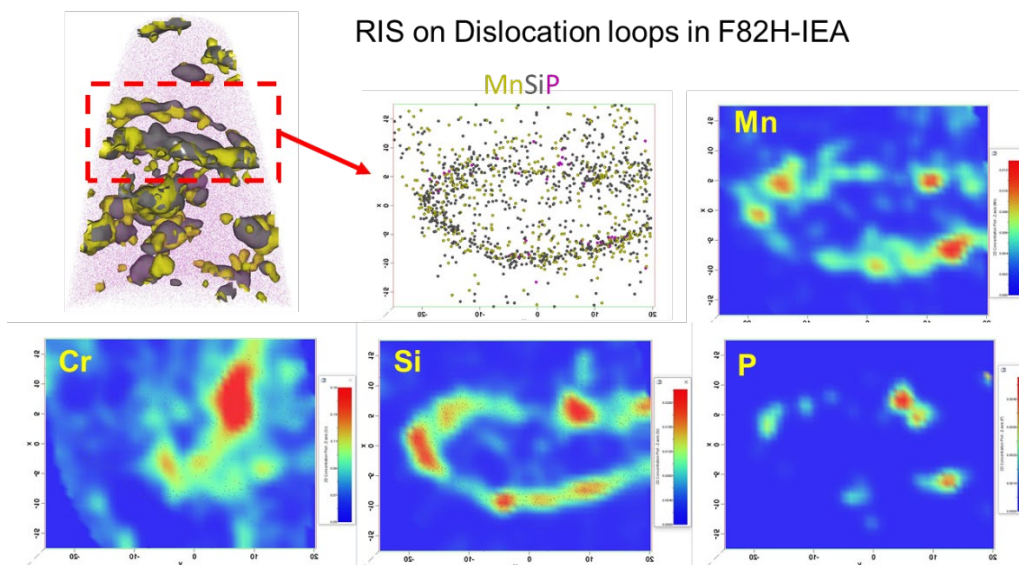


**Figure 19.** APT study of RIS on dislocation loops in HFIR-irradiated F82H-IEA steel, ~4.5 dpa, 300°C. The figure shows 2D contour plots of elemental segregation on a dislocation loop.

## 2.9 IRRADIATION CREEP OF F82H PRESSURIZED TUBES

A.A. Campbell ([campbellaa@ornl.gov](mailto:campbellaa@ornl.gov)), Y. Katoh, J.W. Geringer J.D. Reed, K.R. Smith, P.L. Mulligan (ORNL), and M. Ando (QST)

### OBJECTIVE

The objective of this task was to measure neutron irradiation-induced creep of reduced activation ferritic/martensitic (RAFM) steel alloy F82H at 300°C. The stress necessary to drive irradiation creep was provided using thin-walled pressurized tubes. The internal inert gas pressure induces a hoop stress in the sealed tubes that drives creep, which is measured as changes in the tube diameter.

### SUMMARY

Four rabbit-type creep capsules designed for irradiation at 300°C with hoop stresses of 0, 150, 300, and 380 MPa, were irradiated in the HFIR cycles 475 and 476. Disassembly, post-irradiation dimensional inspection, and preliminary temperature analysis of the four creep tube samples were completed and reported previously [1]. The work completed this year focused on the analysis of the internal capsule thermometry.

### PROGRESS AND STATUS

Irradiation creep of RAFM steels is important for the design of fusion reactor blanket systems. This work is reestablishing the ORNL capability for pressurized creep tube (PCT) experiments in HFIR.

The four capsules completed two irradiation cycles in HFIR in December 2017, with a nominal radiation damage of 3.7 dpa. The capsules were disassembled, and post-irradiation examination (PIE) was performed, in the ORNL hot cells IMET facility.

The irradiation capsules each contained three temperature monitors, one located inside the PCT and two in the PCT holder. The monitors were recovered during disassembly and shipped to the Low Activation Materials Development (LAMDA) laboratory for analysis. The determination of the irradiation temperature by the continuous dilatometer method [1] of annealing the silicon carbide monitors. The results from the TM analysis, listed in **Table 2**, show good agreement between the two in-holder TMs, with the inner TMs being significantly hotter due to the thermal properties of the capsules.

The results of TM analysis were compared with thermal models developed during capsule design. The net difference between the measured/calculated (last column in **Table 2**) and modeled TM average temperatures was used to adjust the average PCT temperature achieved during irradiation. The summary of the average PCT and SiC TM temperatures from the thermal design, the measured average SiC TM temperatures and the percent difference from the model, and the achieved average PCT temperature are listed in **Table 3** for the inner TMs and **Table 4** for the holder TMs.

**Table 2. Summary of continuous dilatometer analysis [1] of PCT TMs**

Capsule ID	Hoop Stress (MPa)	HFIR Location	TM ID	Maximum Temperature (°C)	Median Temperature (°C)	Minimum Temperature (°C)	Transition Temperature (°C)	Average Temperature (°C)
FHC01	0	TTRH-5	16-01	320.8	299.4	266.4	396.1	293.6
			16-02	315.1	296.9	279.5	386.7	297.3
			Inner	433.3	413.4	395.8	513.6	414.6
FHC02	150	TTRH-5	16-03	330	311.3	290	400.6	310
			16-09	337.2	320.3	298.4	399.4	317.8
			Inner	448.9	434	416.8	508	432.9
FHC03*	300	TTRH-3	16-05	252.9	235.5	210.7	317.5	231.8
			16-06	254	236.4	219	323.2	236.5
			Inner	330.7	310	276.4	405	303.6
FHC04*	380	TTRH-3	16-07	259.3	244	231.1	321.6	245.2
			16-08	251.1	233.4	214.1	319.3	232.6
			Inner	300.3	278	241.7	380	271

\*Failed creep tube

**Table 3. Summary of thermal design results and achieved PCT temperature from inner TMs**

Rabbit Number	Average PCT Design Temperature (°C)	Average SiC Design Temperature (°C)	Average SiC TM Measured Average (°C)	% Difference from Average SiC Design Temperature	Expected Average PCT Temperature (°C)
FHC01	300	335	414.6	23.7%	371
FHC02	300	335	432.9	29.2%	388
FHC03*	297	330	303.6	-8.0%	273
FHC04*	297	330	271.0	-17.9%	244

\*Failed creep tube

**Table 4. Summary of thermal design results and achieved PCT temperature from holder TMs**

Rabbit Number	Average PCT Design Temperature (°C)	Average SiC Design Temperature (°C)	Average SiC TM Measured Average (°C)	% Difference from Average SiC Design Temperature	Expected Average PCT Temperature (°C)
FHC01	300	259	295.5	14.1%	342
FHC02	300	259	313.9	21.2%	364
FHC03*	297	259	234.2	-9.6%	269
FHC04*	297	259	238.9	-7.8%	274

\*Failed creep tube

Analysis of both types of TMs revealed that PCTs in holders FHC01 and -02 were 50-80°C hotter than target whereas the capsules FHC03 and -04 were about 30°C cooler than design. The cooler temperature of the failed specimens is not surprising because once the specimens failed the pressurization gas will expand to the gas volume in the capsule, including the design gas gap, resulting in higher gas pressure of a gas with a higher thermal conductivity resulting in an overall cooler capsule and PCT.

A remaining question is determining whether the failed PCTs lost pressure before irradiation, at low irradiation dose, or near the end of irradiation. The fact that the capsule containment retained the gas from the failed PCTs suggests that burst of the PCTs occurred after the capsule was assembled and welded shut, and not prior to insertion in HFIR. In the temperature range of these capsules, 250-350°C, the radiation swelling in SiC at a given temperature saturates around 1 dpa, which is equivalent to half of a HFIR irradiation cycle (12-13 days). Therefore, if the failed PCTs were still retaining pressure after half of the first irradiation cycle, we should expect to observe some annealing of radiation damage at higher temperatures. From the data presented previously it is deduced that failures either occurred before irradiation started or early in the first irradiation cycle, otherwise there should have been some SiC annealing occurring at temperatures above 400°C.

Preliminary analysis of the laser profilometer-measured PCT diameters showed ~2.15% diametral strain in each failed specimen. This amount of strain is not expected without temperature and radiation damage, suggesting that the PCTs did not fail prior to irradiation but likely occurred early in the first irradiation cycle. The similar strain in both failed PCTs suggests that both reached a creep strain limit and then failed. The burst behavior observed for FHC04 suggests the strain rate at rupture was larger than in FHC03, leading to the bursting rather than the formation of a small pinhole, which is expected to be found in FHC03.

### **Future Work**

The future effort will include continued analysis of dimensional changes, microhardness measurements, and preparation of a journal article. Microstructural characterization may be performed if warranted by the creep measurement results.

### **References**

- [1.] A.A. Campbell, Y. Katoh, J.W. Geringer, J.D. Reed, K.R. Smith, P.L. Mulligan, M. Ando, "11.1 Irradiation Creep of F82H Pressurized Tubes", *FUSION MATERIALS SEMI-ANNUAL PROGRESS REPORT FOR THE PERIOD ENDING December 31, 2019*, DOE-ER-0313/67, p 147-153 (2020).
- [2.] Campbell, A.A., W.D. Porter, Y. Katoh, and L.L. Snead, "Method for analyzing passive silicon carbide thermometry with a continuous dilatometer to determine irradiation temperature", *Nuclear Instruments and Methods in Physics Research, Section B: Beam Interactions with Materials and Atoms*, 370, (2016) 49-58.

## 2.10 STEM AND APT CHARACTERIZATION OF IRRADIATED EUROFER97

A. Bhattacharya ([bhattacharya@ornl.gov](mailto:bhattacharya@ornl.gov)), S.M. Levine, J. Poplawsky, J.W. Geringer, Y. Katoh (ORNL), and M. Rieth (KIT-Germany)

### OBJECTIVE

This task is aimed at quantifying microstructural defects and radiation-driven segregation/clustering in neutron-irradiated Eurofer97 type steel. Eurofer97 steel irradiated in HFIR to 2.94-3.24 dpa at 300 °C as a part of the EUROfusion program was available for this study. The microstructures were analyzed using scanning transmission electron microscopy (STEM) and atom probe tomography (APT),

### SUMMARY

Diffraction contrast TEM and STEM characterization used focused ion beam (FIB)-prepared neutron-irradiated Eurofer97. Detailed g.b analysis identified both  $a\langle 100 \rangle$  and  $a/2\langle 111 \rangle$  type dislocation loops. The fraction of  $a\langle 100 \rangle$  loops was  $>35\%$ , which supports results on F82H-IEA and  $^{54}\text{Fe}$  based F82H steels studied in this program (and reported in companion reports). Collectively analyzing, the TEM results from Eurofer97 and F82H variants of RAFM steels suggest microstructure evolve differently under neutron irradiation than under ions, where few or no  $a\langle 100 \rangle$  loops are reported for temperatures below 350°C. The APT experiments revealed extensive Mn and N co-segregation to dislocation loops and dislocation lines that will contribute to hardening.

### PROGRESS AND STATUS

- Irradiation Experiment: HFIR-ES22
- Material: Eurofer97
- Conditions:  $\sim 2.94 - 3.24$  dpa at  $300 \pm 30$  °C
- Sample ID: M100 and M014

The STEM characterization revealed a homogeneous distribution of dislocation loops in Eurofer97. The g.b analysis was performed on the laths to identify the Burgers vector of the dislocation loops. Using this method, 34% of the loops were  $a\langle 100 \rangle$  type while the rest were  $a/2\langle 111 \rangle$  type. Similar to results on F82H-IEA and  $^{54}\text{Fe}$  F82H described in companion reports, the STEM characterization reveals high fraction of  $a\langle 100 \rangle$  type loops at this temperature. An example of g.b analysis is shown in **Figure 20**, where the same nanograin was tilted along different g vectors to identify the visibility-invisibility patterns. In **Figure 20**, blue arrows point to  $a\langle 100 \rangle$  type loops while the red arrows point to  $a/2\langle 111 \rangle$  type loops. The presence of  $a\langle 100 \rangle$  loops, which has a slightly longer Burgers vector and are sessile, should be properly evaluated to better understand the contribution of different microstructural defects to hardening-embrittlement. No cavities were detected in the irradiated sample. Raft formation or clustering of dislocation loops around pre-existing dislocations was not observed, in contrast to results typically reported for ion irradiation at this temperature.

The APT experiments were conducted to quantify any nanoscale radiation-induced chemical changes. The APT atom maps in **Figure 20** show inhomogeneous distribution of Mn and N. Analysis using iso-concentration algorithm, detected co-segregation of Mn and N. This segregation primarily occurred on microstructural defects such as pre-existing dislocation lines and dislocation loops. The results are similar to those reported for irradiated F82H in the companion reports- with difference being F82H showed Mn and Si co-segregation whereas Eurofer97 showed Mn and N co-segregation. This co-segregation may

exacerbate the irradiation-induced hardening-embrittlement problem in this class of steel under neutron irradiation.

**Future Work**

Modeling using dispersed barrier hardening will quantify the irradiated microstructure contributions to radiation hardening. Additional analysis of the APT data sets will improve statistics of Mn and N co-segregation.

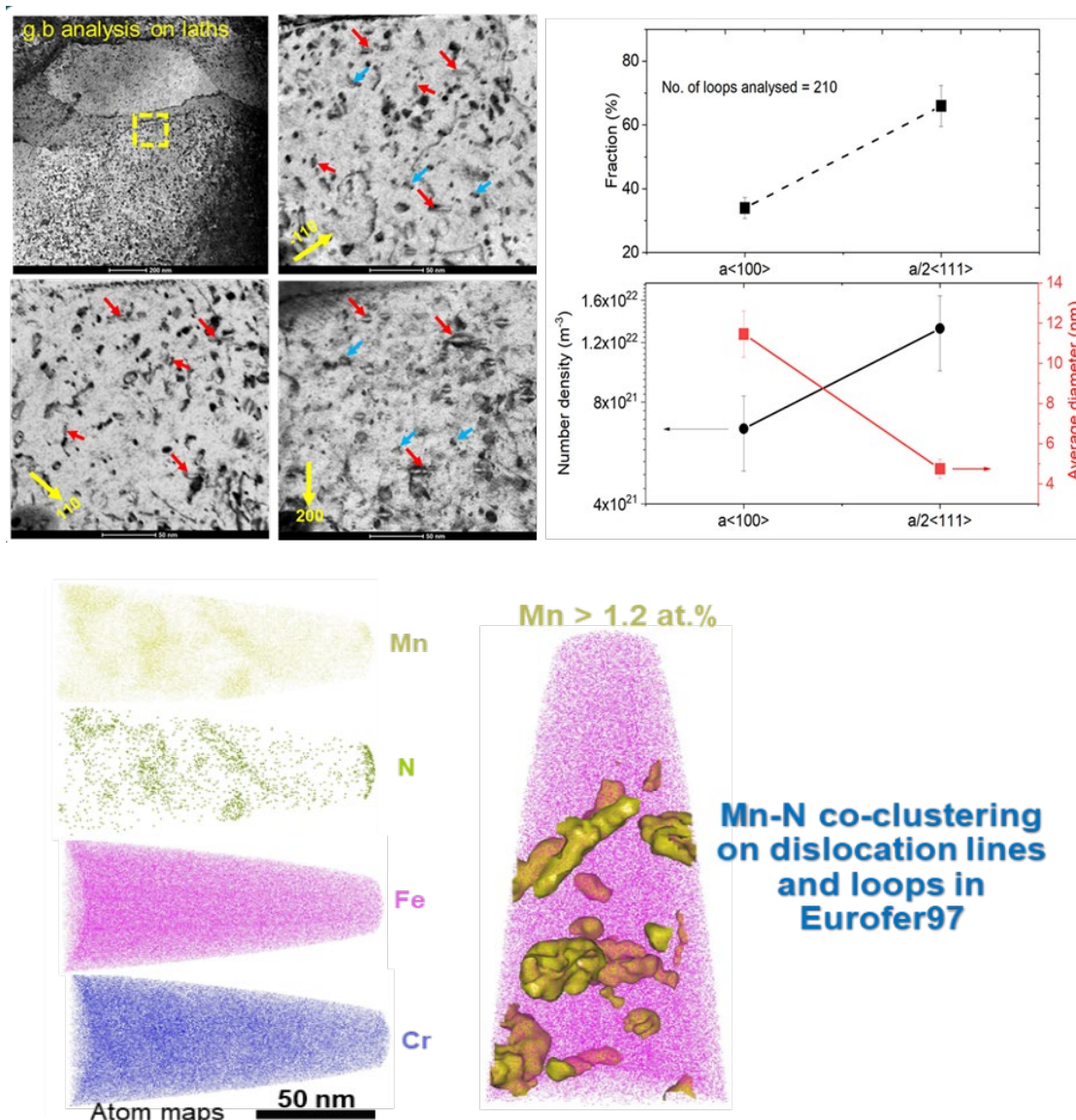


**Figure 20. STEM analysis of dislocation loops in HFIR irradiated Eurofer97 (2.94 - 3.24 dpa, 300±30°C) showing fraction of sessile a<100> loops and glissile a/2<111> loops. Blue arrows point to a<100> type loops while red arrows show a/2<111> type loops. Same area was imaged under different diffraction vectors (g vectors) noted in the figure, along Z = [001] zone axis. APT characterization (lower section) shows RIS driven Mn-N co-segregation along dislocation lines and dislocation loops (using a X% Mn and Y% N iso-concentration surface). Quantitative APT analysis with OSCAR data analysis algorithm is ongoing.**

## 2.11 DEFECTS IN IRRADIATED ISOTOPICALLY-TAILORED RAFM STEELS

A. Bhattacharya ([bhattacharya@ornl.gov](mailto:bhattacharya@ornl.gov)), J.W. Geringer, Y. Katoh (ORNL), and T. Nozawa (QST-Japan)

### OBJECTIVE

This task is aimed at understanding the microstructural defects in neutron-irradiated isotopically-tailored RAFM steels. A  $^{54}\text{Fe}$ -based F82H steel was irradiated in HFIR to 66 dpa at 300°C, producing 2.3 appm He/dpa, and was studied by conventional transmission electron microscopy (TEM) and analytical scanning transmission electron microscopy (STEM) – energy dispersive X-ray (EDX) microanalysis.

### SUMMARY

Using the TEM technique, He-induced nanoscale (~2-3 nm diameter) cavities were detected in the irradiated steel; however, no evidence of grain boundary cavity formation was observed. The STEM analysis revealed the presence of irradiation-induced dislocation loops distributed homogeneously in the microstructure. These dislocation loops were expected to be  $a\langle 100 \rangle$  type, which is similar to low dose F82H-IEA and Eurofer97 data presented in companion sections of this report. The STEM-EDX microanalysis revealed that all dislocation loops were enriched in Cr. In addition, depletion of Cr and enrichment of Si was detected on the grain boundaries. The APT data are needed to independently quantify any radiation-induced segregation (RIS)-driven segregation of Mn, Si, and P to the dislocation loops, as identified in companion reports on reference F82H-IEA steel.

### PROGRESS AND STATUS

- Irradiation Experiment: HFIR-JP29
- Material:  $^{54}\text{Fe}$ -F82H-IEA
- Conditions: ~66 dpa, 2.3 appm He/dpa, 300 °C
- Sample ID: S60 and S61
- Two FIB samples characterized

The STEM characterization of  $^{54}\text{Fe}$  F82H steel, revealed a high fraction (>50%) of  $a\langle 100 \rangle$  type dislocation loops in the microstructure (**Figure 21**), which is qualitatively similar to low dose data reported for F82H and Eurofer97. The  $a\langle 100 \rangle$  type dislocation loops were large (>50-70 nm in diameter). Unlike the low dose F82H-IEA and Eurofer97 where no enrichment of Cr was detected on the loops, STEM-EDX analysis revealed that dislocation loops were decorated with Cr rich clusters, (believed to be driven by RIS [1]). In addition to loops with Cr segregation, STEM-EDX analysis also revealed RIS driven Si segregation to the grain/packet/lath boundaries and Cr depletion from such microstructural features (**Figure 22**). Depletion of Cr at grain boundaries is opposite to low dose behavior detected in F82H-IEA where enhanced Cr segregation is reported in a companion report. Therefore, a detailed dose dependent study of microstructural characterization is needed to determine at what dose levels Cr starts to segregate to dislocation loops and/or at what level Cr segregation may change to depletion. Because He generation by the  $^{54}\text{Fe}$ , nanometer cavities (2-3 nm) in high number density were detected throughout the sample. However, no grain boundary cavity formation was detectable in this steel.

In addition to the analysis of dislocation loops and RIS,  $\text{M}_{23}\text{C}_6$  carbides were characterized in the steel. High resolution (HR)-TEM characterization revealed no major structural deterioration of  $\text{M}_{23}\text{C}_6$ , which remained fully crystalline (**Figure 23**). This result contrasts with data from Eurofer97 irradiated to similar

conditions where amorphization and disintegration of initial particles into smaller satellite type particle distribution was shown after irradiations in the same HFIR-JP29 irradiation experiments.

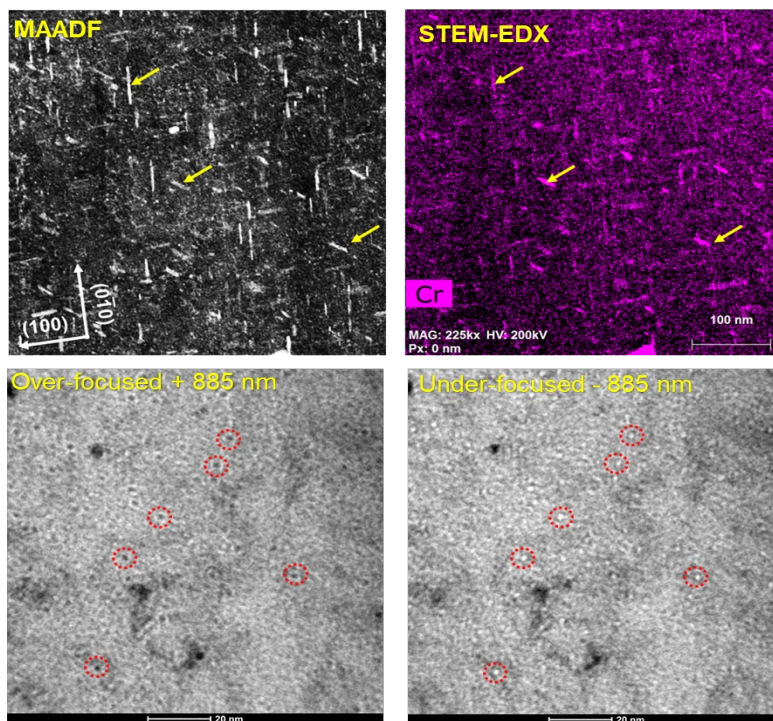


**Figure 21.** STEM analysis of  $^{54}\text{Fe}$ -F82H alloy irradiated to  $\sim 66$  dpa, 2.3 appm He/dpa at  $300^\circ\text{C}$ . Medium angle annular dark field image down  $[001]$  zone axis showing large ( $>50$ - $70$  nm diameter)  $a\langle 100 \rangle$  type dislocation loops (indicated by arrows). STEM-EDXS elemental maps showed dislocation loops that appeared to include Cr segregation driven by RIS. Under and over-focus bright-field TEM images show nanoscale cavities in the irradiated steel because He generation. No grain boundary cavity formation was detected in this steel.

### Future Work

The APT characterization of the irradiated  $^{54}\text{Fe}$  specimen is planned to independently corroborate the STEM-EDXS RIS observations. Additional HRTEM experiments and data analysis are ongoing to further assess the irradiation-induced microstructural evolution in this steel.

### References

- [1] A. Bhattacharya, E. Meslin, J. Henry et al. Chromium enrichment on the habit plane of dislocation loops in ion irradiated FeCr alloys, *Acta Mater.* 78 (2014) 398-403.
- [2] K. Wang, C.M Parish, K.G. Field, L. Tan, Y. Katoh, Segregation behavior and phase instability of Eurofer97 after neutron irradiation to 72 dpa. *J. Nucl. Mater.* 547 (2021) 152834.

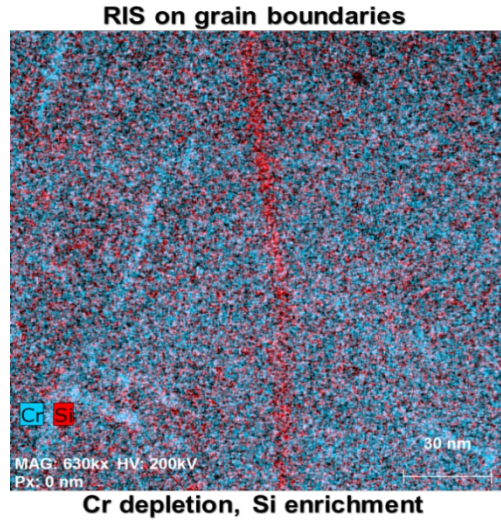


**Figure 22.** Combined Cr and Si STEM-EDX elemental map indicating RIS of Si and depletion of Cr on boundaries.

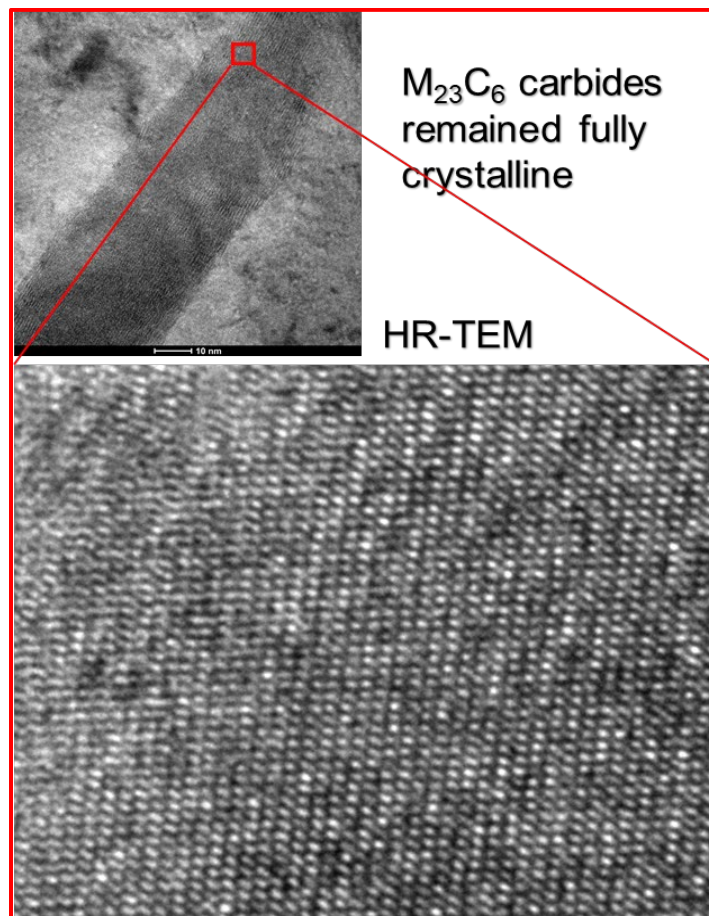


**Figure 23.** HR-TEM image of an  $M_{23}C_6$  carbide in  $^{54}Fe$ -F82H steel remained crystalline after irradiation to ~66 dpa, 2.3 appm He/dpa at 300°C.

## 2.12 DEVELOPMENT OF TRANSFORMATION ENHANCED ODS Fe-Cr ALLOYS

D.T. Hoelzer ([hoelzerd@ornl.gov](mailto:hoelzerd@ornl.gov))

### OBJECTIVE

A transformation-enhanced oxide dispersion strengthened (ODS) Fe-10Cr alloy is being developed for fusion reactor applications requiring high-temperature strength and toughness properties and microstructural stability during exposure to energetic neutrons producing high dpa and transmuted He concentrations. The objective of this task is to produce a larger heat of the ODS Fe-10Cr alloy containing 1%W (M4) for further development.

### SUMMARY

Two transformation-enhanced ODS Fe-10Cr alloys (M4 and M5) were initially developed to investigate if the addition of 1%W to the M4 alloy was beneficial to the microstructure and mechanical properties compared to the W-free M5 alloy. Previous results showed no apparent differences in the size and number density of the nano-size oxide particles between the M4 alloy containing 1%W and the M5 alloy with no W addition. However, the tensile and creep properties of M4 showed overall improvement in the balance of strength and ductility up to 800°C and creep performance between 550-800°C. Based on conclusions of this comparison further alloy development efforts will concentrate on M4 containing 1%W.

### PROGRESS AND STATUS

The nominal composition of M4 is Fe-10Cr-1W-0.3Ti-0.2V+0.3Y<sub>2</sub>O<sub>3</sub> (weight %). *Figure 24* shows the microstructure of M4 obtained in past studies. The bright-field TEM micrograph (*Figure 24a*) shows submicron grains and a high dislocation density. The grains are elongated along the extrusion axis with length-to-width grain aspect ratios of <2. The energy-filtered TEM (EFTEM) Fe-M jump ratio map (*Figure 24b*) shows the dispersion of nano-size Y-Ti-oxide particles in M4. The dark contrast of the nano-size oxide particles observed in the Fe-M jump ratio map is due to local depletion of Fe by the Y-Ti-oxide particles. The average size of the Y-Ti-oxide particles was determined using the Image J software to process each oxide particle observed in the EFTEM Fe-M jump ratio map, yielding an average size of 2.3 +/- 0.8 nm diameter. The number density of the oxide particles was also determined using the Image J software to count all of the oxide particles in a local area of the sample and the local thickness was measured using the t/l approach, where t is the thickness and l is the inelastic scattering mean free path which is ~140 nm for Fe. The resulting number density of the Y-Ti-oxide particles in M4 was 4.5 +/- 0.8 × 10<sup>23</sup>m<sup>-3</sup>.

A larger heat of M4 was produced for further alloy development. Two 1 kg batches of gas atomized Fe-10Cr-1W-0.3Ti-0.2V powder were blended with 0.3% Y<sub>2</sub>O<sub>3</sub> powder and ball milled for 40 hrs. using the high kinetic energy CM08 Simoloyer. The two 1 kg batches of ball-milled powder were blended and loaded into a 4-inch diameter mild steel can. The filled can was vacuum degassed at 300°C, sealed, heated for 2 hrs. at 850°C then extruded through a rectangular cross section die. *Figure 25* shows the extruded bar with the steel can enclosing the M4 section.

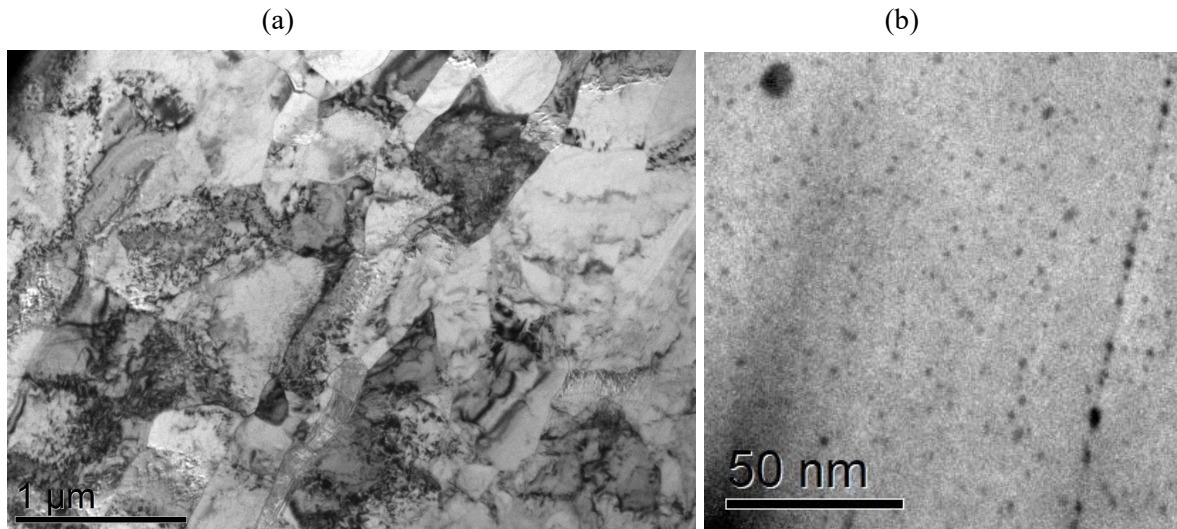


**Figure 24. Microstructure of the M4 alloy. (a) Bright-field TEM micrograph showing the ultra-fine grain containing a high dislocation density and (b) EFTEM Fe-M jump ratio map showing the nano-size oxide particles dispersed within grains and on the grain boundary.**



**Figure 25. Cross-section of the extruded M4 bar showing the ODS section enclosed in the steel can.**

### **Future Work**

The effects of thermomechanical treatments on the transformation kinetics and volume fraction of the austenite and ferritic phases that occur above  $\sim 910^{\circ}\text{C}$  will be determined. The objective is to improve the strength, ductility, creep, and fracture toughness properties of M4.

## 2.13 ATOM PROBE TOMOGRAPHY OF HARDENING IN IRRADIATED ODS STEELS

A. Bhattacharya ([bhattacharya@ornl.gov](mailto:bhattacharya@ornl.gov)), S.M. Levine, D.T. Hoelzer, J. Poplawsky, J.W. Geringer, Y. Katoh, and S.J Zinkle

### OBJECTIVE

This task is aimed at understanding irradiation-induced microstructural features in ODS steels that can cause hardening-embrittlement. A few different ODS alloys neutron-irradiated in HFIR between ~4.5 – 50.7 dpa 285-500 °C were also characterized using atom probe tomography (APT).

### SUMMARY

Unexpected irradiation hardening was detected in numerous ODS steels after HFIR irradiation between ~4.5 - 50.7 dpa at temperatures of 285 to 500 °C (detailed in a companion report). To understand the reason for hardening, APT characterized irradiated 14wt.%Cr MA957 (from INCO) and 20wt.%Cr-5.5wt.%Al PM2000 (from Plansee). In MA957 and PM2000, high temperature irradiation-induced hardening (greater than typically reported for RAFM steels) was associated with solute clustering of Cr ( $\alpha'$  phase – expected), Ni and Ti in MA957 (new observation) and Al and Ti clustering in PM2000 (new observation). These results show that ODS steels are not immune to low temperature hardening-embrittlement as is generally assumed.

### PROGRESS AND STATUS

The APT experiments were conducted on samples of PM2000 and MA957 following irradiation in the HFIR to doses ranging from 4.5 to 50.7 dpa at temperatures between 285 and 500 °C. Needle-shaped APT samples were milled in the Low Activation Materials Development and Analysis (LAMDA) laboratory using a FEI Quanta Focused Ion Beam (FIB), and subsequently analyzed at 50K with a detection rate of 0.5 using the Local Electron Atom Probe (LEAP) 4000X HR at the Center for Nanophase Materials Sciences (CNMS). Reconstructions of the tip volumes were performed using Cameca's Integrated Visualization and Analysis Software (IVAS). The plane spacing of an indexed pole was used to calibrate the depth (z) direction of each reconstruction. The field factor (k) and image compression factor (ICF) of reconstructions varied between 4.1 – 6.1 and 1.4 – 1.65, respectively. Subsequent cluster analysis used the Open-Source Characterization of APT Reconstructions (OSCAR) program [2]. Parameters used for cluster analysis are in *Table 5*.

**Table 5. OSCAR APT Cluster Analysis Parameters**

Material	Solute Atom	Concentration Threshold ( $c_{th}$ ) (at. %)	Linking Distance ( $d_{link}$ ) (nm)	Minimum Solute Atoms per Cluster ( $N_{min}$ )
PM2000	Cr	34.0	0.46	20
PM2000	Ti	5.0	1.16	8
MA957	Cr	30.0	0.45	16
MA957	Ni	5.5	0.90	8

Selected atom maps extracted from a typical dataset of neutron-irradiated PM2000 after irradiation to 8.7 dpa at 500°C are provided in *Figure 26*. For PM2000, Cr-rich regions were observed at all irradiation conditions. *Table 6* contains size, density, and compositional information. Given the Cr content of this alloy, radiation-enhanced precipitation of  $\alpha'$  is expected. It is notable that average core concentration of Cr was well below the 80 – 90 at. % Cr that is typically observed in neutron-irradiated Fe-Cr binary

alloys. Further analysis is needed to rule out trajectory aberrations. However, these relatively low core Cr concentrations are consistent with previous results from APT studies of neutron-irradiated FeCrAl alloys [1,2]. *Ab initio* calculations by Li et al. [3] indicate that Al increases the formation energy of

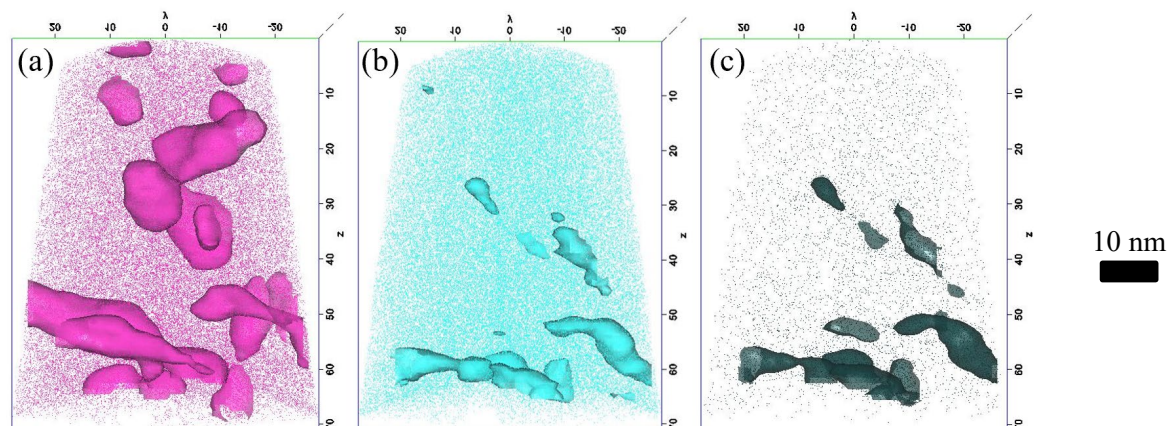


**Figure 26. Atom maps from PM2000 irradiated at 500°C to 8.7 dpa. (a) Cr map with 30 at.% iso-surfaces (b) Al map with 15 at.% iso-surfaces (c) Ti map with 3 at.% iso-surfaces.**

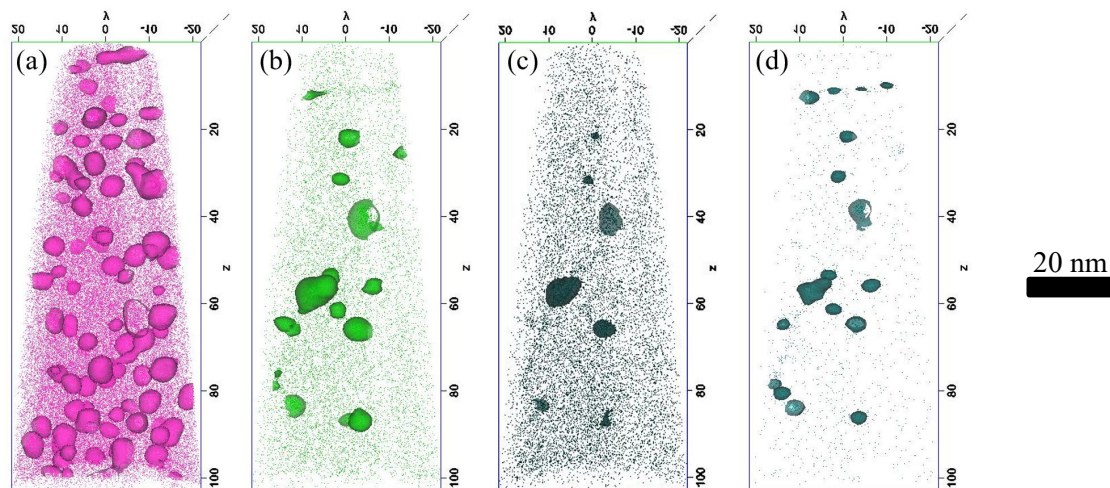
$\alpha'$  and thus destabilizes the  $\alpha'$  phase. Size and number density of  $\alpha'$  did not vary significantly as irradiation dose increased from 4.5 to 50.7 dpa. This is consistent with previous studies of Fe-Cr binary alloys where  $\alpha'$  reaches equilibrium at low ( $< 1.0$  dpa) irradiation doses. For the irradiations between 285 – 449 °C, the average Guinier radius of these Cr-enriched clusters was  $\sim 1.4 - 1.6$  nm and the number density of features was  $\sim 2 \times 10^{24} - 4 \times 10^{24} \text{ m}^{-3}$ . In contrast, for the irradiation conducted at 500 °C, the average Guinier radius of the Cr clusters was  $\sim 4.5$  nm and number density of Cr-enriched zones was reduced an order of magnitude to  $\sim 2.4 \times 10^{23} \text{ m}^{-3}$ . The dramatic increase in Cr-enriched “cluster” size corresponded to the onset of Al/Ti solute clustering. **Table 7** gives the size, density, and compositional information. The Al/Ti-enriched clusters were observed adjacent to Cr-enriched features. This suggests that the formation of  $\alpha'$  and Al/Ti-enriched clusters may be linked. Similar Al/Ti-enriched clustering occurring heterogeneously at  $\alpha'$  interfaces was observed by Capdevilla, et. al. [4] in thermally-aged PM2000. The core composition of the Al/Ti-enriched clusters in this study was close to the  $\beta'$  phase ( $\text{Fe}_2\text{AlTi}_{0.6}\text{Cr}_{0.4}$ ) proposed in [4].

**Table 6. Quantitative results for Cr-rich clusters in neutron irradiated PM2000**

Irradiation Temp. (°C)	Dose (dpa)	Avg. Radius (nm)	Density ( $\text{m}^{-3}$ )	Avg. Core Fe (at. %)	Avg. Core Cr (at. %)	Avg. Core Al (at. %)
$285 \pm 20$	50.7	$1.50 \pm 0.11$	$1.44 \times 10^{24}$	$45.4 \pm 3.3$	$43.0 \pm 3.1$	$8.86 \pm 0.6$
$335 \pm 20$	4.5	$1.43 \pm 0.12$	$3.95 \times 10^{24}$	$43.5 \pm 3.4$	$46.0 \pm 3.6$	$9.60 \pm 0.8$
$449 \pm 20$	5.5	$1.57 \pm 0.08$	$1.72 \times 10^{24}$	$46.0 \pm 2.4$	$45.2 \pm 2.4$	$9.82 \pm 0.5$
$500 \pm 20$	8.7	$4.83 \pm 0.72$	$2.43 \times 10^{23}$	$40.0 \pm 6$	$51.4 \pm 7.7$	$7.51 \pm 1.1$

**Table 7. Quantitative results for Al/Ti enriched clusters in neutron irradiated PM2000**

Irradiation Temp. (°C)	Dose (dpa)	Avg. Radius (nm)	Density (m <sup>-3</sup> )	Avg. Core Fe (at. %)	Avg. Core Cr (at. %)	Avg. Core Al (at%)	Avg. Core Ti (at%)
285 ± 20	50.7	n/a	0	n/a	n/a	n/a	n/a
335 ± 20	4.5	n/a	0	n/a	n/a	n/a	n/a
449 ± 20	5.5	1.66 ± 0.68	3.00 x 10 <sup>22</sup>	55.6 ± 22.7	19.0 ± 7.7	14.4 ± 6.0	8.7 ± 3.5
500 ± 20	8.7	5.30 ± 1.16	1.13 x 10 <sup>23</sup>	50.4 ± 11.0	13.4 ± 3.0	19.6 ± 4.3	14.4 ± 3.2

**Figure 27. Atom maps from MA957 irradiated at 500°C to 8.7 dpa. (a) Cr map with 25 at.% iso-surfaces (b) Ni map with 3 at.% iso-surfaces (c) Ti map with 3 at.% iso-surfaces (d) TiO map with 2 at.% iso-surfaces.**

Selected atom maps from a typical analysis volume of neutron-irradiated MA957 after 8.7 dpa at 500°C are provided in **Figure 27**. Unlike PM2000, much finer Cr-enriched clusters were observed in MA957 for all irradiation conditions. **Table 8** contains size, density, and compositional information of the irradiation-induced features. The formation of  $\alpha'$  in MA957 under irradiation at 500°C is unexpected given that at 500°C the solubility limit of Cr in Fe is close to 14 wt. %. By comparison,  $\alpha'$  was observed in MA957 containing 13.8 wt. % Cr after irradiation in the Fast Flux Test Facility–Materials Open Test Assembly (FFTF–MOTA) to 109 – 113 dpa at 412°C, but not at 550 and 670°C [5]. In this study, Cr-rich clusters appear to coarsen from 335 – 500°C as irradiation temperature increases and with increasing dose. The observation that  $\alpha'$  did not reach equilibrium by ~1 dpa (as expected) merits further study. It is also possible that during irradiation at 285°C to 50.7 dpa, ballistic effects may have resulted in dissolution of finer clusters. For all irradiation conditions, measured Cr cluster core concentration was notably less than fully mature  $\alpha'$  (80 – 90 at. % Cr). Further work is needed to determine whether this is due to APT trajectory aberrations or if  $\alpha'$  formation is being suppressed.

**Table 8. Quantitative results for Cr-rich clusters in neutron-irradiated MA957**

Irradiation Temp. (°C)	Dose (dpa)	Avg. Radius (nm)	Density (m <sup>-3</sup> )	Avg. Core Fe (at. %)	Avg. Core Cr (at. %)
285 ± 20	50.7	1.68 ± 0.10	1.44 x 10 <sup>24</sup>	43.0 ± 2.5	53.9 ± 3.1
335 ± 20	4.5	1.16 ± 0.05	3.95 x 10 <sup>24</sup>	53.6 ± 2.4	44.9 ± 2.0
449 ± 20	5.5	1.35 ± 0.06	1.72 x 10 <sup>24</sup>	49.1 ± 2.0	49.3 ± 2.0
500 ± 20	8.7	1.95 ± 0.11	2.43 x 10 <sup>23</sup>	38.5 ± 2.3	60.2 ± 3.5

In addition to Cr-enriched clusters, Ni/Ti-enriched clusters were also observed in MA957. This is consistent with previous work in which multivariate statistical analysis (MVSA) was used to characterize scanning transmission electron microscopy (STEM) energy dispersive X-ray spectroscopy (EDXS) spectrum image datasets of MA957 following irradiation at 285°C to 50.7 dpa [6]. **Table 9** contains size, density, and compositional information for each irradiation condition. After irradiation at 500°C, Ni and Ti enrichment was most pronounced, and clusters also contained ~ 3 at. % Si. For irradiations between 285 and 449°C, a portion of the Ni/Ti-enriched clusters were detected at the interface of the oxides. In contrast, following the irradiation at 500°C, almost all Ni/Ti-enriched solute clusters were associated with an oxide. With respect to dose, Ni/Ti-enriched clusters continued to nucleate beyond 4.5 – 8.7 dpa and roughly doubled in number density by 50.7 dpa. The ratio of Ni to Ti in these solute clusters was ~2.

**Table 9. Quantitative results from Ni/Ti-enriched solute clusters in neutron-irradiated MA957**

Irradiation Temp. (°C)	Dose (dpa)	Avg. Radius (nm)	Density (m <sup>-3</sup> )
285 ± 20	50.7	1.68 ± 0.10	1.44 x 10 <sup>24</sup>
335 ± 20	4.5	1.16 ± 0.05	3.95 x 10 <sup>24</sup>
449 ± 20	5.5	1.35 ± 0.06	1.72 x 10 <sup>24</sup>
500 ± 20	8.7	1.95 ± 0.11	2.43 x 10 <sup>23</sup>

Irradiation Temp. (°C)	Dose (dpa)	Avg. Core Fe (at. %)	Avg. Core Cr (at. %)	Avg. Core Ni (at. %)	Avg. Core Ti (at. %)	Avg. Core Si (at. %)
285 ± 20	50.7	67.6 ± 5.0	7.2 ± 0.5	12.0 ± 1.0	3.8 ± 0.3	0.6 ± 0.0
335 ± 20	4.5	65.7 ± 8.2	9.3 ± 1.2	12.6 ± 1.6	6.1 ± 0.8	1.2 ± 0.1
449 ± 20	5.5	48.1 ± 5.2	8.7 ± 1.0	12.7 ± 1.4	6.1 ± 0.7	1.0 ± 0.1
500 ± 20	8.7	72.8 ± 13.1	6.6 ± 1.2	21.4 ± 3.8	12.0 ± 2.1	3.3 ± 0.6

### Future Work

The APT data sets from 12 YWT are also available. Analysis of the collected data will be performed to evaluate Cr-dependent irradiation hardening mechanisms. In addition, APT experiments using HFIR-irradiated 14YWT will also be performed.

### References

- [1] P. Edmondson et al. Irradiation-enhanced  $\alpha'$  precipitation in model FeCrAl alloys. *Scripta Mater.*, 116 (2016): 112-116.
- [2] C. Massey, et al. Deconvoluting the Effect of Chromium and Aluminum on the Radiation Response of Wrought FeCrAl Alloys After Low-Dose Neutron Irradiation. *J. Nucl. Mater.*, 549 (2021): 152804.

- [3]. Li et. al., The effect of Al on the 475 C embrittlement of Fe–Cr alloys. *Comp. Mater. Sci.*, 74 (2013): 101-106.
- [4] C Capdevilla et al., Strengthening by intermetallic nanoprecipitation in Fe–Cr–Al–Ti alloy, *Acta Mater.*, 107 (2016): 27-37.
- [5] N. Bailey et al., Atom probe tomography analysis of high dose MA957 at selected irradiation temperatures, *J. Nucl. Mater.*, 459 (2015): 225-234.
- [6] S. M. Levine et. al., “Neutron irradiation induced phase separation in oxide dispersion strengthened alloys.” ORNL/TM2020/1837, December 2020.

## 2.14 Fe-Cr-Al ODS ALLOYS FOR FUSION REACTOR APPLICATIONS

Sebastien Dryepondt( [dryepondtsn@ornl.gov](mailto:dryepondtsn@ornl.gov)), and Caleb Massey

### OBJECTIVE

Our goal is to develop, fabricate using conventional and advanced manufacturing techniques, and characterize oxide dispersion strengthened (ODS) Fe-10/12Cr-5/6Al-0.3Zr + Y<sub>2</sub>O<sub>3</sub> alloys with a high number density of nano-scale oxide precipitates. The strengthening nano-precipitates will improve the alloy creep and irradiation resistance at T>600°C whereas the high Al-content will ensure the formation of an Al-rich scale and provide adequate compatibility with Pb-Li at 550-650°C.

### SUMMARY

The dual coolant lead-lithium (DCLL) blanket is the leading US concept for a DEMO fusion reactor, and Pb-Li compatibility with containment structural materials is a major material requirement. Alumina-forming alloys in contact with PbLi can form “semi-protective” LiAlO<sub>2</sub> oxide layers leading to acceptable PbLi compatibility up to ~650°C [1]. The ODS FeCrAl alloys are prime candidate materials for advanced fusion reactors operating at temperatures ~650°C due to their superior irradiation and creep resistance compared to RAFM steels at T>650°C. The ORNL has developed several ODS Fe-10/12-Cr-5/6Al-0.3Zr + 0.25Y<sub>2</sub>O<sub>3</sub> alloys and demonstrated their potential for fusion applications [2-3]. However, the complex processing route for ODS FeCrAl results in high production cost and batch-to-batch property variations. Additive manufacturing (AM) offers a new route to fabricate near-net shape complex ODS components, and both ODS FeCr and FeCrAl alloys have been fabricated by laser powder bed fusion (LPBF) using ball-milled powders [4,5]. In both cases, nano-precipitates were observed, but one concern is that powder deformation during ball-milling can affect powder flowability during printing. Zhong et al.[6] ball-milled 316L powder with 800 nm Y<sub>2</sub>O<sub>3</sub> powder using a low rotating speed (250 rpm) for only 2 h to reduce the 316L powder deformation and “deposit” Y<sub>2</sub>O<sub>3</sub> particles on the powder surface. They observed mainly (Y,Si,O)-rich precipitates, ~40nm in size in the LPBF ODS 316L with limited impact on the alloy tensile properties. Donate-Buendia et al. [7] produced ODS FeCrAl alloys by LPBF and directed energy deposition (DED) using dielectrophoretic-controlled adsorption of 0.08 wt% laser-synthesized Y<sub>2</sub>O<sub>3</sub> at the surface of FeCrAl ferritic steel powder. This method preserved the shape of the gas-atomized FeCrAl powder and resulted in an increase in compression yield strength at 600°C for the ODS alloys, in particular the one fabricated by LPBF, in comparison with the LPBF and DED FeCrAl alloy without Y<sub>2</sub>O<sub>3</sub> addition.

Our goal is to characterize ODS FeCrAl powders produced using different ball-milling conditions and develop a strategy for the fabrication of ODS FeCrAl by DED and/or LPBF.

### PROGRESS AND STATUS

Gas-atomized Fe-12Cr-6.1Al-0.3Zr (wt.%) powder from ATI Powder Metals was ball-milled in a CM08 Simoloyer under Ar with nanocrystalline Y<sub>2</sub>O<sub>3</sub> (17-31 nm in diameter.) Ball-milling durations of 2 h and 40 h with rotating speed alternating from 350 to 600 rpm were selected based on a previous study conducted with Fe-14Cr-0.4Ti+Y<sub>2</sub>O<sub>3</sub> powders. Ball-milling for 40 h produced an excellent dispersion of Y<sub>2</sub>O<sub>3</sub> in the FeCrAlZr powder and is considered optimum for the fabrication of ODS alloys via powder extrusion [2], whereas 2 h resulted in acceptable Y<sub>2</sub>O<sub>3</sub> mixing. Characterization of the resulting powder was conducted by optical microscopy, backscattered scanning electron microscopy (BSE-SEM) and energy-dispersive X-ray spectroscopy (EDS). The Leica LAS image analysis software was employed to determine particle size (equivalent diameter) and roundness.

## Results

**Figure 28** shows optical micrographs of the powders in the as-received condition (AR) and after ball-milling for 2 h (2hBM) and 40 h (40hBM). The cylindrical morphology of the AR FeCrAlZr powder is typical of gas atomized powder with voids and/or satellites in a few of them. In contrast, elongated particles were observed for the 2hBM and 40hBM powders with the main defects located at interfaces between particles that have been cold-welded together. The main difference between the 2hBM and 40hBM powders was the powder size as confirmed by the measurements displayed in **Figure 29a**. The particle size for the 2hBM powder was close to the AR particle size except for a shift in the count peak from  $\sim 45 \mu\text{m}$  to  $\sim 35 \mu\text{m}$ . The count peak was  $\sim 25 \mu\text{m}$  for the 40hBM powder resulting in average particle size/D50 (50% of the particles are either smaller or larger) of 33/32  $\mu\text{m}$  compared to 47/44  $\mu\text{m}$  for the 2hBM powder and 51/49  $\mu\text{m}$  for the AR powder. These numbers need to be compared with the D50 optimum values for LPBF and DED systems, which are 29.4 and 64.2  $\mu\text{m}$ , respectively [8].

The particle roundness, defined in equation 1, is also a critical parameter for additive manufacturing and measurements are presented in **Figure 29b**.

$$\text{roundness} = \frac{p^2}{4\pi A} \quad p = \text{perimeter}, A = \text{Area} \quad (1)$$

A perfect circle has a roundness of 1, and the roundness number increases with particle deformation.

As expected, the roundness values were close to 1 for  $\sim 90\%$  of the particles for the AR powder but much higher roundness values were measured for the ball milled powders. Surprisingly, particle roundness did not change significantly between the 2hBM and 40hBM powder, indicating that the particle shape during ball milling is already established after  $\sim 2$  h.

In addition, Hall flow tests were conducted on the three powders to determine powder flowability and the results are summarized in **Table 10**. The AR powder exhibited good flowability, but very fine particles would need to be sieved out before printing. The flowability for the 2hBM powder was higher but should still be sufficiently low for DED systems. Overall, short ball-milling duration will result in powders that can be used in DED systems [6], while longer ball-milling times will yield powders more acceptable for LPBF machines [4,5].

The BSE-SEM and EDS characterizations were also conducted to evaluate powder chemistry homogeneity (**Figure 30**). The AR powder exhibited  $\sim 10 \mu\text{m}$  grain size with clear Zr segregation at grain boundaries. The Zr and Y segregation was observed for the 2hBM powder at the particle edges, but this needs to be confirmed as it might simply be due to an edge artifact. Bulk chemistry of the particles appeared homogenous, except for a few Fe-rich regions, likely due to fragments of the high-strength carbon steel ball-milling media being incorporated into the powder. Interestingly, an inhomogeneous segregation of Zr and Y was observed in the 40hBM powder again with a few Fe-rich particles (not shown here). Massey et al. conducted SEM characterization on a similar FeCrAlZrY powder after ball milling for 40 h and highlighted the presence of nano scale grains [3]. Higher magnification STEM-EDS characterization will be required to measure potential segregation at grain boundaries. Compared with techniques aimed at depositing  $\text{Y}_2\text{O}_3$  particles at the surface of FeCrAlZr particles [6,7], ball-milling will lead to the incorporation of Y and O into the FeCrAlZr powder [3,9], which should help with nano-precipitate formation during printing.

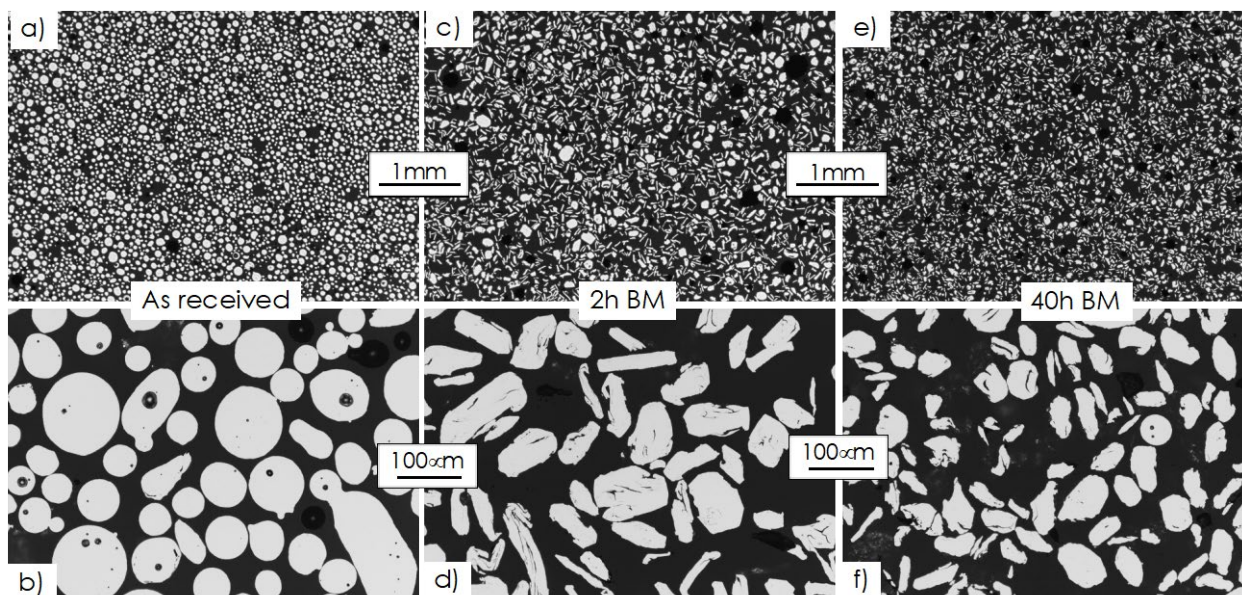


Figure 28. Optical cross-section micrographs of FeCrAlZr powders, a) and b) as-received gas atomized powder, c) and d) powder after 2 h of ball milling, e) and f) powder after 40 h of ball milling.

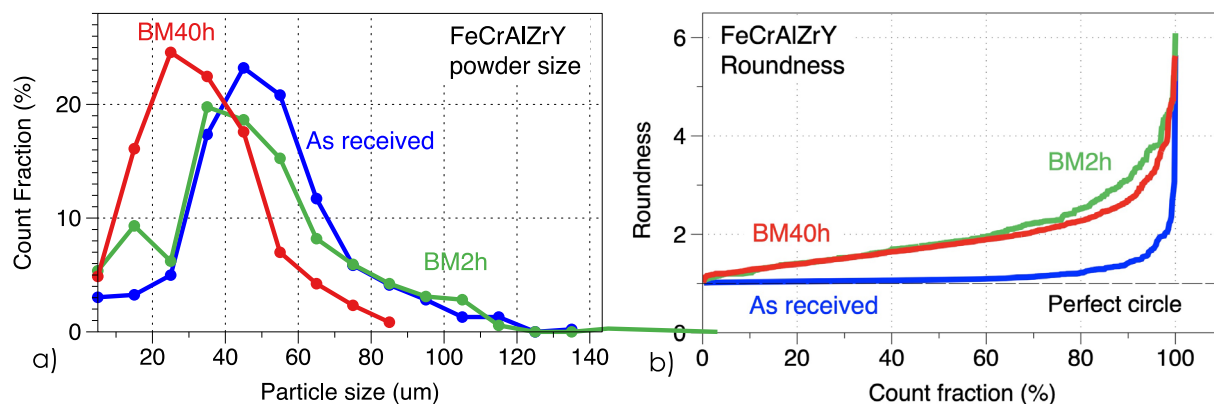


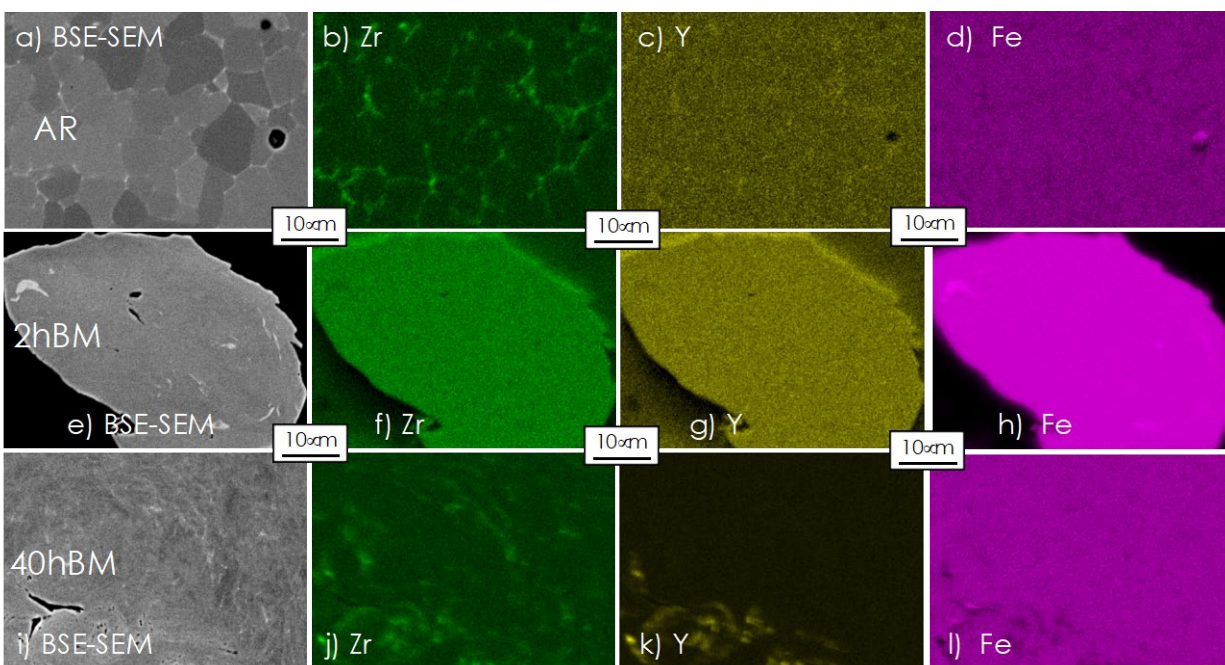
Figure 29. Measurements from optical images shown in Figure 28, a) particle size, b) particle roundness.

Table 10. Hall flow test results

Powder	Flowability (s)	Comments
AR	17.6	Fine particles stuck to funnel after it emptied
2hBM	23	
40hBM	1min 37s	large clumps of material stuck together for 2 <sup>nd</sup> run

## Future Work

Additive manufacturing offers the unique opportunity to fabricate complex near net shape ODS FeCrAl components. Characterization of the shape and flowability of FeCrAlZr powders ball-milled with  $Y_2O_3$  powder for 2 h or 40 h revealed that short or long ball milling times will produce powders adequate for DED and LPBF systems, respectively. A key advantage of powder ball-milling is the incorporation of Y and O into the FeCrAlZr powder that should enhance the formation of nano-precipitates during printing. Six kilograms of the FeCrAlZr powder ball milled for 2 h have been produced and DED trials will take place in FY22.



**Figure 30. BSE-SEM micrographs and corresponding Zr, Y and Fe EDS maps of FeCrAlZr( $Y_2O_3$ ) powders, a)-d) AR, e)-h) 2hBM, i-l) 40hBM.**

## References

- [1] J. Jun, K. A. Unocic, M. J. Lance, H. M. Meyer, III, B. A. Pint, *Journal of Nuclear Materials*, 528, 151847 (2020).
- [2] C.P. Massey, S.N. Dryepontd, P.D. Edmondson, K.A. Terrani and S.J. Zinkle, *Journal of Nuclear Materials*, 15, 227-238 (2018).
- [3] C.P. Massey, S. N. Dryepontd, P.D. Edmondson, M.G. Frith, K C. Littrell, A. Kini, B. Gault, K.A. Terrani, and S.J. Zinkle, *Acta Materialia*, 166, 1-17 (2019).
- [4] T. Boegelein, S.N. Dryepontd, A. Pandey, K. Dawson, G.J. Tatlock, *Acta Materialia*, 87, 201-215 (2015).
- [5] E. Vasquez, P.F. Giroux, F. Lomello, A. Chniouel, H. Maskrot, F. Schuster and P. Castany, *Journal of processing tech.*, 267, 403-413 (2019).
- [6] Y. Zhong, L. Liu, J. Zou, X. Li, D. Cui and Z. Shen, *Journal of Materials Science & Technology*, 42, 97-105 (2020).
- [7] C.Doñate-Buendia, P.Kürnsteiner, F.Stern, M.B.Wilms, R.Streubel, I.M.Kusoglu, J.Tenkamp, E.Bruder, N.Pirch, S.Barcikowski, K.Durste, J.H.Schleifenbaum, F.Walther, B.Gault, B.Gökce, *Acta Materialia*, 206, 116566 (2021).

- [8] S. Vock, B. Klöden, A. Kirchner, T. Weißgärber, B. Kieback, *Progress in Additive Manufacturing*, 4, 383–397 (2019).
- [9] K. Dawson, S. J. Haigh, G. J. Tatlock, and A. R. Jones, *Journal of Nuclear Materials*, 200-209 (2015).

## 2.15 EVALUATION OF ADVANCED 3Cr-3WVTa BAINITIC STEELS

Y. Yamamoto ([yamamotoy@ornl.gov](mailto:yamamotoy@ornl.gov))

### OBJECTIVE

This work aims to evaluate the advantages in the mechanical performance of newly proposed, modified 3Cr-3WVT bainitic steels developed at ORNL. The proposed steel was designed to eliminate the need for post-weld heat treatment (PWHT), as well as providing improved mechanical properties of both base metal and weldments compared to those of existing commercial bainitic steels or ferritic-martensitic (F-M) steels. The target applications are high-temperature structural components in fusion reactors, such as helium-cooled vacuum vessels operating up to 450°C and blanket support structures operating up to 550°C.

### SUMMARY

The major technical achievements in this fiscal year are: (1) the newly proposed modified steel weldment (with a compositionally-matched weld filler metal) exhibited significantly improved impact toughness at room-temperature in the as-welded condition; and (2) the creep performance of the modified steel across the weld metal, without PWHT, demonstrated 20-25% improvement of creep strength compared to the “original” 3Cr-3WVTa steel weldment. These results suggested that the modified steel weldments could be used for high-temperature structural application without requiring PWHT. The modified steel also showed superior mechanical performance in the as-normalized condition, suggesting potentially avoiding tempering. Optimization of the heat-treatment (normalization) conditions is currently in progress.

### PROGRESS AND STATUS

Compositionally modified 3Cr-3WVTa bainitic steel (“Modified” steel) containing a higher Mn and lower C than in the “Original” steel, as summarized in **Table 11**, have been proposed and studied in the present project. The modification was based on an alloy design strategy of high hardenability with low hardness in the as-normalized and as-welded conditions to minimize the variation of mechanical properties between the base metal and weldment in the as-welded condition.

**Table 11. Nominal compositions of the steels in weight percent (balance Fe)**

Wt.%	Cr	Mn	Si	Ta	V	W	C
Original	3.0	<b>0.4</b>	0.16	0.1	0.2	3.0	<b>0.1</b>
Modified	3.0	<b>2.0</b>	0.16-0.5	0.1	0.2	3.0	<b>0.05</b>

(note: N < 50 wppm, P < 50 wppm, S < 20 wppm, and O = 20-60 wppm, from chemical analysis)

Charpy impact tests of weldments of the original and modified steels, with and without PWHT, were conducted at room temperature. The as-welded modified steel showed significantly higher absorbed energy than the original steel, presumably due to the reduced hardness in the as-normalized and as-welded conditions of the modified steel (**Figure 31a**). In contrast, the PWHT resulted in a reduction of the absorbed energy, indicating that the tempering at 700°C triggered the embrittlement of the modified steels. Ductile-to-brittle transition temperatures of the modified steel were measured as a function of the tempering temperature, summarized in **Figure 31b**. This revealed that embrittlement occurred when the steel was tempered at 680-700°C for 1h, possibly due to brittle secondary-phase formation during tempering (which requires detailed characterization). The steel tempered at 720°C for 1h was possibly over-tempered, which would negatively impact the creep-performance. Based on these results, non-

PWHT appears to be favorable for the improved impact toughness balanced with high-temperature creep strength in the modified steel weldments. The questions regarding the residual stress relaxation still exists, so that another approaches (e.g., low-temperature tempering) may need to be considered for the potential solution.

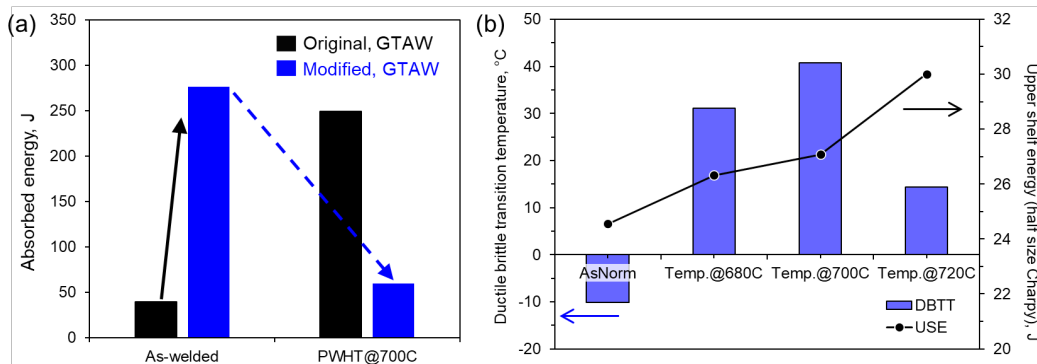


**Figure 31. (a) Charpy absorbed energy of the original and modified steel weldments measured at room temperature, and (b) the DBTT of the modified steel as a function of tempering condition.**

Creep-rupture performance of the base and the cross-weld materials for both original and modified steels is summarized in a Larson-Miller Parameter plot in **Figure 32**. The modified steel cross-weld specimens were tested only in the as-welded (gas tungsten arc weld - GTAW) condition, based on the results of the impact toughness evaluation. The cross-weld creep of the modified steel demonstrated 20-25% improvement of creep strength compared to the original steel after applying a PWHT (at 700°C for 1h), suggesting successful achievement of high performance in the modified steel without PWHT.

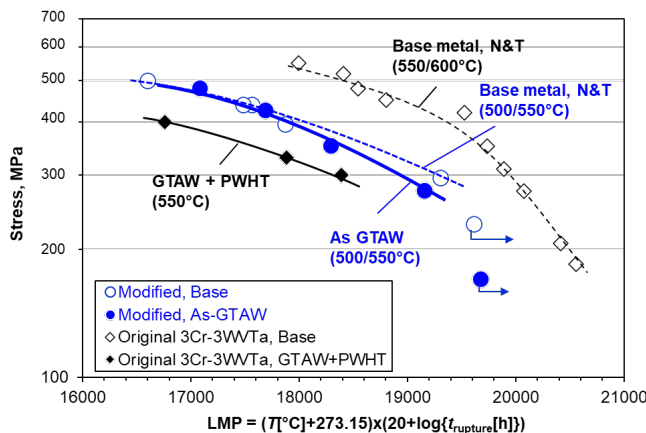


**Figure 32. Larson-Miller Parameter plot of the base and the cross-weld materials for the original and the modified 3Cr-3WVTa steels.**

### Future Work

Property evaluation of as-normalized modified steel base metal will be conducted to prove the advantages in the mechanical performance without tempering. Since the as-welded material showed improved mechanical performance, the modified steel may also be a candidate for additive manufacturing (AM) technology. A trial AM print of the modified steel is planned.

## 2.16 MECHANICAL ALLOYING OF A NOVEL AUSTENITIC DUAL-PRECIPITATION STRENGTHENED STEELS

T. Graening ([graeningt@ornl.gov](mailto:graeningt@ornl.gov))

### OBJECTIVE

Austenitic oxide dispersion strengthened (ODS) steels have been developed at the Karlsruhe Institute of Technology (KIT) and optimized in collaboration with the Oak Ridge National Laboratory. Due to the ductile nature of the austenitic phase the metallurgy production route requires nitrogen as a process control agent during the mechanical alloying process. The nitrogen prevents adhesion of powder particles to the walls of the milling chamber. The FY2021 efforts were focused on understanding and optimizing the alloying process and utilizing the introduced nitrogen to form nano-scale nitride precipitates in the ODS steels.

### SUMMARY

A dual-precipitate austenitic ODS steel was successfully developed using nitrogen as a process control agent to sequester complex V-Ti-N precipitates associated with ODS precipitates. The observed small diameter oxide and nitride precipitates were found to increase high temperature properties and creep behavior of the alloy. The XRD, SEM and TEM results confirm that a two-step mechanical alloying process with an optimized duration of 20 hours was successful in producing the desired microstructures.

### PROGRESS AND STATUS

Mechanical alloying (MA) of austenitic steel results in a large amount of cold-welding of the ductile milled powder and the milling equipment, which significantly reduces the production yield and the reproducibility of the process. To mitigate that issue a novel two-step mechanical alloying process using nitrogen as a process control agent was utilized. In addition, 0.51 wt.-% vanadium as a nitride-forming element was added to the steel pre-alloy to sequester the introduced nitrogen and to promote dual-precipitation of oxides and nitrides, at the same time increasing the production yield to near 100 percent. To optimize the process, dislocation density, chemical composition, phase fractions, crystallite sizes, and particle sizes (as shown in **Figure 33**) were evaluated after 10 milling intervals. The SEM and XRD data provided conclusive results regarding the MA process. The EDS-SEM analysis samples a more limited volume of material than does XRD, which makes determining a stopping point for the mechanical alloying process difficult. However, our research has demonstrated that the vanishing of a peak in a diffractogram is not necessarily required to determine the optimized mechanical alloying duration. Instead, we suggest that, if the crystallite size and dislocation density do not change between two processing intervals and there is no significant shift in the phase fraction, then the shorter milling duration can be selected as the optimized milling parameter. The microstructure of the material after hot-isostatic pressing and hot-rolling is shown in **Figure 34**. Log-normal distribution curves were used to describe the ODS and nitride precipitate sizes. The ODS precipitates of  $Y_4Al_2O_9$  type with a number density of  $6-9 \times 10^{22} \text{ m}^{-3}$  and an average diameter of 2.9 nm were found in the hot-rolled condition. Complex V-Ti-N precipitates with sizes varying between 10 and 120 nm were identified with a mean diameter of 35.5 nm. Larger ODS precipitates were found to be co-located with nitrides.

The results have been published as “On the mechanical alloying of novel austenitic dual-precipitation strengthened steels” in *Materials & Design* 213 (2022) 110316.

**Future Work**

Optimization of this austenitic steel is complete, and no further work is planned.

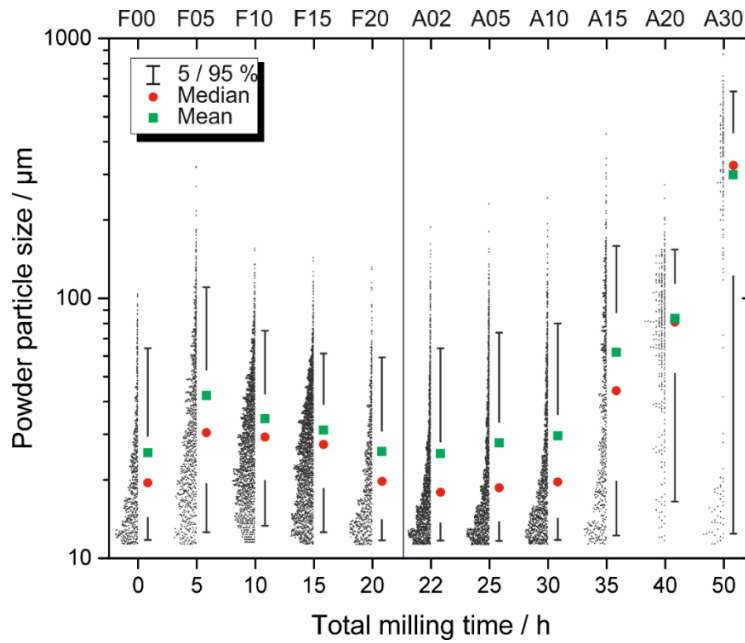


**Figure 33. Log plot of the powder particles size plotted against the milling time. Individual particle sizes (diamond symbol) are shown as data points on the left side, while the mean, median, and the 5, 25, 75, and 95% quartiles are presented on the right side of each milling time. The 25 to 75 % area is shown as the blank area inside the 5 to 95% whiskers. Pure nickel powder particles assumed to be below 12 micron were not counted for the powder particle sizes.**

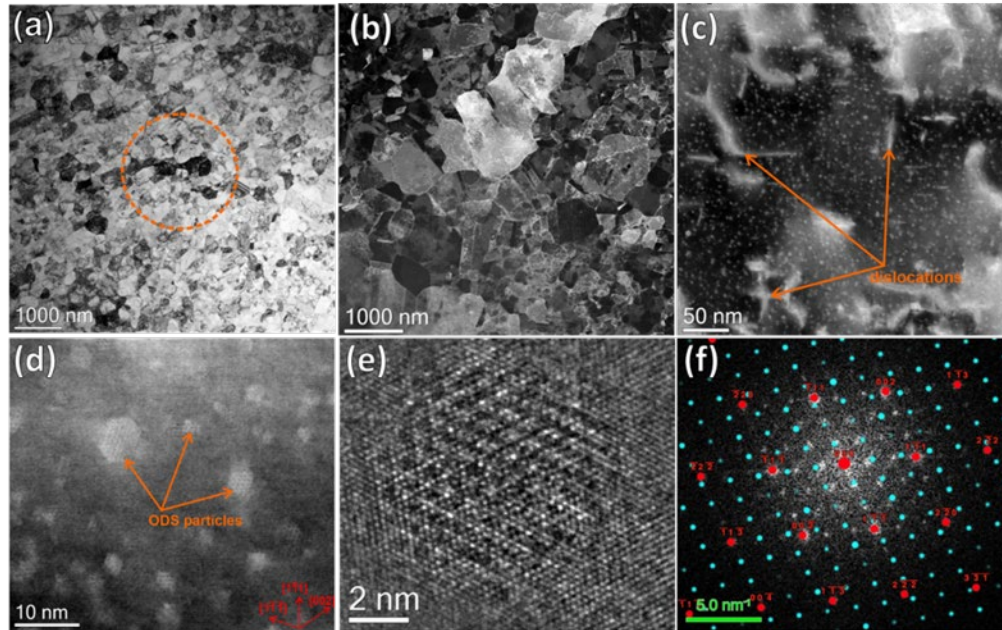


**Figure 34.** STEM-MAADF images taken from a fine-grained austenite area (a) and a bimodal grain size area (b). The interaction of dislocations with ODS particles can be observed in (c) and the size and form of single ODS particles can be extracted from (d). High-resolution phase contrast image of a single ODS particle is exhibited in image (e). (f) Fast Fourier Transformation of (e) with a diffraction pattern simulation of austenite (red) and Y<sub>4</sub>Al<sub>2</sub>O<sub>9</sub> (ICSD No. 252973, cyan pattern) being overlaid by SingleCrystal™. The austenite matrix is oriented along the [110] zone-axis, whereas the ODS particle is oriented in [010] zone-axis.

### 3. CERAMIC AND COMPOSITE MATERIALS

#### 3.1 CHARACTERIZATION OF SiC: HIGH-ENERGY XRD AND MICRO-MECHANICAL TESTING

T. Koyanagi ([koyangit@ornl.gov](mailto:koyangit@ornl.gov)), O. Karakoc, Y. Katoh (ORNL), D. Sprouster, L. L. Snead (Stony Brook University), and T. Nozawa (QST)

##### OBJECTIVE

The goal of this task is to develop advanced characterization techniques for SiC materials that will accelerate the material development. The focus is on high-energy x-ray diffraction (XRD) and micro-mechanical testing techniques.

##### SUMMARY

High-energy XRD was employed to gain insight into the irradiation-induced creep behavior of SiC under neutron irradiation. The initial stress under irradiation clearly leads to an increase in the (111) shoulder peak intensity, an indication of an increase in nano-scale stacking disordering. The findings suggest stress-induced preferential nucleation and/or growth of defect clusters as a key creep mechanism in neutron-irradiated SiC. A manuscript based on this study has been published in *Scripta Materialia* 197 (2021) 113785.

To optimize composite performance, the interfacial mechanical properties of SiC fiber-reinforced SiC matrix (SiC/SiC) composites are investigated using a slant interface micropillar compression testing procedure. The novel micro-compression testing successfully quantifies the debond shear strength of micropillar test samples, analyzed using the Mohr-Coulomb formulation. The micropillar test results were correlated with macroscopic mechanical properties of the neutron-irradiated SiC/SiC composites. A manuscript based on this study has been published in *Composites Part B* 224 (2021) 109189.

##### PROGRESS AND STATUS

###### High-energy XRD

Polycrystalline  $\beta$ -SiC specimens were simultaneously exposed to elevated temperature neutron irradiation and mechanically applied stresses in the HFIR at ORNL. The structural disordering was subsequently examined using transmission mode XRD at the National Synchrotron Light Source-II at Brookhaven National Laboratory.

This research identified atomic-scale anisotropic disordering in SiC irradiated at elevated temperatures (400–800°C) under applied tensile stress, quantified from the analysis of the two-dimensional diffraction patterns at different azimuth angles (see **Figure 35**). The intensity of the (111) shoulder peak, an indication of stacking disorder, increased when the specimens were irradiated under tensile stress. Importantly, previous studies using transmission electron microscopy, the method most commonly used to observe nano-structural defects, did not identify the anisotropic structure, but observed the uniform nanometer-sized defect clusters, similar to those seen in the weak beam dark field TEM image (**Figure 35**). We found that the intensity of the shoulder peak is correlated with the macroscopic creep strain. Considering the possible creep mechanisms, the results of this study suggest creep mechanisms related to stress-induced preferential nucleation of dislocation loops and/or stress-induced preferential absorption of interstitials. The XRD analysis presented in this study showed how those defects are oriented with mechanical strain and irradiation. Such detailed information on the radiation damage evolution will help

to build a mechanistic model to predict the lifetime of the material in future fusion reactors.

### Micro-mechanical testing

Micropillar test specimens, containing an inclined pyrolytic carbon (PyC) interphase, were prepared using a focused ion beam instrument (**Figure 36a**). Micro-compression tests of these specimens used an in-situ nanoindentation system to evaluate fiber/matrix interphase properties that play a key role in the overall mechanical behavior of the composite. A Mohr-Coulomb fracture criterion was implemented to evaluate interface characteristics.

Four types of SiC/SiC composite have been micro-compression tested. The results (**Figure 36b**) showed that interfacial properties and debond mechanisms were significantly affected by the PyC layer thickness, the local bonding mechanism of the PyC interphase on the SiC fiber surface, and the surface roughness of fibers. Regardless of PyC thicknesses, Tyranno SA3 SiC fiber-reinforced SiC/SiC composites were found to have much higher debond shear strengths than Hi-Nicalon Type-S SiC fiber-reinforced SiC/SiC composites.

This information was helpful in explaining the different responses of the SiC/SiC composites with different fiber/interphase systems (IDs: SCF and JCR types [see **Figure 36b**]) to elevated temperature neutron irradiation. The SCF-based composites exhibited outstanding resistance to neutron irradiation, whereas the JCR-based composites experienced severe mechanical degradation at the same levels of neutron dose and temperature. It was found that the difference in the interfacial debond strength did not have significant impact on the irradiation effects although it affected the mechanical properties in the as-processed conditions. Loss of strength in the JCR-based composites was thought to be attributable to the presence of carbon in the JCR-matrix found by Raman spectroscopy, which induces radiation-induced swelling stresses. The details of the discussion are reported in *Composites Part B* 224 (2021) 109189.

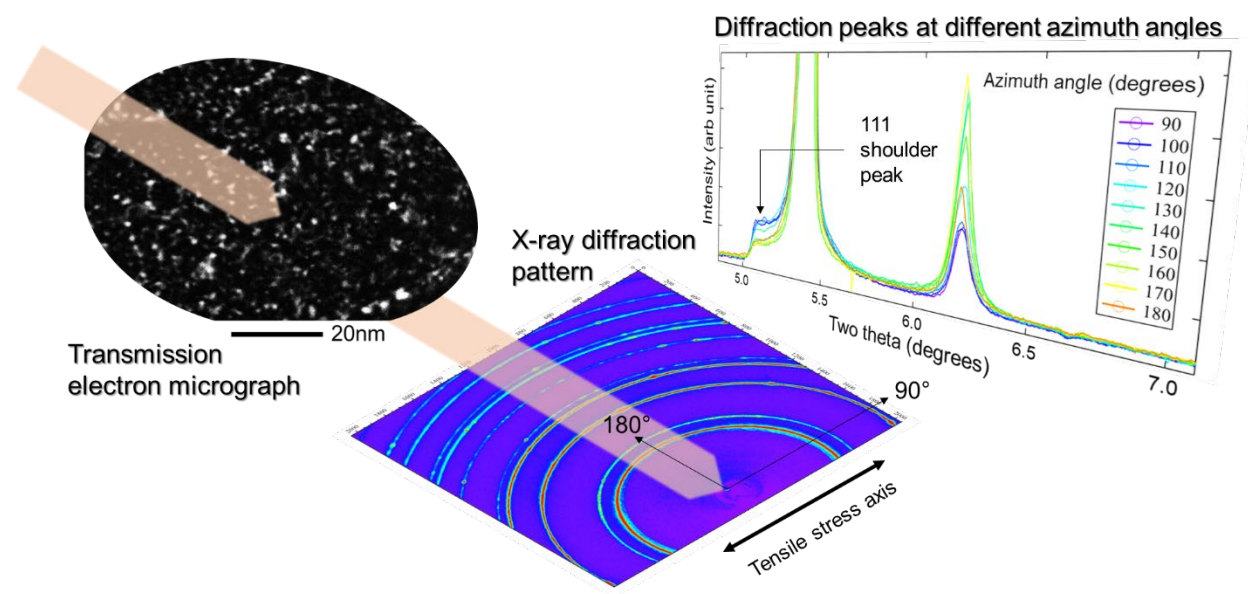


**Figure 35. State-of-the-art X-ray diffraction analysis disclosed hidden damaged structure in SiC neutron irradiated with applied tensile stress.**



## 4. HIGH HEAT FLUX AND PLASMA FACING MATERIALS

### 4.1 ELECTRICAL RESISTIVITY OF IRRADIATED TUNGSTEN: PHENIX COLLABORATION

*J. R. Echols, N. Reid, and L. M. Garrison ([garrisonlm@ornl.gov](mailto:garrisonlm@ornl.gov))*

#### OBJECTIVE

The PHENIX collaboration is expanding the database on neutron irradiation effects in W materials. This task is evaluating the effects of irradiation on the electrical resistivity.

#### SUMMARY

Electrical resistivity measurements conducted on single and polycrystalline W samples neutron irradiated to doses between 0.2 and 0.7 displacements per atom (dpa) show increased resistivity, but do not show clear trends on the basis of dpa alone. Rather, Re content appears to be the dominant factor affecting resistivity. Examining the effects of grain orientation in polycrystalline samples with elongated grains shows measurable variation in resistivity depending on sample orientation with respect to the applied current. This variation is used to calculate grain boundary resistivity in the direction of the current.

#### PROGRESS AND STATUS

The US-Japan collaboration, PHENIX, aims to investigate W and W-based materials' (>1500 total samples) responses to neutron irradiation to provide a data base for the use of W and W-based alloys in future fusion reactors. These samples were neutron irradiated in the RB\*19J irradiation capsule in the High Flux Isotope Reactor (HFIR) to doses of ~0.2 to 0.7 dpa. The irradiation temperatures (measured directly and calculated through SiC thermometry and extrapolation) for the three different subcapsules were 430-670, 740-960, and 880-1080°C. A Gd shield was utilized to reduce the thermal neutron flux, and therefore the rate of W to Re/Os transmutations, to more fusion-relevant values than obtained in previous irradiations such as TITAN.

Small, 3 mm diameter test disks used for resistivity measurements provided two distinct advantages compared to larger specimens: 1) the dose to the experimenter is reduced; and 2) this geometry allows samples with elongated grains to be rotated such that the average grain length in the direction of the current varies. *Figure 37* shows a diagram of the resistivity testing apparatus used and how rotation affects the grain boundary (GB) density.

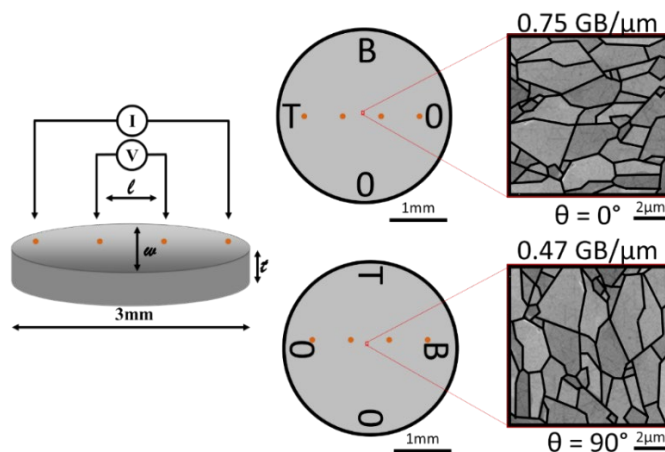


**Figure 37. (Left) Diagram of 3 mm electrical resistivity measurement device. Positions of Cu electrodes are shown in orange. (Right) Effect of sample orientation and GB “length” in the direction of the current.**

Rotating samples that exhibit “elongated” grains and taking a resistivity measurement at several different rotational positions, will capture different GB densities in resistivity measurements. Although sample ID was engraved on one surface, as illustrated in *Figure 37*, the engraved side was always opposite to the measurement surface. Resistivity was measured for thick plate ALMT-produced polycrystalline W (PCW) with elongated grains (material codes AT and BT) and single-crystal W (SCW, material code UE). The measurements were conducted at room temperature, then normalized to 20°C. For the PCW material, the samples were cut in different orientations with respect to the elongated grains: A – in which grains were equiaxed relative to the applied current, and B – in which the grains were not equiaxed relative to the applied current. In general, there was no obvious trend between resistivity and dpa. Electron backscatter diffraction (EBSD) images for unirradiated specimens with the grains color-coded according to the inverse pole figure legend are shown in *Figure 38*. Grain size information was extracted from these maps and is shown in the associated histograms. Measurement of angular dependence of resistivity for a range of samples is shown in *Figure 39*. Unirradiated and low-temperature irradiated BT-series PCW (which does not exhibit equiaxed grains relative to the current for different rotations) showed a resistivity that oscillated with measurement angle. However, the samples that were apparently recrystallized (BT08) and equiaxed relative to the current (AT01) or have no grain boundaries (UE06), do not exhibit this behavior. Thus, it is speculated that the oscillatory behavior might be related to the effects of the GBs, rather than crystallographic texture. Sine curves were fit to the oscillatory data and the amplitude in these oscillations was attributed to a possible GB effect on resistivity.

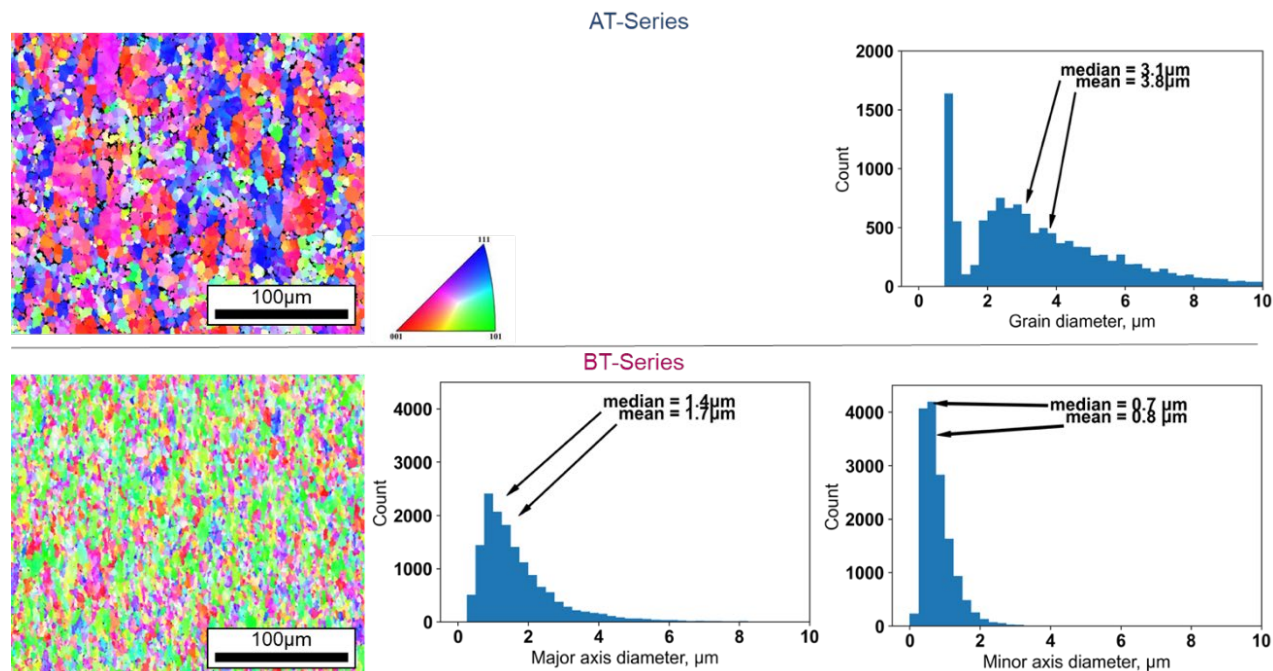


Figure 38. EBSD inverse pole figure grain orientation maps of unirradiated W samples revealed differences in crystallographic texture, grain size and shape for samples cut in the two different directions. Equivalent grain diameter histograms (bin size = 0.25 $\mu\text{m}$ ) are presented for the equiaxed (A-T series) and histograms of the major/minor grain dimensions (B-T series).

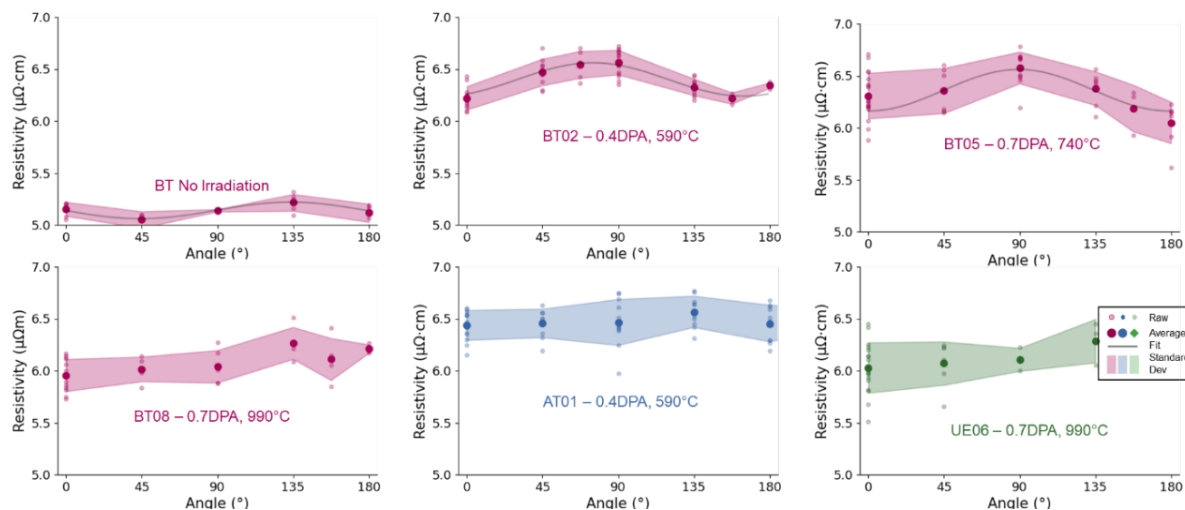
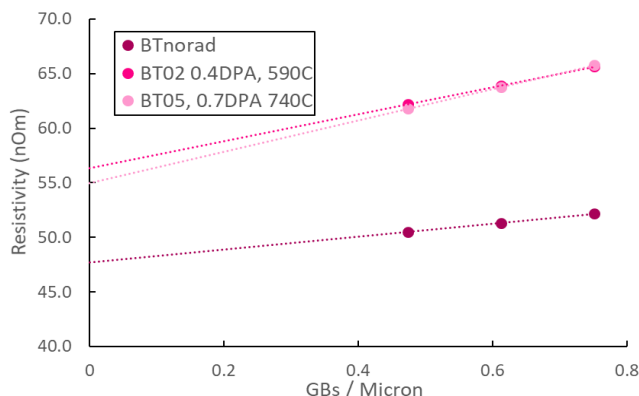


Figure 39. Resistivity of B-oriented samples as a function of arbitrary measurement angle. Average values are shown in large, solid marks with individual measurements given with smaller, lighter marks. A sine wave fit is shown in the first row, approximating expected resistivity for any angle. Samples in the bottom row exhibit no such orientation dependence. The 0° angle is arbitrary for each sample.

In **Figure 40**, the maximum, mid, and minimum resistivities for the oscillatory samples are plotted against the maximum, mid, and minimum GB densities calculated from the EBSD data. Applying a linear fit to these data, an estimate of the apparent “resistivity-per-GB” in the direction of the current is presented for each irradiation condition.

The concentration of Re from transmutation can explain significant changes to the resistivity evolution of irradiated materials due to an almost four times higher resistivity ( $\sim 5.3 \mu\Omega\text{cm}$  for W vs  $\sim 19.3 \mu\Omega\text{cm}$  for Re). In **Figure 41**, the measured resistivity is plotted with respect to the calculated transmutant Re content (at the end of irradiation). Osmium was not included in this analysis as contributions are expected to be negligible compared to the Re contribution at these transmutation levels. In addition to the SCW and PCW samples discussed earlier, measurements from a single irradiated W-3%Re alloyed sample (pre-irradiation) are included. These values are plotted with data from unirradiated W-Re alloys reported by Hasegawa [1] and Tanno [2]. The data presented from the present study are consistent with the trend reported in those published studies, suggesting that Re transmutation plays a dominant effect in the electrical resistivity changes during irradiation. Notably, both authors reported a resistivity of  $\sim 5.9 \mu\Omega\text{cm}$  for the pure W, which is  $\sim 15\%$  greater than the value of  $\sim 5.1 \mu\Omega\text{cm}$  for BT-series PCW (which is also more consistent with other literature values of W resistivity).



**Figure 40.** BT-series resistivity averages plotted with respect to apparent GB density in the direction of the current, with a linear fit extrapolated to approximate the zero-grain boundary case.

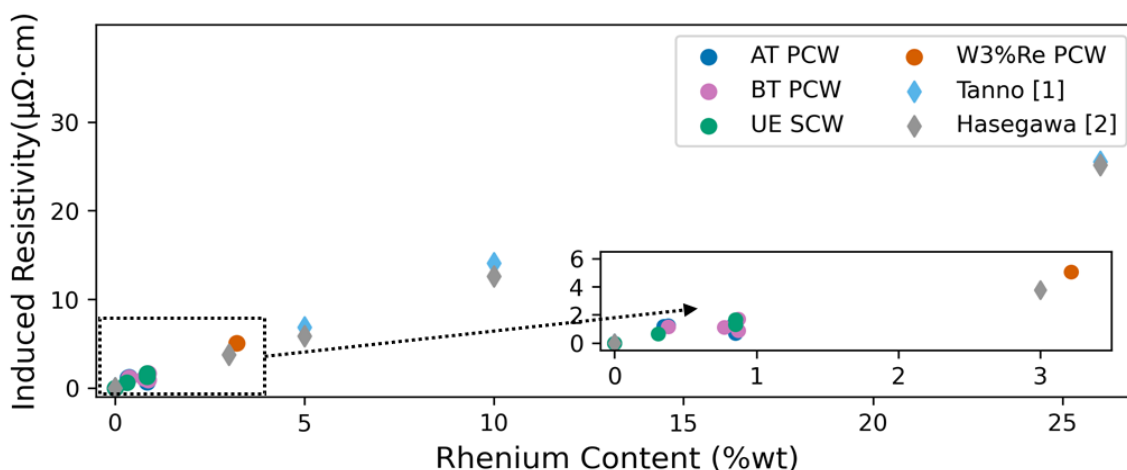


**Figure 41.** Electrical resistivity plotted as a function of calculated Re content for SCW and PCW materials. Data obtained for unirradiated W-Re alloys by Hasegawa [1] and Tanno [2] are included for comparison.

## **Future Work**

Future work will attempt to generalize these observations into a mathematical framework and compare resistivity and thermal conductivity behavior.

## **References**

- [1] Tanno, T., et al. "Effects of transmutation elements on the microstructural evolution and electrical resistivity of neutron-irradiated tungsten." *Journal of Nuclear Materials* 386 (2009) 218-221.
- [2] Hasegawa, Akira, et al. "Neutron irradiation effects on tungsten materials." *Fusion Engineering and Design* 89.7-8 (2014) 1568-1572.

## 4.2 THERMAL DIFFUSIVITY OF IRRADIATED TUNGSTEN – PHENIX/TITAN COLLABORATION

*J. R. Echols, and L. M. Garrison ([garrisonlm@ornl.gov](mailto:garrisonlm@ornl.gov))*

### OBJECTIVE

The goal of the PHENIX and TITAN collaborations is to expand the database on neutron irradiation effects in W materials. This task evaluates the effects of neutron dose, thermal neutron shielding, and temperature on the thermal transport in single and polycrystalline W.

### SUMMARY

Thermal diffusivity measurements, to determine thermal conductivity, have been initiated on W samples irradiated in the PHENIX and TITAN campaigns at Oak Ridge National Laboratory. A phased plan has been developed to quickly provide insight into effects of variables captured by these campaigns, including irradiation temperature, fluence, and shielding of thermal neutrons. Thermal diffusivity of samples correlates most strongly with Re + Os content. Temperature effects, however, have also been identified.

### PROGRESS AND STATUS

The TITAN and PHENIX programs irradiated thousands of W and W alloy samples in the High Flux Isotope Reactor (HFIR) at Oak Ridge National Laboratory. These samples were exposed to a range of neutron fluences ( $0.02\text{-}20 \times 10^{25} \text{ n/m}^2$ ,  $E > 0.1\text{MeV}$ , which is equivalent to a range of 0.0039-3.9 dpa) and irradiation temperatures (100-1000°C). The PHENIX program irradiation capsule utilized a Gd shield to filter out a large fraction of the thermal neutrons (and therefore greatly reduce transmutation), whereas the TITAN campaign exposed samples to the full HFIR neutron spectrum. The thermal diffusivity is being measured on the tab ends of tested tensile specimens from both campaigns. This unique data set will greatly expand the thermal conductivity database for neutron irradiated W, including the effects of irradiation dose, temperature and spectrum.

**Figure 42** shows the irradiation matrix of the single crystal W (SCW) samples from both campaigns, highlighting the planned test phases for these materials. Phase 1 evaluates materials that have similar fast fluences and temperatures, but with variation in the thermal shielding (and therefore amount of transmutation). Phase 2 focuses on varying the irradiation temperature ( $T_{\text{irr}} \approx 90^\circ\text{C}$ ;  $800^\circ\text{C}$ ) and dose ( $0.02 - 20 \times 10^{25} \text{ n/m}^2$ ;  $E > 0.1\text{MeV}$ ; 0.0039 – 3.9 dpa), whereas Phase 3 examines the effects of fluence and transmutation at mid-range temperatures ( $T_{\text{irr}} \approx 500^\circ\text{C}$ ).

Diffusivity measurements are performed using a Netzsch LFA467, which utilizes the laser-flash method of thermal diffusivity measurement. The tensile tab to be measured is thinly coated with a graphene spray to reduce reflectivity, it is then placed in a custom fixture within the device, and finally placed in vacuum. A brief laser pulse (order 0.1ms) heats one side of the tab while the temperature on the other side is monitored to determine the rate of heat transfer through the material.

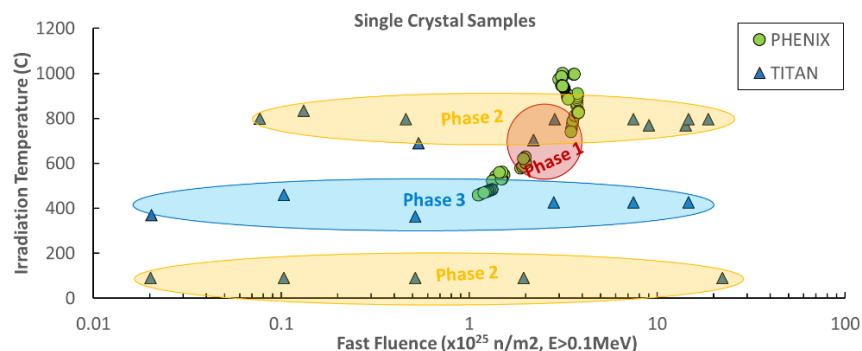


**Figure 42. Schematic showing the temperature-fast fluence irradiation matrix of SCW tensile samples from the PHENIX and TITAN projects. Initial work is divided into phases (represented by the colored ovals) to maximize early insight into thermal, dose, and shielding effects on thermal transport properties.**

Selected diffusivity curves are shown in **Figure 43**. For each sample, five measurements are made at each test temperature. Tests begin at room temperature, after which the device will heat the material and take additional measurements at 50C increments up to the irradiation temperature (minus a safety margin). Measurements are then taken at 100C intervals down to room temperature to ensure that radiation damage has not been annealed out by exceeding the maximum radiation temperature (which would be manifested as an increase in diffusivity). In **Figure 43a**, it is clear that the increased dose has drastically decreased the diffusivity, especially at lower measurement temperatures. Notably, the slope of the diffusivity line inverts for the material irradiated to the highest dose of  $9 \times 10^{25} \text{ n/m}^2$  (1.8 dpa), exhibiting lower diffusivity at measurement temperatures below  $\sim 300^\circ\text{C}$  than for temperatures above that. In **Figure 43b**, diffusivity of samples with similar doses and calculated transmutation levels are compared for shielded and unshielded samples. Importantly, the two samples with similar calculated transmutations have nearly identical diffusivities, despite significant differences in fluence.

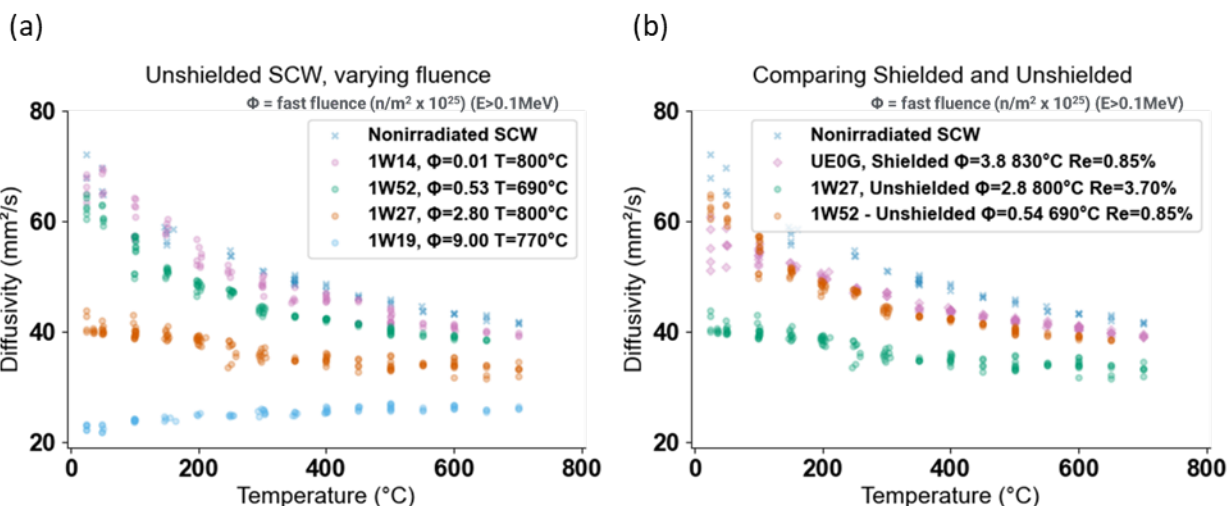


**Figure 43. Selected thermal diffusivity curves for SCW irradiated at high (>690°C) temperature. (a) The unshielded data obtained as a function of fluence, and temperature exhibit a clear effect of dose on diffusivity. (b) Comparison of diffusivity as a function of irradiation temperature and fluence for the shielded and unshielded samples. The calculated transmutation levels are included in the legend.**

**Figure 44** shows the measured diffusivity as a function of calculated Re+Os content (either calculated for this work or taken from [1]) and a function of irradiation temperature for four different measurement temperatures. Recent data from Gietl et al. [2] (for irradiated SCW and W/Re alloys), Tanabe et al [3], and Fukuda et al [4] (on non-irradiated W/Re alloys) are also shown. Important takeaways are: 1) the Shielded/unshielded SCW appear to fall on the same diffusivity versus Re+Os curve; 2) the trendline is approximately the same for irradiated and unirradiated W/Re alloys; and 3) lower temperature irradiation data (purples/magentas in the figure) appear to lie on a slightly lower diffusivity curve.

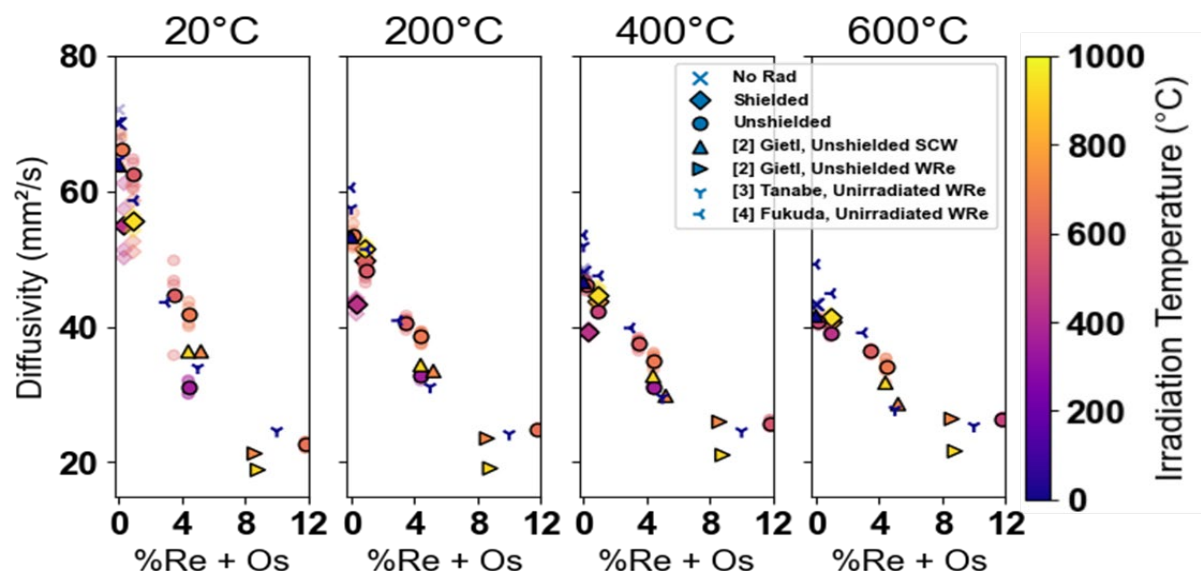


**Figure 44. Relationship between thermal diffusivity data and Re + Os content measured at four different temperatures. Published literature thermal diffusivity values for irradiated and non-irradiated W/Re alloys and irradiated SCW are also included for comparison.**

### Future Work

Future work will include thermal diffusivity measurements from Phase 2 and 3 materials, correlation with irradiation conditions, and correlation with electrical resistivity measurements.

### References

- [1] Katoh, Y., et al. "Response of unalloyed tungsten to mixed spectrum neutrons," *Journal of Nuclear Materials* 520 (2019): 193-207.
- [2] H. Gietl et al. "Neutron irradiation-enhanced grain growth in tungsten and tungsten alloys," Submitted to *Materials and Design* (2021)
- [3] T. Tanabe et al. "Temperature dependence of thermal conductivity in W and W–Re alloys from 300 to 1000 K," *Materials Letters* 57 (2003) 2950-2953
- [4] M. Fukuda et al. "Thermal properties of pure tungsten and its alloys for fusion applications" *Fusion Engineering and Design* 132 (2018) 1-6

### 4.3 TUNGSTEN BASE COMPOSITES

H. Gietl ([gietlha@ornl.gov](mailto:gietlha@ornl.gov)), T. Koyanagi, and Y. Katoh

#### OBJECTIVE

The goal of this task is to design and develop tungsten-based composite materials suitable for fusion applications. Tungsten fiber reinforced tungsten ( $W_f/W$ ) and silicon carbide fiber reinforced tungsten ( $SiC_f/W$ ) composites are targeted.

#### SUMMARY

Irradiation-enhanced recrystallization of W alloys was evaluated for selection and design of W matrices for the composites to be fabricated. The  $SiC_f/W$  composites with zirconia fiber/matrix interphase were fabricated and tested. This task obtained baseline properties of W matrix and W composites for optimization of the composite microstructure.

#### PROGRESS AND STATUS

##### Irradiation-enhanced recrystallization of W

Suitable materials for fusion component service require stable microstructures with adequate mechanical properties. In particular, the development of W-based composites requires incorporating toughening mechanisms which do not rely on ductility of the W matrix or W fiber.

To understand the microstructural stability of candidate matrix material for  $W_f/W$  and  $SiC_f/W$  composites, W and W alloys were neutron irradiation in the mixed spectrum HFIR at nominal temperatures of  $\sim 850$  and  $\sim 1,100$  °C to calculated doses between 0.42-0.47 dpa. This evaluation provided the first experimental evidence of reported radiation-enhanced recrystallization of W and undoped W-Re alloys at  $\sim 850$  °C where thermal annealing does not cause any grain growth in a similar timescale (**Figure 45**). We also found that the radiation-enhanced recrystallization reduced hardness, which was similar to the effects observed for recrystallization during thermal annealing. Solute Re either as alloy addition or as transmutation product did not effectively mitigate grain growth under irradiation in contrast to thermal annealing. The results suggest that radiation-enhanced recrystallization is a limiting factor for the design operational temperature of W in service as a plasma facing material.

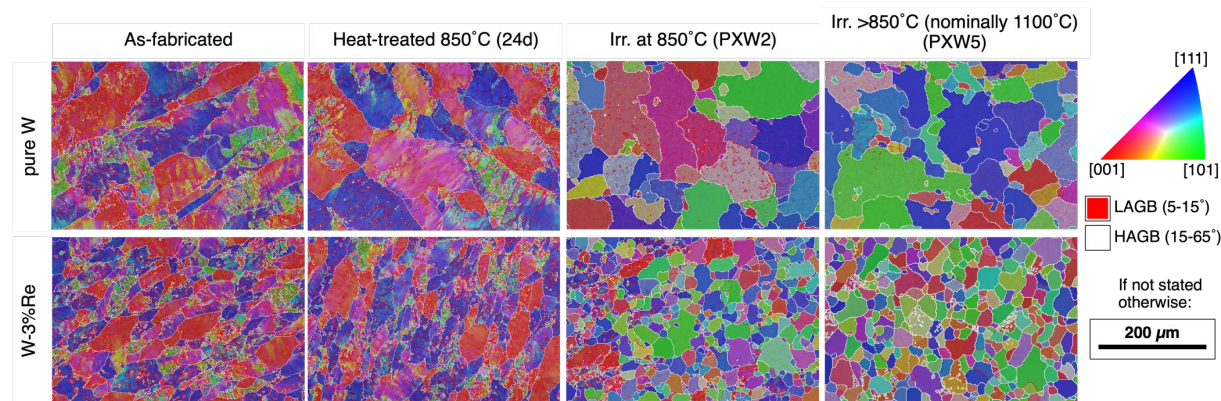


**Figure 45.** EBSD orientation maps of pure W and W-3%Re as-fabricated, heat-treated at 850°C, irradiated at 850°C and at 1100°C.

### SiC<sub>f</sub>/W composite: microstructure and mechanical properties

The single fabric layer SiC<sub>f</sub>/W composite was manufactured and tested in cooperation with the Max-Planck Institute for Plasmaphysik in Garching (Interlayer) and the Forschungszentrum Jülich (Matrix). The zirconia interlayer was deposited in a physical vapor deposition (PVD) process while the W matrix was deposited by chemical vapor deposition (CVD). The interlayer was deposited at room temperature with a Denton Discovery system. For the deposition of the interlayer and matrix the fabric mounting frame was turned to achieve deposition on both sides of the fabric. Thus, the interlayer was only deposited on the outer surfaces of the fibers as PVD is mainly limited to line-of-sight deposition. Furthermore, the specimens had large porosity within the fiber layer as the W matrix was also deposited mainly on the outer surface as the gas path was blocked.

**Figure 46** shows representative flexural behavior of the SiC<sub>f</sub>/W composite at room temperature. Non-linear stress-strain behavior was observed, as intended. The decreasing load at the end of the test is a strong hint of fiber pull out. **Figure 47** shows the ZrO<sub>2</sub> interlayer allowing debonding of the fibers from the matrix. In addition, fiber-pullouts are seen in the middle of the fabric. Future development is required to improve ultimate strength and toughness of the composite.

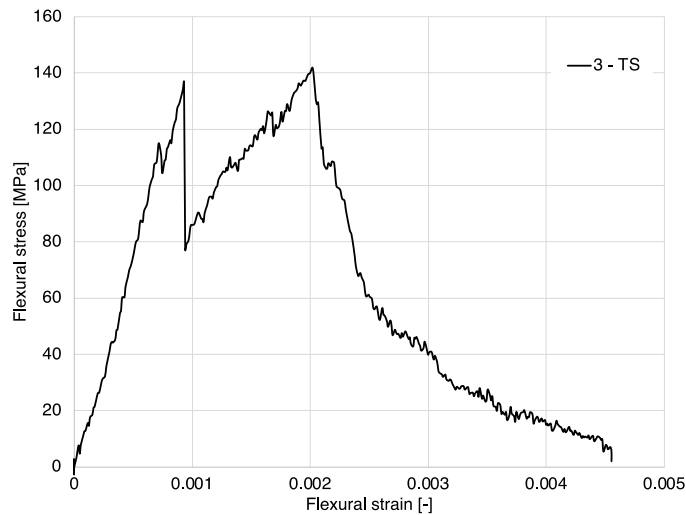


**Figure 46. A 4-point bend test of SiC<sub>f</sub>/W composite specimen. The material does not show overall brittle behavior.**

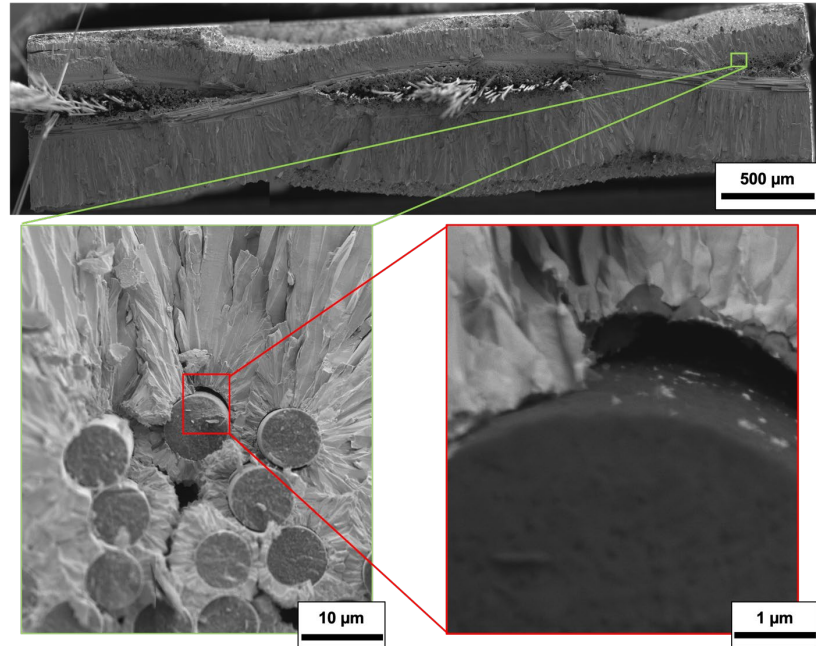


**Figure 47. SiCf/W composite specimen after a 4-point bend test. It is noted that the interlayer where it is present allows debonding of the fiber.**

#### **Future Work**

The ORNL is continuing to process W-based composites. Additional work will be directed at optimizing the resulting microstructures.

#### 4.4 MATERIALS FOR FRONTIER IRRADIATIONS IN HFIR

L. M. Garrison ([garrisonlm@ornl.gov](mailto:garrisonlm@ornl.gov)), N. Reid, Y. Katoh, and J. Echols

##### OBJECTIVE

FRONTIER, the Fusion Research Oriented to Neutron Irradiation and Tritium Behavior at Material Interfaces US-Japan collaboration, seeks to explore and explain the behavior of internal solid interfaces in plasma-facing components (PFCs) under neutron irradiation. Advanced fusion materials, composites, and joints have been designed and are explored in this collaboration.

##### SUMMARY

Materials, material joints, and composites have been prepared for the irradiations in High Flux Isotope Reactor (HFIR) as part of the FRONTIER collaboration. The sample types are 3 mm diameter discs, 6 mm diameter discs, miniature fracture toughness bars, and W fibers. In FY21, materials were procured, machined, joined, and prepared for irradiation.

##### PROGRESS AND STATUS

The FRONTIER US-Japan collaboration is focusing on understanding the behavior of advanced fusion materials for PFCs, especially internal interfaces including those present at a joint between dissimilar materials or in a composite between the constituent parts. To accomplish this, four categories of materials will be irradiated: advanced alloys, fundamental joints, composites, and baseline materials without joints. Some materials were designed and fabricated at Oak Ridge National Laboratory (ORNL). Additional materials for the US side of the project are being supplied by US and international collaborators. These advanced fusion-relevant materials are being irradiated in the HFIR at ORNL, at irradiation temperatures of 300, 500 and 800°C. Samples of each material will be irradiated for 1 cycle and 3 cycles.

The FRONTIER specimens are contained in the rabbit capsules designed to achieve the desired temperatures during irradiation in HFIR, described in *Figure 48b, c*. Details of the status of capsule design and estimates of start of irradiation are also given in those sections.

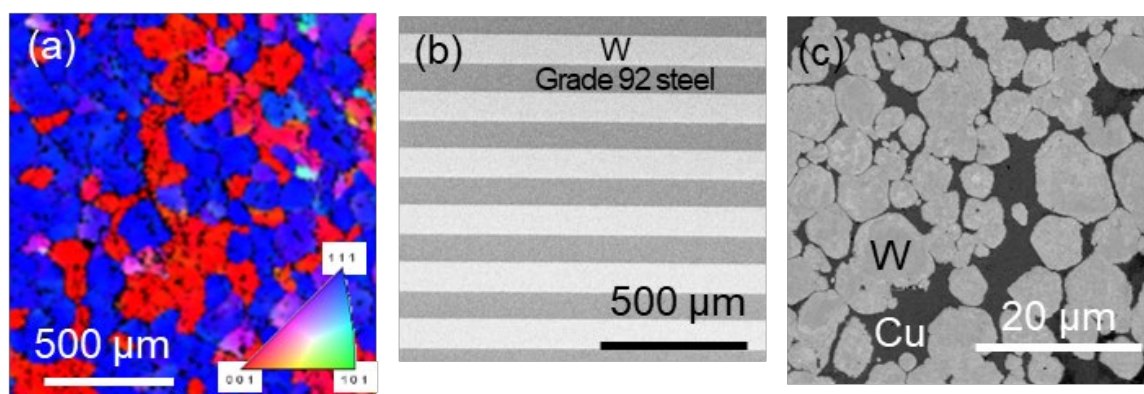


**Figure 48. (a) Electron backscatter diffraction inverse pole figure map of electron beam additively-manufactured W. (b) W-Grade 92 steel laminate. (d) W-Cu particle-reinforced composite.**

There are 35 different materials that have been prepared for the 3 mm diameter disc HFIR irradiation capsules. Three of the materials that were developed at ORNL are shown in **Figure 48**. The electron beam additive-manufactured W (**Figure 48a**) has a (111) and (001) texture in the build direction. The W-Grade 92 steel laminate (**Figure 48b**) was fabricated by hot-rolling a stack of alternating W and steel foils at 1000°C. The W-Cu particle-reinforced composite (**Figure 48c**) was fabricated by sintering.

The 6 mm diameter disc irradiation capsules contain 21 types of materials; they were primarily fabricated by collaborators around the US and in Japan. ORNL fabricated a SiC substrate with a 25  $\mu\text{m}$  thick W foil layer material to be irradiated in the 6 mm diameter disc capsules.

The fracture toughness capsules contain three different W materials as well as miniature holders containing W fibers. The fiber tubes hold a combination of W fibers that are 16 and 150  $\mu\text{m}$  in diameter (**Figure 49a**). The thinner fibers extend beyond the end of the fiber tube during preparation to keep them straight (**Figure 49b**), and then are trimmed to be flush with the ends of the tube when the end caps are attached.

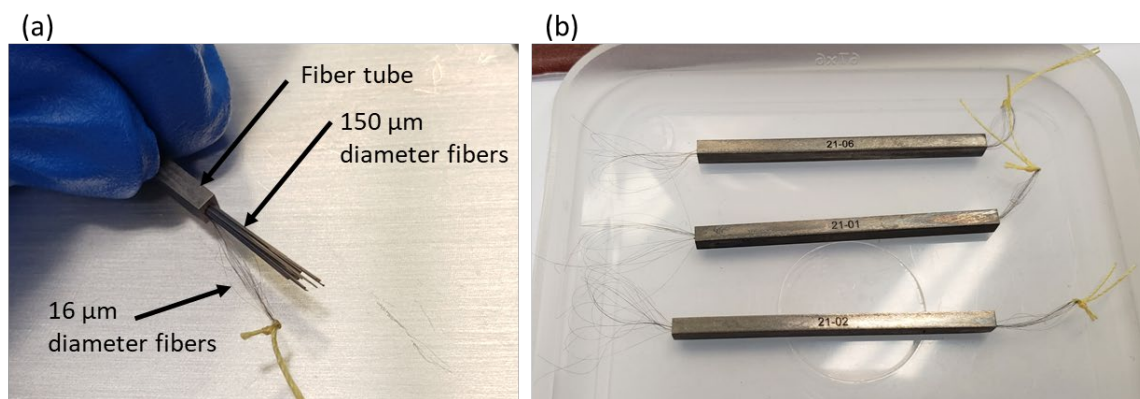


**Figure 49. (a) Fibers loaded in fiber holder tube before they are fully inserted into the tube. (b) Three loaded tubes with the 16  $\mu\text{m}$  fibers extending beyond the ends of the tube.**

## 5. PLASMA MATERIALS INTERACTIONS

### 5.1 DAMAGE-MECHANISM INTERACTIONS AT THE PLASMA-MATERIALS INTERFACE

*C. M. Parish* ([parishcm@ornl.gov](mailto:parishcm@ornl.gov))

#### OBJECTIVE

The overarching objective of this work is to bridge the gap between the atomistic knowledge and models and the phenomenological materials science underlying the design, fabrication, and service of materials in divertors and other plasma-facing components of magnetic confinement fusion. Specifically, in this work we examined helium bubbles in tungsten nano tendrils using monochromated aberration-corrected scanning transmission electron microscopy (MAC-STEM).

#### SUMMARY

We analyzed MAC-STEM data previously obtained at the ORNL Center for Nanophase Materials Sciences (CNMS) via a user proposal in collaboration with J.-C. Idrobo. The “nano fuzz” was grown in the PISCES-A plasma device under helium exposure at UC-San Diego in collaboration with R. Doerner and M. Baldwin.

#### PROGRESS AND STATUS

Several dozen cavities were interrogated using the Nion Hermes MAC-STEM instrument at ORNL CNMS, operated at 100 keV and with an approximately 160 meV beam energy FWHM. Only a small fraction of cavities analyzed provided data that could be clearly interpreted; the exact reason is unclear, but it is believed that the combination of tungsten fiber, oxide skin, carbonaceous contamination, and other layers can overwhelm the helium signal, and not all bubbles are anticipated to contain helium. For instance, bubbles that cut the surface of the fiber will release their helium and will simply be surface divots, but the STEM high-angle annular contrast imaging cannot differentiate a buried bubble from a surface divot.

Despite this low yield of experiments, it was possible to analyze a number of helium bubbles. Multiple models were developed (using the SciPy-Optimize module of the Python programming language) to perform physics-informed fitting of the EELS spectra. The model that was ultimately chosen was to model the unspecified contributions as a linear background, the tungsten contributions as double Gaussians constrained to the tungsten plasmon ( $\approx 24$  eV) and the tungsten surface plasmon ( $\approx 18$  eV), and the helium  $1s \rightarrow 2p$  transition as a gaussian ( $\approx 22$ - $24$  eV). Gaussians were found to provide a better fit than Lorentzians, particularly for the zero-loss-peak (ZLP).

The number of helium atoms per unit volume,  $n_{He}$ , is estimated as [1]:

$$n_{He} = \frac{I_p}{\sigma_p I_Z d}$$

Where  $I_p$  is the integrated intensity of the helium peak,  $I_Z$  is the integrated intensity of the zero-loss peak,  $\sigma_p$  the ionization cross-section (estimated at  $9 \times 10^{-24}$  m<sup>2</sup>) and  $d$  the diameter of the bubble (measured from HAADF and assuming isotropy). Curve fitting is needed because the plasmon and surface plasmon peaks

are very close to the helium peak so that they overlap. This is illustrated for data acquired from one bubble in **Figure 50**.

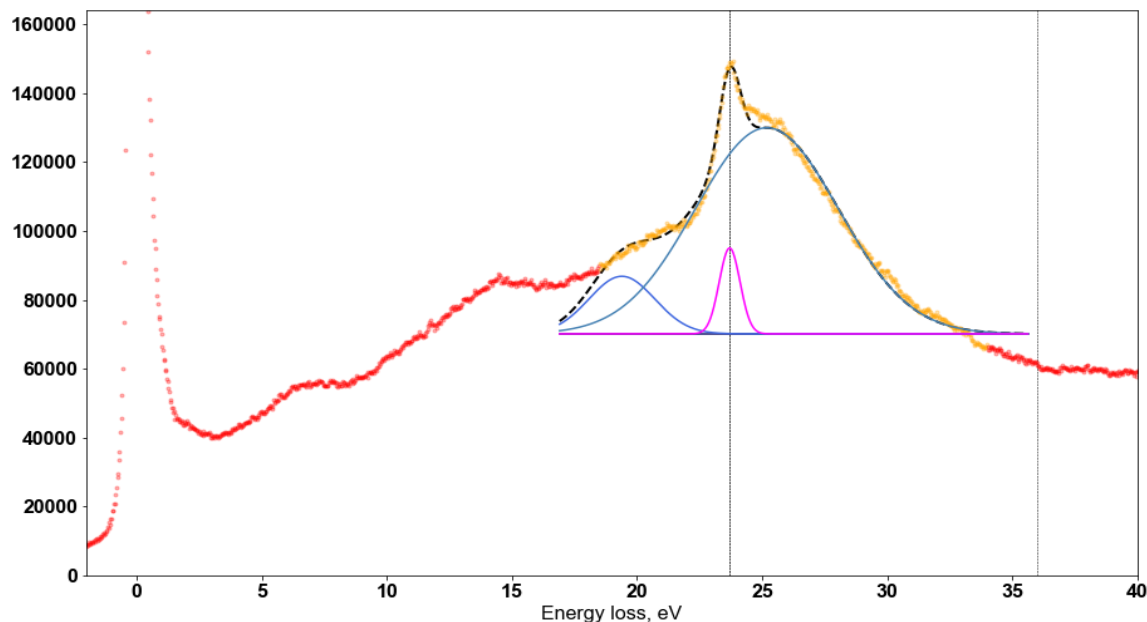


**Figure 50.** An example of a bubble EELS spectrum with the extracted plasmon peaks (blue) and helium peak (pink).

**Figure 51** illustrates the analysis of 12 bubbles for which the measured pressures varied from ~0.1 to ~2 GPa.

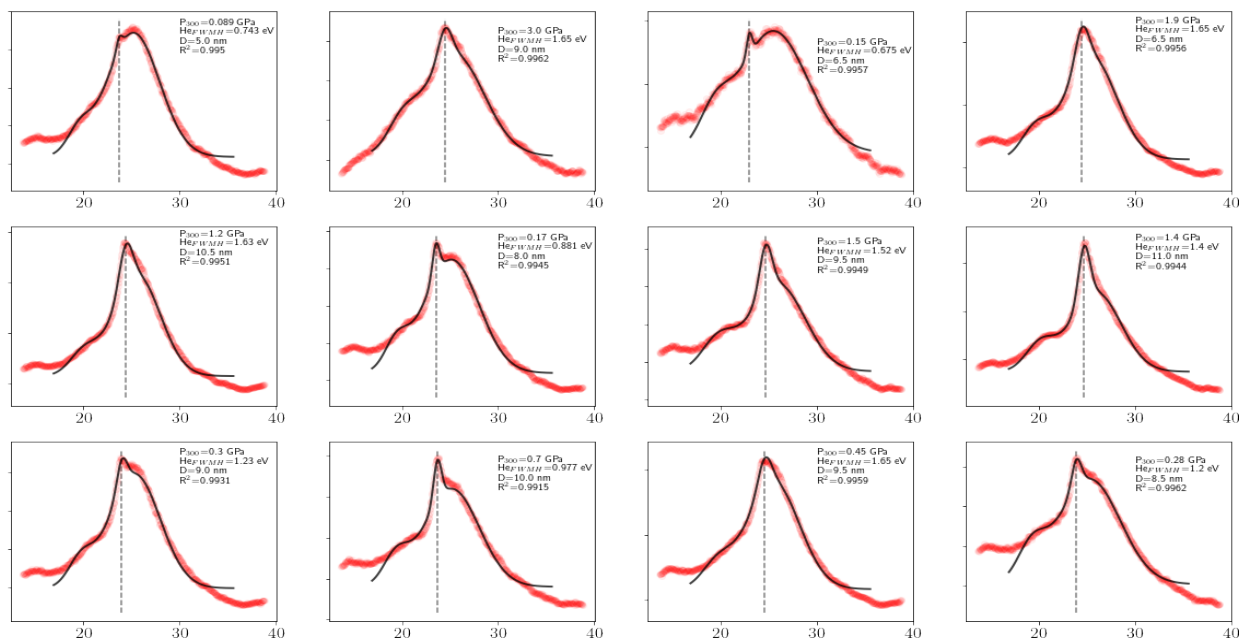


**Figure 51.** A montage of EELS analyses of helium bubbles in tungsten nano-tendrils. Red markers are measured data, vertical dashed lines are the measured helium centroid, and the black lines are the model.

Analysis of these as an ensemble, however, does not lead to the expected functional dependence of pressure proportional to inverse radius; **Figure 52**.

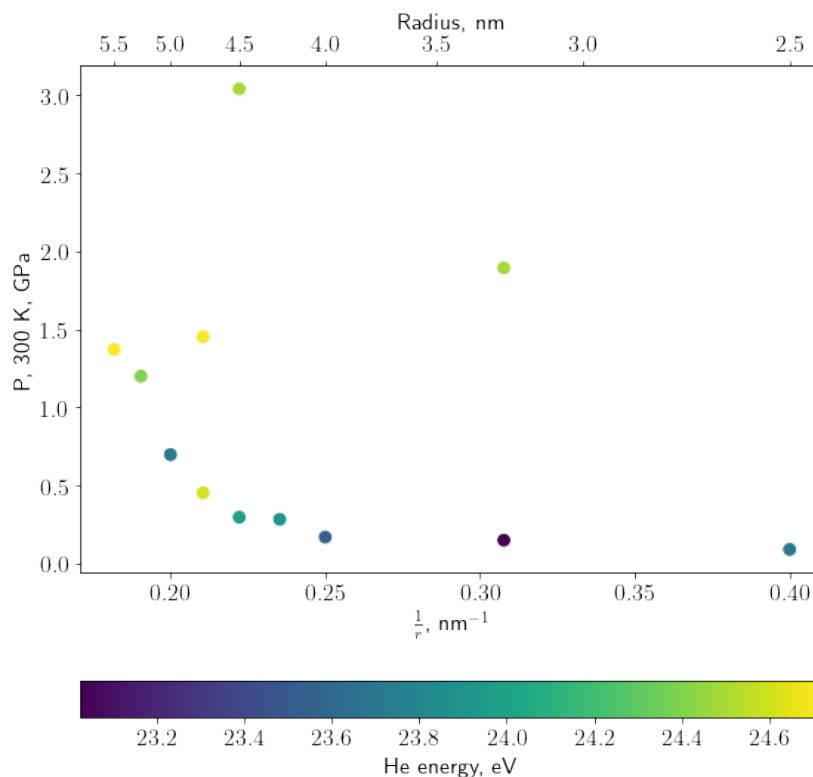


**Figure 52.** Pressures at 300 K, estimated from  $n_{\text{He}}$  via the MLB equation of state, as related to bubble radius and estimated helium peak centroid energy.

The results in **Figure 52** are unexpected. Clearly, the two possibilities are that either the peak-fitting model is incorrect, or the bubbles are not behaving as expected.

The spread of the measured pressures is surprisingly high; whether this is an artifact of uncorrected signals or actual spread due to the highly non-equilibrium nature of the growth process is at present unknown. Several possibilities come to mind and are being examined.

First, the assumptions of the curve fit are for bulk tungsten plasmon, surface tungsten plasmon, and helium peaks to be present on a background. The shape of this background may vary depending upon the nature of the particular bubble examined; **Figure 53**. In **Figure 53**, several likely cases are illustrated. A bubble might be cleanly present in the center of a tendril suspended over vacuum, an ideal case. A bubble might be present in a section of tendril that is also above the lacy carbon support, and the carbon would provide an extra perturbation. There could be oxide or carbonaceous material in excess on the tendril at the point of the bubble. Alternatively, the bubble could be in a rapidly varying shape area of the particle.

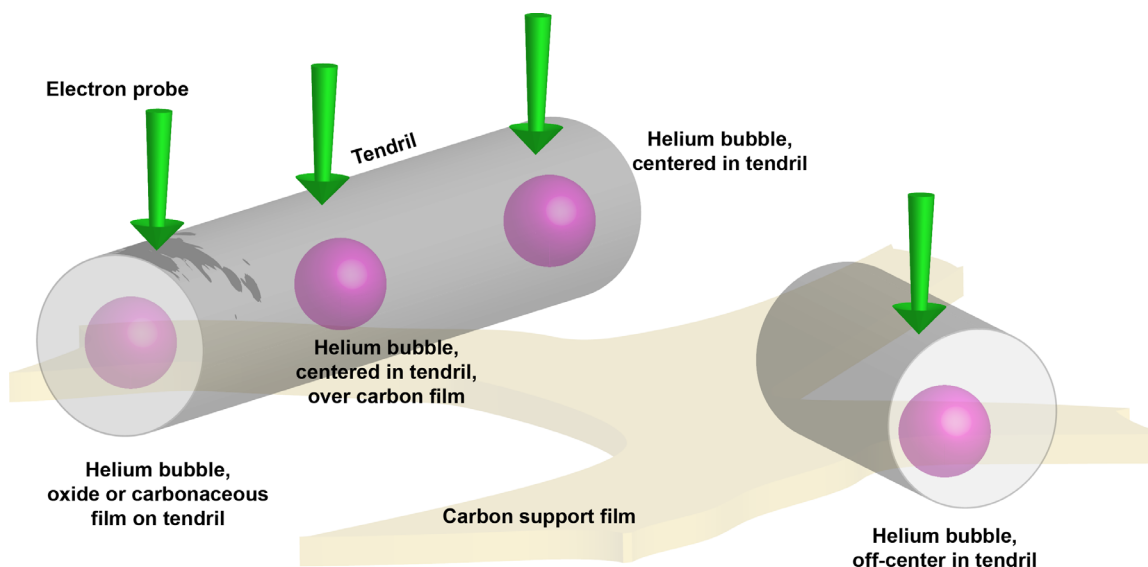


**Figure 53. Several hypothetical configurations of bubbles within the experimental situation.**

Any of these possibilities could result in bias in the integrated helium signal  $I_p$ . Additionally, the materials science of the situation could be different in different bubbles. The tendril growth processes are highly non-equilibrium, so varying bubble pressures is entirely feasible. Further, it's been seen that a 100+ keV electron beam can knock helium atoms out of bubbles in other materials (i.e., Si). A simple calculation indicates that a 100 keV electron can deliver ~60 eV knock-on energy to a helium atom, so it is possible that some bubbles, especially those that are small or near a free surface, might suffer disproportionate depopulation of the helium.

### Future Work

Analysis is ongoing.

### References

[1] C. A. Walsh, J. Yuan, L. M. Brown, *Phil. Mag. A*, 80 (2000) 1507.

## 6. LIQUID METAL COMPATIBILITY

### 6.1 LIQUID METAL COMPATIBILITY IN FUSION SYSTEMS

*B. A. Pint ([pintba@ornl.gov](mailto:pintba@ornl.gov)), J. Jun, and M. Romedenne*

#### OBJECTIVE

Liquid metal compatibility studies consist of three separate tasks evaluating Li, Sn and Pb-17at.%Li for various fusion blanket and plasma-facing applications. Compatibility between Li and RAFM steels has been studied for many years; the current project considers the susceptibility of F82H to liquid metal embrittlement. As static capsule tests showed reasonable compatibility, the Sn and PbLi studies are using thermal convection loops (TCLs) to study compatibility in flowing systems with a temperature gradient.

#### SUMMARY

Two TCL experiments were completed in FY21 and characterization of specimens for both loops is in progress. Both TCLs were fabricated from Kanthal alloy APMT (Fe-21Cr-5Al-3Mo) and studied specimens that were pre-oxidized to form an alumina surface scale to inhibit alloy-liquid interactions. One TCL exposed pre-oxidized FeCrAl specimens for 1000 h to flowing Sn with a peak temperature of 400°C. Large specimen mass losses in the hot leg suggest Sn is very corrosive, which was not observed in previous static capsule testing at 400° and 500°C. The other TCL exposed SiC and aluminized F82H specimens to flowing Pb-Li with a peak temperature of 650°C. Much smaller mass changes were observed compared to a similar experiment conducted in FY20 with a peak temperature of 700°C.

#### PROGRESS AND STATUS

Liquid metals are being explored as a potential solution for the extreme environment at the plasma interface. For Li, the high vapor pressure is not attractive, but compatibility is reasonably good with RAFM steels up to 600°C. One area of concern is the potential for liquid metal embrittlement (LME). An LME evaluation of F82H (Fe-8Cr-2W) is in progress. Hollow F82H specimens have been assembled and loaded with Li and are awaiting testing. An alternative approach for this application is to use Sn, which has a much lower vapor pressure, but is known to be very corrosive to most conventional alloys. Previous static capsule experiments showed good Sn compatibility with pre-oxidized APMT in Mo capsules at 400°C and 500°C for up to 2000 h. The next step in the evaluation with Sn was a flowing TCL experiment in which the specimens consisted of APMT and two ODS FeCrAl alloys (Fe-10Cr-6Al from ORNL and Fe-12Cr-6Al from Japan) that were all pre-oxidized for 2 h at 1000°C in air to form  $\alpha$ -Al<sub>2</sub>O<sub>3</sub>. The experiment ran for 1000 h with a peak temperature of 400°C and a 55 C-deg. temperature gradient. Specimen mass change data are shown in **Figure 54**. Large mass losses including significant specimen pitting were observed in the hot leg. These results suggest that Sn in a plasma-facing application would have to be contained in a refractory metal for adequate compatibility.

The sixth Pb-Li TCL experiment in our series also completed 1000 h with a peak temperature of 650°C. The previous TCL experiment with a 700°C peak temperature exposed CVD SiC, ODS Fe-10Cr-6Al and APMT specimens and revealed a large dissimilar material interaction between SiC and FeCrAl with large metal losses and Fe-Cr carbide and silicide formation on the SiC specimens. By lowering the temperature and using CVD SiC and primarily aluminized and pre-oxidized F82H specimens, much smaller mass changes were measured in this experiment, and are presented in **Figure 55**. Characterization of the exposed specimens is in progress.

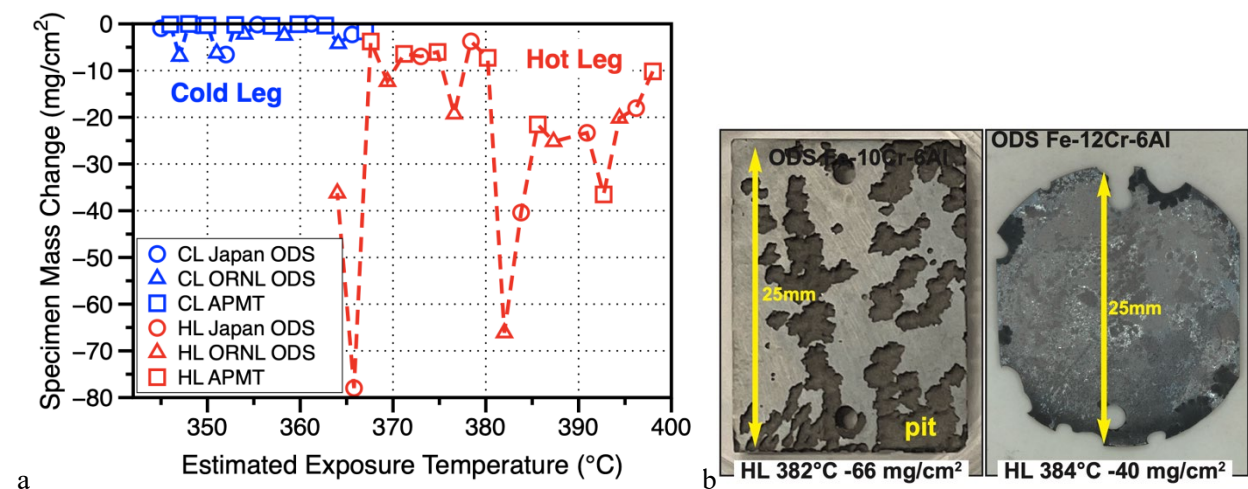


**Figure 54. (a) Specimen mass change of TCL specimens in flowing Sn after 1000 h as a function of estimated temperature in the hot leg (HL) and cold leg (CL). Specimens of three FeCrAl alloys were exposed with large mass losses observed in the hot leg. Examples from two specimens are shown in (b).**

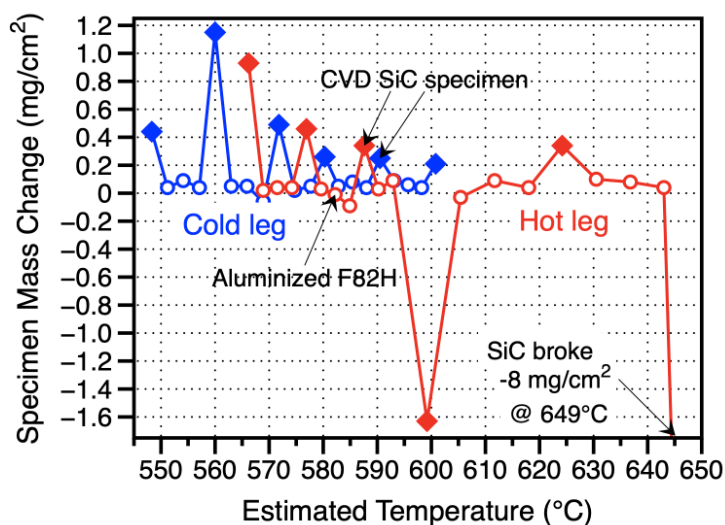


**Figure 55. Specimen mass change of TCL specimens in flowing PbLi after 1000 h as a function of estimated temperature in the hot and cold legs. The CVD SiC specimens are shown with closed diamonds and the aluminized F82H specimens are open circles.**

**Future Work**

During FY22, Task 3 of the FRONTIER collaboration will focus on completing the irradiation of Sn capsules in HFIR and completing the characterization of the Sn TCL specimens. The second and third round of LME experiments will be completed next year. Future objectives for the FESS Blanket and Fuel Cycle project have not been determined at this time. It is desirable to run a longer PbLi TCL experiment in order to determine the reaction kinetics and begin to consider an aluminized steel TCL structure that would be the basis for a future pumped PbLi loop.

## 7. EXPLORATORY, UNIQUE AND INNOVATIVE MATERIALS

### 7.1 IMPROVED CREEP BEHAVIOR OF A COPPER ALLOY FOR FUSION APPLICATIONS

Y. Yang ([yangying@ornl.gov](mailto:yangying@ornl.gov)), L. Tan (ORNL), L. Wang (Stanford University), L. Snead (Stony Brook University), and S. Zinkle (UTK)

#### OBJECTIVE

High creep strength, high thermal conductivity copper alloys are needed for a variety of demanding high heat flux structural components in fusion energy applications. The goal of this work is to develop CuCrNbZr (CCNZ) alloys with improved creep properties by promoting uniform distributions of Laves precipitates on grain boundaries and high concentrations of matrix precipitates.

#### SUMMARY

A newly designed CCNZ G2 (Generation 2) copper alloy achieved the target microstructure of uniformly distributed Laves-Cr<sub>2</sub>Nb precipitates and high-volume fractions of matrix Cr and Cu<sub>5</sub>Zr precipitates. The grain size of this alloy is unimodal and smaller than that of the ITER CuCrZr (CCZ) alloy but greater than the CCNZ G1 alloy. This alloy has electric conductivity of 82.4 %IACs, which is comparable to that of the CCZ alloy (83.4 %IACs) and better than that of CCNZ G1 (72.1 %IACs). The hardness and tensile strength of the new alloy is slightly lower than the CCZ and CCNZ G1 alloys. The creep properties of the CCNZ G2 alloy were tested at 500°C under three stress levels: 90, 110 and 125 MPa. The minimum creep strain rate is higher for the new alloy at low stress levels. But the slope of minimum creep strain rate vs stress is the smallest among the CCZ, CCNZ G1 and CCNZ G2 alloys, which leads to better creep resistance at higher stress levels. The uniformly distributed grain boundary precipitates can effectively pin grain boundary sliding and slow crack propagation. This gives the CCNZ G2 alloy improved creep life in all three test conditions. For stress levels of 110 and 125 MPa, the creep life of CCNZ G2 (600 and 200 h) is almost one order of magnitude higher than those of CCZ and CCNZ G1. This newly developed CCNZ G2 alloy provides an attractive combination of excellent creep properties and thermal conductivity.

A recently developed Generation I CCNZ G1 alloy showed creep properties better than the commercial CCZ alloy used in ITER. The improvement is primarily due to the formation of both grain boundary precipitates of Laves-Cr<sub>2</sub>Nb phase and matrix Cr precipitates, while the CCZ alloys only have matrix Cr precipitates. However, the Laves precipitates in CCNZ G1 are not uniformly distributed along grain boundary. Instead, they form clusters which lead to reduced pinning effect on grain boundary and non-uniform grain size. Both factors limited the materials reaching optimal creep properties.

#### PROGRESS AND STATUS

A new CuCrNbZr alloy, CCNZ G2, with reduced Nb and increased Zr content was designed with the aid of computational thermodynamics. The calculated volume fractions of precipitates as a function of temperature of CCNZ G2 are plotted in **Figure 56(a)** and compared with those in CCNZ G1 in **Figure 56(b)**. By reducing the amount of Laves phase formed from liquid, the clustering of grain boundary precipitate can be reduced. At the same time, we increased the fraction of matrix Cr and Cu<sub>5</sub>Zr precipitates in the new alloy. The CCNZ G2 alloy was fabricated using conventional arc-melting and casting, then cold rolled at room temperature and homogenized at 970°C followed by thermal aging at 475°C for 3h.

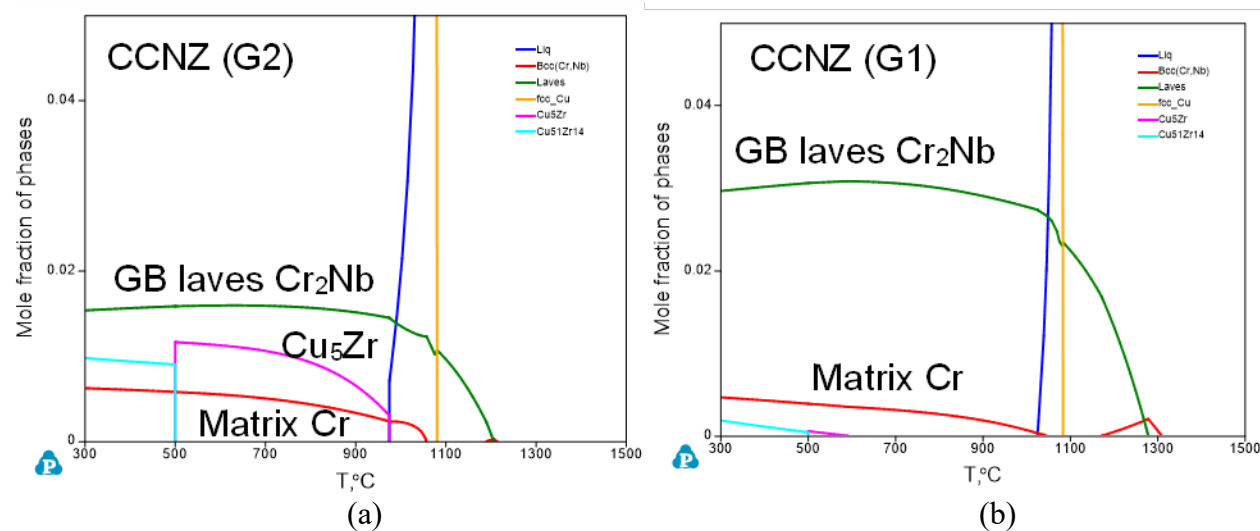


**Figure 56. Calculated volume fraction of precipitates as a function of temperature for (a) CCNZ G2 and (b) CCNZ G1.**

The microstructure of the resulting CCNZ G1 alloy is shown in **Figure 57**. The left panel shows the micron scale  $\text{Cr}_2\text{Nb}$  and Cr precipitates, which are primarily formed during homogenization at  $970^\circ\text{C}$  with a small fraction of  $\text{Cr}_2\text{Nb}$  formed directly on solidification from liquid. The right panel shows the matrix Cr precipitates in purple with number density  $1.62 \times 10^{22}/\text{m}^3$  and mean radius of  $5.5 \pm 1.0$  nm, and the  $\text{Cu}_5\text{Zr}$  ppts in aqua with number density  $4.35 \times 10^{21}/\text{m}^3$  and mean radius of  $11.7 \pm 1.1$  nm.

Creep test results for CCNZ G2 alloy are compared with those of CCZ and CCNZ G1 alloys in **Figure 58**, together with optical micrographs of the fractured creep specimens. The relationship between microstructural features and creep behavior can be summarized as follows: commercial CCZ alloys have no GB precipitates, but only matrix Cr precipitates and uniform grain size, showing the shortest creep life. The CCNZ G1 alloy has clustered GB precipitates and matrix Cr precipitates and bimodal grain size. Its creep life is better than the CCZ alloy, but at high stress level it is still low. The CCNZ G2 alloy, with uniformly distributed GB precipitates, more matrix Cr and  $\text{Cu}_5\text{Zr}$  precipitates, and uniform grain size, showed greater creep life for all test conditions. Specifically for high stress levels of 110 and 125 MPa., creep life of the new alloy increased by almost one order of magnitude.

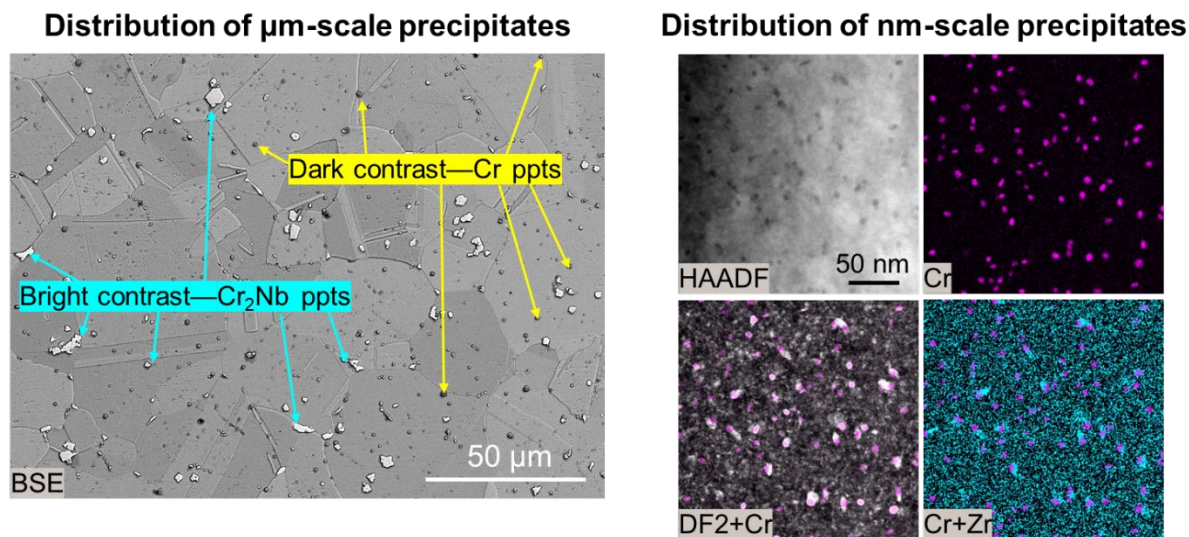


Figure 57. Microstructure of as-aged CCNZ G2 alloy. (Left): micron scale Cr<sub>2</sub>Nb and Cr precipitates and (right): nanoscale Cr and Cu<sub>5</sub>Zr precipitates.

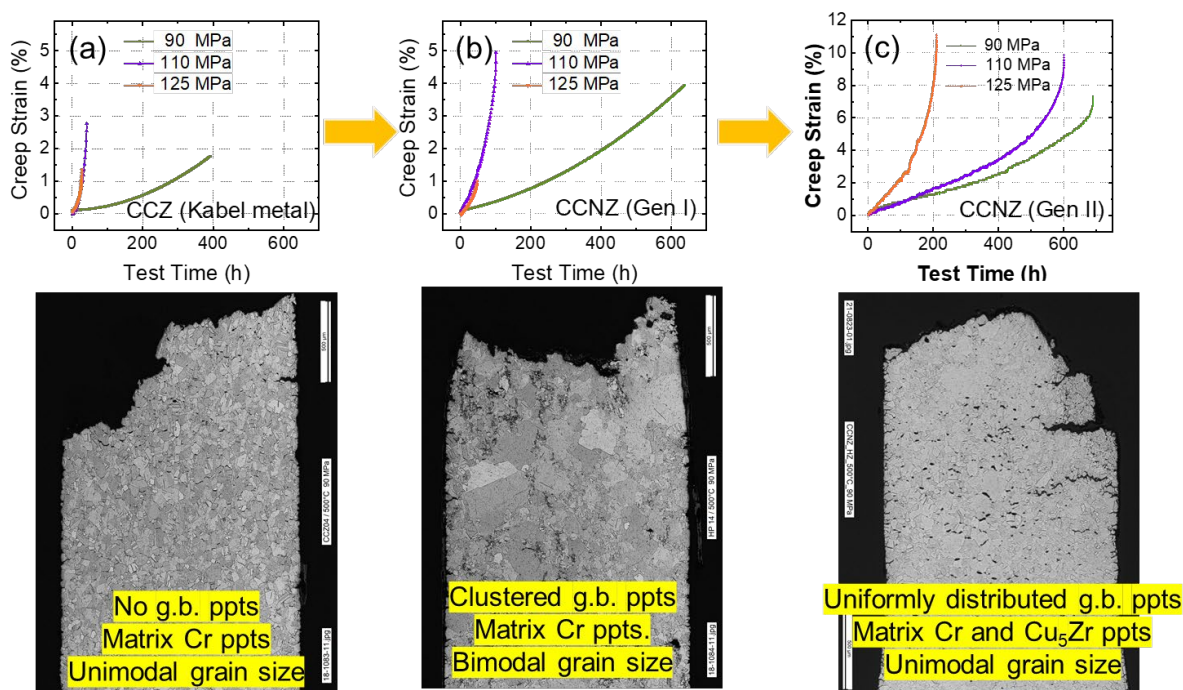


Figure 58. The creep test results of CCNZ G2 alloy compared with those of CCZ and CCNZ G1 alloys, together with optical micrographs of the fractured creep specimens.

**Future Work**

The microstructure- property relationship will be investigated in greater detail to help determine the beneficial mechanisms leading to enhanced creep properties.

## 7.2 SOLID-STATE BREEDER MATERIALS – THEORY AND MODELING

Philip D Edmondson ([edmondsonpd@ornl.com](mailto:edmondsonpd@ornl.com)), and German Samolyuk

### OBJECTIVE

The objective of this task is to use materials theory to explore potential new Li-bearing compounds as fusion breeder materials, and to examine the structural stability of lithium metatitanate ( $\text{Li}_2\text{TiO}_3$ ) as the compound loses Li during transmutation tritium breeding.

### SUMMARY

Nuclear fusion power plants require tritium fuel which must be generated on-site. The fuel cycle includes purification, separation, and pellet formation prior to injection into the reactor core. The generation of tritium occurs in the breeder blanket component of the reactor. For the solid-state breeder reactor concept, there are usually two primary components: the breeding material and a Be containing neutron multiplier.

We have focused on two areas for research into novel solid-state breeder blanket materials: 1) development of novel hybrid materials that combine a neutron multiplier and Li breeder, with a focus on structural stability and tailored thermal stability for improved thermal properties; and 2) examination of the structural stability of a conventional  $\text{Li}_2\text{TiO}_3$  breeder material during operation.

### PROGRESS AND STATUS

#### Novel Material Development

The use of hybrid binary material systems offers potential improvements in efficiency and materials stability compared to conventional materials. We have explored the potential of novel ceramics to offer performance improvements when compared to leading non-hybrid candidate materials. Specifically, we have examined the structural stability of the unit cells, and the thermal properties with a view to being able to better match the thermal conductivity of the neutron multiplier and the breeding material in the graded architecture system for better thermal management and reduced thermal gradients with minimized thermal expansion differences. These properties are critical to the use of such materials as high thermal gradients between the multiplier and breeding materials may result in detrimental cracking. A hybrid functional material with tailored properties might offer the potential to minimize and mitigate detrimental effects.

Our initial approach is to use density functional theory (DFT) based techniques to determine if the structures are stable and have the desired properties, namely thermal conductivity.

Our initial evaluations focused on the thermal conductivities of four different materials,  $\text{Li}_2\text{TiO}_3$  and  $\text{Li}_2\text{ZrO}_3$  as conventional benchmark materials and  $\text{Li}_2\text{BeSiO}_4$  and  $\text{Li}_2\text{BeGeO}_4$  hybrid systems. These four compounds are known to be stable at ambient conditions and this was replicated and confirmed in the initial DFT calculations in which the phonon frequencies throughout the crystals unit cell Brillouin zone were observed to be positive.

Looking at the thermal conductivity, the thermal transport within the materials is defined by the phonon dispersion; thus, the thermal conductivity can be derived by examination of the anharmonic potential determined from the phonon scattering. The results for the conventional  $\text{Li}_2\text{TiO}_3$  and hybrid  $\text{Li}_2\text{BeSiO}_4$  are shown in **Figure 59**. These results demonstrate that the thermal conductivity of the hybrid system is vastly improved compared to that of the conventional material. The reason for this improved thermal

property is the addition of the Si dopant serves to increase the phonon group velocities, resulting in a greater phonon lifetime. It was also demonstrated that the variation in phonon group velocities – and hence the tunability of the thermal conductivity – is determined by the mass of the dopant element, thereby demonstrating that the desired thermal conductivity can be achieved through careful selection of elements within the compound.

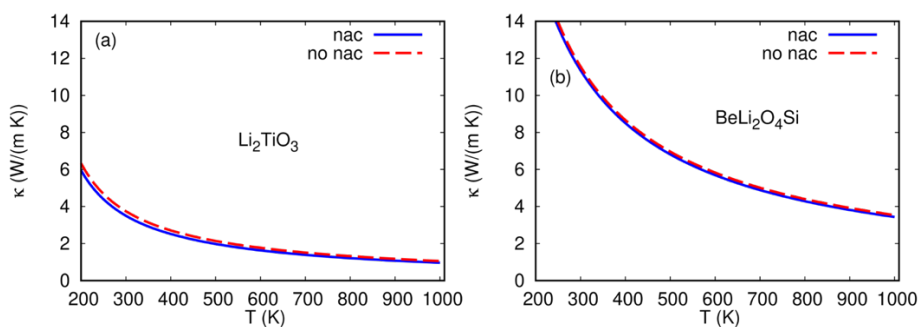


**Figure 59. Thermal conductivity as a function of temperature for  $\text{Li}_2\text{TiO}_3$  (a leading breeder candidate) and a  $\text{Li}_2\text{BeSiO}_4$  hybrid ceramic. Significantly greater thermal conductivity is achieved in the hybrid material.**

#### $\text{Li}_2\text{TiO}_3$ Unit Cell Stability Under Transmutation/Burn-up

A critical question in the use of solid-state breeder materials is their stability during operation. By design, these materials are developed to undergo significant transmutation as the constituent Li is converted to tritium. As the Li is depleted, a structural vacancy remains within the unit cell and the implications on retaining the structure as a solid monolith is unknown. In this study, we are examining the structural stability using DFT techniques as Li-vacancies, i.e., vacancies at the Li positions, are generated in varying concentrations and at various locations.

Preliminary results have shown that for a unit cell with a single Li-vacancy, the structure remains stable, as shown in **Figure 60**. Increasing the concentration of Li-vacancies to two defects, (Li-divacancies) the stability of the system is presented in **Figure 61**. For the two configurations present, it can be seen that in one case (left-hand-side structure, **Figure 61**) the unit cell and hence the overall structure is stable whereas in the second configuration (right-hand-side structure, **Figure 61**) there is a loss of stability. As a result of the loss of this structural stability, the material may fragment.

#### **Future Work**

We will continue to investigate and explore the novel hybrid ceramic routes, including the fabrication of hybrid materials such as Li-Be compounds. We will also seek to establish the structural stability and the impact of Li transmutation/burn-up on tritium retention of candidate materials including  $\text{Li}_2\text{TiO}_3$ ,  $\text{Li}_2\text{ZrO}_3$  and  $\text{Li}_8\text{PbO}_6$ . Lithium orthoplumbate ( $\text{Li}_8\text{PbO}_6$ ) is also an attractive hybrid system due to the neutron multiplication effect of Pb. We will also utilize neutronic calculations to assist in the determination of appropriate Li (and additional element) transmutations on defect generation and configurations.

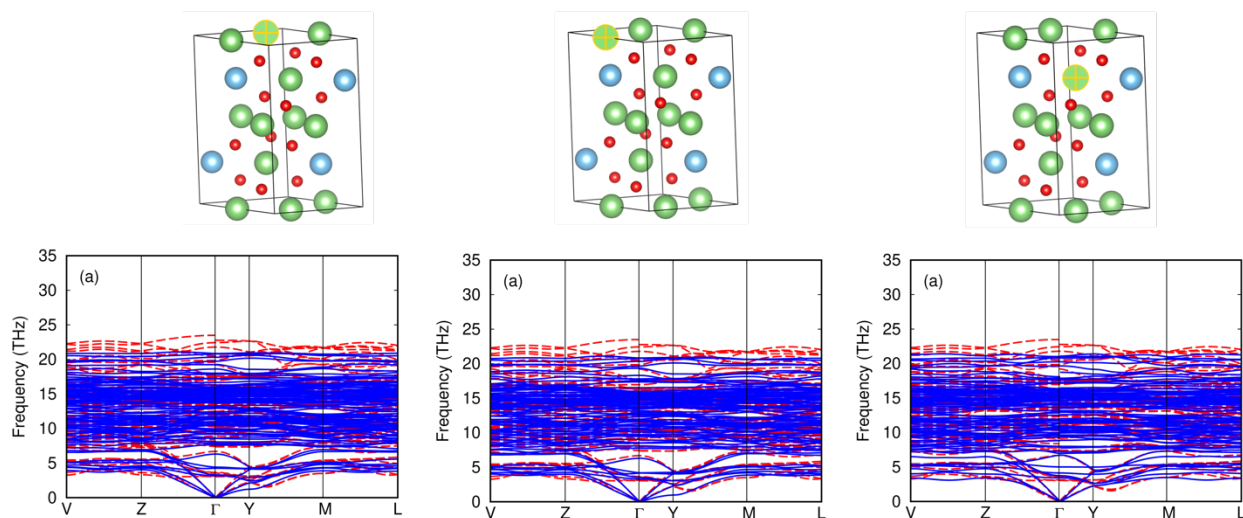


**Figure 60. Phonon dispersion curves for unit cells of  $\text{Li}_2\text{TiO}_3$  with single Li-vacancies (denoted by the + in the cell figures at top.) In all configurations presented, the unit cells are stable.**

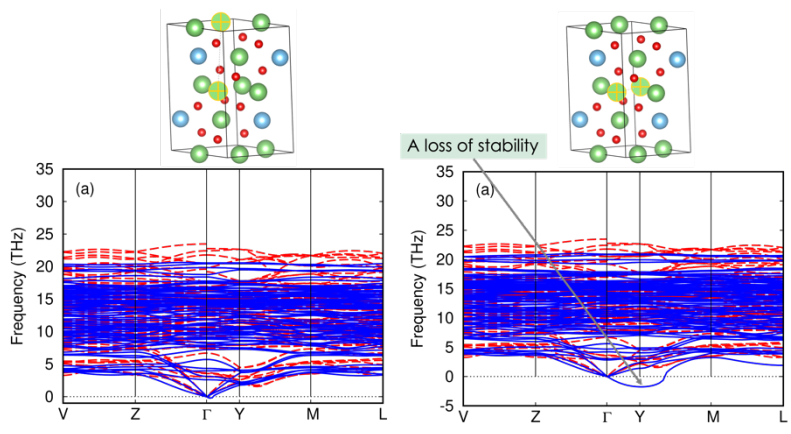


**Figure 61. Phonon dispersion curves for 2 configurations of Li-di-vacancies within the unit cells. In the configuration on the left-hand-side, the structure is stable; the structure on the right is unstable.**

## 8. GASES IN MATERIALS

### 8.1 THERMALLY-DRIVEN EVOLUTION OF HELIUM-IMPLANTED SURFACE GRAINS IN WARM-ROLLED TUNGSTEN

Cuncai Fan (now at University of Hong Kong), and Xunxiang Hu ([huxx@scu.edu.cn](mailto:huxx@scu.edu.cn)) (now at Sichuan University)

#### OBJECTIVE

This work investigates the thermal stability of helium-implanted surface grains in warm-rolled polycrystalline tungsten (W). We are comparing the evolution of the surface of as-polished and He-implanted W following the heat treatment during thermal helium desorption measurements. The underlying mechanisms have been analyzed via detailed microstructure characterization of the subsurface of the materials. These results are expected to provide insights into the performance of W plasma facing materials in fusion environments.

#### SUMMARY

We performed the thermal desorption spectroscopy (TDS) annealing experiment on as-polished polycrystalline W and W samples implanted by 40 keV He<sup>+</sup> to a fluence of  $1 \times 10^{16}$  cm<sup>-2</sup> at room temperature. It was found that the as-polished specimen experienced recovery and recrystallization through the removal of low angle grain boundaries and subgrain coarsening, whereas the implanted specimen retained the stable grain structure. This enhanced thermal stability was attributed to the pinning effect of He bubbles on grain boundaries, and the underlying mechanism was discussed based on the proposed model of a cellular microstructure.

#### PROGRESS AND STATUS

Warm-rolled polycrystalline W of ultra-high purity (nominal 99.999%) was purchased from Goodfellow, USA. The material was machined into small discs, ~1 mm in thickness and ~5 mm in diameter, followed by mechanical polishing to a mirror-like surface. As-polished W was implanted by 40 keV He<sup>+</sup> to a fluence of  $1 \times 10^{16}$  cm<sup>-2</sup> at room temperature by Innovion Corporation, CA. During implantation, the incident He ion beam was controlled to be perpendicular to sample surface. After He implantation, annealing experiments were performed in a high vacuum chamber ( $\sim 10^{-8}$  torr). Both as-polished and He-implanted W were heated to ~1920 K with a constant ramp rate of 0.5 K/s. The released He was measured in a TDS experiment.

The EBSD inverse pole figure (IPF) orientation maps of the annealed specimens are compared in **Figure 62**. For the as-polished W sample shown in **Figure 62(a)-(c)**, it was found that a large fraction of surface grains changed their preferred <110> crystallographic orientations during annealing. Especially interesting was the observation that some of the <110>-oriented grains were not identified and appeared as black regions. However, it is not known how these regions are formed on the W surface. In contrast, no changes in grain size or orientation were detected in the He-implanted W sample after TDS annealing. This implanted and annealed sample shown in **Figure 62(d)-(i)** still exhibited a strong <110> texture and small clustered subgrains, essentially identical to the as-polished unannealed specimen.

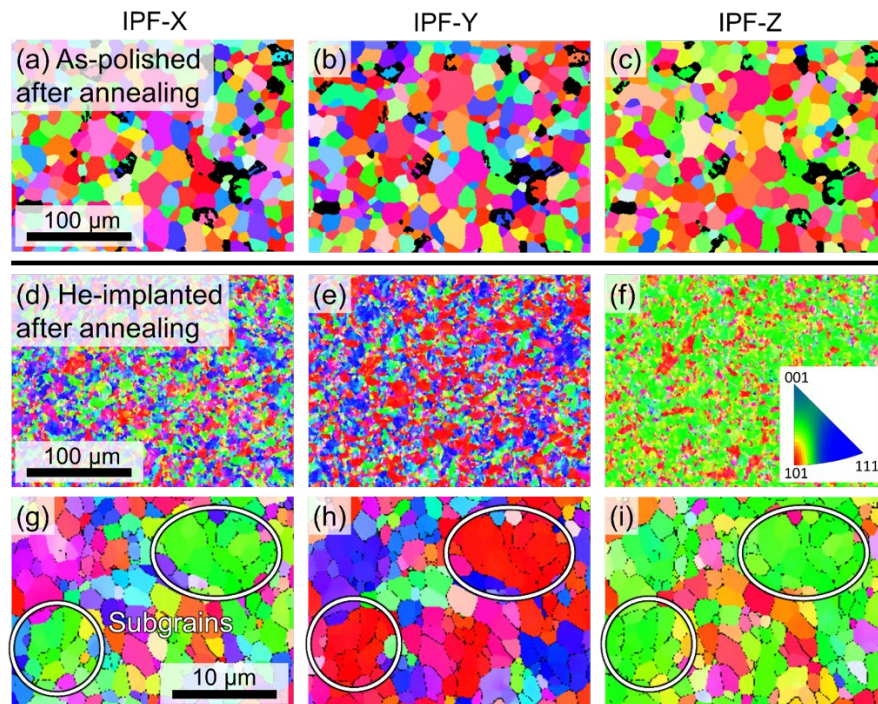


**Figure 62.** EBSD Orientation maps after TDS annealing for (a)-(c) as-polished and (d)-(i) He-implanted W. Inset at bottom-right in (f) shows corresponding IPF.

The statistics of grain size ( $D$ ) and misorientation angle ( $\theta$ ) are summarized in **Figure 63**. As demonstrated by the black, green, and red histograms, the as-polished, He-implanted as well as its annealed specimen are all dominated by small grains ( $D < 5 \mu\text{m}$ ) with low-angle grain boundaries (LAGBs,  $\theta < 15^\circ$ ). In contrast, the blue histograms show that the as-polished W after annealing is composed of large grains with high-angle grain boundaries (HAGBs). Combined with the images in **Figure 62**, it can be concluded that the grain growth in warm-rolled polycrystalline W must occur through the removal of LAGBs and in the form of subgrain coarsening.

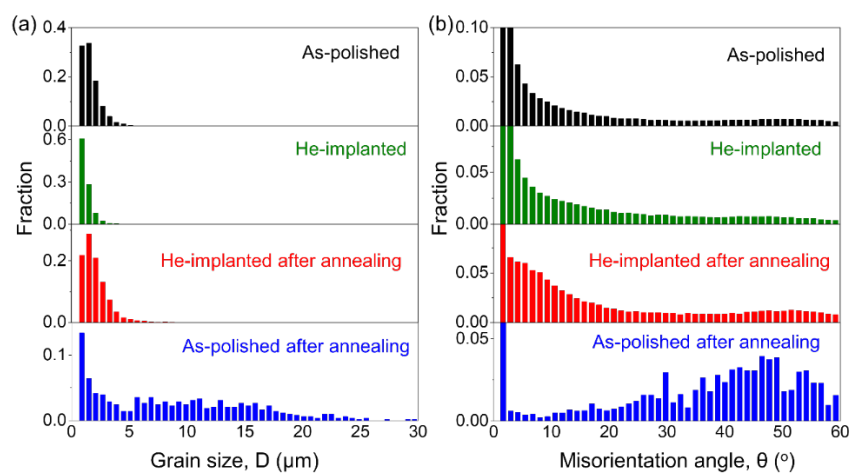


**Figure 63.** Distribution histograms of (a) grain size and (b) misorientation angle  $\theta$  for as-polished and He-implanted W before (black and green) and after (red and blue) annealing.

Further analyses of cross-section samples were performed to better understand the microstructural changes of He-implanted surface grains after TDS annealing. **Figure 64(a)** shows the IPF orientation map of annealed He-implanted W cross section. Evidently, grain growth was triggered in bulk grains that are approximately equiaxed and range from 5 to 25  $\mu\text{m}$  in grain size. As shown in **Figure 64(b)**, the FIB-prepared TEM lift-out sample of the annealed He-implanted W consisted of large bulk grains that are distinct from the small surface grains. The TEM micrograph in **Figure 64(c)** revealed that the small surface grains were located within approximately 100-300 nm of surface, and they contained a high density of He bubbles as demonstrated by the TEM micrograph of **Figure 64(d)**. The bubbles were all located within the ion implantation region, and their number density tended to be consistent with the He concentration profile (superimposed curve) along the ion penetration direction. In addition, a grooving profile developed between two surface grains can also be observed in **Figure 64(c)**.

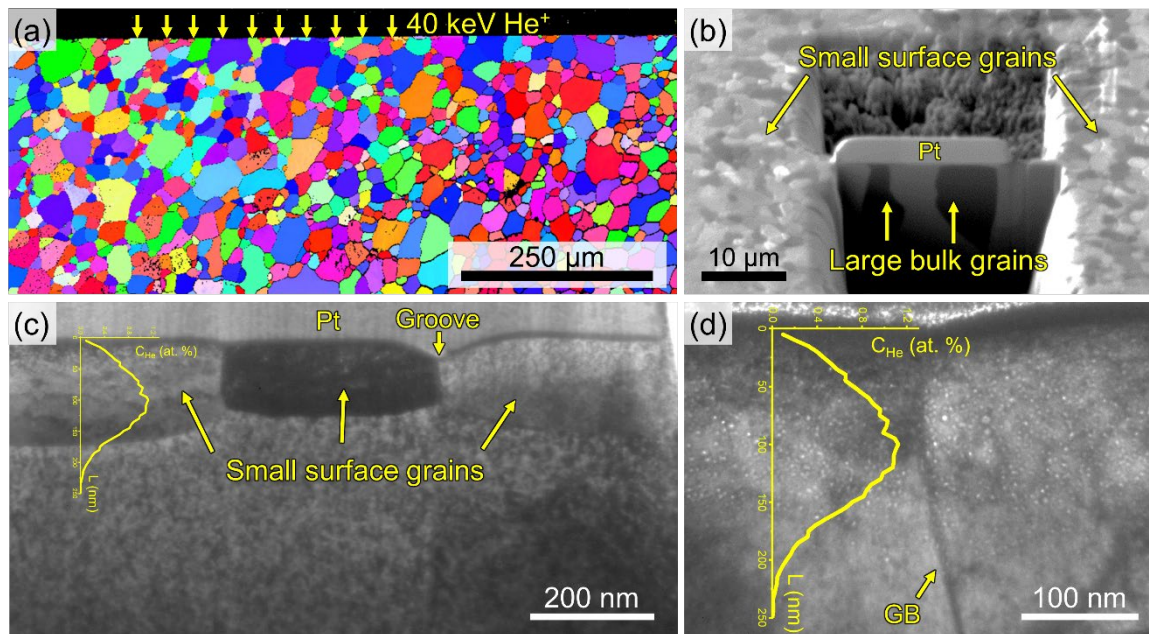


**Figure 64.** Cross-section sample prepared from the He-implanted W specimen after TDS annealing. (a) EBSD IPF orientation map showing the He implanted region near the top surface. (b) FIB ion channeling contrast image showing the small surface grains and large bulk grains. (c) (d) TEM micrographs of the small surface grains and subsurface He bubbles. The superimposed plot in (c) and (d) is the calculated He concentration profile  $C_{\text{He}}$  versus ion penetration depth,  $L$ .

### Future Work

Future work will focus on simulation to understand the mechanism of helium effects on the thermal stability of grain structure in tungsten.

## 9. ADVANCED MANUFACTURING

### 9.1 ADVANCED MANUFACTURING OF TUNGSTEN FOR DIVERTOR COMPONENTS – AN ARPA-E GAMOW PROJECT

Michael Kirka ([kirkamm@ornl.gov](mailto:kirkamm@ornl.gov)), Patxi Fernandez-Zelaia, Christopher Ledford, Michael Sprayberry, Julio Rojas, Andres Marquez-Rossy, and Yutai Katoh

#### OBJECTIVE

The processing of tungsten and associated alloys into complex geometries through conventional means is difficult due to the high temperatures necessary for the densification through solid state and liquid processing. Powder bed additive manufacturing (AM) processes offer the potential to fabricate complex geometry tungsten components needed for fusion energy applications and overcome the limitations of traditional solid-state processing of tungsten. However, tungsten is prone to ductile-to-brittle transitions and cracking due to residual and thermal stresses. The objective of this effort is to develop the necessary processing science to fabricate high-quality tungsten that is both dense and crack free using the electron beam melting (EBM) process and demonstrate the versatility of the EBM process in the fabrication of plasma facing component (PFC) relevant geometries such as tiles for the interior and divertor of a reactor.

#### SUMMARY

A space fill design of experiments approach was taken to sample the process space for tungsten in the EBM process and identified non-unique process parameter sets that resulted in high-quality fully dense and crack free density blocks. Characterization of the grain structure of the fully dense and crack free EBM tungsten indicates the preference for the material to form fiber textures aligned with the build direction that are either of a {001}, {111}, or a mix of {001}/{111} fiber orientations. In subsequent experiments multiple geometries were printed utilizing identical process settings and it was empirically observed that print sequence is important in limiting defect formation. Increasing time-to-print following initial preheat of the layer was observed to result in increasing levels of porosity; the first and last geometries had differing porosity despite being identical in geometry and utilizing identical scan settings. To mitigate against this deleterious cooling effect, additional pre-heating steps were included in the process to maintain a more constant surface temperature during all melt steps.

#### PROGRESS AND STATUS

An Arcam Q10+ was utilized to explore the process space of tungsten through EBM. Previous work at ORNL on the processing of tungsten in EBM identified several key process variables that can be leveraged for improving the density and quality of the material. Amongst these variables is the surface temperature of the build area, hatch spacing, beam speed, and beam current. In this investigation of the process space, we utilized an efficient space fill design of experiments to sample the space, as well as leveraging process maps adapted from Thomas et al. [1] relating the key process variables to material quality such as density.

From the space fill design of experiments approach, EBM builds of density blocks were fabricated with a representative build shown in **Figure 65a**. The process space examined with this approach constrained the area energy density of each process parameter between isosurfaces corresponding to 40 and 100 J/mm<sup>2</sup>; this was chosen based on prior experience printing refractory metals. To rapidly determined the material quality of the density blocks without using metallography of each, the in-situ near-IR layer image analysis technique during a build was utilized. From these near-IR layer images, the density of the samples was determined and used to identify process windows that yield fully dense material as shown in **Figure 65b**. Spanning the process window examined, EBM tungsten material was obtained that varied in density from 38% to greater than 99.95%.

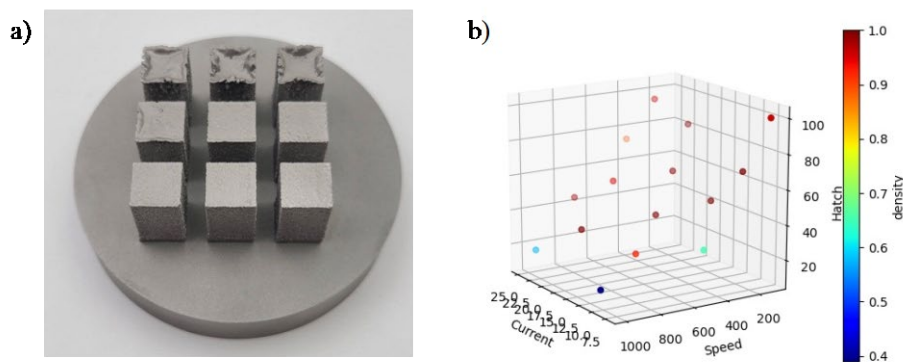


**Figure 65. a) Representative tungsten EBM build of density cubes for exploring process window b) Variation in density of tungsten density cubes as function of process parameters.**

While exploration of the process window identified process parameter sets that resulted in high quality tungsten material that was both fully dense and free of cracking, the repeatability and extension of the parameters to larger scale parts and builds was explored. By altering the build layout or building multiple density blocks with the same process parameter sets a shortcoming in the processing of tungsten was identified; the material quality is extremely sensitive to the time between successive passes of the electron beam. The explanation is that following initial preheat of the powder bed significant time elapses until later geometries are selectively melted and hence the surface cools due to radiation. This is clear from the near-IR image (*Figure 66a*) of a nine-cube build using identical process parameters in which the level of porosity increases from the first row (first to be melted) of density blocks to the last row (last to be melted). To understand the impact of cooling on the energy imparted by a given process parameter set, the process maps were adapted to account for energy loss that a part in a build would experience while waiting its turn to be melted. Shown in *Figure 66b* is an example of an uncorrected process map that does not assume cooling, with the red arrow indicating a select process parameter set, with the red arrow in the process map in *Figure 66c* accounting for energy loss during cooling showing an approximate 20% decrease in the imparted energy for a part that cools for a few seconds at 20°C per second. To overcome the issue of the material cooling too rapidly while awaiting melting, additionally preheat steps were added to the process to allow the material surface temperature to return to a higher state.

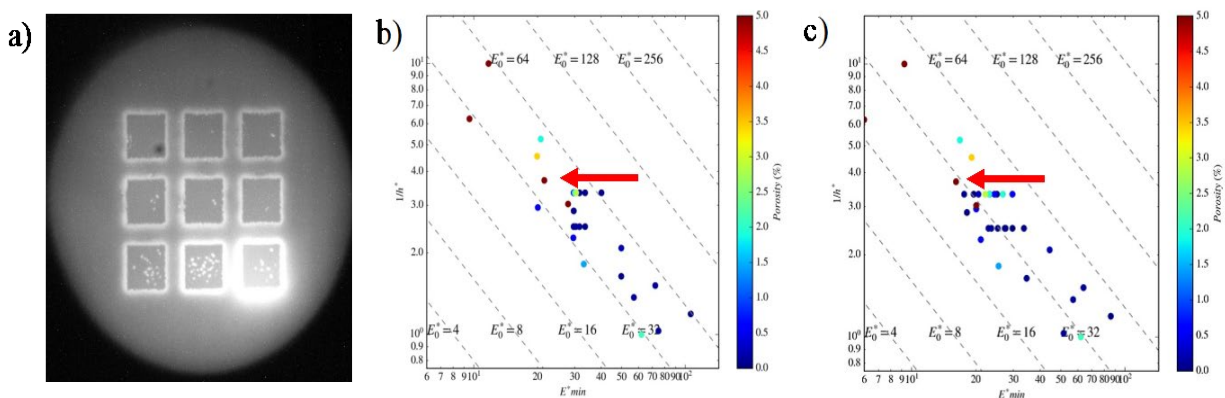


**Figure 66. Impact of cooling on the quality of the EBM tungsten material a) Representative near-IR layer image of a build containing nine tungsten density blocks being processed with identical process parameters. b) Thomas process map showing the imparted normalized energy for the tungsten processing space. c) Modified Thomas processing map accounting for cooling effects on the process space.**

Metallographic analysis of the high-quality density blocks identified through near-IR in-situ defect detection analysis confirmed the ability to obtain tungsten through EBM that is both fully dense and crack free. Representative textures observed in the EBM tungsten are shown in the electron back scatter IPF maps (*Figure 67a-c*). The IPF maps indicate that a key characteristic of high-quality tungsten is the presence of a columnar microstructure with strong  $\{001\}$  and  $\{111\}$  build direction fiber textures. We hypothesize this preference in fiber texture direction is sensitive to the imparted energy density used to fabricate the material and the impact on the resultant melt pool shape. Similarly, other literature on AM of refractory metals has shown that  $\{111\}$  is favored [2]. The generally accepted explanation is that this effect is due to the shape of the weld pool which promotes  $\{001\}$  growth along an angle perpendicular to the liquid-solid interface effectively yielding  $\{111\}$  in the build direction [3].

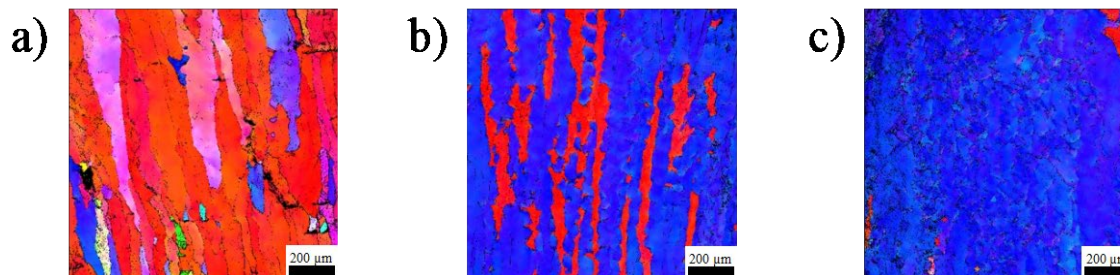


**Figure 67. Obtained fiber textures observed within the process window for high-quality crack free and dense EBM tungsten a)  $\{001\}$  fibers aligned with the build direction b) Mix  $\{001\}/\{111\}$  fiber texture c)  $\{111\}$  fiber texture aligned with the build direction.**

### Future Work

Leveraging the processing science developed during FY21 in the EBM processing of bulk structure tungsten, the processing science will be extended to relevant complex geometries such as the plasma facing tiles that can line the interior of a fusion reactor. Additionally, the high temperature mechanical performance of the EBM tungsten will be investigated and compared to traditionally processed tungsten, using bulk samples fabricated for vertical and horizontal full-scale ASTM E08 sample geometries (*Figure 68*).

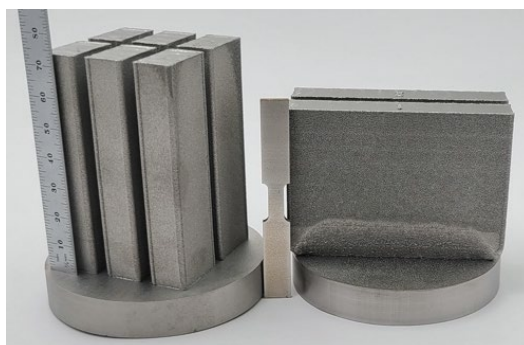


**Figure 68. Repetitive vertical and transverse bulk tungsten sample builds fabricated through EBM for mechanical sample extraction for high temperature quasi-static tensile testing.**

**References**

- [1] Thomas, M., Baxter, G. J., & Todd, I. Normalised model-based processing diagrams for additive layer manufacture of engineering alloys. *Acta Materialia*, 108 (2016) 26-35.
- [2] Fernandez-Zelaia, Patxi, Christopher Ledford, Elizabeth AI Ellis, Quinn Campbell, Andrés Márquez Rosy, Donovan N. Leonard, and Michael M. Kirka. "Crystallographic texture evolution in electron beam melting additive manufacturing of pure Molybdenum," *Materials & Design* 207 (2021) 109809.
- [3] L. Thijs, M. L. M. Sistiaga, R. Wauthle, Q. Xie, J.-P. Kruth, J. Van Humbeeck, Strong morphological and crystallographic texture and resulting yield strength anisotropy in selective laser melted tantalum, *Acta Materialia* 61 (2013) 4657–4668.

## 9.2 TRANSITION STRUCTURE BETWEEN A RAFM STEEL AND TUNGSTEN – AN ARPA-E GAMOW PROJECT

Y. Yang ([yangying@ornl.gov](mailto:yangying@ornl.gov)), T. Graening, L. Tan, Y. Katoh (ORNL), and I. Robin (University of Tennessee Knoxville)

### OBJECTIVE

Fusion power plants (FPPs) will require robust, affordable, and durable plasma-facing components (PFCs). Specifically, divertors must withstand the daunting challenges including high heat flux, plasma compatibility, neutron damage tolerance, tritium cycling and safety. Among the existing PFC engineering solutions, solid PFCs with tungsten (W) armor, helium (He) cooling, and reduced-activation ferritic/martensitic (RAFM) steel structure are among the most attractive concepts. However, there are significant technology gaps in these designs, specifically, there is no method to form a good bond between RAFM steel and tungsten due to the large difference in melting temperatures, susceptibility to form brittle intermetallic compounds, and large mismatch in coefficients of thermal expansion (CTE). This project aims to design and test a novel transition between RAFM steel and tungsten to mitigate these service challenges.

### SUMMARY

A transition structure has been designed consisting of three interlayers between the two end members, i.e., RAFM steel/FeCrAl/VCrAl/VCrTi/W. The alloy system and composition of each interlayer was selected based on computational thermodynamics and diffusion kinetics to meet the following three criteria: 1) no layered brittle intermetallic phase would form at interface and the bcc solid solution phase should form the matrix phase throughout the whole transitional structure; 2) there should be finite interdiffusion between layers to ensure good bond strength; and 3) the CTE mismatch between any two layers in the transitional structure should be smaller than that of RAFMs/W. The selected composition path should satisfy these three criteria for the temperature range 650~1150°C. Although the transitional structure was designed for additive manufacturing, due to the long lead time and cost of powder procurement, the preliminary evaluation of the transitional structure was performed on materials bonded by spark plasma sintering (SPS). Microstructural analysis of SPS-bonded and heat-treated samples showed sufficient diffusion distances (greater than 1  $\mu\text{m}$ ) at all interfaces except the VCrTi/W interface, suggesting adequate diffusion bonding. For the VCrTi/W interface, mixed bonding results were obtained. The region that was not well-bonded was probably associated with the slow diffusion of elements in W and W in V, and to the non-uniform surface roughness. No evidence of brittle intermetallic layers was identified at interfaces. The CTE of FeCrAl is comparable to that RAFM steels ( $12.7\text{E-}6 \text{ K}^{-1}$ ), and that of VCrAl and VCrTi is  $\sim$  about  $10\text{E-}6 \text{ K}^{-1}$ , which is closer to that of tungsten ( $4.6\text{E-}6\text{K}^{-1}$ ) than to the RAFM steels.

### PROGRESS AND STATUS

To identify a path with a continuous bcc single phase region at both high and low temperature, we used phase diagram calculations to screen many ternary systems, and finally settled on the three ternary systems Fe-Cr-Al, V-Cr-Al, and V-Cr-W. These three systems all show extensive bcc single phase region at both 1100°C and 600°, as shown in **Figure 69**. The interlayer compositions are schematically shown by the red stars and connected by the red dashed lines. The VCr layer was replaced by VCrTi (V44) alloy due to material availability and similarity.

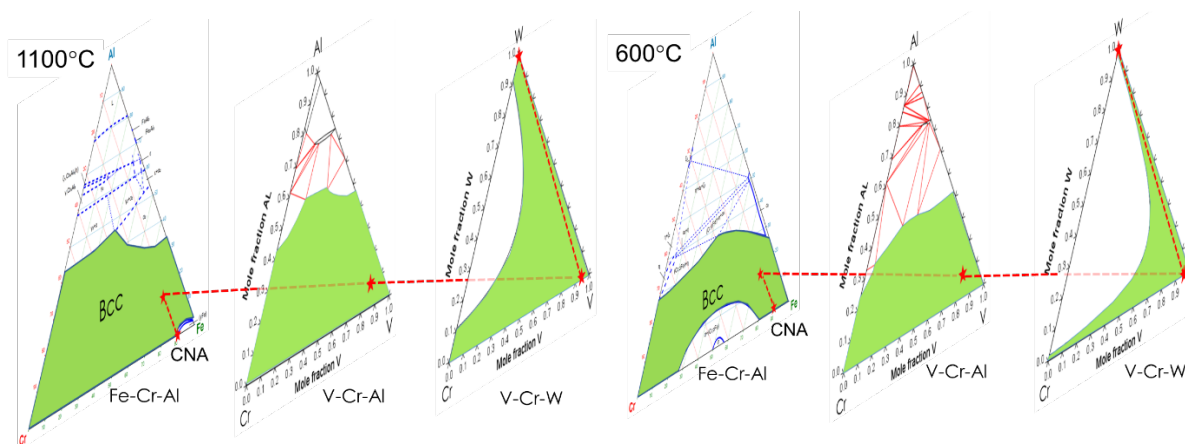


**Figure 69.** Calculated isothermal sections of Fe-Cr-Al, V-Cr-Al and V-Cr-W phase diagrams at 1100 and 600°C, respectively, showing an extensive bcc single solid solution phase (green areas) with individual composition as red stars.

We performed interdiffusion simulations between different interlayers based on the SPS processing parameters, as shown in **Figure 70**. The developmental CNA was the RAFM steel, and the pure W rod (99.97 wt% metal basis, pressed and sintered from powder, unannealed) was used in this work. The interdiffusion distance was determined to be largest for the CNA/FeCrAl interface, second for the FeCrAl/VCrAl interface and third for the VCrAl-VCrTi interface. Despite the high SPS temperature for the V44/W bond, the interdiffusion distance is small. These simulation results suggest that good bonding can be achieved for all interfaces except the VCrTi/W interface.

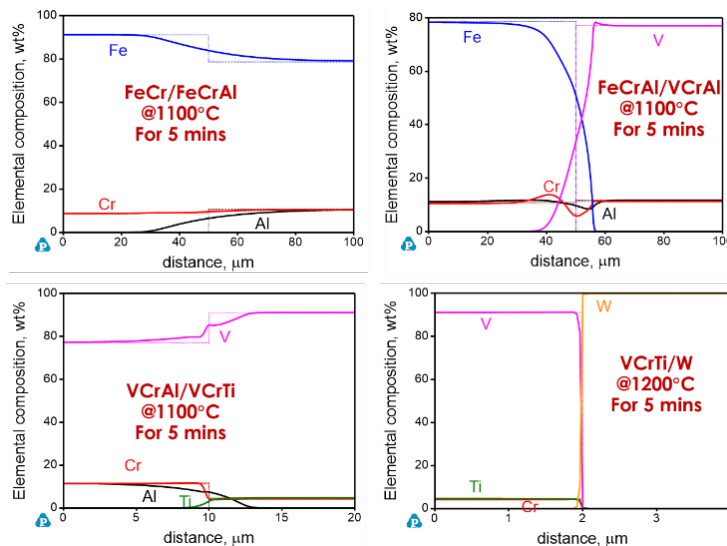


**Figure 70.** Calculated interdiffusion composition profiles at RAFMS/FeCrAl, FeCrAl/VCrAl, VCrAl/VCrTi and VCrTi/W interfaces for given temperature and time.

Microstructural characterization results for an as-sintered multilayer structure are presented and summarized in **Figure 71**. The CNA/FeCrAl interface has a monotonic increase of Al and decrease of Fe with a interdiffusion distance of about ~70~100 μm. This interface is well bonded. The measured composition profile across the diffusion zone is in reasonable agreement with the diffusion simulation. The FeCrAl/VCrAl interface has the bcc matrix phase across the interface. But there are also needle

shaped VC precipitates at the interface. This can be attributed to the higher C content in the FeCrAl layer than in the VCrAl layer. The diffusion distance is about  $\sim 30 \mu\text{m}$ . The VCrAl/VCrTi interface has a diffusion distance between 5 to 10  $\mu\text{m}$ . (V,Ti) carbides were observed on the VCrTi alloy side. The source of C is unclear, which may suggest some carbon contamination during SPS processing. For the V44/W interface, some areas were well bonded, but some areas clearly show gaps. Two factors may contribute to the nonuniform bonding of V44, first is the surface roughness, and second is the slow diffusion of elements in W and W in V. For the area with a good bond, the composition profiles show the interdiffusion distance is around 5  $\mu\text{m}$ , while the diffusion simulation showed this distance to be no more than one half  $\mu\text{m}$ . Additional work is needed to explain the discrepancy.

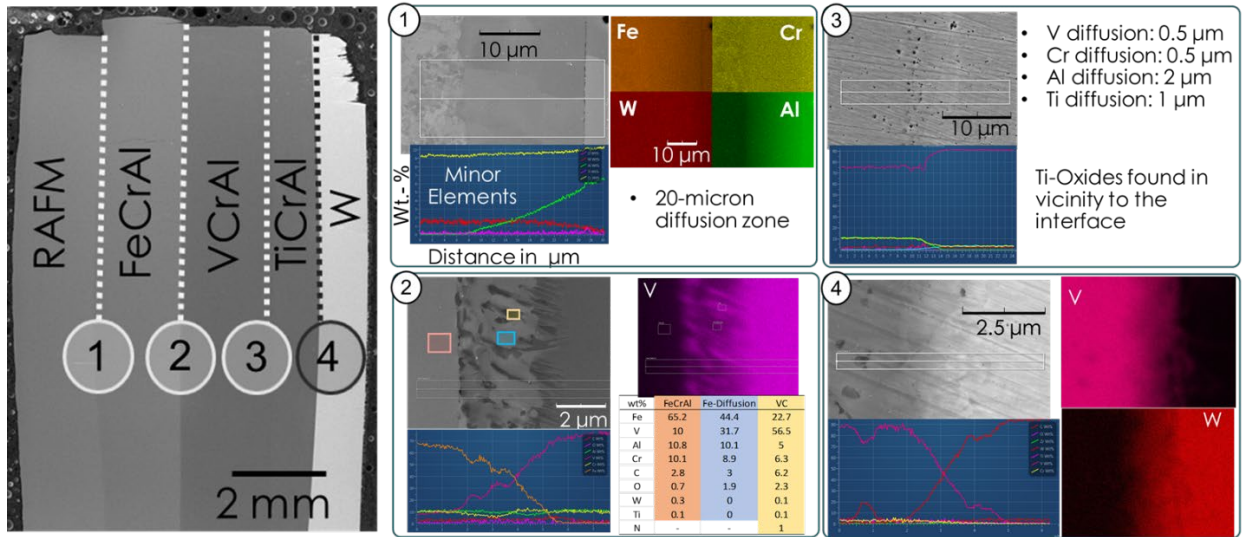


**Figure 71. Microstructural characterization of interfaces in an as-sintered multilayer structure.**

**Future Work**

Future work will include diffusion studies of the SPS-bonded multilayer structure and application of other techniques such as additive manufacturing to fabricate the designed multilayer structure into complex components for fusion Plasma-Facing Components.

### 9.3 BENCHMARKING ADDITIVE MANUFACTURING OF A 9Cr-2WVTa STEEL

T. Graening ([graeningt@ornl.gov](mailto:graeningt@ornl.gov)), and Niyanth Sridharan

#### OBJECTIVE

Additive manufacturing (AM) can offer a unique layer-by-layer deposition strategy to come up with a temper bead deposition techniques to eliminate post-processing heat treatments (PPHT). However, it is necessary to benchmark the properties of reduced activation ferritic-martensitic (RAFM) steels fabricated by AM and compare with wrought counterparts to identify the process-structure-properties correlations. The benchmarking is the goal of this study.

#### SUMMARY

The RAFM steel developed at Oak Ridge National Laboratory was deposited using laser blown powder additive manufacturing (LAM). Detailed mechanical and microstructural characterizations were performed. Tensile properties at room temperature and high temperatures are satisfactory, but the as-fabricated and PPHT samples show significant variability in tensile elongation. This scatter is attributed to the presence of defects developed during the build. Characterization of microstructure at various length scales shows that the as-fabricated structure has a significant fraction of delta ferrite in a lath martensitic matrix. No precipitates could be identified in the as fabricated structure. The PPHT resulted in a decrease in the delta ferrite and promoted precipitation of  $M_{23}C_6$  and MX phases. Higher normalization temperatures and shorter tempering times led to the smallest precipitates with the highest number density. This knowledge should be applied and implemented in future LAM processes.

#### PROGRESS AND STATUS

Four samples approximately 30x30x10 mm were manufactured using LAM techniques. Three of the four samples were annealed to investigate the impact of typical heat treatments used for EUROFER and CNA steels on the microstructure of AM steels. An additional shorter experimental heat treatment was included for comparison. Optical microscopy, scanning electron and transmission electron microscopy (SEM and TEM, respectively) were used to investigate the as-printed and heat-treated conditions. Electron backscattered diffraction inverse pole figure maps in combination with kernel average misorientation maps were utilized to identify delta ferrite phases. Tensile tests were performed at room and elevated temperatures. Chromium-rich and vanadium-rich precipitates were identified via energy-dispersive X-ray spectroscopy and identify by high resolution TEM as  $M_{23}C_6$  and MX phases, as shown in **Figure 72**. Delta ferrite area fractions, martensite lath sizes, precipitates sizes, and precipitate number densities for  $M_{23}C_6$  and MX phases were evaluated and are plotted in **Figure 73**. It is clear that the low normalization temperature of a EUROFER heat treatment (HT-1) does not dissolve  $M_{23}C_6$  precipitates but promotes their growth whereas the higher CNA-like (HT-2) and shorter experimental heat treatment (HT-3) dissolved all precipitates during normalization. Precipitate formation occurred during subsequent tempering. Reduced tempering times resulted in smaller precipitates with an increased number density.

A manuscript has been published - T. Gräning, N. Sridharan, "Benchmarking a 9Cr-2WVTa Reduced Activation Ferritic Martensitic Steel Fabricated via Additive Manufacturing," *Metals* 12 (2022) 342. <https://doi.org/10.3390/met12020342>".

**Future Work**

Additive manufacturing of CNA will be further evaluated and is part of the ongoing ARPA-E GAMOW project of the GAP/3T team.

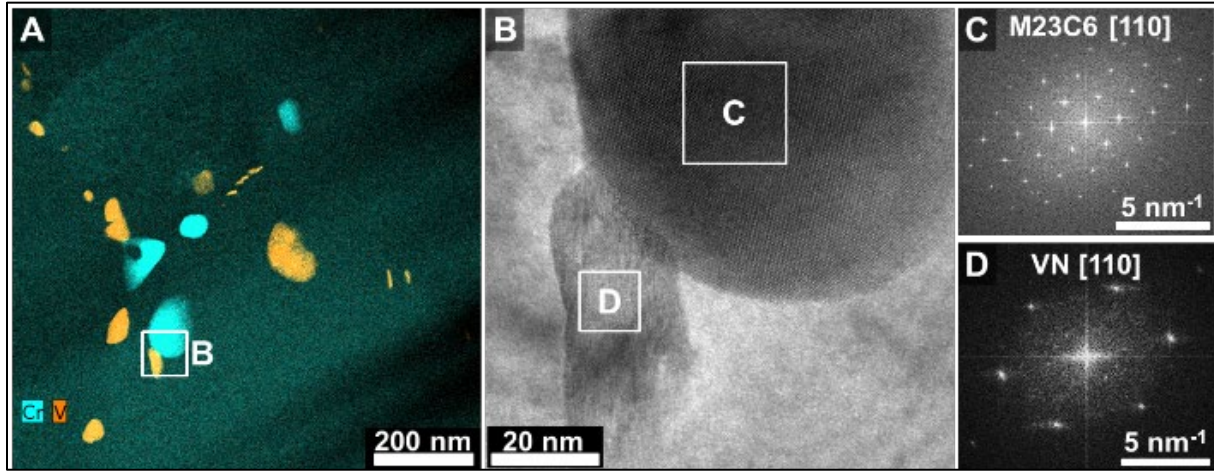


**Figure 72. STEM-EDX map and corresponding HR-TEM image and FFTs of V-rich MX and Cr-rich M<sub>23</sub>C<sub>6</sub>.**

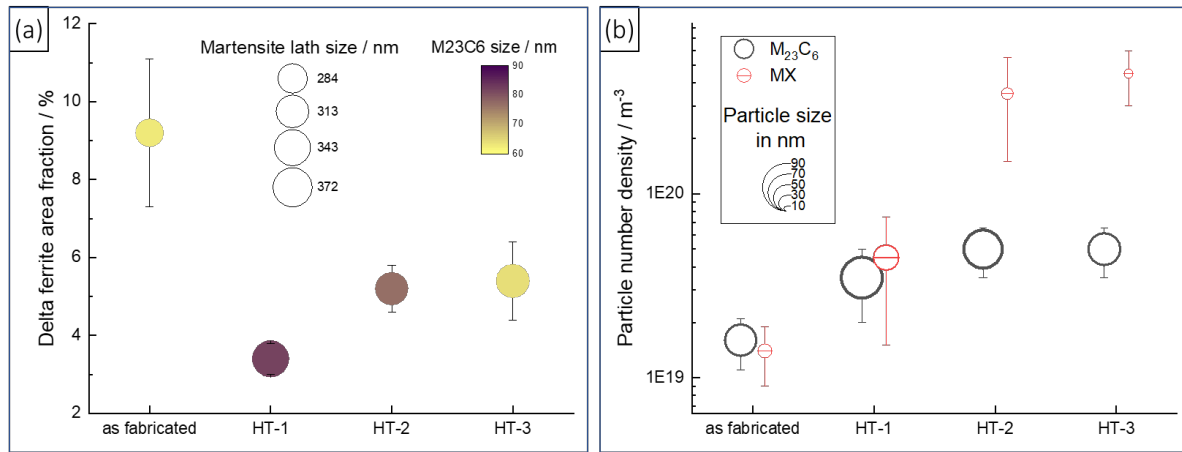


**Figure 73. (a) Delta ferrite area fraction, martensite lath size and M<sub>23</sub>C<sub>6</sub> sizes plotted for the different heat treatments; (b) Particle number density and particle sizes of MX and M<sub>23</sub>C<sub>6</sub> precipitates are plotted for all conditions.**

## 9.4 ADDITIVE MANUFACTURING OF SILICON CARBIDE FOR FUSION APPLICATIONS

T. Koyanagi ([koyangit@ornl.gov](mailto:koyangit@ornl.gov)), and Y. Katoh

### OBJECTIVE

The goal of this task is to develop the additive manufacturing (AM) technology for SiC ceramics for potential use in fusion reactors.

### SUMMARY

The AM of SiC is a rapidly evolving technology being applied or considered for a wide variety of applications. We provided the first evaluated review and general guidance on the development of additively manufactured SiC materials that are resistant to irradiation damage, with the details published in the *Journal of Nuclear Materials* 543 (2021) 152577.

### PROGRESS AND STATUS

Irradiation resistance is a demanding requirement for nuclear core structures, whether in fusion or fission systems. The different feedstocks selected, and manufacturing routes used in AM of SiC result in different component microstructures and consequently affect the response to neutron irradiation. Although irradiation studies of AM SiC are rare, it is possible to predict the behavior using the accumulated knowledge established for bulk SiC materials fabricated by traditional methods.

Dimensional instability under neutron irradiation is generally one of the lifetime-limiting factors for nuclear materials. **Figure 74** summarizes irradiation-induced volumetric change trends in various SiC materials relevant to the matrix densification in AM of SiC. Irradiation temperatures ranged between 260°C and 1300°C, which are above the threshold temperature for irradiation-induced amorphization of SiC. A clear dimensional stability trend is seen for this wide range of irradiation temperatures. SiC consisting mainly of crystalline SiC grains undergoes swelling; amorphous-like SiC shrinks. Such shrinkage is associated with irradiation-induced structural modifications involving SiC crystal growth from the amorphous silicon(oxy)carbide phase. Other than the significant volume shrinkage, relatively limited data on dimensional instability under different conditions make prediction of the behavior difficult. Therefore, the use of amorphous-like ceramics made from pre-ceramic polymers is likely to introduce challenges related to dimensional stability in a fusion reactor application, so more crystalline forms of the material are recommended.

The effect of neutron irradiation on strength of SiC is also critically important for fusion applications. **Figure 75** shows irradiated strength normalized to unirradiated values for various SiC materials. Independent of the irradiation condition, the strength of high-purity chemical vapor deposited (CVD) SiC did not undergo notable degradation up to ~30 dpa. Degradation of the strength due to irradiation is also insignificant up to ~10 dpa when limited secondary phases are present (e.g., in liquid phase sintered (LPS) SiC with oxide phases, and Tyranno SA and Hi-Nicalon S SiC fibers with free carbon). However, degradation was consistently reported for reaction-sintered SiC containing free silicon phases even at the low damage level of 0.1 dpa. That material usually contained segregated silicon surrounding SiC grains. The cause of degradation was shown to be spontaneous cracking as a result of differential swelling between SiC and silicon grains. This was a significant issue for reaction-sintered SiC, with an observed strength decrease of ~60%.

To summarize, a crystalline SiC system with minimal secondary phases is recommended for AM SiC processing to yield material for service in moderate or high fusion neutron flux components.

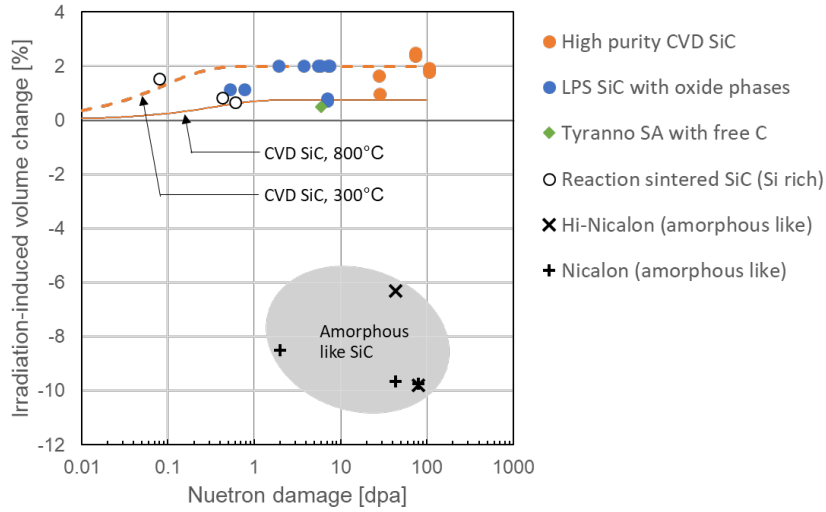


**Figure 74. Irradiation-induced volume changes in various SiC ceramics.**

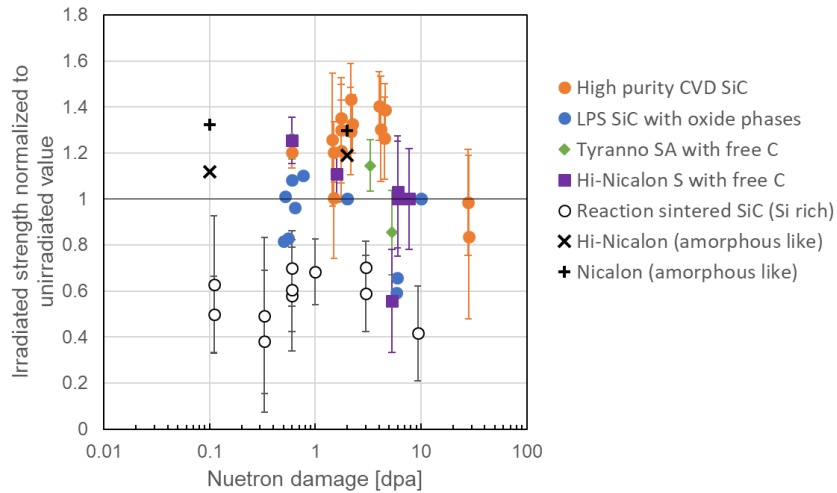


**Figure 75. Strength of irradiated SiC ceramics relative to strengths of unirradiated materials.**

**Future Work**

Further development of AM processing of SiC based on the guidance presented in this report will be conducted in the next year.

## 9.5 SOLID-STATE BREEDER MATERIALS BY ADDITIVE MANUFACTURING

Philip D Edmondson ([edmondsonpd@ornl.com](mailto:edmondsonpd@ornl.com)), and David Sprouster (Stony Brook University)

### OBJECTIVE

The objective of this task is to manufacture breeder materials using additive manufacturing routes, with the potential to offer higher Li volumetric loading with acceptable tritium permeation.

### SUMMARY

Current breeder blanket designs use pebble bed concepts with packing fraction of ~74%. Here, we are exploring the development and application of additive manufacturing techniques to build solid structures of  $\text{Li}_2\text{TiO}_3$  with improved volumetric loading of Li.

We will use the additive manufacturing technique of binder jet printing that uses a powder slurry and a liquid binder. We have procured the powder and are performing detailed microstructural characterization of the powder and a solid bulk comparative material to establish the starting variances. Through the build process, we will characterize the manufactured material to establish: 1) if the build is suitable for the application in the as-built form; 2) if post-processing is required and if there are any changes to the microstructure; and 3) if the use of a liquid binder results in any effect on the Li loading of the material.

### PROGRESS AND STATUS

Detailed microstructural analysis of the initial powder and bulk material has been conducted. Both materials were supplied by Praxair Ltd., with the powdered material prepared using spray granulation followed by sintering.

Scanning Electron Microscope (SEM) secondary electron (SE) micrographs of the powder, along with the size distributions as measured from the SEM SE images are presented in **Figure 76**, with higher magnification micrograph shown in **Figure 77**. From these data, the size distribution of powder particles was determined to be of the correct range for the binder jet printing process. Furthermore, the surfaces of the particles were found to be rough with a texture similar to nano tendrils.

Results of X-ray diffraction (XRD) analysis of both the bulk and powdered specimens at Brookhaven National Laboratory's SNLS-II, are presented in **Figure 78**. This revealed that both materials were monoclinic  $\beta$ -phase with the space group  $C2/c$  consistent with previous studies. Further processing to determine the pair distribution functions (PDFs) of the two materials revealed subtle changes in the short-range ordering. This suggests a loss of long-range order in the powdered material compared to the bulk, indicating a change in the unit cell, consistent with the loss of elements from specific lattice sites. More examination is required to determine the cause of this shifting of the correlation peaks in the PDF.

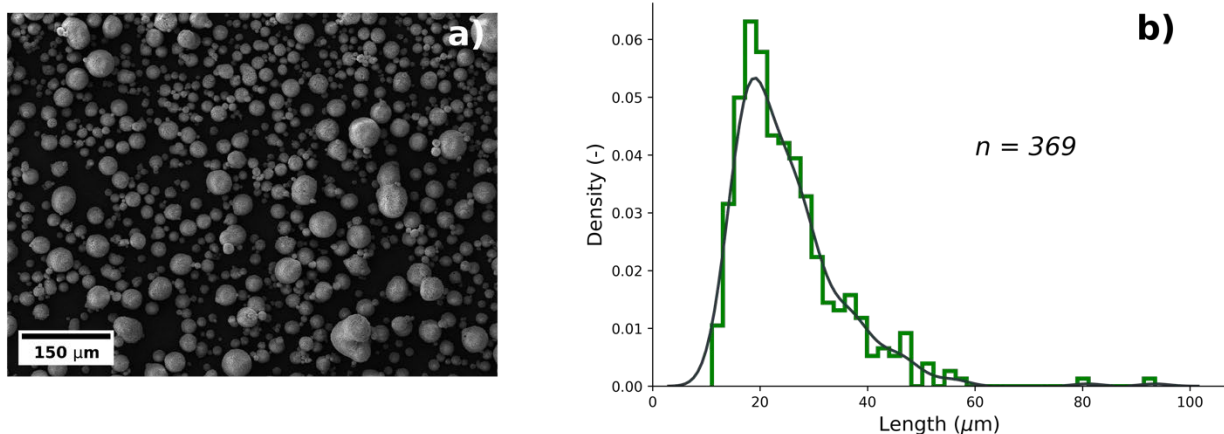


**Figure 76. a) SEM SE micrograph showing powder particles distributed on a carbon sticky pad. b) powder particle size distribution as determined from the micrograph.**

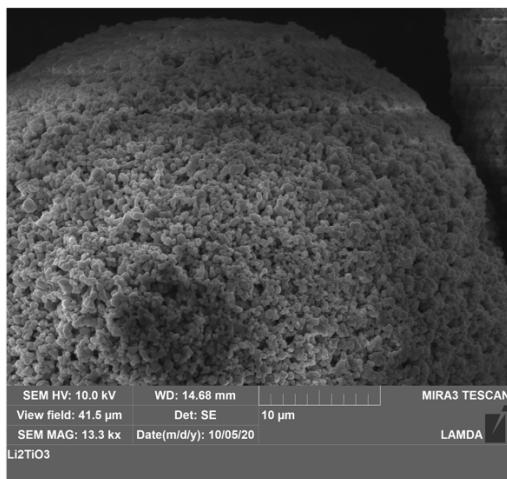


**Figure 77. Higher magnification SEM SE micrograph showing surface topography of a typical powder particle.**

In addition to characterization of the pre-build material, we have attempted to print a structure using the binder jet process, **Figure 79**. On this first attempt, the build did not appear to consolidate sufficiently, and the structure disintegrated. The underlying reason for this failure is unknown but is thought to arise from the use of a degraded binder liquid. A button-size slurry of the powder and a fresh binder solution were created and appeared to consolidate sufficiently but as yet no new build has been created.

In addition to the binder jet printing, a technique known as direct-write AM has been discussed and will be explored further to determine if this is a viable option to binder jet printing. With both printing techniques, the as-printed and post-processed materials will be evaluated for the impact of the processing on the Li loading to establish if AM is a viable route for Li ceramic breeder components.

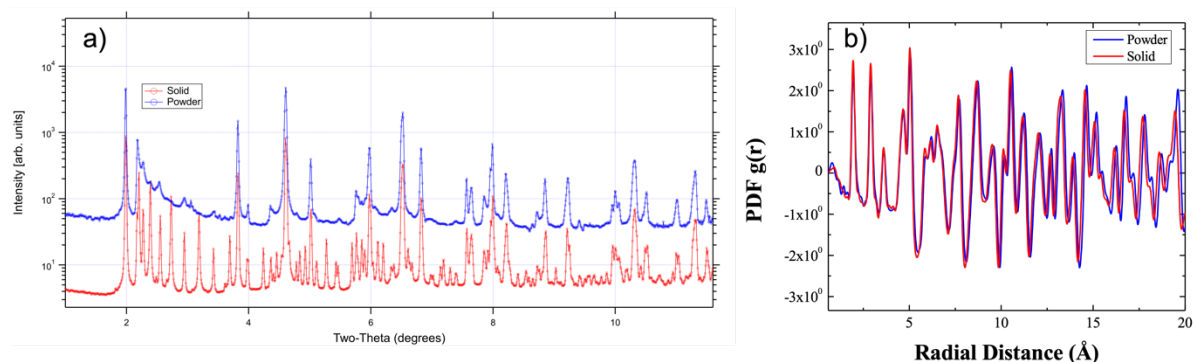


**Figure 78.** XRD results a) from both materials showing same structure and phase; b) pair distribution function showing evidence of loss of short-range ordering in the powder compared to the bulk.



**Figure 79.** Photograph showing the results from the first attempt of binder jet print at ORNL. The resultant material was not adequately consolidated.

### Future Work

Additional efforts will explore the additive manufacturing. This will include outsourcing the AM process to a third party to ensure a more rapid turnaround of build attempts. We aim to have a monolithic component built using either of the above-mentioned techniques and to explore the post-build processing required to maximize volumetric Li loading. It may also be desired to extend the candidate materials to be used for the AM efforts to include  $\text{Li}_2\text{ZrO}_3$  – another potential solid-state breeder material. Given that the zirconate has the same crystal structure as the titanate, the effect of chemistry may be studied and understood prior to exploration of other compositions such as  $\text{Li}_8\text{PbO}_3$ .

## 10. COMPUTATIONAL MATERIALS SCIENCE

### 10.1 MECHANICAL PROPERTIES AND RADIATION EFFECTS IN FUSION MATERIALS

Y. Osetskiy ([osetskiy@ornl.gov](mailto:osetskiy@ornl.gov)), and G. Samolyuk

#### OBJECTIVE

The objective of this task is to obtain a better understanding of the atomic-scale mechanisms operating in fusion materials. Two main groups of effects are under consideration: mechanisms of radiation damage and properties of irradiated materials. Main materials studied are ferritic steels and tungsten-based alloys.

#### SUMMARY

Experimental data show that accumulation of rhenium (Re) and osmium (Os) from transmutation reactions severely affect the microstructural evolution and property degradation of W-based materials under neutron irradiation. Theory and modeling have shown that Re atom transport in W is by irradiation-produced migrating self-interstitial atoms. This research shows the effect of small coherent Re-rich precipitates on the dislocation glide under stress, investigated using the molecular dynamics approach with empirical interatomic potentials. The modeling results are compared with an earlier simulation of void hardening in W and an analytical expression is developed for the obstacle strength parameter  $\alpha$  used in the dispersed-barrier hardening model.

#### PROGRESS AND STATUS

The stress-strain dependence of the interaction of edge dislocation with coherent 100 at.% Re precipitates of different size in W at 300K is shown in **Figure 80**, in which the legend includes the critical resolved shear stress (CRSS) calculated for each precipitate size. As expected, the CRSS increases with the precipitate size. The interaction is of the Orowan-type and at the CRSS the dislocation bows out of the precipitates with zero angle between dislocation segments, thus creating a dipole of parallel screw segments.

Atomistic modeling results obtained here can be fitted to the expression obtained from continuum modeling by Bacon, Kocks, and Scattergood (BKS) [1,2].

$$CRSS = A \frac{\mu b}{L} \left[ \ln(D_{prpt}^{-1} + L^{-1})^{-1} + B \right] \quad (1)$$

were  $A = 1/2\pi$  and  $A = 1/2\pi(1 - \nu)$  for edge and screw dislocations, respectively, and  $\nu$  is the Poisson ratio ( $\nu=0.282$  at 300K). The parameter  $B$  in eq. (1) characterizes interaction between the dislocation and matrix-obstacle interface. **Figure 81** presents all results for 300K compared with the results for voids studied in ref. [3] at the same conditions, and eq. (1) for edge and screw dislocations. The 50 at.% Re-50 at.% W precipitates are the weakest obstacles and can be described quite well by eq. (1) for the edge dislocation with  $B = -1.15$  (green line in **Figure 81**). Interactions between voids and edge dislocation are well described by eq. (1) for screw dislocation with  $B = -0.68$  [3] (black line in **Figure 81**). The 100 at.% Re precipitates demonstrate even stronger size dependence and to fit their data  $B = -1.15$  and an additional coefficient 1.3 should be added to eq. (1) for screw dislocation, as indicated in **Figure 81** by the red line.

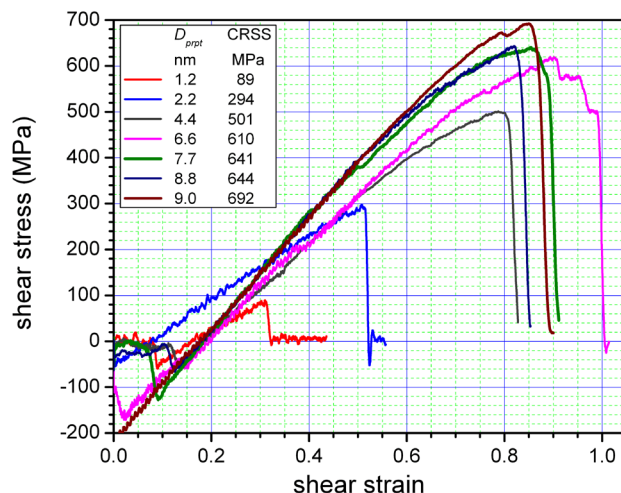


**Figure 80.** Stress-strain dependence of an  $\frac{1}{2}\langle 111 \rangle \{110\}$  edge dislocation passing through the center of spherical 100 at.% Re coherent bcc precipitates of different sizes at 300K. The maximum stress on each curve is the corresponding critical resolved shear stress (CRSS) and is shown in the plot insert.

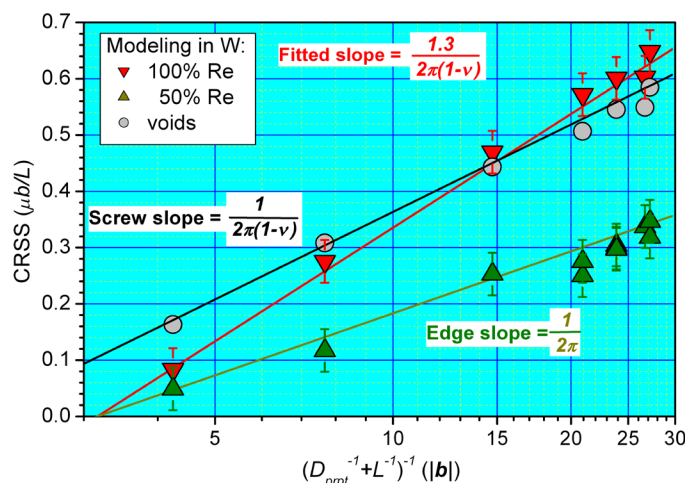


**Figure 81.** Calculated CRSS of all precipitates modeled in this work and voids in W from [3] for the ambient temperature of 300K treated within the BSK model [1, 2].

The data presented in **Figure 81** are used to calculate strength parameters for the widely used dispersed-barrier hardening (DBH) model that describes CRSS increase from localized obstacles with a density  $N$  and a mean diameter  $D$ :

$$CRSS = M\alpha\mu b\sqrt{ND}, \quad (2)$$

where,  $M$  is the Taylor factor that we omit here for simplicity and  $\alpha$  is the obstacle strength parameter. Here  $1/\sqrt{ND}$  is an estimation of the mean distance between obstacles, which, in the current approach, is

equal exactly to the modeled dislocation segment length  $L$ . Combining eq. (1) and (2) and considering the case of reasonably low obstacle density,  $L \gg D$ , one can get the expression for the strength parameter:

$$\alpha = A[\ln(D) + B] \quad (3)$$

**Table 12** presents the expressions for calculating the strength parameter for different obstacles and particular values of  $\alpha$  calculated for the relevant sizes. This shows that the obstacle strength is size dependent, which is usually not considered. The logarithmic dependence on the obstacle diameter is not a strong function, however,  $\alpha$  increases by >3 times when the obstacle diameter changes from 2 nm to 20 nm. This might induce quite a significant difference to the strengthening compared with estimations using the size-independent  $\alpha$ .

**Table 12. Expressions for estimating the obstacle strength parameter  $\alpha$  for Re precipitates and voids, and particular values of  $\alpha$  for obstacles of different diameters. The core radius of the  $\frac{1}{2}\langle 111 \rangle$  dislocation is taken as its Burgers vector length in W at T=300K:  $r_0=|b|=0.273\text{nm}$ .**

obstacle	$\alpha$	2 nm	5 nm	10 nm	20 nm
50at.% Re	$0.159[\ln(D_{prpt}/r_0) - 1.15]$	0.13	0.28	0.39	0.50
Void	$0.221[\ln(D_{void}/r_0) - 0.68]$	0.29	0.49	0.65	0.80
100at.% Re	$0.287[\ln(D_{prpt}/r_0) - 1.15]$	0.24	0.50	0.70	0.90

### References

- [1.] D.J. Bacon, U.F. Kocks, R.O. Scattergood. The effect of dislocation self-interaction on the Orowan stress, *Philos. Mag.* 28 (1973) 1241.
- [2.] R.O. Scattergood, D.J. Bacon. The strengthening effect of voids, *Acta Metall.* 30 (1982) 1665.
- [3.] Y. Osetsky, Strengthening of tungsten by coherent rhenium precipitates formed during low fluence irradiation, *Tungsten*, 33 (2021) DOI: [10.1007/s42864-021-00088-4](https://doi.org/10.1007/s42864-021-00088-4).

## 10.2 STUDY OF DEFECT DIFFUSION PROPERTIES IN TUNGSTEN-BASED ALLOYS

Y. Osetskiy ([osetskiyyn@ornl.gov](mailto:osetskiyyn@ornl.gov)), and G. Samolyuk

### OBJECTIVE

The purpose of this research is to understand defect and atomic transport in W-based alloys under irradiation conditions. We use classical atomistic molecular dynamics and *ab initio* density functional theory (DFT) based molecular dynamics (MD) to study dynamic properties of point defects and clusters, atomic transport due to defects diffusion, segregation and precipitation in W-Re-Os system.

### SUMMARY

Diffusion of interstitial atoms was modeled for W and W-Re alloys. The suggestion in the literature of fast non-dissociative transport of Re atoms by an interstitial mechanism was not confirmed. Instead, unprecedentedly long-run-time DFT MD modeling has unambiguously demonstrated that Re transport occurs via a dissociative mechanism that is controlled by the Re-interstitial binding energy. Re significantly decelerates interstitial atom diffusion and its migration occurred only via a random dissociation of Re-interstitial complexes. This result significantly changes the accepted understanding of radiation damage evolution in W-Re alloys.

### PROGRESS AND STATUS

The main modeling work is completed, and a large database of accumulated raw results is under treatment. The treatment includes analysis of instant defect configurations, their statistics and revealing the governing mechanisms. An example of such treatment is presented in **Figure 82**. **Figure 82a** shows the temporal evolution of the distance between the interstitial defect (dumbbell or crowdion) center and a Re atom (blue line). It can be seen that most of the time the W-W dumbbell and Re atom are separated by more than two jump distances ( $d_{nn} = \frac{\sqrt{3}}{2}a$  – nearest neighbor distance in bcc lattice, “a” is the lattice parameter). This means that the Re-interstitial complex dissociates. The green line indicates the instant interstitial atom configuration: “0” means it is a  $\frac{1}{2}\langle 110 \rangle$  dumbbell whereas “1” means that is a  $\frac{1}{2}\langle 111 \rangle$  crowdion. Note that our and earlier DFT calculations defined the ground state interstitial configuration in pure W was  $\frac{1}{2}\langle 111 \rangle$  crowdion, whereas a Re atom enhances formation of a mixed Re-W  $\frac{1}{2}\langle 110 \rangle$  dumbbell. Therefore, when the interstitial defect is complexed with a Re atom it spends its time mainly in a  $\frac{1}{2}\langle 110 \rangle$  dumbbell configuration. When an interstitial is dissociated from the Re atom it travels as the W  $\frac{1}{2}\langle 111 \rangle$  crowdion. **Figure 82b** shows the temporal evolution of the distance between the initial,  $d_0$ , and instant,  $d_i$ , positions of the interstitial defect (dumbbell or crowdion) center (red line) and the Re atom (blue line). It can be seen that the maximum displacement of the Re atom is about three jumps whereas the interstitial passes through the box boundaries several times. This is additional clear evidence of the dissociative mechanism. The temporal evolution of the mean square displacement distances of W (blue line) and Re (red line) atoms are presented in **Figure 83**, in which the displacements of Re are multiplied by a factor of 10 to aid visualization. Thus, W atoms displacements are accumulated very quickly whereas a Re atom is displaced only over 2-3 jump distances. Intensive accumulation of W displacements is due to free migration of W interstitial via the fast one-dimensional glide of a  $\frac{1}{2}\langle 111 \rangle$  crowdion when it is dissociated from a Re atom.

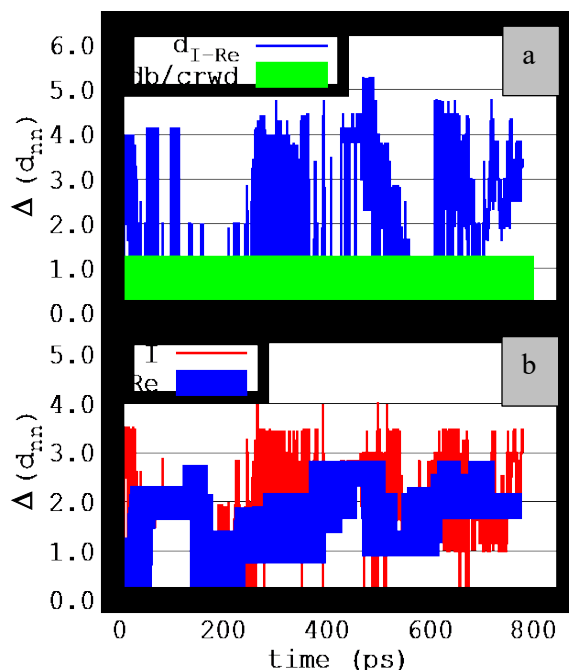


**Figure 82.** Analysis of data generated from the model. a) The temporal evolution of the distance between the interstitial defect (dumbbell or crowdion) center and Re atom (blue line):  $\Delta = d_{int} - d_{Re}$ . The green line indicates the instant interstitial atom configuration: “0” means it is a  $\frac{1}{2}\langle 110 \rangle$  dumbbell whereas “1” means that is a  $\frac{1}{2}\langle 111 \rangle$  crowdion.; b) The temporal evolution of the distance between the initial,  $d_0$ , and instant,  $d_t$ , positions of interstitial defect (dumbbell or crowdion) center (red line) and Re atom (blue line)  $\Delta = d_t - d_0$ .

### Experimental Procedure

The modeling results presented here imply quite different mechanisms governing microstructure evolution under irradiation in pure W and W-Re alloys. This can now be rationalized using the rate theory and kinetic Monte Carlo modeling utilizing the new diffusion mechanisms. The new Re-transport mechanisms are also necessary for predictive modeling of phase stability in W-Re systems under irradiation.

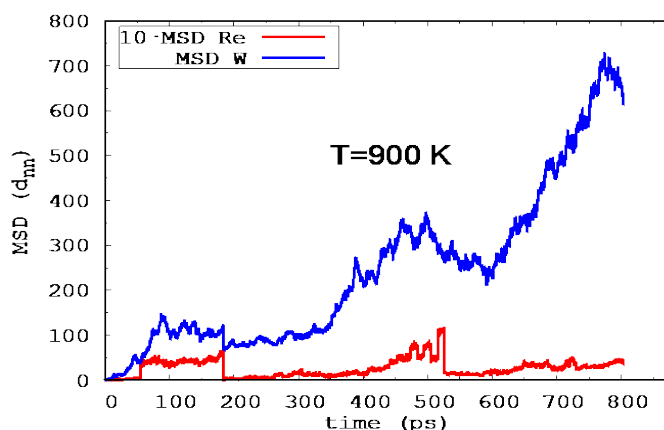


**Figure 83.** Temporal evolution of mean square displacements (MSD) of W (blue line) and Re (red line). Displacements of Re-atom are multiplied by 10 for visualization.

### **Future Work**

Kinetic Monte Carlo modeling of vacancy and interstitial atom diffusion in W-Re alloys and Re-precipitation is currently continuing. This will include DFT-based MD to study fundamental mechanisms of Re diffusion in W-Re alloys and validating interatomic potentials and accumulating data for fitting new interatomic potentials for W-R-Os systems.

## 11. INTERNATIONAL COLLABORATIONS

### 11.1 US-JAPAN (QST) COLLABORATION ON STRUCTURAL MATERIALS

*J.W. Geringer (geringerjw@ornl.gov), A. Bhattacharya, X. Cheng, Y. Katoh (ORNL), T. Nozawa, M. Ando, T. Kato, and H. Tanigawa (QST)*

#### BACKGROUND

This long-standing collaboration between the U.S. DOE and the Japan National Institutes for Quantum and Radiological Science and Technology (QST), jointly pursues activities using the advanced capabilities for materials irradiation and post-irradiated examination at ORNL, especially the HFIR, the hot cells, and LAMDA. The focus is on ferritic steels and other advanced materials, especially the development of the materials database for the design of facilities beyond ITER. The goals include achieving DEMO-relevant performance data on structural materials neutron irradiated in HFIR to high levels of displacement damage.

The DOE-QST collaboration continues to steadily build the materials data bases for the reduced activation ferritic/martensitic (RAFM) alloys that include F82H, ODS and Eurofer97 steels and other materials such as nuclear grade SiC composites and copper alloys. This database is being used by QST to predict changes in mechanical performance of components of a fusion DEMO reactor.

#### PROGRESS AND STATUS

The annual Steering Committee Meeting was hosted by ORNL as a virtual meeting on February 24-26, 2021. The restrictions of the COVID-19 pandemic continued to prevent QST assignees to visit Oak Ridge. However, both parties noted with satisfaction that the steady progress and high productivity of this partnership continued despite the limitations imposed by the COVID restrictions.

During the past year irradiation experiments that continued irradiation in HFIR included rabbit capsules of the F13 series, the JCR series, the SCF series for FSM-P8 and the FMP series. The rabbit capsules with RAFM steels, mainly F82H as well as some SiC specimens, have completed irradiation while other high fluence capsules remain in the reactor. Rabbit capsules with copper alloy variations completed irradiation. The first three capsules of a new rabbit capsule irradiation series, the FH series with F82H alloy variations which targets 5 dpa, completed their irradiation cycles end of HFIR cycle 493. The next set (of the FH series) planned for 80 dpa exposure is scheduled to start irradiation during FY22.

The post-irradiation examination (PIE) completed this past year included hardness measurements, tensile tests, and microstructural analysis of steel and SiC materials. The PIE on specimens from experiment JP28-31, RB-15J, RB-19J is continuing.

Detail reporting on the hardness and tensile measurements can be found in Chapter 2, while those on the design, fabrication and assembly of new rabbit capsules are in Chapter 13 of this report.

#### Future Work

The next QST steering committee meeting was hosted remotely by ORNL during the third week of February 2022. Experimental activities will continue to follow the work plans approved by the steering committee.

## 11.2 US-JAPAN FRONTIER PROGRAM

*J.W. Geringer ([geringerjw@ornl.gov](mailto:geringerjw@ornl.gov)), L. Garrison, B. Pint, C. Kessel, and Y. Katoh*

### BACKGROUND

The US/Japan Fusion Project, FRONTIER (Fusion Research Oriented to Neutron irradiation effects and Tritium behavior at material InterFaces), started in April 2019 has the objective of evaluating Reaction Kinetics and Neutron Irradiation Effects at Interfaces in DEMO Divertor Systems. The FRONTIER consists of four tasks; (1) evaluate irradiation effects on reaction dynamics at plasma-facing material/structural material interfaces, (2) perform tritium transport through interface and reaction dynamics in accidental conditions, (3) measure corrosion dynamics at liquid-solid interfaces under neutron irradiation for liquid divertor concepts and (4) engineering modeling. The project participants include ORNL, INL, SNL, NIFS and Japanese Universities. The ORNL leads tasks 1, 3 and 4.

### PROGRESS AND STATUS

During the FY21 the FRONTIER efforts continued to focus on maturing the bonded or jointed plasma facing materials, the development of irradiation capsules to support the irradiation matrices for the various tasks, the execution of a flowing Sn compatibility test and the examination of a specific liquid lithium, divertor concept that focusses on a LM PFC with flowing liquid metal, to define a more detailed engineering design model.

The second FRONTIER steering committee meeting was held on January 14-15, 2021, as a virtual meeting hosted by Japan. The majority of planned personnel exchanges and workshops were either postponed or held virtually due to the ongoing COVID19 pandemic restrictions. These included at least four virtual workshops held during the second half of the FY21. Three of the meetings, February 17, June 21-22, and August 10 of, 2021 were devoted to discussion of HFIR irradiation plans, including capsule design and fabrication progress for phase I and experimental suggestions for Phase II irradiations. Virtual meetings during FY21 worked out details for the irradiation effects on compatibility experiments in HFIR and related activities (Task 3).

Four rabbit-type HFIR irradiation capsules have been designed for FRONTIER-Phase I. These are designed to contain 3 mm discs, 6 mm discs, fracture toughness bend bars and the Sn-structural material corrosion experiments. All the designs are complete and capsule parts have been procured. All capsules will be assembled once all the specimens have been received. Six of the thirty-one capsules have already completed their scheduled irradiation in HFIR cycle 495. Five of the remaining capsules are assembled and scheduled to start irradiation in HFIR cycle 496.

Progress on the various FRONTIER experiments is reported in other sections, and details of the capsule designs are reported in Chapter 13 of this report.

### Future Work

The third FRONTIER steering committee meeting was held again as a virtual meeting during the first week of February 2022.

### 11.3 US-EUROFUSION PROJECT

*J.W. Geringer (geringerjw@ornl.gov), A. Bhattacharya, T. Graening, Y. Katoh (ORNL), and M. Reith (KIT)*

#### BACKGROUND

The Karlsruhe Institute of Technology (KIT), as a EUROfusion project partner seeks to provide blanket, baseline, design-relevant data and basic material properties evaluation of EUROFER material variants. The ORNL is under contract to assist the Neutron Irradiation and Material Data task by preparation, irradiation and post irradiation examination of these steels to determine their suitability for use in fusion energy systems. This research involves irradiation in HFIR, testing in the Irradiated Materials Examination and Testing (IMET) hot cell facility, and some examination and characterization in ORNL facilities.

#### PROGRESS AND STATUS

Phase I of this contract ended in 2019, but 14 remaining irradiation vehicles (“rabbit” capsules) completed the planned irradiation period in HFIR to reach 20 dpa (~12 cycles) at temperatures ranging between 200 and 400°C. The capsules contain tensile specimens, bend bars, and multipurpose coupons of the Eurofer-97 alloy provided by KIT and the EUROfusion program collaborators.

#### Future Work

Post-irradiation examination of the irradiated Eurofer-97 materials is pending completion and approval of Phase 2 of the contract with KIT and is expected to start during spring of FY22.

## 12. EXPERIMENTAL TECHNIQUES AND LABORATORY SYSTEMS

### 12.1 ADVANCED CHARACTERIZATION

Philip D. Edmondson ([edmondsonpd@ornl.com](mailto:edmondsonpd@ornl.com))

#### OBJECTIVE

The objective of this task is to provide support to the Fusion Materials program through advanced characterization using atom probe tomography (APT) analysis of materials.

#### SUMMARY

To better understand the effects of extreme environments (corrosion, high temperatures, radiation fields, etc.) on the microstructure and properties of materials, it is imperative to conduct examination of the structure and how this is affected and changed by these environments. As we strive to gain insights into the changes of materials at the phenomenological and mechanistic level, the level of characterization increases, and advanced techniques are required to obtain the desired information and understanding.

In this task, APT has been used to characterize materials included in the Fusion Materials program. Specifically, two separate projects are active. First, APT has been used to examine the abundance of specific isotopes in two classes of materials. Second, characterization of a refractory high entropy alloy has been conducted in collaboration with the University of Sheffield (UK).

#### PROGRESS AND STATUS

##### Isotopic abundance

Two classes of materials have been characterized as part of this project – ceramic diborides, and an isotopically-tailored F82H steel variant with Fe enriched in  $^{54}\text{Fe}$ .

The diboride specimen chosen for analysis was an unirradiated  $\text{TiB}_2$  material. The interest in this material from an application standpoint is due to its high temperature capabilities, with exceptional fabricability. However, during neutron irradiation  $^{10}\text{B}$ , 20 percent of natural boron, transmutes to He and Li. In this case APT can be used to accurately determine the extent of  $^{10}\text{B}$  burn-up but in order to do this, significant calibration of the experimental set-up is required. The APT data collection from ceramics typically requires laser pulsing in order to induce field evaporation of the constituent atoms of the material; however, the use of laser pulsing is well known to alter the local chemistry of the material if the laser power is too great. This requires careful choice of the laser power to ensure correct analysis of the compositions (and in turn isotope levels) is conducted.

The results of such a calibration experiment are provided in *Figure 84* in which the region of the mass spectrum from mass-to-charge ratio (m/c), which is also termed ‘Da’, 4 to 12 is shown. This range is selected as it displays both the  $^{10}\text{B}$  and  $^{11}\text{B}$  peaks in the single-charged and double-charged states. These graphs show a clear change in the  $^{10}\text{B}/^{11}\text{B}$  ratios. Field evaporation images were also obtained (not shown) and show that artifacts are also induced for high laser powers.

From this work we conclude that a laser power in the range of 100-150 pJ at a specimen temperature of 50K is appropriate for the collection of data for observation and analysis of  $^{10}\text{B}$  burn-up in neutron-irradiated materials. Similar experiments conducted for ZrC have not yet been fully analyzed.

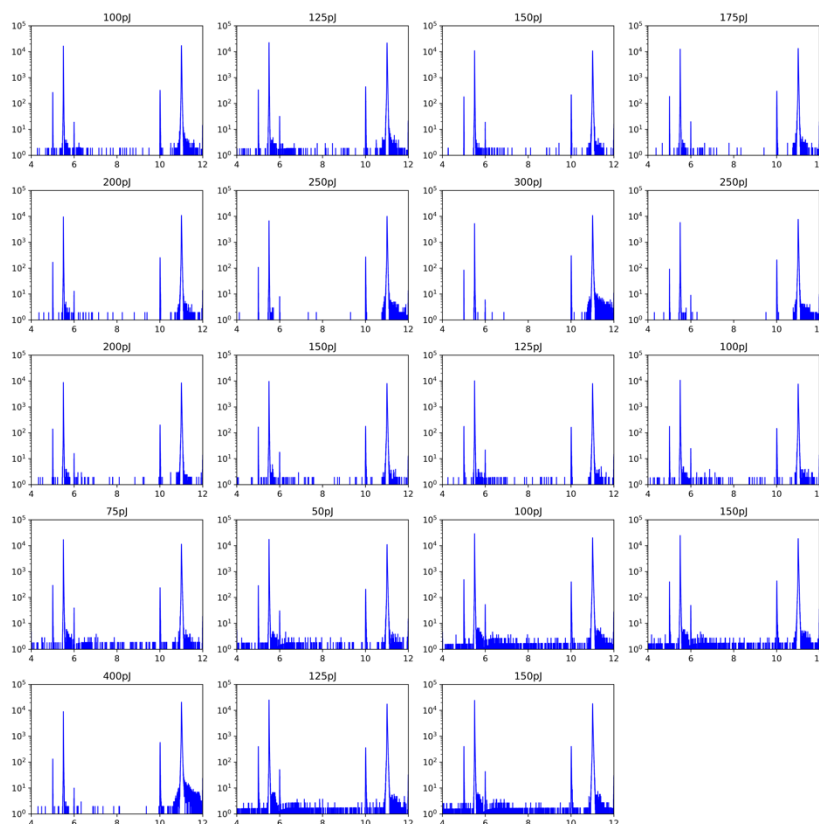


**Figure 84. Mass spectra in the 4-12 m/c (Da) region of a TiB<sub>2</sub> specimen displaying the single and double charged <sup>10/11</sup>B isotopic peaks as a function of laser power during APT data acquisition. A change in the peak ratios is observed.**

The <sup>54</sup>Fe-enriched specimen was nominally based on a F82H composition and irradiated in HFIR as part of the Fusion Materials program. Atom probe tomography was conducted using voltage pulsing mode to determine how the irradiation had altered the <sup>54</sup>Fe isotope abundance through transmutation. The mass spectrum showing the mass-to-charge-state range between 25 and 30 Da (double charge state region for the Fe isotopes) is shown in **Figure 85**. The mass spectrum obtained from the APT is shown as a green line with the natural abundances relative to the peak <sup>56</sup>Fe presented as red circles. There is significant enrichment of the <sup>54</sup>Fe, <sup>57</sup>Fe, and <sup>58</sup>Fe with isotopic overlaps present for the 54 peak (Fe and Cr) and the 58 peak (Fe and Ni).

To fully evaluate the extent of the irradiation induced burn-up of the <sup>54</sup>Fe during this experiment, the non-irradiated material needs to be examined using the same methodologies. As has been performed before when examining W transmutation, analysis informed using neutronic calculations would be beneficial.

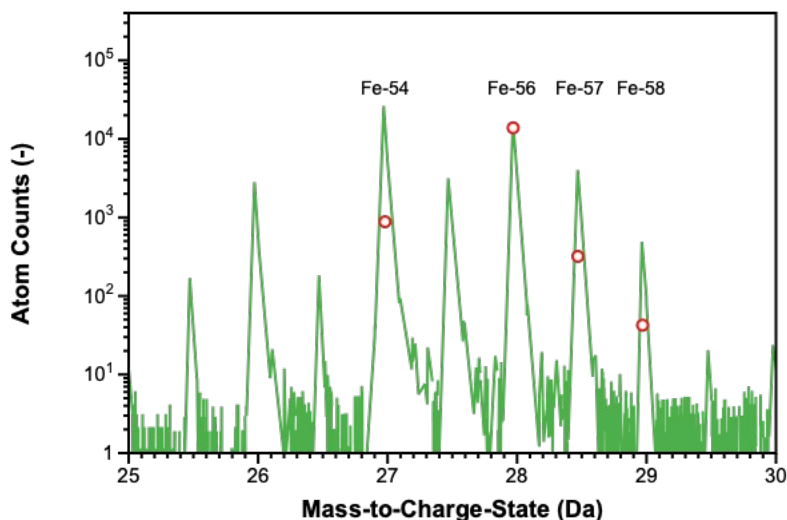


**Figure 85. Mass-to-Charge-State for the range in which the double charge state Fe isotopes lie. The green line shows the data obtained from APT experiments; the red circles shows the relative natural abundances scaled to the  $^{56}\text{Fe}^{2+}$  peak. An excess of  $^{54}\text{Fe}$ ,  $^{57}\text{Fe}$ , and  $^{58}\text{Fe}$  is evident.**

#### Refractory High Entropy Alloy Analysis

High entropy alloys have been proposed for use in nuclear environments due to their anticipated exceptional radiation tolerance. In this project, we have collaborated with researchers at the UK to conduct advanced characterization of a novel refractory high entropy alloy (HEA) with a 30Ta-30V-30Ti-5W-5C (in at.%) composition. This particular HEA may be of relevance to the fusion community due to its high temperature behavior and its low activation components. The resultant atom maps are shown in **Figure 86**. In all maps presented, the elements appear to be in solid solution. There are some features visible in the atom maps (two curved lines with depletion in W and enrichment in Ta) that have resulted from small fractures that occurred during data acquisition. The nominal chemistry was evaluated and showed that the material was lean in C and Ta (0.03 and 11.7 at.% respectively) and enriched in W (14.8 at.%), compared to the bulk composition analysis. The discrepancies in the compositions between the bulk and those derived through APT could be due to the two-phase nature of the specimen. Further work will be needed with data generated from the second phase to determine if the overall material composition is close to the measured bulk composition.

#### **Future Work**

In the isotope examination work, further work will examine the burn-up of the  $^{10}\text{B}$  in the diboride case. In the  $^{54}\text{Fe}$ -enriched F82H variant, analysis of the non-irradiated material will be conducted. Both of these experiments will contribute to a better understanding of how burn-up occurs in these materials. (In both cases, He generation is expected to be significant.) Combined with other property measurements this will allow an improved understanding of property changes during irradiation.

The refractory HEA will be analyzed in more detail. A second sample that has been ion irradiated by our Sheffield colleagues will be analyzed to establish if any decomposition or precipitation occurs during irradiation.

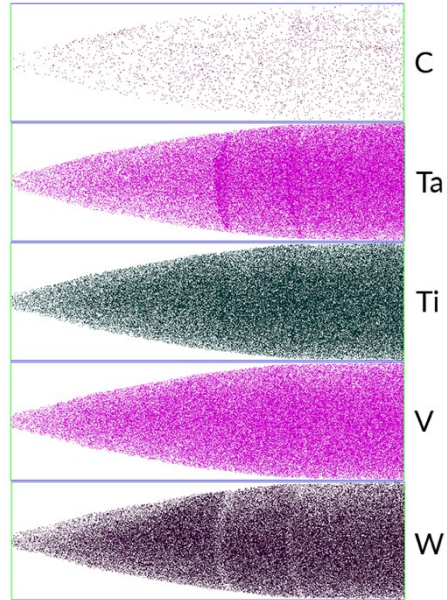


**Figure 86. APT atom maps of the primary elements from the refractory high entropy alloy. A uniform distribution of elements is observed in all cases. Artifacts observed in the Ta and W maps arise from specimen fractures during data acquisition. The length of the reconstruction is 250 nm.**

## 12.2 SMALL SPECIMEN TEST TECHNIQUE (SSTT) DEVELOPMENT: MASTER CURVE FRACTURE TOUGHNESS ROUND ROBIN STUDY

X. Chen ([chenx2@ornl.gov](mailto:chenx2@ornl.gov)), J. Reed, E. Mannes Schmidt, and M. A. Sokolov

### OBJECTIVE

The goal of this task is to develop reliable fracture toughness testing and analysis techniques for small size specimens. Under the framework of the International Atomic Energy Agency (IAEA) Coordinated Research Projects (CRP), the work aims to standardize the fracture toughness test technique for small specimens, which is critical for qualification of materials for fusion reactors.

### SUMMARY

A round robin study of specimen size and geometry effects on the fracture toughness properties of RAFM steels is ongoing among ORNL, Centre for Energy, Environment and Technology (CIEMAT), and UK Atomic Energy Authority (UKAEA), as part of the IAEA Small Specimen Test Technique (SSTT) Project. Based on ORNL results, the ASTM Master Curve (MC) and its tolerance bounds show excellent representation of transition fracture toughness for Eurofer97 batch-3 and F82H-BA12. No specimen size effect was observed in the 0.5T and 4 mm compact specimens on the measured MC reference temperature  $T_{0Q}$  whereas 1.65 mm bend specimens yielded a higher  $T_{0Q}$  (giving more conservative values). The minimum number of specimens needed for each specimen geometry has been defined. Experimental quality control is of critical importance for generating valid MC results..

### PROGRESS AND STATUS

The ORNL is leading the MC Round Robin tests with participation from the CIEMAT and the UKAEA. The materials used in the round-robin project are Eurofer97 batch-3 and F82H-BA12 RAFM steels. The ORNL test matrix included 0.5T compact, 4 mm compact, and 1.65 mm bend bar specimens. The entire test matrix including specimen sizes and geometries has been finalized with the details given in Ref. [1]. A wide variety of specimen sizes and geometries are included, allowing full investigation of the specimen size effect on measured fracture toughness. Although the Round Robin tests are still ongoing at CIEMAT and UKAEA, ORNL has completed the planned test matrix. The initial findings are:

- 1) The ASTM MC and its tolerance bounds show excellent representation of transition fracture toughness for Eurofer97 batch-3 and F82H-BA12. **Figure 87** shows that, except for a few data points from the 1.65 mm bend bar specimen, all valid data are bounded by the MC tolerance bounds and as expected, the MC predicts the medium fracture toughness values.
- 2) Within  $\pm$  one standard deviation ( $\pm 1\sigma$ ), there was no obvious specimen size effect in 0.5T and 4 mm compact specimens for the measured MC reference temperature  $T_{0Q}$ , whereas the 1.65 mm bend specimens yielded a higher  $T_{0Q}$  (a more conservative value) as shown in **Figure 88**.
- 3) We have determined the minimum number of specimens needed for each specimen geometry to yield valid MC results. More details can be found in Ref. [2].
- 4) Experimental quality control is critical for generating valid MC results. **Figure 89** shows one example of the impact of fatigue pre-crack front straightness on measured MC reference temperature. Due to the fatigue frame alignment issue, the first batch of 0.5T compact specimens had a skewed fatigue pre-crack front, and an unrealistically low MC reference temperature (-168°C) was measured from these specimens. After improving the fatigue frame alignment, we obtained a straight fatigue pre-crack front with the second batch of specimens and the measured MC reference temperature (-126°C) was within the expected range.

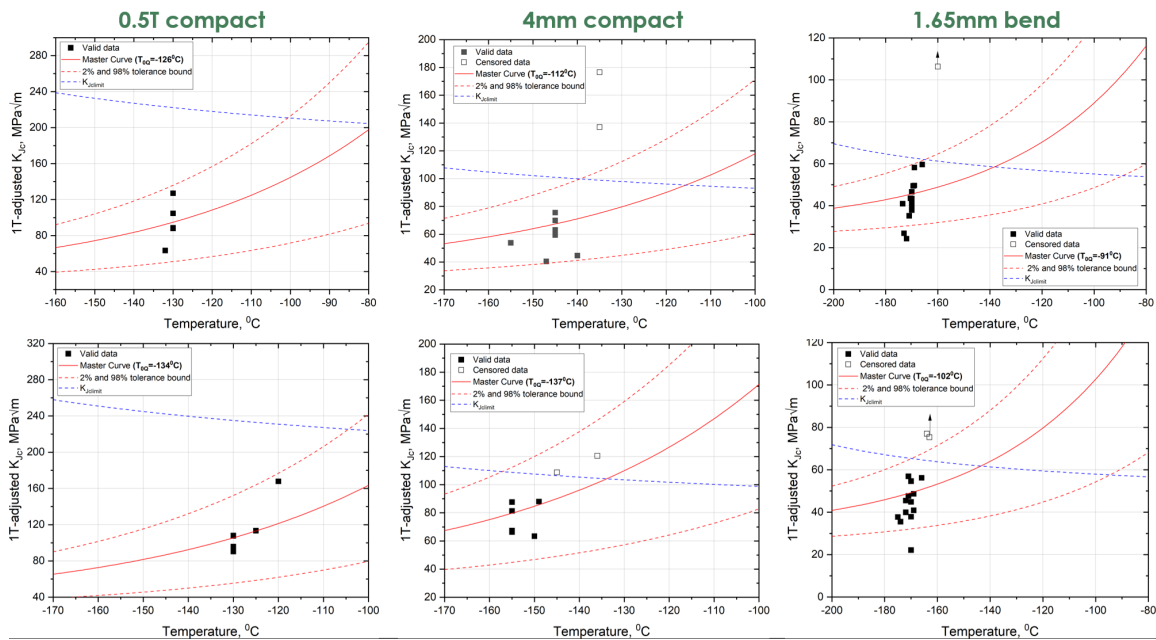


Figure 87. Master Curve test results for Eurofer97 batch-3 in the top row and F82H-BA12 in the bottom row.

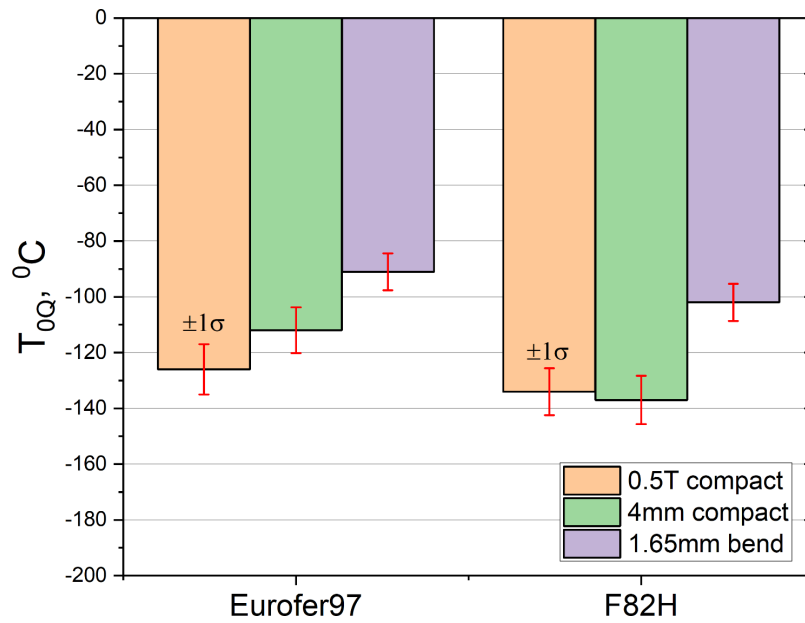
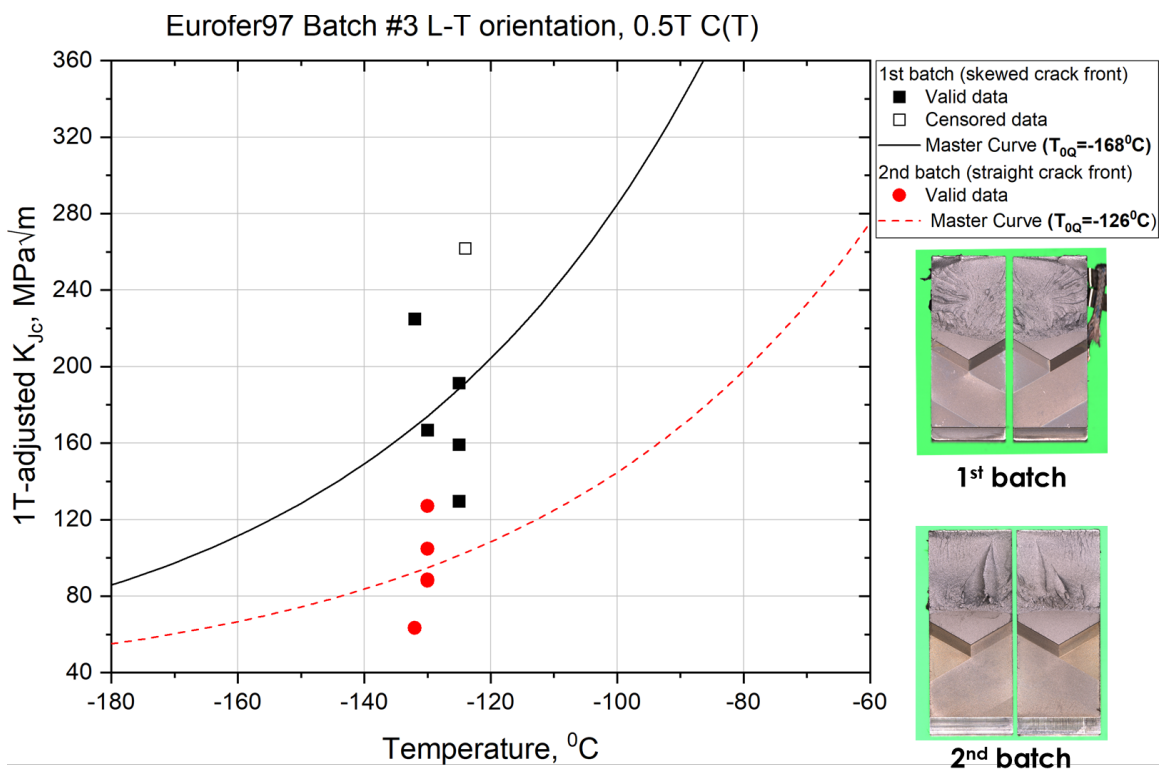


Figure 88. Comparison of measured Master Curve reference temperature  $T_{0Q}$  for Eurofer97 batch-3 and F82H-BA12 tested with three different specimen types. Error bars correspond to  $\pm$  one standard deviation.



**Figure 89. Effect of fatigue pre-crack front straightness on the measured Master Curve reference temperatures.**

**Future Work**

An in-depth analysis of existing results, including the CIEMAT and UKAEA data when available, will be published in the open literature. In addition, we plan to participate the Phase II of the IAEA CRP “Towards the Standardization of SSTT for Fusion Applications” starting in 2022.

**References**

[1] X. Chen et al., “Guidelines for IAEA Small Specimen Test Techniques Master Curve Fracture Toughness Testing”, ORNL/LTR-2020/27, July 2020.  
 [2] IAEA Final Report of the CRP F1.30.17 on “Towards the Standardization of Small Specimen Test Techniques for Fusion Applications”.

### 12.3 MINIATURE MECHANICAL TESTS FOR TUNGSTEN-BASED MATERIALS

L. M. Garrison ([garrisonlm@ornl.gov](mailto:garrisonlm@ornl.gov)), N. Reid, and J. Echols

#### OBJECTIVE

The aim of this work is to develop miniature mechanical test methods that can be used to evaluate neutron-irradiated W and W composite samples in the LAMDA Laboratory.

#### SUMMARY

Three-point bend and shear punch tests will be used to measure mechanical properties of W-based samples loaded in flexural and shear stresses, respectively. Because of simplicity and economy, these tests are suitable to use on irradiated TEM discs. Three-point bend testing is conventionally performed on beams of rectangular cross sections and has been adapted for use with disc specimens at the plane of symmetry in the center of the sample. A fixture has been modeled, designed and procured for testing W samples in LAMDA.

#### PROGRESS AND STATUS

The mechanical properties of fusion materials need to be measured on disc geometry specimens, including the neutron-irradiated 3 mm discs included in the FRONTIER US-Japan collaboration. A three-point bend fixture was designed to determine fracture and ductility of W alloys and composite materials. A shear punch method has also been explored to determine the shear yield and fracture strength of small volumes of material.

Specimens of polycrystalline tungsten (PCW), a silicon carbide composite with a 25  $\mu\text{m}$  thick tungsten foil layer (W-SiC), and 75 wt% W - 25 wt% Cu sintered composite (W-Cu) were tested by three-point bending and shear punch using the MTS Insight Electromechanical Test Frame in LAMDA. The load was measured by a 1 kN load cell from which the flexural and shear stress was calculated. The flexural strain and normalized displacement were calculated from the measured displacement. **Figure 90** shows the stress-strain curves in three-point bending and **Figure 91** shows the stress-displacement curves of a shear punch test. Only the 0.25 mm thick PCW and W-Cu exhibited any room temperature plasticity in bend testing and only W-Cu in shear punch testing. All other specimens were highly brittle at room temperature, probably due to room temperature brittleness of bulk W and thickness effects.

Specimens of 0.5 mm thickness had a span-to-width ratio of 4-to-1 for the span length of 2 mm used. Low span:width ratios promote brittle cleavage fracture, whereas high span:width ratios promote shear slip, ductility, and greater toughness. Thickness effects on PCW are shown in **Figure 92**. The thickness that achieved room temperature ductile fracture in W without exceeding machining and polishing limits was the 0.25 mm thick disc specimens with a ratio of 8:1.

For these W-based samples, even when ductility was observed in the three-point bend test, all of the discs broke in half at the conclusion of the test. SEM micrographs of the fracture surfaces after the three-point bend tests are shown in **Figure 93**. The 0.25 mm thick PCW and W-SiC show signs of brittle cleavage. The PCW shows a clear crack front propagating on the tension side of the disk in the form of a chevron pattern, indicating slip by dislocation motion and ductile fracture. The W-SiC sample was tested with the W layer in tension (and on the bottom of the image) and revealed large, blocky grains in the W. Both the W foil layer and the SiC substrate had brittle cleavage failure. In contrast, the W-Cu fracture surface shows ductile deformation of the Cu around the ridged W grains. For the shear test (**Figure 94**), the disks were imaged on the side that was in contact with the die during the test (opposite side as the punch). The

W-Cu hole was punched out cleanly with the ductility of the Cu matrix creating parabolic shear rupture dimples in the direction of the shear force. This is the fine, rough texture seen inside the cylindrical hole in **Figure 94a**. The PCW die side shows a different behavior in **Figure 94b**. The PCW absorbed the energy of the punch in brittle cracks along weak grain boundaries inside the punch zone, causing the sharp, fragmented pieces to bulge on the die side of the disc.

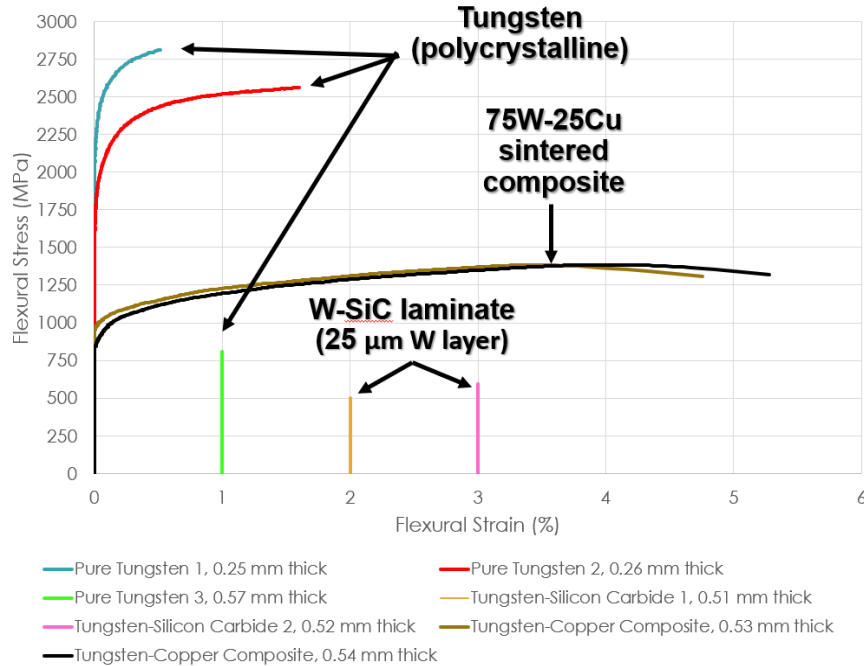


**Figure 90. Bend test results for the 3 mm discs. Specimens were 0.5 mm thick except for polycrystalline tungsten (PCW) that was machined to a thickness of 0.25 mm. Specimens were bent until fracture and the elastic strain is not shown. Only the 0.25 mm thick PC-W and W-Cu showed room temperature plasticity. Tungsten-silicon carbide (W-SiC) fractured in the elastic region for discs of the thicknesses tested.**

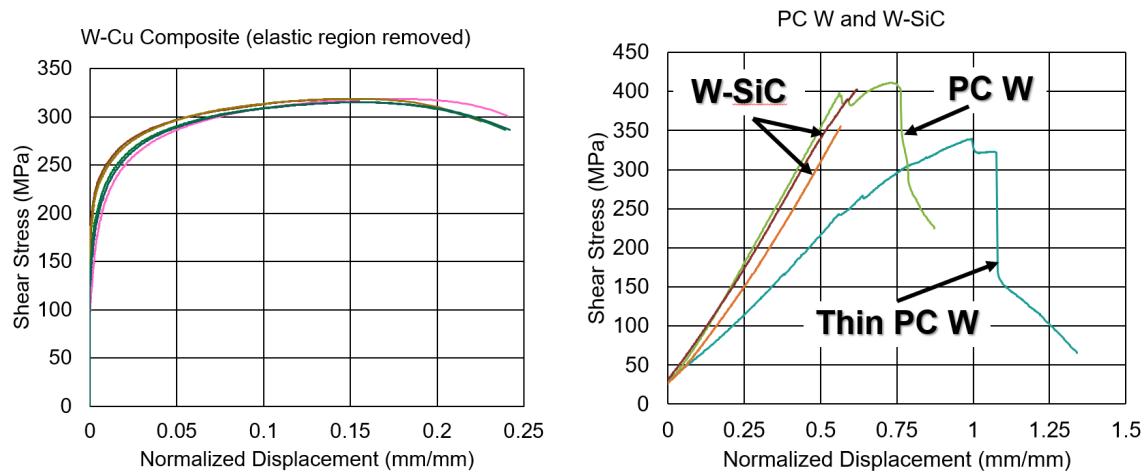


**Figure 91. Shear punch test results for W-Cu shown with the elastic region removed and other specimens with the elastic region shown to best illustrate room temperature brittleness. Five shear punch tests were performed on tabs from W-Cu tensile specimens. The other tests were performed on 0.5 mm thick W-SiC and PCW discs and on a 0.25 mm thick PCW disc.**

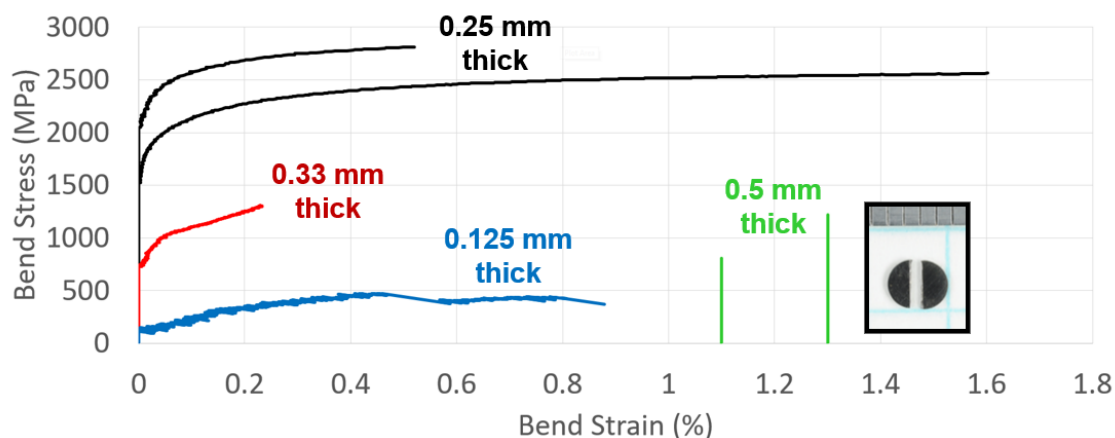


Figure 92. Span-thickness analysis to select the appropriate thickness for room temperature testing W within the specimen size constraints for neutron-irradiated materials. At a 16 to 1 ratio (blue), the load measurement was near the limits of the load cell sensitivity. Additionally, the preloading due to the weight of load train parts caused the bend stress calculation to be artificially low by 220 MPa. The sample with the 8 to 1 ratio (black) showed the most plasticity consistent with the ductile fracture surface. At a 6 to 1 ratio (red), curve was closer in strength value to the brittle fracture stress for the 4 to 1 ratio sample and exhibited little plasticity. All W specimens at a ratio of 4 to 1 showed brittle fracture, with Weibull statistic deviations in flexural strength.

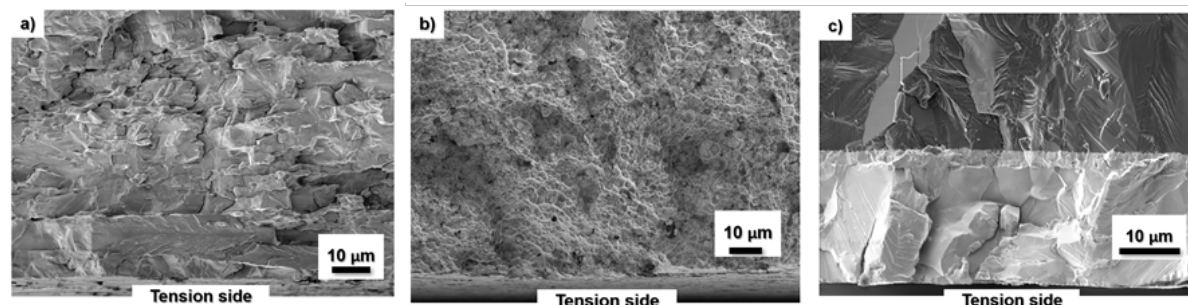
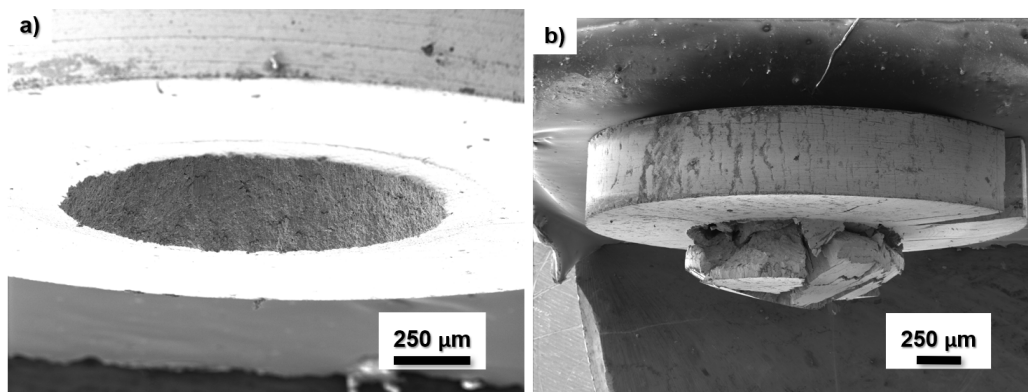
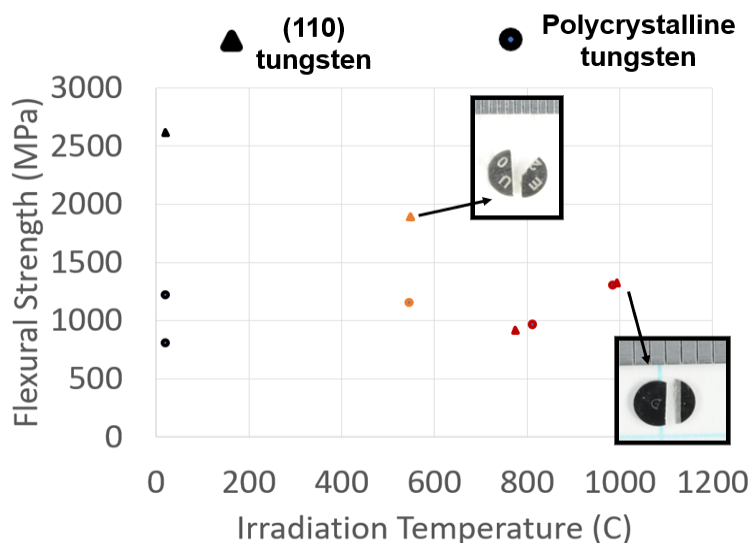


Figure 93. Fracture surfaces are oriented so the side that was in tension during the 3-point bend test is shown on the lower edge of each image. The a) PCW and b) W-Cu composite have indications of ductile-like fracture. The c) W-SiC composite image displays the secondary electron (SE) contrast between the darker SiC and brighter W. This material exhibited brittle failure.



**Figure 94. SEM SE images of the die side of the discs (opposite of the side the punch acted on) after shear punch testing. a) The punch cleanly removed a cylindrical section from the W-Cu sample. On the inside walls of the hole, vertical striations are seen because of the ductility of the Cu. b) The PCW micrograph shows the fractured partially-punched out center of the specimen with no view of the shear fracture surface.**

Specimens of single crystal (SC) and polycrystalline (P) W from the PHENIX program were tested after neutron irradiation with no additional thinning (**Figure 95**). All samples were 3 mm diameter 0.5 mm thick with 4 to 1 ratio of span to thickness. The SCW specimen was cut with the (110) plane at the tension surface. The W specimens irradiated to 0.3 dpa and 0.7 dpa fractured in a brittle manner and exhibited similar strengths to the non-irradiated W samples. The specimens that were irradiated near 1000 °C for 94 days had slightly higher strengths than the 800 °C specimens at the same fluence. Due to the brittleness of these thicker specimens, they will be tested at smaller thicknesses near the 8 to 1 ratio in the future. The SCW fractures through preferred slip systems in the {110} planes; its critical resolved shear stress depends on the Schmid factor of the induced slip. Future testing will keep the single crystal orientation constant. For these specimens, only the non-irradiated single crystal specimen was ductile at room temperature, and the strength decreased with dose and temperature.



**Figure 95. Results of the 3-point bend test of irradiated specimens at a 4:1 span:thickness ratio. PCW with 1.5 μm grain size shown by circles. SCW with (110) face at the tension surface shown by triangles. Color corresponds to dose: black = 0 dpa, orange = 0.30 dpa, red = 0.70 dpa.**

### 13. HFIR IRRADIATION PROGRAM

#### 13.1 CAPSULE DESIGN FOR FRONTIER TASK 1 HFIR IRRADIATIONS

N. Russell ([russellng@ornl.gov](mailto:russellng@ornl.gov)), A.M. Schrell, and P. Champlin

##### OBJECTIVE

The Fusion 2021 Frontier Task 1 irradiation program plans to irradiate 13 capsules, 7 designed to contain 3 mm diameter disc specimens and 6 to contain fracture toughness specimens. These irradiation capsules are designed to reach temperatures 300 °C, 500 °C, and 800 °C during one and three HFIR cycles. The capsules will include tungsten, tungsten alloys, and tungsten laminated composite materials.

##### SUMMARY

The Fusion 2021 Frontier Task 1 irradiation program has two different capsule designs to accommodate 3 mm diameter disc specimens and fracture toughness specimens. Each of these capsule designs reach target temperatures by optimizing the size of the insulating gas gap between the specimen holders and capsule housing. Images of the thermal analyses for the two capsule formats are shown in **Figure 96**. In addition to the fracture toughness specimens, this design allows for a tungsten fiber irradiation option. This option permits a line of three specimens to be replaced by a tungsten container with a bundle of tungsten fibers.

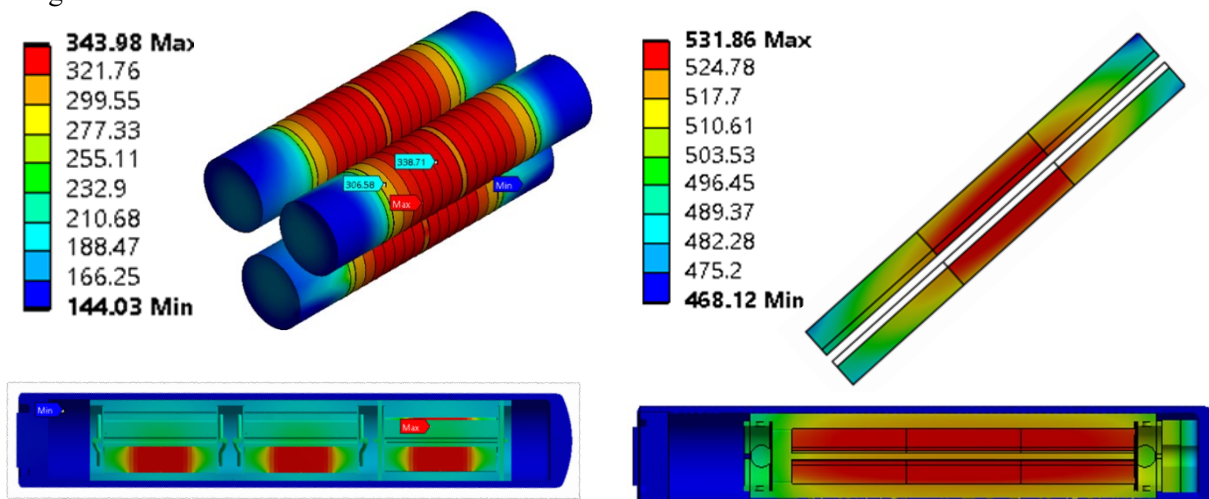


**Figure 96. Representative thermal analysis of Frontier Task 1 tungsten irradiation capsules with 3 mm diameter disc design (left) and fracture toughness design (right) for irradiation in HFIR.**

##### PROGRESS AND STATUS

The 3 mm diameter disc and fracture toughness formats are entirely new designs. Throughout the last year, both designs have a fully approved package of engineering drawings as well as thermal safety calculations for insertion in HFIR. Parts for these irradiation capsules have been ordered, received, and inspected. The one cycle fracture toughness capsules have been built and will be ready for insertion in HFIR cycle 496. The part layout is shown in **Figure 97**, and the fiber container with K doped W fibers is shown in **Figure 98**. One of the 3 mm diameter disc capsules is being assembled currently and will also be inserted in cycle 496. Assembly parts for this capsule are shown in **Figure 99**.

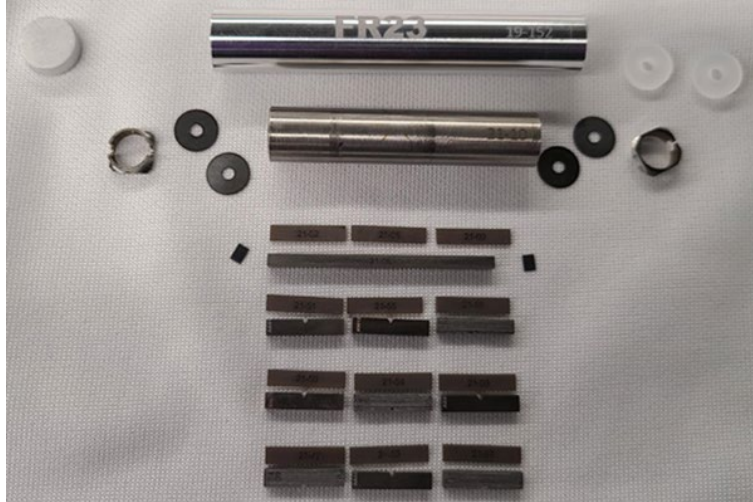


Figure 97. Frontier Task 1 W fracture toughness capsule build, with fiber option.



Figure 98. W fiber container with fiber specimens prior to fiber ends trimmed.

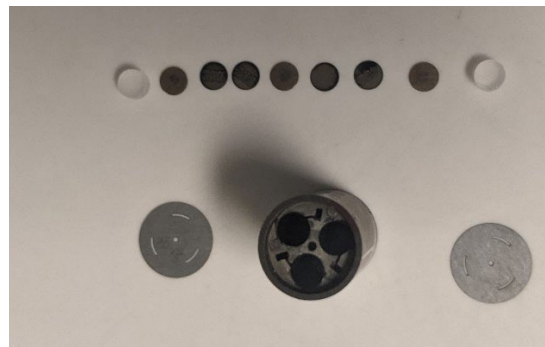


Figure 99. FR32 – 3mm diameter disc capsule parts at beginning of assembly.

### 13.2 CAPSULE DESIGN FOR FRONTIER TASK 2 HFIR IRRADIATIONS

P. Champlin ([champlinpa@ornl.gov](mailto:champlinpa@ornl.gov)), and N. Russell

#### OBJECTIVE

The Fusion 2021 Frontier Task 2 irradiation program plans to irradiate 14 capsules designed to accommodate 6 mm diameter disc specimens. These irradiation capsules are designed to reach temperatures ranging from 300 °C to 800 °C for one and three HFIR cycles, with a specimen loading that includes tungsten, tungsten alloys, and tungsten laminated composite materials.

#### SUMMARY

The Fusion 2021 Frontier Task 2 irradiation program plans to irradiate 6 mm diameter tungsten disc specimens. The capsule design uses a flat disk configuration for better temperature distribution. The design has target average specimen temperatures of 300°C, 500°C, and 800°C. The design incorporates a tungsten coating on SiC components in contact with the specimens to ensure that no reaction will occur with the specimens. Images of the thermal analysis for the 6 mm format are shown in *Figure 100*.

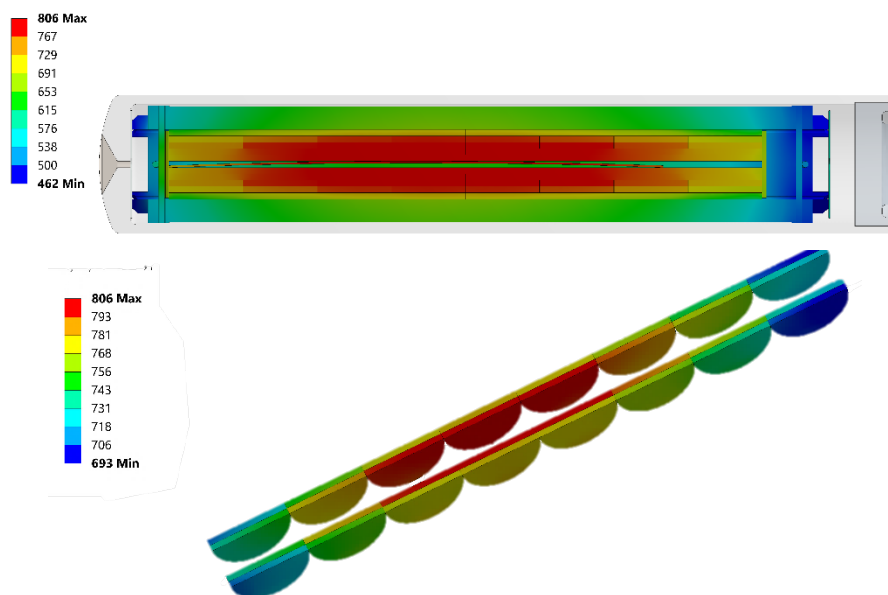


**Figure 100. Representative thermal analysis of Frontier Task 2 tungsten irradiation capsules with 6 mm diameter disc design for irradiation in HFIR.**

#### PROGRESS AND STATUS

The 6 mm disk format was adapted from an existing design that bounds the irradiation conditions for tungsten specimens. The capsules have been built and are being checked prior to delivery to HFIR. These capsules are planned for irradiation beginning in HFIR cycle 496. Layouts for these capsule parts and specimens prior to assembly and delivery to HFIR are shown in *Figure 101* and *Figure 102*.

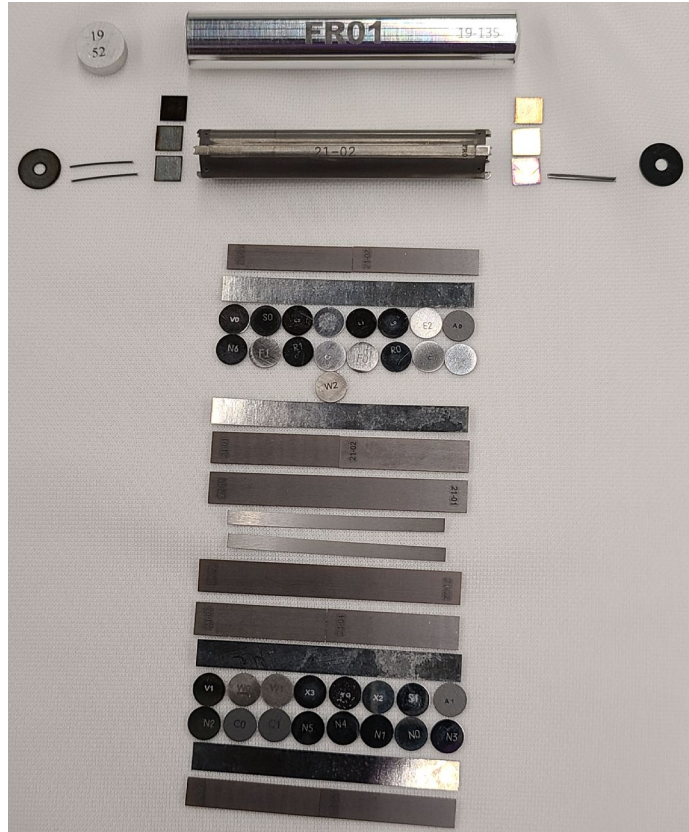


Figure 101. Layout of Frontier 6 mm diameter disc capsule prior to assembly.



Figure 102. W and W/Cu 6 mm diameter disc specimens.

### 13.3 FRONTIER TASK 3 – HFIR LIQUID METAL COMPATIBILITY CAPSULE

N. Russell ([russellng@ornl.gov](mailto:russellng@ornl.gov))

#### OBJECTIVE

The Fusion 2021 FRONTIER Task 3 irradiation program is directed at determining the compatibility of structural metals with liquid metal during irradiation. The plan is to irradiate five capsules with a design temperature of 400°C. Capsule loading will include FeCrAl tensile specimens and Sn shot designed to melt and interact with the specimens.

#### SUMMARY

The Fusion 2021 FRONTIER Task 3 irradiation program plans to irradiate FeCrAl tensile specimens submerged in molten Sn to determine corrosion effects occurring during neutron irradiation. The capsule design uses a sealed molybdenum holder to provide secondary containment within the aluminum housing. The target average specimen temperature is 400°C for one HFIR cycle. Images of the thermal analysis for the molten Sn corrosion design are shown in *Figure 103*.

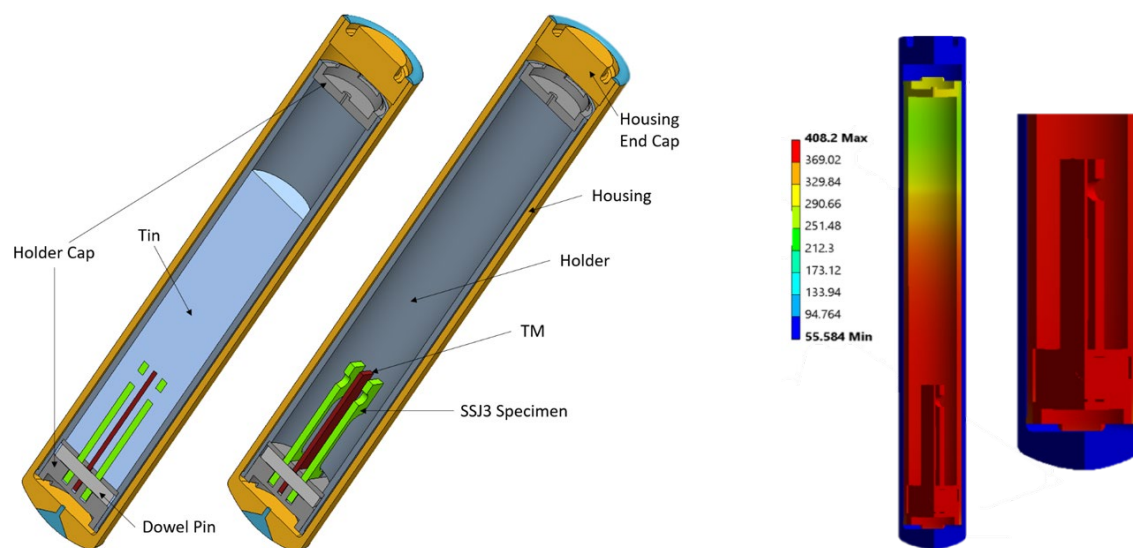


**Figure 103.** CAD representation (left) with Sn hidden for ease of viewing and representative thermal analysis (right) of Frontier Task 3 molten Sn corrosion irradiation capsules.

#### PROGRESS AND STATUS

The capsule design is complete. Parts and specimens for these capsules have been delivered. A few extra sets of parts will be assembled and used for destructive out-of-pile testing to confirm reliability of the experiment as well to allow the hot cell operators an opportunity to test disassembly prior to working on the irradiated capsules. A draft documenting the thermal safety calculations is underway. Internal parts and specimens for these capsules are shown in *Figure 104* and *Figure 105*.

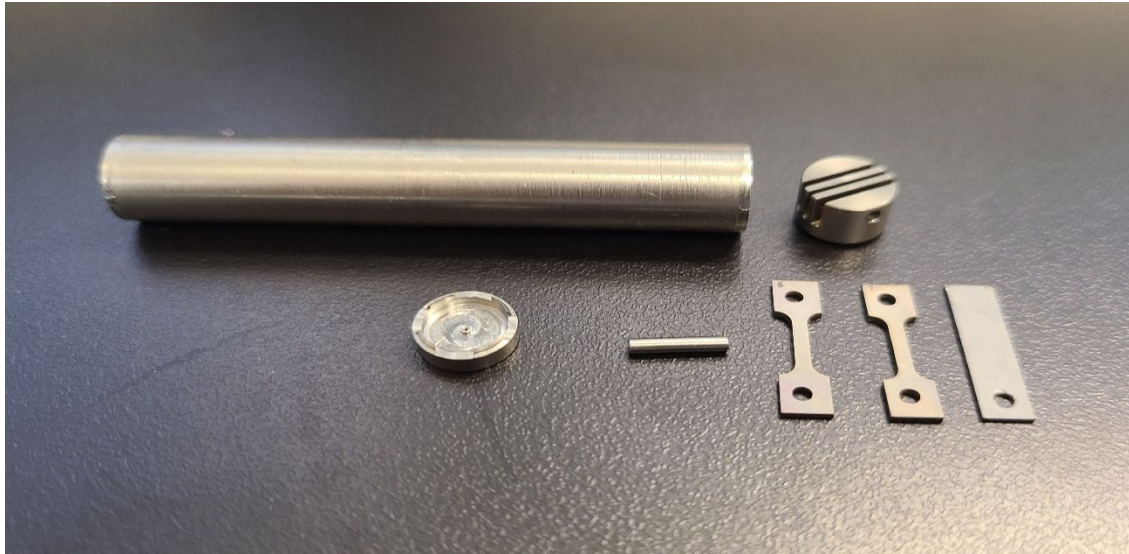


**Figure 104. Frontier Task 3 molten Sn rabbit capsule internal parts.**



**Figure 105. Frontier Task 3 molten Sn rabbit capsule specimen region assembly.**

### 13.4 CAPSULE DESIGN FOR THE QST IRRADIATION OF F82H STEEL IN HFIR

N. Russell ([russellng@ornl.gov](mailto:russellng@ornl.gov))

#### OBJECTIVE

The DOE-QST Fusion Collaboration plans to irradiate RAFM steel in HFIR in 21 capsules with design temperatures of 300°C, 400°C, and 500°C. These irradiations will include 3 low dose (5 dpa) capsules and 18 high dose (50 and 80 dpa) capsules. Capsule loading will include tensile and bend bar specimens of F82H.

#### SUMMARY

The Fusion 2021 QST F82H irradiation program plans to irradiate 21 capsules. Three of these capsules (1 tensile and 2 bend bar) are low dose (5 dpa) capsules that will be irradiated first to verify that target temperature can be successfully achieved. With successful results, the irradiation of the remaining 18 capsules (6 tensile and 12 bend bar) to high dose (50 and 80 dpa) will begin. These capsules are using the general SSJ tensile (GENTEN) and general M4PCCVN multi-notch bend bar (GENBEN) designs.

#### PROGRESS AND STATUS

The designs are approved for use in the reactor and the holder design diameters have been determined and the experiments approved by the project PI and QST representative. Capsule parts and specimens for the 2 capsule types are shown in layout in *Figure 106* and *Figure 107*. The low dose capsules began irradiation in HFIR cycle 490. The high dose tensile capsules are currently being built with the 80 dpa capsules planned to start irradiation in HFIR cycle 496.

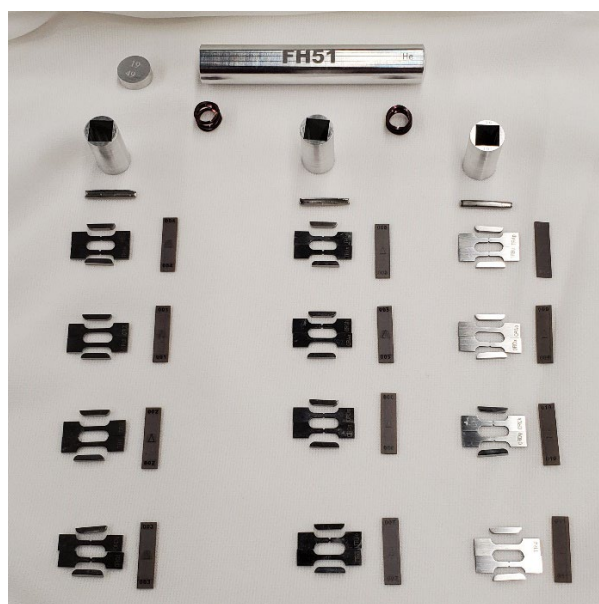


Figure 106. Components for the FH51 low dose tensile capsule during assembly.



**Figure 107. FH62 low dose bend bar capsule components during assembly.**

### 13.5 HFIR IRRADIATION EXPERIMENTS

C. On ([oncl@ornl.gov](mailto:oncl@ornl.gov)), J. W. Geringer, and J. L. McDuffee

#### SUMMARY

Neutron irradiation experiments in support of the research and development of fusion reactor materials are performed using various irradiation facilities in the High Flux Isotope Reactor (HFIR). The reactor operating history for the period October 1, 2020 to September 30, 2021 included continuation of a long shutdown until March of 2021. Operating details after restart are given in **Table 13** and consists of five operating cycles.

**Table 13. HFIR operating record for FY2021**

Cycle Number	Cycle End Date	Power (MWD)
490*	March 27	2107.27
491	May 8	2163.95
492	June 20	2165.66
493	July 25	2184.03
494	September 4	2195.21

\*Cycle was in three parts, due to reactor scrams. Cycle 490A achieved 6.90 MWD, 490B 22.33 MWD, and cycle 490C was 2107.27 MWD.

Eighteen target zone rabbit capsules remain in the reactor to complete scheduled irradiations. These capsules are listed in **Table 14** along with condensed information on the material, specimen type, temperature, fluence, and period of irradiation. Twenty-three rabbits have completed the scheduled irradiation as shown in **Table 15**.

**Table 14. The rabbit capsules to continue irradiation in HFIR**

Experiment Designation	Primary Materials	Specimen Types	Irradiation Temperature (°C)	Max Exposure (dpa)	Number of Reactor Cycles	HFIR Cycles Start – End
F13B4	FeCrAlY Steel	Tensile	300	50	29	451 - 497
FMP07	F82H	Tensile	300	20	11	487 - 497
FMP08	F82H	Tensile	300	80	45	487 - 531
FMP11	F82H	Tensile	385	20	21	488 - 508
FMP12	F82H	Tensile	385	80	45	488 - 532
FMP14	F82H	Tensile	525	20	21	484 - 504
FMP17	F82H	Tensile/MPC*	650	80	45	484 - 528
FMP22	F82H	Bend Bars	300	20	21	488 - 508
FMP23	F82H	Bend Bars	300	80	45	488 - 532
JCR11-03	SiC/SiC	Mini bend bars	950	200	100	487 - 586
JCR11-05	SiC/SiC	Mini bend bars	950	200	115	444 - 568
JCR11-08	SiC/SiC	Mini bend bars	950	200	115	444 - 560
JCR11-11	SiC/SiC	Mini bend bars	950	100	55	448 - 524
SCF4	SiC/SiC	Miniature flexure bar	250	100	90	457 - 547
SCF5	SiC/SiC	Miniature flexure bar	250	200	45	457 - 511

SCF8	SiC/SiC	Miniature flexure bar	600	100	45	457 - 502
SCF9	SiC/SiC	Miniature flexure bar	600	200	90	457 - 548
SCF11	SiC/SiC	Miniature flexure bar	950	100	57	458 - 517

\*MPC= Multi-Purpose Coupon

**Table 15. The rabbit capsules that completed irradiation in FY2021**

Experiment Designation	Primary Materials	Specimen Types	Irradiation Temperature (°C)	Max Exposure (dpa)	Number of Reactor Cycles	HFIR Cycles Start – End
ES01	EUROFER 97	Tensile/MPC*	220	20	12	479 - 491
ES02	EUROFER 97	Tensile/MPC*	275	20	12	480 - 492
ES03	EUROFER 97	Tensile/MPC*	275	20	12	479 - 491
ES04	EUROFER 97	Tensile/MPC*	300	20	12	479 - 491
ES05	EUROFER 97	Tensile/MPC*	325	20	12	479 - 491
ES06	EUROFER 97	Tensile/MPC*	350	20	12	479 - 491
ES07	EUROFER 97	Tensile/MPC*	375	20	12	479 - 491
ES11	EUROFER 97	Bend bars	220	20	12	479 - 492
ES12	EUROFER 97	Bend bars	240	20	12	479 - 492
ES13	EUROFER 97	Bend bars	275	20	12	479 - 492
ES14	EUROFER 97	Bend bars	300	20	12	479 - 492
ES15	EUROFER 97	Bend bars	325	20	12	479 - 494
ES16	EUROFER 97	Bend bars	350	20	12	479 - 494
ES17	EUROFER 97	Bend bars	375	20	12	479 - 494
FH51	F82H-IEA, F82H-BA12	Tensile	300	5	3	490 - 492
FH61	F82H-IEA, F82H-BA12	Bend bars	300	5	4	490 - 493
FH62	F82H-IEA, F82H-BA12	Bend bars	300	5	4	490 - 493
FMP16	F82H	Tensile/MPC*	650	20	11	484 - 494
JCR11-07	SiC/SiC	Mini bend bars	950	100	47	444 - 492
VNH1	W, Graphite, SiC, V	Disk	400	0.1	31.5**	490 - 490
VNH2	W, Graphite, SiC, V	Disk	400	0.02	6.24**	490 - 490
VH01	W, Graphite, SiC, V	Disk	400	01	31.5**	490 - 490
VH02	W, Graphite, SiC, V	Disk	400	0.02	6.24**	490 - 490

\*MPC= Multi-Purpose Coupon

\*\*Irradiation time in hours instead of cycles

## **14. AWARDS, HONORS AND RECOGNITION**

### **14.1 AWARDS DURING FY2021**

Yutai Katoh was promoted to ORNL Corporate Fellow, “For revolutionizing the understanding of radiation interactions with metals and ceramic in nuclear energy applications and outstanding leadership and mentoring of the next generation of scientists.”

## 14.2 PUBLICATION HONORS IN FY2021

The *Journal of Nuclear Materials* listed as one of the most downloaded articles the paper:

Koyanagi, T., Terrani, K., Harrison, S., Liu, J., & Katoh, Y., “Additive manufacturing of silicon carbide for nuclear applications,” *Journal of Nuclear Materials*, 543 (2021) 152577.

### 14.3 PROFESSIONAL RECOGNITION IN FY2021 AND CONTINUING

Anne Campbell:

- Assistant Technical Chair MiNES (Oct 2019-Nov 2021) (Will automatically move to Technical Chair Nov 2021-2023, then General Chair 2023-2025).
- Lead organizer, symposium “Composite Materials for Nuclear Applications”, TMS Annual Meeting 2021.
- Member, Organizing Committee of INGSM-21 (International Nuclear Graphite Specialists Meeting).
- Member, Editorial Board of “Materials Today Communications”.

Frank Chen:

- Co-chair, ASTM subcommittee E08.07.06 in charge of ductile-brittle transition fracture toughness standard (ASTM E1921).
- Co-chair, ASME 2021 PVP conference MF-06-02 session “Materials and Technologies for Nuclear Power Plants”.

Lauren Garrison:

- Organized the Nuclear Composites Symposium at TMS 2021.
- Organizing the Refractory Metals Symposium for TMS 2022.
- Vice Chair, ANS Fusion Energy Division.
- Chaired the Student Paper Competition at TOFE 2020.
- Member, Organizing Committee for TOFE 2022.

Yutai Katoh:

- International Advisory Board, Materials Challenges in Alternative & Renewable Energy (MCARE 2020), July 2021.
- International Steering Committee, The 8th International Ceramic Congress (ICC-8), April 2021, Busan, Korea.
- International Steering Committee, Pacific Rim Conference on Ceramic and Glass Technology, (PACRIM 14), May 2021, Vancouver.
- International Advisory Board, International Ceramics Congress and Forum on New Materials (CIMTEC 2021), June 2021, Italy.
- International Advisory Board, CIMTEC 2022 - 4th International Conference “Materials Challenges for Sustainable Nuclear Fission and Fusion Technologies,” Perugia, Italy June 20-29, 2022.

Takaaki Koyanagi:

- Lead organizer for symposium S13 “Development and Applications of Advanced Ceramics and Composites for Nuclear Fission and Fusion Energy Systems,” 45<sup>th</sup> International Conference and Expo on Advanced Ceramics and Composites, ICACC.
- Member, Brookhaven National Laboratory NSLSII Technical Review Panel for beam time proposals, high-energy X-ray diffraction experiments.

Chad Parish:

- Executive Committee, The Microanalysis Society.

- International Advisory Committee, International Conference on Fusion Reactor Materials, ICFRM-21, October 2023, Granada, Spain.

## 15. PUBLICATIONS AND PRESENTATIONS IN FISCAL YEAR 2021

### 15.1 PAPERS PUBLISHED IN FY21 – alphabetically by first listed ORNL Fusion Materials Program coauthor

Arunodaya Bhattacharya, Jean Henry, Brigitte Décamps, Steven J. Zinkle, Estelle Meslin, “Helium causing disappearance of  $a/2\langle 111 \rangle$  dislocation loops in binary Fe-Cr ferritic alloys,” *Journal of Nuclear Materials* 556 (2021) 153213

Y.R. Lin, A. Bhattacharya, D. Chen, J.J. Kai, J. Henry, S.J. Zinkle,” Temperature-dependent cavity swelling in dual-ion irradiated Fe and Fe-Cr ferritic alloys,” *Acta Mater.* 207 (2021) 116660, <https://doi.org/10.1016/j.actamat.2021.116660>

Edmondson, P. D., Gault, B., & Gilbert, M. R. “An atom probe tomography and inventory calculation examination of second phase precipitates in neutron irradiated single crystal tungsten,” *Nuclear Fusion* 60 (2020) 126013. <https://doi.org/10.1088/1741-4326/abb149>

E.A.I. Ellis, M.A. Sprayberry, C. Ledford, J.P. Hankwitz, M.M. Kirka, C.D. Rock, T.J. Horn, Y. Katoh, Ryan R. Dehoff, “Processing of tungsten through electron beam melting,” *J. Nucl. Mater.*, 555 (2021) 153041

C. Fan, Y. Katoh, X. Hu, “Impact of helium irradiation on the crystallographic orientation change in single-crystalline tungsten,” *Nucl. Fusion*, 61 (2021) 076011

Fan, C., Li, C., Parish, C. M., Katoh, Y., & Hu, X. “Helium effects on the surface and subsurface evolutions in single-crystalline tungsten,” *Acta Materialia*, 203 (2021) 116420

Akiyoshi, M., Garrison, L. M., Geringer, J. W., Wang, H., Hasegawa, A., Nogami, S., & Katoh, Y. “Thermal diffusivity of irradiated tungsten and tungsten-rhenium alloys,” *Journal of Nuclear Materials*, 543 (2021) 152594, <https://doi.org/10.1016/j.jnucmat.2020.152594>

Miyazawa, T., Garrison, L. M., Geringer, J. W., Echols, J. R., Fukuda, M., Katoh, Y., Hinoki, T., & Hasegawa, A., “Tensile properties of powder-metallurgical-processed tungsten alloys after neutron irradiation near recrystallization temperatures,” *Journal of Nuclear Materials*, 542 (2020) 152505, <https://doi.org/10.1016/j.jnucmat.2020.152505>

Nathan Reid, Lauren Garrison, Maxim Gussev, “Design and analysis of an advanced three-point bend test approach for miniature irradiated disk specimens,” *Fusion Science and Technology* (2021), <https://doi.org/10.1080/15361055.2021.1925032>

H. Gietl, J. Riesch, M. Zielinski, T. Höschen, J.W. Coenen, S. Schönen, R. Neu, “Interlayer properties of tungsten fibre-reinforced composites and their determination by different methods,” *Nuclear Materials and Energy*, 28 (2021) 101060

Leonard Raumann, Jan Willem Coenen, Johann Riesch, Yiran Mao, Daniel Schwalenberg, Hanns Gietl, Christian Linsmeier, Olivier Guillon, “Improving the W coating uniformity by a COMSOL model-based CVD parameter study for denser W<sub>f</sub>/W composites,” *Metals*, 11-7 (2021) 1089 [*Special Issue Tungsten and Tungsten Alloys*]

L. Raumann, J.W. Coenen, J. Riesch, Y. Mao, D. Schwalenberg, T. Wegener, H. Gietl, T. Höschen, Ch. Linsmeier, O. Guillon, “Modeling and experimental validation of a W<sub>p</sub>/W-fabrication by chemical vapor deposition and infiltration,” *Nuclear Materials and Energy*, 28 (2021) 101048

M. Rieth, E. Simondon, G. Pintsuk, G. Aiello, J. Henryd, D. Terentyev, A. Puype, C. Cristalli, L. Pillonih, O. Tassa, M. Klimenkov, H.-C. Schneider, P. Fernandez, T. Graening, X. Chen, A. Bhattacharya, J. Reed, J.W. Geringer, M. Sokolov, Y. Katoh, L. Snead, “Technological aspects in blanket design: Effects of micro-alloying and thermo-mechanical treatments of EUROFER97 type steels after neutron irradiation,” *Fusion Engineering and Design*, 168 (2021) 112645

Sprouster, D. J., Trelewicz, J. R., Snead, L. L., Hu, X., Morrall, D., Koyanagi, T., Parish, C. M., Tan, L., Katoh, Y., & Wirth, B.D., “Advanced synchrotron characterization techniques for fusion materials. *Journal of Nuclear Materials*,” 543 (2021)152574, <https://doi.org/10.1016/j.jnucmat.2020.152574>

M.R. Gilbert, K. Arakawa, Z. Bergstrom, M.J. Caturla, S.L. Dudarev, F. Gao, A.M. Goryaeva, S.Y. Hu, X. Hu, R.J. Kurtz, A. Litnovsky, J. Marian, M-C Marinica, E. Martinez, E.A. Marquis, D.R. Mason, B.N. Nguyen, P. Olsson, Y. Osetskiy, D. Senor, W. Setyawan, M.P. Short, T. Suzudo, J.R. Trelewicz, T. Tsuru, G.S. Was, B.D. Wirth, L. Yang, Y. Zhang, S.J. Zinkle, “Prospectives on multiscale modelling and experiments to accelerate materials development for fusion,” *J. Nucl. Mater.* 554 (Oct. 2021) 153113, <https://doi.org/10.1016/j.jnucmat.2021.153113>

Omer Karakoc, Takaaki Koyanagi, Takashi Nozawa, Yutai Katoh, “Fiber/matrix debonding evaluation of SiCf/SiC composites using micropillar compression technique,” *Composites Part B* 224 (2021) 109189

Koyanagi, T., Terrani, K., Harrison, S., Liu, J., & Katoh, Y., “Additive manufacturing of silicon carbide for nuclear applications,” *Journal of Nuclear Materials*, 543 (2021) 152577, <https://doi.org/10.1016/j.jnucmat.2020.152577>

Koyanagi, T., Sprouster, D. J., Snead, L. L., & Katoh, Y., “X-ray characterization of anisotropic defect formation in SiC under irradiation with applied stress,” *Scripta Materialia*, 197 (2021) 113785, <https://doi.org/10.1016/j.scriptamat.2021.113785>

Takaaki Koyanagi, David J. Sprouster, Lance L. Snead, Yutai Katoh, “X-ray characterization of atomistic defects causing irradiation creep of SiC,” 2020 ANS Winter Meeting and Nuclear Technology Expo, peer reviewed Conference paper, (November 2020)

Li, H., Koyanagi, T., Ang, C., & Y. Katoh, “Electric current–assisted direct joining of silicon carbide,” *Journal of the European Ceramic Society*, 41-5 (2021) 3072-3081, <https://doi.org/10.1016/j.jeurceramsoc.2020.05.072>

Y. Osetsky, “Atomic-scale mechanisms of void strengthening in tungsten,” *Tungsten* 3 (2021) 65-71, <https://doi.org/10.1007/s42864-020-00070-6>

Y.N. Osetsky, “Strengthening of tungsten by coherent rhenium precipitates formed during low fluence irradiation,” *Tungsten*, (2021) <https://link.springer.com/article/10.1007/s42864-021-00088-4>

B.A. Pint, J. Jun, M. Romedenne, “Compatibility of SiC with ODS FeCrAl in flowing Pb-Li at 600°–700,” *Fusion Engineering and Design* 166 (2021) 112389

B. A. Pint and J. Jun, “Pre-oxidation to improve liquid metal compatibility,” *Oxidation of Metals* 96 (2021) 231-240, <https://doi.org/10.1007/s11085-021-10057-4>

B. A. Pint, J. Jun, E. Cakmak, D. J. Sprouster, N. Olynik and L. L. Snead, "Compatibility of FeCrAlMo in flowing Pb-Li at 600°-700°C," *Fusion Science and Technology*, (2021, on line and in press), DOI: [10.1080/15361055.2021.1898305](https://doi.org/10.1080/15361055.2021.1898305)

Masatoshi KONDO, Bruce A. PINT, Jiheon JUN, Nick RUSSELL, Joel McDUFFEE, Masafumi AKIYOSHI, Teruya TANAKA, Naoko OONO, Junichi MIYAZAWA, Josina W. GERINGER, Yutai KATOH and Yuji HATANNO, "Conceptual design of HFIR irradiation experiment for material compatibility study on liquid Sn divertor," *Plasma and Fusion Research: Regular Articles* 16 (2021) 2405040

T. Nozawa, H. Tanigawa, T. Kojima, T. Itoh, N. Hiyoshi, M. Ohata, T. Katoh, M. Ando, M. Nakajima, T. Hirose, J. D. Reed, X. Chen, J. W. Geringer, and Y. Katoh, "Status and the challenge of Japanese materials property handbook to facilitate structural design criteria for DEMO in-vessel components," *Nuclear Fusion* 61 (2021) 116054

G.D. Samolyuk, P.D. Edmondson, "First principles study of the stability and thermal conductivity of novel Li-Be hybrid ceramics," *Acta Materialia* 215 (2021) 117052

G. D. Samolyuk, Y.N. Osetsky, "Equilibrium distribution of point defects in Fe-Y-O as a typical representative of nanocluster-strengthened alloys", *J. Nucl. Matter.* 549 (2021) 152875, <https://doi.org/10.1016/j.jnucmat.2021.152875>

E. Zarkadoula, G. Samolyuk, Y. Zhang, W. J. Weber, "Electronic stopping in molecular dynamics simulations of cascades in 3C-SiC," *J. Nucl. Mater.* 540 (2020) 152371, <https://doi.org/10.1016/j.jnucmat.2020.152371>

L. Tan, T. Graening, X. Hu, W. Zhong, Y. Yang, S.J. Zinkle, Y. Katoh, "Effects of carbonitrides and carbides on microstructure and properties of castable nanostructured alloys," *Journal of Nuclear Materials* 540 (2020) 152376

L. Tan, J.D. Poplawsky, Y. Yang, "Effects of niobium and tantalum on microstructure and strength of ferritic-martensitic steels," *Mater. Sci. Eng. A* 807 (2021) 140900

B.K. Kim, L. Tan, H. Sakasegawa, C.M. Parish, W. Zhong, H. Tanigawa, Y. Katoh, "Effects of helium on irradiation response of reduced-activation ferritic-martensitic steels: Using nickel isotopes to simulate fusion neutron response," *J. Nucl. Mater.* 545 (2021) 152634

Yan-Ru Lin, Wei-Ying Chen, Lizhen Tan, D.T. Hoelzer, Zhanfeng Yan, Cheng-Yu Hsieh, Chun-Wei Huang and S.J. Zinkle, "Bubble formation in helium-implanted nanostructured ferritic alloys at elevated temperature," *Acta Materialia* 217 (2021) 117165, <https://doi.org/10.1016/j.actamat.2021.117165>

Wang, K., Parish, C. M., Field, K. G., Tan, L., & Katoh, Y. "Segregation behavior and phase instability of Eurofer97 after neutron irradiation to 72 dpa," *Journal of Nuclear Materials*, 547 (2021) 152834, <https://doi.org/10.1016/j.jnucmat.2021.152834>

Bin Cheng, Ling Wang, David J. Sprouster, Jason R Trelewicz, Weicheng Zhong, Ying Yang, Steven J. Zinkle, and Lance L. Snead, "Tailoring microstructure in sintered Cu-Cr-Nb-Zr alloys for fusion components," *J. Nucl. Mater.* 551 (2021) 152956, <https://doi.org/10.1016/j.jnucmat.2021.152956>

Zhong, W., Tan, L., “Radiological analysis and transmutation calculation of representative castable nanostructured alloys,” *Fusion Engineering and Design*, 160 (2020) 111899, <https://doi.org/10.1016/j.fusengdes.2020.111899>

## 15.2 REPORTS ISSUED IN FY21

F.W. Wiffen, Y. Katoh, S. Melton, “Fusion Materials Research at Oak Ridge National Laboratory in Fiscal Year 2020,” ORNL/TM-2020/1837, December 2020

Yutai Katoh, Nasr Ghoniem, Jaime Marian, Bob Odette, Lance Snead, Jean Paul Allain, Jason Trelewicz, Brian Wirth, Bill Wiffen, Rick Kurtz, Steve Zinkle, “Summary Report on the Refined User Requirements for U.S. Fusion Prototypic Neutron Source,” VLT-2021-001 (ORNL/TM-2021/1972), April 2021

Chad Parish, Lauren Garrison, Ezekial Unterberg. “Priority Research Directions for Fusion Plasma-Materials Interactions: A Materials Science Perspective” ORNL/TM-2020/1768

----- Fusion Materials Semiannual Progress Report for the Period Ending December 31, 2020, DOE-ER-0313/69 (ORNL/SPR-2021/2151), March 2021

----- Fusion Materials Semiannual Progress Report for the Period Ending June 30, 2021, DOE-ER-0313/70 (ORNL/SPR-2021/1910), August 2021

**15.3 PAPERS SUBMITTED IN FY21**

L. M. Garrison, Y. Katoh, T. Hinoki, N. Hashimoto, J. R. Echols, J. W. Geringer, N. C. Reid, J. P. Allain, B. Cheng, D. Dorow-Gerspach, V. Ganesh, H. Gietl, S. A. Humphry-Baker, E. Lang, I. McCue, J. Riesch, L. L. Snead, G. D. W. Smith, J. R. Trelewicz, Y. Yang, S. J. Zinkle. “Materials development for FRONTIER US-Japan collaboration,” submitted to *Physica Scripta*

CM Parish, A Bhattacharya and A. Plotkowski, “An approach to high-throughput X-ray spectrum image mapping,” submitted to *Microscopy and Microanalysis*

CM Parish, “Cluster analysis of combined EDS and EBSD data to solve ambiguous phase identifications,” accepted by *Microscopy and Microanalysis*

N. Olynik, B. Cheng, DJ Sprouster, CM Parish, and JR Trelewicz, “Microstructural Transitions during Powder Metallurgical Processing of Solute Stabilized Nanostructured Tungsten Alloys,” accepted by *Metals*

**15.4 PRESENTATIONS DELIVERED IN FY21** – *all FY21 presentations were remote, at virtual conferences or other remote-connection events*

**NuMat2020: The Nuclear Materials Conference, October 26-30, 2020**

***Oral Presentation***

Hanns Gietl, Takaaki Koyanagi, Ying Yang, Yutai Katoh, “Design and strategy of tungsten based refractory material composite for fusion applications”

**Technology of Fusion Energy Conference (TOFE) 2020, November 16-19, 2020**

***Contributed Oral Presentation***

John Echols, Lauren Garrison, Yutai Katoh. “Effects of neutron radiation on electrical resistivity of tungsten”

Lauren Garrison. “Highlights of the Fusion, Plasma, and Technology Community Planning Process Report”

Nathan Reid, Lauren Garrison, Maxim Gussev, Jean Paul Allain. “Design and analysis of an advanced three-point bend test approach for miniature irradiated disk specimens”

**Webinar for the Microanalysis Society, December 2020**

***Invited Oral Presentation***

CM Parish, “Transmission Kikuchi Diffraction 101”

**45<sup>th</sup> International Conference and Expo on Advanced Ceramics and Composites (ICACC2021) – February 8-11, 2021**

***Oral Presentation***

Hanns Gietl, Takaaki Koyanagi, Ying Yang, Yutai Katoh, “Design and strategy of tungsten based refractory material composite for fusion applications”

**TMS 2021 Annual Meeting and Exhibition, March 15-18, 2021**

***Invited Presentation in the symposium “Mechanical Behavior of Nuclear Reactor Components”***

Yukinori Yamamoto, Roger G. Miller, Arthur F. Rowcliffe, “Development of modified 3Cr-3WVTa base bainitic steels for fusion structural applications”

***Oral Presentation***

John Echols, Amy Eliot, Lauren Garrison, M. Delmas, Yutai Katoh. “Densification of Binder Jetted Tungsten through Chemical Vapor Infiltration for Fusion Energy Application”

**18th International Conference on Plasma-Facing Materials and Components for Fusion Applications (PFMC-18), May 17-21, 2021**

***Invited Oral Presentation***

L. M. Garrison, Y. Katoh, T. Hinoki, N. Hashimoto, J. R. Echols, J. W. Geringer, N. C. Reid, J. P. Allain, B. Cheng, D. Dorow-Gerspach, V. Ganesh, H. Gietl, S. A. Humphry-Baker, E. Lang, I. McCue, J. Riesch, L. L. Snead, G. D. W. Smith, J. R. Trelewicz, Y. Yang, S. J. Zinkle. “Development of plasma-facing material joints and composites for neutron irradiation in the FRONTIER US-Japan collaboration”

***Contributed Oral Presentation***

Daniel Morrall et al., “Void swelling and transmutation in tungsten metals and alloys after fusion relevant neutron irradiation”

***Poster Presentations***

John Echols et al., “Effects of Grain Elongation on Electrical Resistivity of Neutron Irradiated Tungsten”

Wendy Garcia et al., “Helium and Oxygen Depth Profiling in Tungsten Exposed to Helium Plasma in WEST Measured by Laser Induced Breakdown Spectroscopy and Laser Ablation Mass Spectrometry”

Hanns Gietl, Takaaki Koyanagi, Ying Yang, Yutai Katoh, “Design and strategy of tungsten based refractory material composite for fusion applications”

Bruce Pint, Jiheon Jun, “Liquid Metal Compatibility Evaluations for Sn and Li Plasma-Facing Concepts”

Nathan Reid et al., “Miniature mechanical testing of candidate fusion material joints and composites”

***THERMEC'2021 International Conference on Processing & Manufacturing of Advanced Materials, June 1-5, 2021******Invited Oral Presentations***

Xiang (Frank) Chen, Logan Clowers, Mikhail A. Sokolov, Keven Field, Andrew Nelson, Yutai Katoh, “Novel Miniature Bend Bar Testing Technique for Fracture Toughness Characterization of Materials for Fusion and Fission Reactors”

Chad M. Parish, Kun Wang, Russell Doerner, Matthew Baldwin, Fred Meyer, Mark Bannister, Daniel Morrall, and Yutai Katoh, “Application of electron microscopy to study plasma-materials interactions”

Steven J. Zinkle, Lizhen Tan, Caleb P. Massey, “Development of advanced high-performance radiation-resistant ferritic/martensitic steels”

***Tungsten 2021, June 21-24, 2021, Orlando, FL******Contributed Oral Presentation***

E.A.I. Ellis et al., “Structure Property Relationships of Refractory Metals Fabricated Using Electron Beam Powder Bed Fusion”

**Second MPEX Users' Research Forum, September 2021**

***Invited Oral Presentations***

CM Parish and M Baldwin, "Tungsten Fuzz Precursors and Evolution"

W. Zhong and X. Hu, "Interpretation of Thermal Desorption Results of Hydrogen and Helium in Tungsten"